ELECTRONIC TRANSPORT IN TOPOLOGICAL AND STRONGLY CORRELATED SYSTEMS

A Dissertation
Presented to the Faculty of the Graduate School
of Cornell University
in Partial Fulfillment of the Requirements for the Degree of
Doctor of Philosophy

by
Aaron Wan-Hin Hui
Aug 2021

ELECTRONIC TRANSPORT IN TOPOLOGICAL AND STRONGLY CORRELATED SYSTEMS

Aaron Wan-Hin Hui, Ph.D.
Cornell University 2021

In this dissertation, we attack the problem of strongly correlated and topological systems via a creative variety of approaches in the hopes of extracting and elucidating meaningful electronic transport phenomena.

In the first part, we study the long-standing puzzle of the anomalously large and superuniversal correlation length exponent ν in the fractional quantum Hall effect. To tackle this, we utilize the newly conjectured Chern-Simons dualities as a powerful non-perturbative tool. By exploring the new descriptions of FQHE transitions afforded by the dualities, we find that large flavor expansions compare unfavorably to the experimental ν. However, the non-Abelian nature of these dualities motivated us to try large color expansions. Utilizing duality techniques in combination with modular transformations, we were able to use large color expansions to demonstrate superuniversality across FQHE transitions. This was the first theoretical demonstration of superuniversality, as well as one of the first uses of the non-Abelian Chern-Simons dualities.

In the second part, we critically examine transport features of the strongly-correlated electron hydrodynamic regime. Electron hydrodynamics has been claimed to be observed in a number of experiments, generating much excitement. However, clear demonstration of this regime is tricky since direct measurement of the electron-electron scattering length is difficult. Measurements of non-local transport behavior have been argued to be a signature of viscous

flow and therefore provide indirect evidence of a short electron-electron scattering length. We begin by showing, on the contrary, that non-local transport behavior can occur even for disordered non-interacting fermionic systems which sits far from the hydrodynamic regime. Therefore, non-local transport is not unique to hydrodynamics. Furthermore, the linearized Navier-Stokes equation is structurally equivalent to common momentum-dependent Ohm's law; disentangling the hydrodynamic contribution requires precise understanding of the phenomenological parameters. By contrast, the fully nonlinear Navier-Stokes equation is distinct from the linear Ohm's law and can give rise to distinctive signatures. We therefore proposed three experiments to manifest unique nonlinear phenomena well-known in the classical fluids literature - the Bernoulli effect, Eckart streaming, and Rayleigh streaming. Analysis of experimental parameters suggests that these proposals are feasible and therefore provide strong signatures of a hydrodynamic regime. Moreover, as one of the first works to comprehensively study nonlinear effects, we hope that it would motivate further exploration of nonlinear electron fluid dynamics.

In the third part, we look for optical signatures of the chiral anomaly in Weyl semimetals. Direct detection of the chiral anomaly via a negative longitudinal magnetoresistance has been difficult as this signature can arise from other mechanisms. Other works have proposed anomalous IR reflectance signatures as a smoking gun for the chiral anomaly in non-mirror-symmetric Weyl semimetals. However, they neglected that the presence of a magnetic field, necessary for the chiral anomaly, will generically break mirror symmetries. We go on to argue that the background magnetic field can break mirror symmetry strongly enough in physical systems to yield observable IR signatures of the chiral anomaly, even for mirror-symmetric crystals.

In the fourth part, we study transport along topological domain wall networks in moiré systems. While most excitement around moiré physics have focused around the moiré miniband, recent experiments have suggest that moiré systems can also feature sharp domain walls and provide a natural setting to study networks of 1D topological modes. Previous works focused either on non-interacting models or utilized interacting models to find gapped correlated phases by imposing a single-particle gap. However, away from commensurate fillings we expect intervalley scattering to be suppressed so that a single-particle gap cannot open. Therefore, we study a triangular network of valley-helical Luttinger wires where we enforce no intervalley scattering. We find that transport in this network is inherently non-local, distinct from the local diffusive behavior of a resistor network. In particular, at strong repulsive interactions we predict a novel orbital antiferromagnetic-ordering phase.

BIOGRAPHICAL SKETCH

Aaron Hui was born and raised in Austin, Texas to two immigrants from Hong Kong. He attended Cornell University from 2011-2015 where he obtained a Bachelor of Science in Applied & Engineering Physics (AEP). During this time, he worked with Professor Jeevak Parpia in experimental physics on the non-linear dynamics of suspended graphene mechanical resonators. In the fall of 2015, he continued at Cornell University to pursue a Ph.D. also in AEP, working with Professor Eun-Ah Kim in theoretical condensed matter physics. As far as he knows, he is the first in his extended family to pursue any form of higher education. In his spare time, Aaron likes to sleep. He also enjoys spending time with friends, playing games, playing badminton, playing guitar, singing, and eating good food.

Dedicated to the Lord my God, my parents, my brother, and to my aunt 許玉琴
for whom I could not finish my PhD in time.

ACKNOWLEDGEMENTS

First and foremost, I'd like to thank my advisor Eun-Ah Kim for taking me on as a naïve and ignorant PhD student and shepherding me into someone a little less naïve and ignorant. Other than teaching me almost everything I know about being a researcher, she has also spent long hours and much energy in helping to advance my career and promote my work, encouraging me and pushing me to improve at every step. I am grateful that she is an advisor who deeply invests into her students and into their future. Additionally, I am thankful that she did not send me "across the bridge" to the high-energy folks, but continued to suggest a diverse set of problems for me to work on during my PhD.

I'd also like to thank my long-standing collaborators Mike Mulligan and Vadim Oganesyan. They have consistently helped me as I have worked through nitty-gritty calculational details. As I threw many of my half-baked ideas and (sometimes incorrect) results at them, they remained steady as wise sounding boards. Without them, I might still be spinning my wheels on some of our previous projects. Moreover, I am grateful that they took me under their wing though I was not their student, giving me advice and encouragement especially as my future career path seemed uncertain.

I am also deeply appreciative of Jeevak Parpia and his research lab - Bob de Alba, Abhilash Sebastian, Nikolay Zhelev. Prior to joining Jeevak's lab late in my undergraduate career, I still had no physics research experience. They showed me the physics world for the first time. If it wasn't for them, I may not have pursued a PhD in physics, much less condensed matter physics, and may have gone after math instead.

Thanks also to all the Cornell physics and AEP faculty and postdocs who have interacted with me. Special thanks to Tom Hartman and Sachin Jain, who

helped immensely to get my feet off the ground on my first project with Eun-Ah. Sachin particularly was helpful, patient, and available as I fumbled through the quantum field theory that I never thought I would use again. Thanks also to Brad, just across our office in Clark 535, who I've had to pleasure to discuss physics with and sometimes comes to chat with our office for fun. He has been a joy to share an office hallway with. I'd also like to thank my committee members Craig Fennie and Debdeep Jena for their time and effort in giving good feedback on my work during the A and B exams.

Of course, I also want to thank all my lab members - Kyungmin Lee, Yi-Ting Hsu, Andrej Mesaros, Jian-Huang She, Frank Yi Zhang, Jordan Venderley, Mike Matty, Eli Gerber, Peter Cha, Sam Lederer, Cole Miles, Kevin Zhang, Yiqing Zhou, Tim Skaras, and Krishna Mallayya - for all the physics discussions as well as making the PhD more enjoyable. Special thanks to Frank and Sam for working closely with me; it was fun to tackle physics problems together. I especially want to thank my office mates in Clark 535 - Jordan Venderley, Mike Matty, Eli Gerber, and Peter Cha - most of my best memories in the Kim group were made with you guys, whether that be our March meeting housing fiasco, the creation of beautiful emojis, or our futile attempts to remove the curséd clown sticker. I hope we will never forget that "stars, planets, and Man [sic] can suck energy through the vortex hole of our donuts, to increase our spinning in the clockwise direction."

Outside of physics, I also want to thank all the many teachers I have had over the years who have contributed in bringing me this far. In particular, I want to thank Sarah Griffin, Doug Skinner, MilyBett Llanos-Gremillion, Kelly Saenz, Paula Holmes, Jeff Mickel, Kimberly Fritch, and Shu-Yi Scott for being great teachers not only academically, but also in life.

There are many mentors who may not have been able to teach me academically, but have taught me about deeper aspects of life. Their wisdom has helped to preserve my sanity and keep the big picture in mind during my PhD. I'd like to thank Ricky Tam for being critical in setting my foundation of faith and how to live life; he has always been an example for me. I'd also like to thank Robert Chin (Uncle Bob) for helping to send me to Cornell and helping me to walk the fine line of academia and faith. Thanks to Dave Smith, who has faithfully discipled and walked alongside me for the majority of my time at Cornell, helping to grow me in maturity and wisdom. I will also miss learning about all of the random Ithaca history and about his clock collections. Thanks to my older prayer partner Yipu Wang for discipling me and for always keeping me in his prayers. Thanks also to (Pastor) Paul Epp and Hildy Epp for their love and care to me for all these years.

I'd also like to thank the many Cornellians and Ithacans who have supported and encouraged me during the past decade in Ithaca. This list is tremendous, so I apologize that I won't be able to explicitly list everyone here. I'd first like to thank Chinese Bible Study (CBS), who have been my close-knit family and my very heart during these Cornell years. I've overlapped and befriended 13 classes of CBSers, and have made the majority of my lifelong friends through CBS. I'd also like to thank my landlords Ray and Gretchen Crognale for their hospitality during the entire length of my PhD. Special thanks to Mike Cao for our long friendship and housemate-ship, as well as for staying behind in Ithaca with me for all these years. Thanks to the doctorates who have gone before me - Henry Wen, KK Yu, Kayla Nguyen, Nikolay Zhelev, and Mark Dong - for giving me lots of PhD-related advice. Special thanks also to the PSB party crew who made working in PSB much more fun; in particular thanks to Aaron Chen for crowning me King of PSB and for Helen Kwon for keeping up the PSB party hype.

There are a number of particular Cornell friends that I would like to highlight. Thanks to Vanha Pham for keeping in close contact and for always bantering with me, to Zoe Chan for always being hype in my corner, and to Kelvin Lu for always asking "how are you" and for sharing life together. Thanks to my younger prayer partners Charlie Qian and Kevin Gao who have been a joy to disciple as we explored deep life questions and have also supported me in my life struggles. Thanks to Jevon Yu for letting me keep an account of his many stories, as well as for continually challenging me to grow in the Lord. Thanks to my "little sister" Stephanie Deng for her support and for lending her listening ear. Also thanks to Stephanie Deng, Darren Chang, and Lucy Lu for "co-graduating" with me and making my final COVID year much more enjoyable. Thanks to Deborah Liu, David Ho, Tim Hu, Kim Hui, Samantha Fung, Elbert Chang, and Mark Dong who have continued to be older siblings to me. I want to thank Melanie Lim, Newton Ni, Jeffrey Huang, Daegun Chung Kim, Nathalia Lie, Alice Zhao, Xinran Pan, Stephanie Chan, Joyce Wang, Katherine Jaw, Christine Loui, Cassie Jia, Zhijiang Li, and Frank Lin for their friendship and support. Thanks to the CBS '16 class for taking me in as an honorary member. Thanks again to all my Cornell friends who have been with me over these many years, who have supported me in all ways big or small.

I want to thank First Ithaca Chinese Christian Church (FICCC) for being my church home. In particular, I want thank the FICCC youth for making me continually feel young with their crazily abundant energy. Having served with the youth for the past 10 years, it has been a great joy to watch them mature and graduate high school and even college. They constantly remind me that there is more to life than my ivory tower. I also want to thank the youth parents for being supportive of me in all of my endeavors, whether related to their children or not. Special thanks to David Ng who has given me a lot of career and life advice.

There have also been many people from Austin who have continued to support me though I have been far away. Thanks to former and current members of Austin Chinese Church who have continually welcomed me home when I go back as if nothing has changed. I also want to thank all the Cantonese families who have loved and supported me, and always been so warm and hospitable and welcoming. Specific thanks to my friends Maytee Chantharayukhonthorn, Sierra Reed, Victoria Chu, and Kevin Tian for keeping in touch. Also, special thanks to my childhood friends Jon Lee, James Feng, Vicki Chiu, Rachel Chen, and Danielle (Dani) Cummings for a life's worth of friendship and support.

I would not have survived my PhD without the constant loving support of Felicia Setiono, who has seen me during my lowest lows these past six years. She is always willing to go above and beyond to care for me, whether it be make food or move her schedule around or take up extra tasks, when I am at times overwhelmed with life itself. Thanks for all the love and sacrifice, even when I'm being a potato.

I also want to thank all my extended family for their support. Though none of them reside in the Americas, much less the US, they have all continued to support me in their own ways. If it were not for the COVID pandemic, many of them would have made the long trip to be physically present for my graduation. It is uncommon for such a large extended family to continue to be tight-knit, especially since I only see them once a year at best, and I am extremely thankful for it.

I want to thank my parents and my brother for all their support. Being immigrants to the US, they not only raised me and my brother but gave their everything so that we could have the comfort and education that they didn't have growing up. Thanks to my mom for always cleaning and cooking and doing all the chores around the house. As she never complained, for the longest time I thought this was normal; I always wondered why other people's houses were not as spotless as my own. Thanks to my dad for not trusting the American public education system and pushing me to study more despite any resistance I may have had. He would always stay up late and put aside his own work to help my brother and I on our studies or anything else we may have needed help with. They spared no effort to allow me to even dream of being able to finish a PhD. I also want to thank my brother for helping me to relax and destress, whether that be through playing games together or just hanging out.

Finally, I want to thank my 二姑媽(許玉琴), my aunt who has loved me very dearly. She always made chicken soup for me every time I visited Hong Kong and wished for my best despite being so far away in Hong Kong. In particular, she wanted us to get the education she was never able to afford; my grandparents were never able to pay her fees for primary school on time, and she was publically mocked in class for it. My father was the first and only one to get a college degree in his entire family, and my aunt was the one who fought on his behalf to pursue college despite the financial challenges. As the first in my family to pursue a PhD, she was always rooting for me and waiting eagerly for my graduation. However, after a decade-long battle with cancer, she passed away in April 2019. I regret that I was not smart nor diligent enough to graduate in time for her to see it.

Thanks again to the many, many people who have encouraged me and supported me in this journey. Last but definitely not least, I thank the Lord for His sustaining hand. As it says in Psalms 3:5: “I lay down and slept. I woke again for the Lord sustained me.” This PhD would not have been possible without all of your support.

TABLE OF CONTENTS

LIST OF TABLES

LIST OF FIGURES

CHAPTER 1

INTRODUCTION

1.1 Overview

In the past 200 years, technological progress has been marked by our increasing control over the transport of electronic charge. Beginning with the light bulb, development of electronic technologies such as the electric motor, the telephone, radio, television, the computer, and the Internet have revolutionized the world. One of the crowning achievements of modern condensed matter physics is the silicon chip, where precise understanding of its band-structure gave rise to the digital revolution and the Internet age. While we may understand much of electronic transport, the discovery of superconductivity and the quantum Hall effect gave rise to a rich host of strongly correlated and topological regimes of transport still to be fully understood. For instance, two of the holy grails of condensed matter physics - room-temperature superconductivity and a universal quantum computer - are both electronic transport phenomena of immense technological interest but yet to be physically realized.

The fundamental problem of understanding strongly correlated and topological phenomena is that of scale: from a system with $\mathcal{O}(10^{26})$ degrees of freedom, we want to extract a few macroscopic properties. Indeed, the great effectiveness of band-structure theory comes from the fact that momentum space simplifies the $\mathcal{O}(10^{26})$ degrees of freedom down to $\mathcal{O}(1)$. However, not all systems are best described by a band structure. Non-interacting topological systems, such as the integer quantum Hall effect, are characterized by a topological invariant that is largely independent of band structure details. Furthermore, strongly correlated phases, such as superconductivity, require treatments beyond naïve perturbation theory around a given band-structure. Therefore, the study of strongly correlated and topological phases of matter have engendered a flurry of novel and creative non-perturbative approaches such as BCS mean field theory, the Laughlin wavefunction ansatz, the renormalization group, the ten-fold way, and many others.

In this thesis, we study electronic transport across a number of different physical systems, primarily employing analytic techniques. Two techniques in particular - Chern-Simons dualities and hydrodynamics - have been motivated by work in the high-energy and fluid dynamics communities, respectively. It is our hope that the work in this thesis contributes to new creative approaches to strongly correlated problems, both in condensed matter physics and beyond.

1.2 Thesis Roadmap

In chapter 2, we study the superuniversality of the correlation length exponent ν in fractional quantum Hall (FQH) transitions with the help of the newly conjectured Chern-Simons dualities. We first give a brief review of Chern-Simons field theory descriptions of the FQH transitions. In section 2.1, we explore the new phase space of theories afforded by the new Chern-Simons duality transformations and calculate ν in a large flavor expansion. However, we find that large flavor computations do not give superuniversality nor a good numerical approximation of the experimentally measured ν. In section 2.2, we instead take a large color approach motivated by the non-Abelian nature of the Chern-Simons dualities. Using the dualities in combination with modular transformations, we find exact large color descriptions of the FQH transitions. Calculating ν in a large color expansion, we find superuniversality in this class of theories.

In chapter 3, we investigate transport features associated with the strongly interacting electron hydrodynamic regime. In section. 3.1, we begin by critically re-examining previous experimental claims that observations of non-local "viscous" transport was evidence of the hydrodynamic regime. Taking a disordered non-interacting fermion model, we compute the conductivity to $\mathcal{O}(q^2)$ and find that this model also exhibits non-local "viscous" transport. Ultimately, we realized that qualitative non-local transport features are not distinctive because the Navier-Stokes equations are equivalent to a momentum-dependent Ohm's law. Therefore, in search of sharper signatures of the hydrodynamic regime, in section. 3.2 we look at nonlinear phenomena lying outside the purview of linear response. We propose three experiments motivated by classic hydrodynamic phenomena - the Bernoulli effect, Eckart streaming, and Rayleigh streaming - driven by the convective nonlinearity present in the Navier-Stokes equations. Analysis of experimental parameters suggest that these effects are observable and therefore can serve as strong signatures of the electron hydrodynamic regime.

In chapter 4, we search for distinctive signatures of the chiral anomaly in Weyl semimetals. We begin with a brief introduction to Weyl semimetals and the chiral anomaly. In section. 4.1, we re-examine previous IR reflectance proposals to observe the chiral anomaly which argued that mirror-symmetric Weyl semimetals do not host the anomalous IR signature. Finding that they neglected the symmetry-breaking effect of the applied magnetic field, which is necessarily present, we argue that mirror-symmetric Weyl semimetals should in fact host the IR signature. Furthermore, estimates of the symmetry-breaking from the magnetic field suggest that mirror-symmetry is sufficiently broken to observable manifest the anomalous IR peaks.

In chapter 5, we study transport in a network of topological 1D edge modes afforded by moiré systems. We begin with a brief introduction to moiré systems. In section 5.1, motivated by experimental observations of sharp domain walls in moiré systems, we consider a triangular network of interacting valley-helical edge modes. In contrast to previous interacting models which looked at gapped correlated phases, we forbid intervalley scattering; away from commensurate fillings, intervalley scattering is suppressed due the large momentum separation between valleys. This constraint prevents a single-particle gap from forming, so our network must remain conductive. By performing a perturbative RG analysis on tunneling operators which conserve particle number and valley number, we obtain the resulting phase diagram. We find that transport in this model is non-local, unlike the local diffusive behavior of a resistor network. In particular, at strong repulsive interactions we predict a novel orbital antiferromagnetic-ordering phase.

CHAPTER 2

FRACTIONAL QUANTUM HALL SUPERUNIVERSALITY AND CHERN-SIMONS DUALITIES

The fractional quantum Hall effect (FQHE) is the premier example of a strongly correlated and topological phase. While its cousin, the integer quantum Hall effect, can be described by a free electron in a magnetic field, the fractionalization present in the FQHE necessitates proper treatment of the Coulomb interaction. However, this is a difficult many-body problem. The large degeneracy of the non-interacting Landau levels makes it difficult perturbatively treat the Coulomb interaction, and even numerical exact diagonalization of this problem can only treat at most a handful of particles [276]. This motivated an effective description of FQH phases by Chern-Simons field theories (See [318, 292, 276] for a review).

We briefly review here Chern-Simons theories. The abelian Chern-Simons action at level k is given by

$$S = \frac{k}{4\pi} \int d^3x \epsilon^{\mu\nu\rho} A_\mu \partial_\nu A_\rho \tag{2.1}$$

for an abelian background gauge field A_μ. Interpreting A_μ as the physical electromagnetic field, it couples to physical currents via $\int d^3x A_\mu J^\mu$. Using $J_\mu = \frac{\delta S}{\delta A_\mu}$, one finds that the conductivity is $\sigma_{xy} = \frac{k}{2\pi}$. For proper quantization of this theory, we must have $k \in \mathbb{Z}$ [276]. Therefore, Chern-Simons theories naturally describe the transport in the integer quantum Hall effect. Furthermore, we can combine multiple gauge fields to recreate transport in the fractional quantum

Hall effect. For instance, consider

$$S = \int d^3x \epsilon^{\mu\nu\rho} \left[\frac{m}{4\pi} b_\mu \partial_\nu b_\rho + \frac{1}{2\pi} A_\mu \partial_\nu b_\mu \right] \tag{2.2}$$

$$= \frac{1}{3} \frac{1}{4\pi} \int d^3x \epsilon^{\mu\nu\rho} A_\mu \partial_\nu A_\rho \tag{2.3}$$

where b is a dynamical gauge field and in the second line we integrate out b to obtain the effective action. Therefore, this theory describes the fractional quantum Hall $1/m$ state.[1]

To describe FQH transitions, one needs a dynamical way to transition between different values of k. Two simple ways to do this are by providing a Dirac mass gap or by Higgsing a gauge field. Recall that a free Dirac fermion

$$S = \int d^3x \bar{\psi} \gamma^\mu (i\partial_\mu + A_\mu) \psi + m \bar{\psi} \psi - \frac{1}{8\pi} \epsilon^{\mu\nu\rho} A_\mu \partial_\nu A_\rho \tag{2.4}$$

undergoes a $0 \to 1$ Hall transition (in the IR) as one tunes the Dirac mass, and therefore naturally describes a quantum Hall transition.[2] Similarly, the bosonic theory

$$S = \int d^3x |(\partial_\mu - i a_\mu) \phi|^2 + m |\phi|^2 + \frac{1}{4\pi} \epsilon^{\mu\nu\rho} \left[a_\mu \partial_\nu a_\rho + A_\mu \partial_\nu a_\rho \right] \tag{2.5}$$

also describes a $0 \to 1$ Hall transition (in the IR) as one tunes the bosonic mass m. In the $m < 0$ Higgs phase, $a_\mu = 0$ so the theory is a trivial insulator, but in the trivial $m > 0$ phase we can set $\phi = 0$ and the remaining action has a $k = 1$ Hall conductivity. Generalizations of these theories can therefore describe generic quantum Hall transitions. The seeming similarity of the fermionic and

---

[1] To integrate out b, complete the square and shift b to remove the bdA cross term. We also remark that, strictly speaking, one cannot integrate out b as there will be topological obstructions; this can be seen in the non-integer $1/m$ level in the resulting effective theory. Nonetheless, the Hall conductivity is correct [276].

[2] The additional half-integer Chern-Simons level is there as a normalization; gapping a single Dirac fermion gives a $\mathrm{sign}(m)\frac{1}{8\pi}$ in the IR, so that the combination is properly normalized. Strictly speaking, this is a shorthand for the η invariant (see [245]).

bosonic descriptions was given explicit foundation with the conjecture of the Chern-Simons (plus matter) dualities. The full duality statements are nicely summarized in [4] (see also [245, 137, 136]). We will use these dualities to great effect in what follows.

2.1 Non-Abelian fermionization and fractional quantum Hall transitions

This section is adapted from a PRB paper [117] with Michael Mulligan and Eun-Ah Kim.

There has been a recent surge of interest in dualities relating theories of Chern-Simons gauge fields coupled to either bosons or fermions within the condensed matter community, particularly in the context of topological insulators and the half-filled Landau level. Here, we study the application of one such duality to the long-standing problem of quantum Hall inter-plateaux transitions. The key motivating experimental observations are the anomalously large value of the correlation length exponent $\nu \approx 2.3$ and that ν is observed to be super-universal, i.e., the same in the vicinity of distinct critical points [S.L. Sondhi et al., Rev. Mod. Phys. **69**, 315 (1997)]. Duality motivates effective descriptions for a fractional quantum Hall plateau transition involving a Chern-Simons field with $U(N_c)$ gauge group coupled to $N_f = 1$ fermion. We study one class of theories in a controlled limit where $N_f \gg N_c$ and calculate ν to leading nontrivial order in the absence of disorder. Although these theories do not yield an anomalously large exponent ν within the large $N_f \gg N_c$ expansion, they do offer a new parameter space of theories that is apparently different from prior works involving abelian Chern-Simons gauge fields [X.-G. Wen and Y.-S. Wu, Phys. Rev. Lett. **70**, 1501 (1993); W. Chen. et al., Phys. Rev. B. **48**, 13749 (1993)].

2.1.1 Introduction

Phase transitions between different quantum Hall states have long been viewed as poster-child examples of quantum critical phenomena.[259] The longitudinal resistivity ρ_{xx}, the width ΔB of the transition region, and $(d\rho_{xy}/dB)_{\text{max}}$ exhibit scaling collapse in the vicinity of the transition over almost two decades of temperature,[168, 169, 291, 302, 247, 68] frequency,[69] and current.[290] Furthermore, although each plateau is believed to represent a distinct topologically ordered phase with (generally) different sets of fractionalized excitations, inter-plateaux transitions appear to possess the same values for the correlation length exponent $\nu \approx 2.3$ and dynamical critical exponent $z \approx 1$: distinct critical points exhibit "super-universality."[144, 250, 259, 125] The anomalously large value of $\nu \approx 2.3$ and the apparent super-universality remain a major mystery from the theoretical standpoint, as an accurate description clearly involves strong interactions as well as some form of translational symmetry breaking, such as disorder. This problem has been studied from a field-theoretic perspective using a theory of flux-attached bosons.[144] However it has been difficult to make progress due to the fact that the the quantum field theory of interest (matter coupled to an abelian Chern-Simons gauge field) is strongly coupled.[144, 177, 78, 323, 322, 239, 99] Controlled approximations to this theory yield correlation length exponents that strongly depend on the particular quantum Hall transition.[293, 41]

Duality provides a powerful perspective for studying strongly coupled quantum field theories that has been used in the past with great success.[47, 189, 184, 242, 244, 123, 1] There are two senses in which different theories are said to be dual. The first is as an exact equivalence of theories. A familiar example is bosonization in $1+1$ dimensions where a self-interacting Dirac fermion can be equivalently described by the theory of a free boson. [47, 189, 184] The second type of duality is as an IR equivalence: two theories are IR dual if they belong to the same universality class. In this paper, we use duality in this second sense. A famous example is particle-vortex duality in $2+1$ dimensions.[56, 214, 71] This duality identifies the IR content of the XY model to that of a lattice superconductor coupled to a $U(1)$ gauge field, i.e., the Abelian-Higgs model. Historically, particle-vortex duality was used as a means to understand the Abelian-Higgs model, as applied to superconductivity; the XY model was relatively well understood, so duality allowed one to predict the existence of a continuous phase transition as well as its critical behavior. Similarly, level-rank dualities were discovered, and in fact proven, for pure Chern-Simons theories.[202, 203] As its name implies, these dualities swap the Chern-Simons level and the rank of the gauge group (in Yang-Mills regularization) up to $U(1)$ factors.[4]

Recently, generalizations of level-rank duality have been proposed.[86, 3, 7, 4, 109] The conjectured duals relate theories of Chern-Simons gauge fields coupled to either fermionic or bosonic matter fields and may, in some cases, be thought of as bosonization in $2+1$ dimensions. These dualities have been of particular interest to the condensed matter community[245, 137, 286, 198] in explaining[285, 193, 307] the T-Pfaffian surface state of a topological insulator as well as providing a new effective description[257] for the half-filled Landau level that is manifestly particle-hole symmetric,[200, 254, 131, 83, 197] thereby "symmetrizing" the seminal work by Halperin, Lee, and Read.[99]

We suggest that these new dualities could also be useful in understanding phase transitions between fractional quantum Hall states, as they involve theories that generalize prior effective descriptions consisting of abelian Chern-Simons gauge fields coupled to matter.[144, 293, 41]

To this end, we expand in this paper upon previous efforts to understand fractional quantum Hall transitions in field theoretic models without disorder. In contrast to prior works,[293, 41] the class of theories we study consists of a Chern-Simons gauge field with non-abelian $U(N_c)$ gauge group for $N_c > 1$ coupled to N_f Dirac fermions. When $N_f = 1$, this model is dual to the theory of a fractional quantum Hall transition first studied by Wen and Wu[293] and may be viewed as a generalization of the theory studied by Chen, Fisher, and Wu. [41] Although our model is strongly coupled, it can be reliably studied in various controlled limits. In this paper, we consider the limit where $N_f \gg N_c \gg 1$. In this large $N_f \gg N_c$ limit, we compute the correlation length exponent ν to leading non-trivial order. Although we do not find an anomalously large ν within this expansion, effective theories with non-abelian gauge symmetry provide a larger parameter space for exploration that could yield new insights.

The remainder of this paper is organized as follows. In section 2.1.2, we write down our starting theory and discuss its fermonic dual. In section 2.1.3, we discuss the calculation of the correlation length exponent ν in the fermionic theory in the large $N_f \gg N_c$ expansion. In section 2.1.4, we discuss our results. An appendix contains details on the calculation of ν.

2.1.2 Dualities

Our starting point is the field theory studied by Wen and Wu[293] that describes a fractional quantum Hall to insulator transition on a lattice (without disorder) as a superfluid-Mott transition of composite bosons, tuned by the (repulsive) onsite lattice potential;[72] the phases are identified via their Hall conductivities. When these bosons are at unit filling (appropriate to a fractional quantum Hall transition of electrons), the latter transition has an emergent relativistic symmetry. As shown in [293], such a model can be generalized to arbitrary fractional quantum Hall to fractional quantum Hall transitions by adding additional abelian gauge fields; in this paper, we choose to focus on the simplest case. The $2+1$-dimensional Lagrangian in Euclidean signature is

$$\mathcal{L} = |(\partial_\mu - ie^* A_\mu - ia_\mu)\phi|^2 + m^2|\phi|^2 + g|\phi|^4 - \frac{i}{4\pi k^B}\epsilon^{\mu\nu\lambda} a_\mu \partial_\nu a_\lambda. \qquad (2.6)$$

In this theory, the fluctuating $U(1)$ Chern-Simons gauge field a_μ with $\mu \in \{1,2,3\}$ attaches k^B flux quanta to the complex bosonic field ϕ. These flux-attached bosons are probed by the external electromagnetic gauge field A_μ and carry charge e^*. The coupling g is understood to take its IR fixed point value. In Eq. (2.6), the transition is tuned by the renormalized mass m^2: in the $m^2 > 0$ phase (where ϕ is gapped), the Hall conductivity $\sigma_{xy} = 0$; in the $m^2 < 0$ phase (where ϕ condenses), $\sigma_{xy} = -\frac{1}{k^B}\frac{(e^*)^2}{h}$; in both phases, $\sigma_{xx} = 0$ (σ_{ij} refers to the zero-temperature dc conductivity). For the fractional quantum Hall - Mott insulator transition, we must choose $k^B \in \mathbb{Z}$. For instance, to describe the $0 \to 1/3$, transition, one sets $e^* = 1$ and $k^B = 3$. We are interested in the critical properties of Eq. (2.6), so we set $m^2 = 0$ for the remainder of this paper.

We would like to study a dual description of this fractional quantum Hall to Mott insulator transition using a Chern-Simons theory with $U(N_c)$ gauge symmetry coupled to a fermion. For this, we need to remedy the fact that the Chern-Simons level (equal to $-1/k^B$) for a_μ in Eq. (2.6) is not quantized when $k^B \in \mathbb{Z}$ is greater than one (see footnote[3]). Further using a generalized particle-vortex duality,[276] we arrive at

$$\mathcal{L} = |(\partial_\mu - i\hat{a}_\mu)\hat{\phi}|^2 + g|\hat{\phi}|^4 + \frac{i}{4\pi}\epsilon^{\mu\nu\lambda}\left(k^B \hat{a}_\mu \partial_\nu \hat{a}_\lambda + A_\mu \partial_\nu \hat{a}_\lambda\right). \tag{2.7}$$

Note that $\hat{\phi}$ and the $U(1)$ gauge field $\hat{a}_\mu$ in Eq. (2.7) are different from the corresponding fields in Eq. 2.6. A non-relativistic version of the duality between Eqs. (2.6) and (2.7) was also proposed by Lee.[154] From this point forth, we will drop the non-dynamical background gauge field A_μ.

In the hopes of understanding the effects of the strong interactions in Eq. (2.7), we can generalize the theory in several ways: we enlarge the gauge symmetry from $U(1) \to U(N_c^B)$, where the integer $N_c^B > 1$ is the rank of the gauge group, and introduce N_f flavors of bosons transforming in the fundamental representation of $U(N_c^B)$, i.e., each of the N_f bosons is a vector with N_c^B components. The corresponding three-dimensional parameter space of theories is shown in the left cube in Fig. 2.1. The labels for the axes are chosen to hold N_c^B/k^B finite in the large N_c^B limit (within the dimensional regularization scheme discussed later). The horizontal axis is on a $\tan^{-1}$ scale to make it finite in length, while the vertical axis corresponds to the 't Hooft coupling N_c^B/k^B, whose norm is bounded by 1. The physical theory of interest with $N_f = N_c^B = 1$ and $k^B \in \mathbb{Z}$ is denoted by a red dot and is located behind the front face where $k^B \to \infty$. Since a generic theory in Fig. 2.1 is strongly inter-

---

[3] One can legalize the theory by introducing a new dynamical gauge field b as a constraint, giving us the Lagrangian

$$\mathcal{L} = |(\partial_\mu - ie^* A_\mu - ia_\mu)\phi|^2 + g|\phi|^4 + \frac{i}{4\pi}\epsilon^{\mu\nu\lambda}\left(-k^B b_\mu \partial_\nu b_\lambda + 2a_\mu \partial_\nu b_\lambda\right)$$

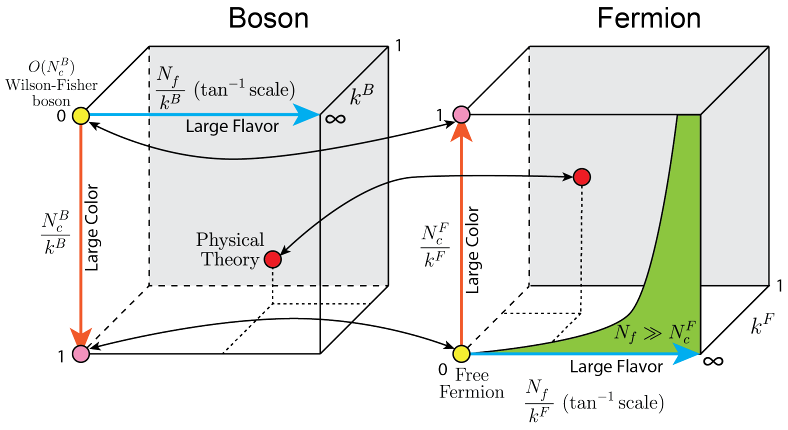

Figure 2.1: A schematic plot of parameter space for Chern-Simons theories with bosonic and fermionic matter. Note that the orientation of the y-axis is inverted between the bosonic and fermionic cubes. The double arrows indicate a duality between the connected points. The pink points refer to free theories and the yellow points to "infinitely coupled" theories. Previous works have studied the large color and large flavor theories both in the fermionic and bosonic cases, labeled in orange and blue.[293, 41, 86, 85, 6] The red dot corresponds to our physical theory, while our calculation in the $N_f \gg N_c$ expansion is done in the green region. All calculations give $\nu = 1$ at leading order,[293, 41, 86, 85, 6] while experiments give $\nu \approx 2.3$.[259]

acting, reliable predictions are limited to small regions of the parameter space. The best understood part is the yellow point in the top-left corner, which corresponds to the Wilson-Fisher $O(N_c^B)$ vector model, since $k^B \to \infty$ faster than N_c^B and, consequently, completely suppresses the gauge fluctuations. In addition, large N_f expansions[293] (blue axis) and large N_c^B expansions[85] (orange axis) have been carried out to the subleading order and leading order. The pink point in the bottom-left corner corresponds to "infinite coupling," $N_c^B/k^B = 1$ and $k^B, N_c^B \to \infty$.

Remarkably, the recent Chern-Simons plus matter dualities sometimes relate a strongly correlated theory to a free one, and thereby constitute a non-perturbative solution to an interacting problem. Unfortunately, this does not appear to occur for the theory described by Eq. (2.7). Instead, duality relates the

IR limit of Eq. (2.7) to the IR limit of the theory of a Chern-Simons gauge field coupled to a Dirac fermion:

$$\begin{gathered}\mathcal{L} = |(\partial_\mu - i\hat{a}_\mu)\hat{\phi}|^2 + g|\hat{\phi}|^4 + \frac{ik^B}{4\pi}\epsilon^{\mu\nu\lambda}\hat{a}_\mu\partial_\nu\hat{a}_\lambda \\ \updownarrow \\ \mathcal{L} = \bar{\psi}\gamma^\mu(\partial_\mu - i\tilde{a}_\mu)\psi + \frac{ik^F}{4\pi}\epsilon^{\mu\nu\lambda}\mathrm{Tr}\left(\tilde{a}_\mu\partial_\nu\tilde{a}_\lambda + \frac{2}{3}\tilde{a}_\mu\tilde{a}_\nu\tilde{a}_\lambda\right).\end{gathered} \tag{2.8}$$

In the bottom half of (2.8), ψ is a 2-component fermionic field transforming in the fundamental representation of $U(k^B - 1)$, $\tilde{a}_\mu$ is a $U(k^B - 1)$ gauge field, $k^F = -k^B + 1/2$, and the γ-matrices satisfy $\{\gamma^\mu, \gamma^\nu\} = 2\delta^{\mu\nu}$. The trace in the non-abelian Chern-Simons term is taken with respect to the fundamental representation. Note that we are working within dimensional regularization.[4] See the appendix for further details.

Applying dualities[4, 109] to the generalized bosonic theories with non-abelian gauge group $U(N_c^B)$ and multiple flavors N_f, we may schematically write:

$$\begin{gathered}U(N_c^B)_{k^B,k^B} \text{ with } N_f \text{ bosons} \\ \updownarrow \\ U(k^B - N_c^B)_{-k^B+N_f/2,-k^B+N_f/2} \text{ with } N_f \text{ fermions}.\end{gathered} \tag{2.9}$$

The duality in (2.8) is recovered by setting $N_c^B = N_f = 1$. For the dualities in (2.9), the subscripts on $U(N)$ signify the levels of the $SU(N) \subset U(N)$ and $U(1) \subset U(N)$ Chern-Simons gauge fields; we will denote the rank of the gauge group in the fermionic theory of Eq. (2.9) with the integer $N_c^F = k^B - N_c^B$.

---

[4] By dimensional regularization, we mean that one contracts tensor indices in 3 dimensions, while analytically continuing integrals to $3-\epsilon$ dimensions. This is sometimes called dimensional reduction in the literature.[42] An alternative scheme where one regularizes with a small Yang-Mills term is equivalent to dimensional regularization, up to a constant shift of the $SU(N)$ level, so we will work exclusively in dimensional regularization for simplicity.

Armed with the dualities between generalized theories, we can now consider the three-dimensional parameter space associated with the fermionic theories (see Fig. 2.1). Duality presents the choice of which representation of the same physics to study.

Fig. 2.1 depicts the duality mappings in (2.9). We denote dualities between specific points in Fig. 2.1 with double-headed arrows that relate bosonic theories to fermionic theories. We intentionally chose the vertical axis of the two cubes to point in opposite directions in order to visually indicate how a strongly coupled theory on one side can map to a weakly coupled theory. For example, the yellow point in the bottom left corner represents the theory of a free fermion maps to an "infinitely coupled" bosonic theory. Similarly, the pink point on the top-right corner representing the "infinitely coupled" fermionic theory maps to the $O(N_c^B \to \infty)$ Wilson-Fisher boson. Unfortunately, the physical bosonic theory of interest (the red point), which is far from any known solvable point in the bosonic parameter space, maps to another strongly coupled theory on the fermionic side. Short of being able to directly access the physical theory, large N_f expansions[41] (blue axis) and large N_c^F expansions[86, 85] (orange axis) have been studied on the purely fermionic side.

In the remainder of this paper, we study the fermionic dual our physical bosonic theory (red point) using the dualities stated in (2.8). We attempt to access this strongly coupled fermionic theory by employing a $N_f \gg N_c^F$ expansion, valid within the green region of Fig 2.1. The dualities in (2.9) are only conjectured to hold when $N_f \leq N_c^B$[109]: by employing the $N_f \gg N_c^F$ expansion, we are exploring a class of fermionic theories that is different from the previously studied class of bosonic theories.

2.1.3 $N_f \gg N_c$ expansion

We generalize the fermionic side of Eq. (2.8) to an arbitrary number of flavors N_f so that the Lagrangian becomes

$$\begin{aligned}\mathcal{L} = \sum_{i=j}^{N_f} \bar{\psi}_j \gamma^\mu (\partial_\mu - i a_\mu) \psi_j \\ + \frac{ik^F}{4\pi} \epsilon^{\mu\nu\lambda} \mathrm{Tr}\left(a_\mu \partial_\nu a_\lambda + \frac{2}{3} a_\mu a_\nu a_\lambda \right). \end{aligned} \tag{2.10}$$

(We have dropped the tildes on a in Eq. (2.10).) The fermionic dual of the physical boson theory has $N_f = 1$, $N_c^B = 1$, $N_c^F = k^B - N_c^B$ and $k^F = -k^B + N_f/2$.

We calculate the correlation length exponent ν via the definition $\nu^{-1} = 3 - [\bar{\psi}\psi(x)]$, which comes from the fact that the correlation length $\xi \sim m^{-1}$ as the mass m is the critical tuning parameter.[293] To obtain ν, we will compute the scaling dimension of the (momentum space) mass operator $J_0(p) = (\bar{\psi}\psi)(p)$. Recall that in position space, the scaling dimension δ is defined by the algebraic decay of $\langle J_0(x) J_0(0) \rangle \sim x^{-2\delta}$. Upon Fourier transforming, we have $\langle J_0(p) J_0(-p) \rangle \sim p^{2\delta - d}$, where $d = 3$ is the spacetime dimension. We control the calculation in the $N_f \gg N_c^F$ limit taking $k^F, N_c^F, N_f \to \infty$ while keeping the ratios $\lambda = N_f/k^F$ and $\alpha = N_c^F/N_f$ finite, along with $\alpha \ll 1$. Therefore, we calculate perturbatively in α to first subleading order and exactly in λ. Note that λ can (effectively) take any value in $\mathbb{R}$ – it is not the 't Hooft coupling N_c^F/k^F.

This calculation was first investigated in a beautiful paper by Gurucharan and Prakash, where the primary motivation was to find tractable non-supersymmetric conformal field theories with gravitational duals.[95] Here, we use Eq. (2.10) to model inter-plateaux transitions and, in the course of our study, we correct a minor error in Ref. [[95]].

The leading order piece $\delta^{(0)}$ of the scaling dimension of the mass operator J_0 in d Euclidean dimensions is related to the leading order decay of the correlator by

$$\langle J_0(p) J_0(-p)\rangle_{\text{leading}} \sim p^{2\delta^{(0)}-d}, \tag{2.11}$$

where p is the momentum inserted at the J_0 vertex. Only the tree-level diagram contributes, which results in $\delta^{(0)} = 2$. To calculate the anomalous dimension $\delta^{(1)}$ of the mass operator J_0, we extract the logarithmic divergences of the 2-point correlator as in, e.g., Ref. [[43]]:

$$\langle J_0 J_0\rangle = (1 - 2\delta^{(1)} \ln\Lambda + \ldots)\langle J_0 J_0\rangle_{\text{leading}}. \tag{2.12}$$

Keeping terms to $\mathcal{O}(\alpha)$, we arrive at the result:

$$[\bar{\psi}\psi] = 2 - \alpha\frac{64\lambda^2}{64+\pi^2\lambda^2}\left(\frac{1}{3} + 2\cdot\frac{1}{2}\frac{64-\lambda^2\pi^2}{64+\lambda^2\pi^2}\right) \tag{2.13}$$

$$= 2 - \alpha\frac{128\lambda^2}{3}\frac{128-\pi^2\lambda^2}{(64+\pi^2\lambda^2)^2}. \tag{2.14}$$

The factor of "2" appearing before the second term in the parentheses above is the quantitative difference between our result and that in Ref. [[95]], and results from an additional Feynman diagram. For calculational details, see the appendix. Therefore, we arrive at the result:

$$\nu = 1 - \alpha\frac{128\lambda^2}{3}\frac{128-\pi^2\lambda^2}{(64+\pi^2\lambda^2)^2}. \tag{2.15}$$

We plot the anomalous dimension correction to ν at $\mathcal{O}(\alpha)$ in Fig. 2.2 as a function of the original bosonic parameters using the relation $\lambda^{-1} = -k^B/N_f + 1/2$, with the y-axis measured in units of α. Note that the correction is positive only when $1.29 < N_f/k^B < 4.50$. In the fermionic variables, this corresponds to $\lambda > 3.6$.

If we want to consider the $0 \to 1/3$ transition, then we should set $N_f = 1$, $N_c^B = 1$, $e^* = 1$, and $k^B = 3$. Substituting these values into Eq. (2.14), we find

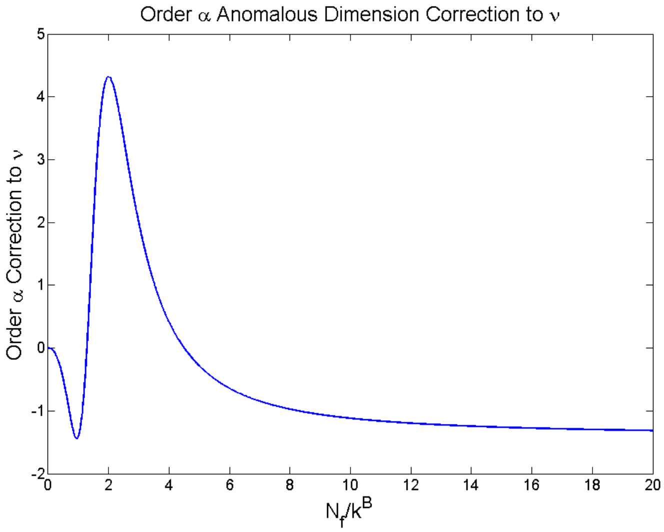

Figure 2.2: A plot of the anomalous dimension correction to ν to $\mathcal{O}(\alpha)$ in the original bosonic parameters. The y axis is in units of α. It is positive for $1.29 < N_f/k^B < 4.50$. The parameter λ used in Eq. (2.15) is related to N_f/k^B by $\lambda^{-1} = -k^B/N_f + 1/2$.

$\nu = 1 - .4014$. In this case, the correction to ν is negative. The dynamical critical exponent $z = 1$ automatically, since our theory is Lorentz-invariant.

Chen, Fisher, and Wu studied the abelian version of Eq. (2.10) given by

$$\mathcal{L} = \sum_{i=1}^{N_f} \bar{\psi}_i \gamma^\mu (\partial_\mu - i a_\mu) \psi_i + \frac{ik^F}{4\pi} \epsilon^{\mu\nu\lambda} a_\mu \partial_\nu a_\lambda, \tag{2.16}$$

where a_μ is a $U(1)$ gauge field. We have rescaled a_μ to make the comparison between their theory and ours more transparent. They extract ν from the scaling dimension $[\bar{\psi}\psi]$ in a large N_f expansion and arrive at the result,

$$\nu_{CFW} = 1 - \frac{1}{N_f} \frac{128\lambda_{CFW}^2}{3} \frac{128 - \pi^2\lambda_{CFW}^2}{(64 + \pi^2\lambda_{CFW}^2)^2}, \tag{2.17}$$

where $\lambda_{CFW} = N_f/k^F$. Comparing Eq. (2.15) and Eq. (2.17), we see that the two expressions formally match. To $\mathcal{O}(\alpha)$, our non-abelian extension to $U(N_c^F)$ only contributes an additional color factor. It turns out that the diagrams contributing to ν in a $N_f \gg N_c$ expansion are the same as those of a large N_f expansion to subleading order, up to color factors. At higher orders, this equivalence is no longer expected to be true: the subleading in N_f diagrams are planar because gauge lines are $1/N_f$-suppressed. (This formal equivalence of expansions to subleading order is likely to be true on the bosonic side as well, though we have not explicitly verified this.) Note, however, that the two models give different results when considering a particular fractional quantum Hall transition. For example, in the $0 \to 1/3$ transition, our model has $N_c^F = \alpha = 2$ and $k^F = -5/2$, so $\nu = 1 - .4014$. In the model studied by Chen, Fisher, and Wu, they set $N_f = 1$, $N_c^F = 1$, $e^* = 1/3$ and $k^F = 3/2$,[41, 239] corresponding to "$\alpha_{CFW} = 1$" and $\lambda_{CFW} = 2/3$, so that $\nu_{CFW} = 1 - .5012$. Although the expressions for ν formally agree, the physical values of the parameters are different, so they should be thought of as describing different physics. [5]

2.1.4 Discussion

The observations of super-universality and the anomalously large correlation exponent ν associated with quantum Hall inter-plateaux transitions remain a long-standing conundrum. Duality motivates an exploration of a large space of theories that may provide new insight. We focused on an effective description of a fractional quantum Hall transition involving a non-abelian Chern-Simons gauge field with $U(N_c)$ gauge group and N_f fermions. This theory is dual to the critical theory of an abelian Chern-Simons gauge field coupled to a boson.

---

[5] This conclusion might be further supported by the fact that the bosonization dual of the model studied by Chen, Fisher, and Wu involves a boson coupled to a Chern-Simons gauge field with non-abelian gauge group, rather than an abelian gauge field. In particular,

$$U(1)_{k^B-1/2,k^B-1/2} \text{ with one fermion} \leftrightarrow U(k^B-1)_{-k^B,-k^B} \text{ with one boson}$$

.

We calculated the correlation length exponent ν to first subleading order in the large $N_f \gg N_c$ expansion, filling in the green region in Fig. 2.1. We found the $N_f \gg N_c^F$ expansion to be formally equivalent to a fermionic large N_f expansion (blue axis) to first subleading order,[41] although the precise values of the ν inferred differ. Accordingly the exponent ν continues to depend on the pair of plateaux in question, rather than showing any super-universality. Moreover, the calculated exponent ν continues to be far below the experimental value.

Clearly there are many aspects of the physical problem that were left out in our model. It may be that translational symmetry breaking needs to be incorporated so as to include the effect of disorder. Also, the thus-far unexplored subleading correction in the large N_c limit may prove enlightening. However, it appears plausible that calculating the exponent order by order with respect to some perturbative control parameter may not be the best strategy. Rather, it would be interesting to address the apparent super-universality in a more wholesome manner from the outset.[114]

Acknowledgements

We would like to thank S. Chakravarty, G.Y. Cho, M. Fisher, T. Hartman, S. Jain, S. Kivelson, M. Lawler, S. Prakash, S. Sachdev, E. Shimshoni, and S. Sondhi for helpful discussions and comments. A.H. was supported by the National Science Foundation Graduate Research Fellowship under Grant No. DGE-1650441. M.M. was supported in part by the UCR Academic Senate. M.M. is grateful for the generous hospitality of the Aspen Center for Physics, which is supported by the National Science Foundation (NSF) grant PHY-1607611. E.-A.K. was supported by the U.S. Department of Energy, Office of Basic Energy Sciences, Division of Materials Science and Engineering under Award DE-SC0010313. E.-A.K. acknowledges Simons Fellow in Theoretical Physics Award #392182. The authors are also grateful for the hospitality of the Kavli Institute for Theoretical Physics, under Grant No. NSF PHY-1125915, where some of this work was performed.

2.1.5 Appendix: Calculational Details

The Lagrangian we study is

$$\mathcal{L} = \sum_{i=1}^{N_f} \bar{\psi}_i \gamma^\mu (\partial_\mu - i a_\mu) \psi_i + \frac{ik^F}{4\pi} \epsilon^{\mu\nu\lambda} \mathrm{Tr} \left(a_\mu \partial_\nu a_\lambda + \frac{2}{3} a_\mu a_\nu a_\lambda \right) \tag{2.18}$$

Define light-cone coordinates via analytic continuation to be $x^\pm = (x^1 \pm ix^2)/\sqrt{2}$, and let $x_s^2 = x_1^2 + x_2^2 = 2x_+x_-$. We will work in light-cone gauge $a_- = 0$, which decouples the ghosts and removes the cubic gauge interaction term.[95] We will also take $\gamma^i = \sigma^i$, the Pauli matrices. We normalize our gauge group generators by $\mathrm{Tr}\, T^a T^b = \delta^{ab}/2$.

We will regularize our theory by using a momentum-cutoff Λ in the 1-2 plane and dimensional-regularization in the x^3 direction, as has been done by others.[7, 95]

The Feynman rules for the bare propagators and interactions are

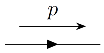

$$\frac{1}{i\not{p}}$$

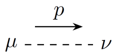

$$D_{+3}(p) = -D_{3+}(p) = \frac{4\pi}{ikp^+}, \text{ all others are 0}$$

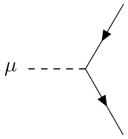

$$i\gamma^\mu$$

Under duality, we expect $\phi^\dagger\phi \leftrightarrow \bar{\psi}\psi$. Hence, $\nu^{-1} = 3 - [\bar{\psi}\psi]$.[293] In what follows, we will be calculating the scaling dimension $[\bar{\psi}\psi]$.

Denote the mass operator in momentum space as $J_0(p) = (\bar{\psi}\psi)(p)$, where p is the momentum inserted into the vertex. The leading order in α term of $\langle J_0(p)J_0(-p)\rangle \sim p$, and we know that the leading order scaling dimension $\Delta^{(0)}$ of the mass operator J_0 is given by $\langle J_0(p)J_0(-p)\rangle_{\text{leading}} \sim p^{2\Delta^{(0)}-d}$, where d is the number of spacetime dimensions. Hence, the scaling dimension of J_0 at leading order in (2+1)D is 2. We will calculate the anomalous dimension $\delta^{(1)}$ of J_0, which amounts to extracting the logarithmic divergences of the 2-point function as[43]

$$\langle J_0 J_0\rangle = (1 - 2\delta^{(1)}\ln\Lambda + \ldots)\langle J_0 J_0\rangle_{\text{leading}} \tag{2.19}$$

First, let us calculate the exact gauge propagator $G_{\mu\nu}$ to leading order in α, which we denote by a squiggle. The only diagrams that contribute are strings of bubble diagrams, and hence satisfies the following Schwinger-Dyson equation

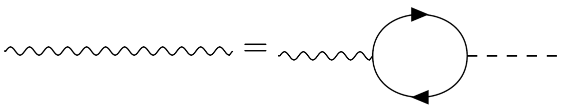

(2.20)

The 1PI self-energy diagram $\Sigma^{\mu\nu}$ at leading order is given by

$$\begin{aligned}\Sigma^{\mu\nu}(p) &= (-1)\,\mathrm{Tr}(T^aT^b)\delta^{ab}\,\mathrm{Tr}\int\frac{d^3q}{(2\pi)^3}\frac{-i\not{q}}{q^2}(i\gamma^\mu)\frac{-i(\not{p}+\not{q})}{(p+q)^2}(i\gamma^\nu)\\ &= -\frac{N_f p}{32}\left(\delta^{\mu\nu}-\frac{p^\mu p^\nu}{p^2}\right)\end{aligned} \tag{2.21}$$

Summing the bubbles via $\mathbf{G}(p)=(1-\mathbf{D}\mathbf{\Sigma})^{-1}\mathbf{D}(p)$, we get

$$\begin{pmatrix} G_{33} & G_{3+} \\ G_{+3} & G_{++}\end{pmatrix}(p)=\frac{1}{N_f}\frac{2\pi^2p_+^2}{pp_s^4}\frac{64}{64+\pi^2\lambda^2}\begin{pmatrix}\lambda^2p_-^2 & \frac{8i\lambda}{\pi}p_-p-\lambda^2p_-p_3 \\ -\frac{8i\lambda}{\pi}p_-p-\lambda^2p_-p_3 & -p_s^2\lambda^2\end{pmatrix} \tag{2.22}$$

There are four diagrams at subleading order in α that contribute to $\langle J_0J_0\rangle$. We denote a J_0 insertion by a crossed circle.

First, the fermion self-energy contribution.

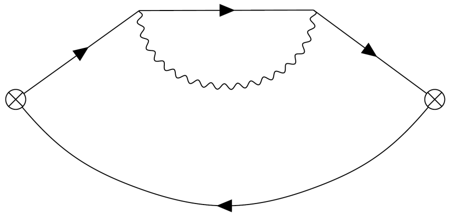

We focus on the fermion self-energy subdiagram first.

$$\Sigma_\psi(p)=\frac{N}{2}\int\frac{d^3q}{(2\pi)^3}(i\gamma^\mu)\frac{-i(\not{p}+\not{q})}{(p+q)^2}(i\gamma^\nu)G_{\mu\nu}(q) \tag{2.23}$$

Using the relations $\gamma^+\gamma^-=1+\gamma^3$, $\gamma^-\gamma^+=1-\gamma^3$, and $(\gamma^3)^2=1$, we get that

$$\gamma^\mu\not{p}\gamma^\nu G_{\mu\nu}=G_{33}(p_3\gamma^3-p_-\gamma^--p_+\gamma^+)+(G_{+3}+G_{3+})(p_3\gamma^++p_-\gamma^3)+(G_{+3}-G_{3+})p_-+2G_{++}p_-\gamma^+ \tag{2.24}$$

Substituting $\not{p} \to \not{p} + \not{q}$ in the above equation, we get

$$\Sigma_\psi(p) = i\alpha \frac{64\pi^2}{64+\pi^2\lambda^2} \int \frac{d^3q}{(2\pi)^3} \frac{1}{(p+q)^2} (K_\mu \gamma^\mu + K_I) \tag{2.25}$$

where

$$K_- = -\frac{p_- + q_-}{4q}\lambda^2 \tag{2.26}$$

$$K_+ = -\frac{p_+ + q_+}{4q}\lambda^2 - (p_3+q_3)\frac{q_+ q_3}{q q_s^2}\lambda^2 - 2p_- \frac{q_+^2}{q q_s^2}\lambda^2 - \frac{q_+}{q}\lambda^2 \tag{2.27}$$

$$K_3 = \frac{p_3 + q_3}{4q}\lambda^2 - p_- \frac{q_3 q_+}{q q_s^2}\lambda^2 - \frac{q_3}{2q}\lambda^2 \tag{2.28}$$

$$K_I = -p_- \frac{8i}{\pi} \frac{q_+}{q_s^2}\lambda - \frac{4i}{\pi}\lambda \tag{2.29}$$

We use Feynman parameters to evaluate these integrals, and we will only keep the logarithmic divergences. The relevant formulas are

$$\int \frac{d^3q}{(2\pi)^3} \frac{f(q)}{q(p+q)^2} = \frac{1}{2}\int_0^1 dx \int \frac{d^3q}{(2\pi)^3} (1-x)^{-1/2} \frac{f(q-xp)}{(q^2 + x(1-x)p^2)^{3/2}} \tag{2.30}$$

$$\int \frac{d^3q}{(2\pi)^3} \frac{f(q)}{q^2(p+q)^2} = \int_0^1 dx \int \frac{d^3q}{(2\pi)^3} \frac{f(q-xp)}{(q^2 + x(1-x)p^2} \tag{2.31}$$

$$\begin{aligned} \int \frac{d^3q}{(2\pi)^3} \frac{f(q_3, \vec{q}_s)}{q_s^2 q(p+q)^2} = \frac{3}{4}\int_0^1 dy \int_0^{1-y} dz \int \frac{d^3q}{(2\pi)^3} y^{-1/2} \\ \times \frac{f(q_3 - \frac{z}{y+z}p_3, \vec{q}_s - z\vec{p}_s)}{\Big(q_s^2 + z(1-z)p_s^2 + (y+z)q_3^2 + \frac{yz}{y+z}p_3^2\Big)^{5/2}} \end{aligned} \tag{2.32}$$

The result for the fermionic self-energy is

$$\Sigma_\psi(p) = i\alpha \frac{64}{64+\pi^2\lambda^2} \frac{\lambda^2}{24} (-p_\mu \gamma^\mu + 6p_3\gamma^3 + 12p_+\gamma^+) \ln\Lambda + \ldots \tag{2.33}$$

Putting this into the two point function at zero external momenta, we can extract the logarithmic contribution via

$$\frac{1}{2}\operatorname{Tr} \frac{\not{p}}{ip^2}\Sigma_\psi(p) = \frac{1}{2}\operatorname{Tr} \frac{\not{p}}{ip^2} i\alpha \frac{64}{64+\pi^2\lambda^2} \frac{\lambda^2}{24} (-p_\mu\gamma^\mu + 6p_3\gamma^3 + 12p_+\gamma^+) \ln\Lambda \tag{2.34}$$

$$= \alpha \frac{64\lambda^2}{64+\pi^2\lambda^2} \frac{\lambda^2}{24} (-p^2 + 6p_3^2 + 6p_s^2) \frac{1}{p^2} \ln\Lambda \tag{2.35}$$

$$= \alpha \frac{64\lambda^2}{64+\pi^2\lambda^2} \frac{5}{24} \ln\Lambda \tag{2.36}$$

Since this diagram contributes with a weight of 2, it contributes $\delta_1 = -\alpha\frac{64\lambda^2}{64+\pi^2\lambda^2}\frac{5}{24}$

Next, the 1-loop vertex correction.

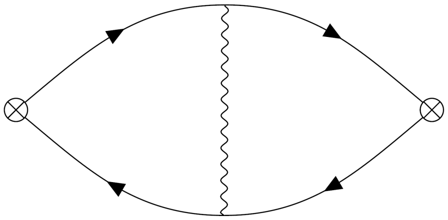

Note that to extract logarithmic divergences it is easier to calculate the vertex correction with external momenta 0 than to calculate the full two-loop integral. Also, since we will combine the two free ends to a single vertex, we only care about the identity component, which can be extracted by applying $1/2\,\mathrm{Tr}$ over the gamma matrices. Hence, the divergence is given by

$$\frac{N}{2}\frac{1}{2}\mathrm{Tr}\int\frac{d^3q}{(2\pi)^3}(i\gamma^\mu)\frac{1}{-q^2}(i\gamma^\nu)G_{\mu\nu}(q) = \alpha\frac{\lambda^2}{64+\pi^2\lambda^2}\frac{1}{8}\ln\Lambda \tag{2.37}$$

Each vertex contributes once to the divergence, so there is an overall factor of 2. In total, this diagram contributes $\delta_2 = -\alpha\frac{64\lambda^2}{64+\pi^2\lambda^2}\frac{1}{8}$.

Finally, the last diagrams

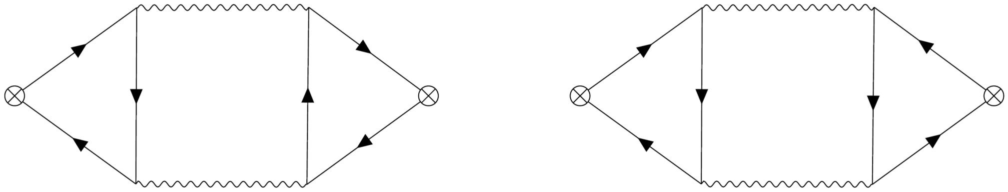

These are two-loop vertex corrections, so again it's simpler to focus only on the vertex. Note that since we will combine the two free ends to a single vertex, we only care about the identity component, which can be extracted by applying $1/2\,\mathrm{Tr}$ over the gamma matrices. We focus first on the left one.

$$(-1)N_f\frac{N}{4}\int\frac{d^3p}{(2\pi)^3}\int\frac{d^3k}{(2\pi)^3}\frac{1}{2}\,\mathrm{Tr}\left(\frac{1}{i\not{p}}\frac{1}{i\not{p}}\gamma^{\sigma}\frac{1}{i(\not{p}+\not{k})}\gamma^{\nu}\right)\mathrm{Tr}\left(\gamma^{\mu}\frac{1}{i\not{k}}\gamma^{\eta}\right)G_{\mu\nu}(k)G_{\sigma\eta}(k)$$
$$=\alpha\frac{1}{2}\frac{64}{64+\pi^2\lambda^2}\frac{64-\pi^2\lambda^2}{64+\pi^2\lambda^2}\ln\Lambda \tag{2.38}$$

This diagram contributes with a factor of 2 because there are two vertices. The right diagram also gives the same result because of the relation $\mathrm{Tr}\,\gamma^{\alpha}\gamma^{\beta}\gamma^{\delta} = -\mathrm{Tr}\,\gamma^{\gamma}\gamma^{\beta}\gamma^{\alpha}$. Hence, the two diagrams together contribute $\delta_3 = -\alpha\frac{64}{64+\pi^2\lambda^2}\frac{64-\pi^2\lambda^2}{64+\pi^2\lambda^2}$.

Therefore, the scaling dimension of $\bar{\psi}\psi$ is

$$[\bar{\psi}\psi] = 2-(\delta_1+\delta_2+\delta_3) = 2-\alpha\frac{128\lambda^2}{3}\frac{128-\pi^2\lambda^2}{(64+\pi^2\lambda^2)^2} \tag{2.39}$$

Note that our answer differs with Gurucharan and Prakash, as they did not include the last diagram which contributes an extra factor of 2 in δ_3.

2.2 Non-Abelian bosonization and modular transformation approach to superuniversality

This section is adapted from a PRB paper [115] with Eun-Ah Kim and Michael Mulligan.

Quantum Hall inter-plateaux transitions are physical exemplars of quantum phase transitions. Near each of these transitions, the measured electrical conductivity scales with the same correlation length and dynamical critical exponents, i.e., the critical points are superuniversal. In apparent contradiction to these experiments, prior theoretical studies of quantum Hall phase transitions within the framework of Abelian Chern-Simons theory coupled to matter found correlation length exponents that depend on the value of the quantum critical Hall conductivity. Here, we use non-Abelian bosonization and modular transformations to theoretically study the phenomenon of superuniversality. Specifically, we introduce a new effective theory that has an emergent $U(N)$ gauge symmetry with any $N > 1$ for a quantum phase transition between an integer quantum Hall state and an insulator. We then use modular transformations to generate from this theory effective descriptions for transitions between a large class of fractional quantum Hall states whose quasiparticle excitations have Abelian statistics. We find the correlation length and dynamical critical exponents are independent of the particular transition within a controlled 't Hooft large N expansion, i.e., superuniversal! We argue that this superuniversality could survive away from this controlled large N limit using recent duality conjectures.

2.2.1 Introduction

As a two-dimensional electron gas is tuned by a perpendicular magnetic field from one quantum Hall state to another, the longitudinal electrical resistance exhibits a peak with a width $\Delta B \propto T^{1/\nu z}$, where ν and z are correlation length and dynamical critical exponents and T is the temperature; the slope of the Hall resistance likewise diverges as ΔB as a particular transition is approached [6].

---

[6] Similar scaling is observed if the temperature is replaced by frequency, applied current, or inverse system size.

The surprising feature is that the observed $\nu \approx 7/3$ and $z \approx 1$ appear to be insensitive to whether the transition is between integer or fractional Abelian quantum Hall states [291, 68, 145, 69, 290, 302, 167, 168, 169] (See note [7]) Taken at face value, the implication is that the associated quantum critical points [259, 240] have the same critical indices for comparable observables [152, 125, 144, 185, 76, 250, 25, 88] and are instead distinguished by their critical conductivity [121, 247, 289] (see [8]); this phenomenon is known as *superuniversality* [250].

The root cause of superuniversality has been a puzzle since its observation over three decades ago. Numerical studies of the integer quantum Hall transition, modeled by disordered noninteracting electrons, find a correlation length exponent in qualitative agreement with experiment [33, 113, 253], however, these theories have $z \approx 2$ and it is challenging to generalize these works to transitions between fractional quantum Hall states [155]. Theories of Abelian Chern-Simons gauge fields coupled to matter, i.e., theories of composite bosons or composite fermions [87, 124, 226, 322, 177, 99, 134], provide a unifying, physical framework for studying both integer and fractional quantum Hall transitions. Thus far, controlled approximations to these strongly coupled theories, obtained when the number of fermion or boson flavors is large and there is no disorder, have failed to yield superuniversal behavior: the calculated correlation length exponent depends on the particular quantum Hall transition [294, 41, 156, 118]. It is important to determine whether these calculations reveal a generic behavior of the field theoretical models or, instead, reflect certain artifacts of the approximation scheme [9]. In this paper, we provide evidence for

---

[7] Strictly speaking, the product νz has only been factorized at integer plateau transitions, however, dimensional analysis suggests $z = 1$ for both types of transitions if the Coulomb interaction provides the dominant scale.

[8] See [217] for an explanation of the low-temperature conductivity in the scaling region in terms of variable-range hopping.

[9] Superuniversality has been found in studies of disordered Dirac fermions of various sym-

the latter.

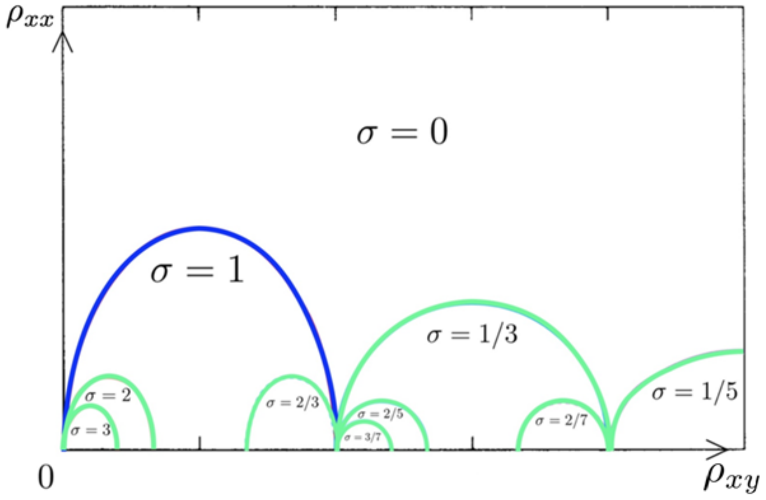

Figure 2.3: Schematic zero-temperature phase diagram [144] in the space of Hall ρ_{xy} and longitudinal resistivity ρ_{xx}. Phases are denoted by their zero-temperature complex conductivity $\sigma = \sigma_{xy} + i\sigma_{xx}$, measured in units of e^2/h. The blue boundary denotes the $1 \to 0$ integer quantum Hall transition, while the green boundaries denote transitions we derive from the $1 \to 0$ transition via modular transformations.

As a step towards understanding the observed behavior, we focus here on the fundamental theoretical question raised by the appearance of superuniversality, i.e., how distinct interacting critical points can share the same critical exponents. To this end, we introduce new theories, involving a single Dirac fermion coupled to a *non-Abelian* $U(N)$ Chern-Simons gauge field for any $N > 1$, that exhibit quantum phase transitions between Abelian quantum Hall states. Intuitively, the $U(N)$ gauge symmetry of our theories generalizes the Abelian gauge symmetry implementing flux attachment in familiar composite boson/fermion theories. In fact, as demonstrated in Appendix 2.2.11, these $U(N)$ gauge theories are dual to theories with an Abelian group. The advantage of the enlarged gauge group is that it motivates an alternate approximation to

---

metry classes in $3+1$ dimensions [90] and in certain models with long-ranged statistical interactions [82] $2+1$ dimensions.

our strongly coupled theories, namely, a controlled 't Hooft large N expansion [271] [10], within which we find that superuniversality occurs without the inclusion of disorder.

We emphasize that the theories we consider here have more symmetries than the physical systems motivating our work; for instance, our theories are Lorentz-invariant and, in particular, preserve translational invariance. Our hope is that our theories might represent "parent" theories for more realistic descriptions of the experimental systems. Consequently, we defer quantitative questions specific to the particular experimental systems to the future.

The remainder of this paper is organized as follows. In Sec. 2.2.2, we introduce a new description for an integer quantum Hall transition; this theory is inspired by fermion particle-vortex duality [257, 285, 193, 137, 243] (see the related work [131, 83, 307, 198, 197]) and various bosonization dualities in $2+1$ dimensions [85, 3, 2, 126, 94, 4, 201, 109, 132, 133, 39, 196, 284]. Guided by Ref. [144], where the phase diagram in Fig. 2.3 was proposed by extending the theory of two-parameter scaling of the Hall and longitudinal resistivity for the integer Hall effect [160] to the fractional Hall regime using the "law of corresponding states" [125, 144], we then derive in Sec. 2.2.3 new effective theories for various fractional quantum Hall transitions using modular transformations [300]. In Sec. 2.2.4, we show that the correlation length and dynamical critical exponents of our theories are insensitive to the particular quantum Hall phase transition within a controlled 't Hooft large N limit. In Sec. 2.2.5, we discuss how recent duality conjectures imply that the physics of our $U(N)$ Chern-Simons coupled to matter theories is *independent* of $N > 1$. This is the crucial feature that allows

---

[10] See [73, 295, 223, 288, 81] for earlier applications of the large N expansion in condensed matter physics. Gauge/gravity duality can provide an alternative framework where large N naturally appears [57].

us to argue that critical exponents, calculated in the 't Hooft large N limit, are exact at the leading planar order and that superuniversality may persist away from the controlled 't Hooft large N limit. In addition, there are six appendices that discuss details of arguments presented in the main text.

2.2.2 Integer quantum Hall transition

Our starting point is an effective Lagrangian for an integer quantum Hall transition,

$$\begin{aligned}\mathcal{L}_{\rm IQHT}(A) = i\bar{\psi}\, \not{D}_a\psi - M_\psi\bar{\psi}\psi - \frac{1}{2}\frac{1}{4\pi}\mathrm{Tr}\Big[ada - \frac{2}{3}ia^3\Big] \\ - \frac{1}{2\pi}\mathrm{Tr}[a]db - \frac{N+1}{4\pi}bdb - \frac{1}{2\pi}bdA. \end{aligned} \tag{2.40}$$

The notation is as follows: ψ is a two-component Dirac fermion transforming in the fundamental representation of $U(N)$; a and b are dynamical $U(N)$ and $U(1)$ Chern-Simons gauge fields; A (above and throughout) is a non-dynamical Abelian gauge field that we think of as electromagnetism; $\not{D}_a = \gamma^\mu(\partial_\mu - ia_\mu)$ for $\mu \in \{t, x, y\}$ and γ-matrices satisfying $\{\gamma^\mu, \gamma^\nu\} = 2\eta^{\mu\nu}$ where $\eta^{\mu\nu} = \mathrm{diag}(1, -1, -1)$; $\bar{\psi} = \psi^\dagger\gamma^t$; N is a positive integer; Abelian Chern-Simons terms $AdB = \epsilon^{\mu\nu\rho}A_\mu\partial_\nu B_\rho$, and the cubic interaction in the non-Abelian Chern-Simons term $a^3 = \frac{1}{2}\epsilon^{\mu\nu\rho}a_\mu a_\nu a_\rho$. For simplicity of presentation, we regularize the theory in (2.40) by implicitly including a Yang-Mills term for a and Maxwell term for b [301, 42]. See Appendix 2.2.7 for further explanation of the notation and for a few pertinent facts about Chern-Simons theories.

Prior work studying Chern-Simons gauge theories coupled to matter suggests that the theory in (2.40) realizes a critical point with conformal symmetry

[42, 16]. In Appendix 2.2.11, we argue nonperturbatively that this critical point is in the free Dirac fermion universality class for any integer $N \geq 1$.

For the moment, we verify that (2.40) describes a transition between an integer quantum Hall state and an insulator as the fermion mass M_ψ is tuned through zero, consistent with our identification in Appendix 2.2.11 of (2.40) with the theory of a free Dirac fermion. See Appendix 2.2.8 for additional details. Remarkably, this demonstration applies for any integer $N \geq 1$. In our theory, the mass M_ψ represents an *effective* control parameter for a particular quantum phase transition. For definiteness, it may be helpful to think about M_ψ in terms of the analogous tuning parameter that appears in lattice models for integer quantum Hall transitions [98, 183]. In these latter models, the transition is controlled by the ratio of the on-site chemical potential to the second nearest-neighbor hopping. This theory matches the realistic integer quantum Hall transition insofar that it describes some transition between two integer quantum Hall states, as is commonly done in the literature.

Our strategy is to identify the insulating and integer quantum Hall states through their electrical response to the electromagnetic gauge field A. Below the energy scale of the mass $|M_\psi|$, we can integrate out ψ to obtain:

$$\mathcal{L}_{\text{eff}} = \frac{\operatorname{sign}(M_\psi) - 1}{2} \frac{1}{4\pi} \operatorname{Tr}\left[ada - \frac{2}{3}ia^3\right] - \frac{1}{2\pi}\operatorname{Tr}[a]db - \frac{N+1}{4\pi} bdb - \frac{1}{2\pi} bdA. \tag{2.41}$$

In this effective Lagrangian, only relevant and marginal terms in the renormalization group sense are written. If $M_\psi < 0$, rank/level duality [202, 203, 109] (Appendix 2.2.8) implies that

$$\mathcal{L}_{\text{eff}}(M_\psi < 0) = \frac{1}{4\pi} AdA, \tag{2.42}$$

i.e., the effective electrical response Lagrangian of an integer quantum Hall state. Consequently, we identify the phase obtained for $M_\psi < 0$ with an integer quantum Hall state. Integrating out fermions with $M_\psi > 0$, the non-Abelian Chern-Simons term for a disappears. Only $\mathrm{Tr}[a]$ remains in the effective Lagrangian; the $SU(N) \subset U(N)$ component of a decouples and we assume it confines [70]. The equation of motion for $\mathrm{Tr}[a]$ sets $b = 0$ [300] and the resulting effective Lagrangian,

$$\mathcal{L}_{\text{eff}}(M_\psi > 0) = 0, \tag{2.43}$$

describes an electrical insulator. We expect the leading irrelevant operator supplementing the effective Lagrangian in Eq. (2.43) to be a Maxwell term for A, consistent with our identification of the phase obtained when $M_\psi > 0$ with an insulator.

2.2.3 Generating fractional quantum Hall transitions

We now show how to generate effective descriptions with $U(N)$ gauge symmetry for fractional quantum Hall transitions using the modular group, $PSL(2, \mathbb{Z})$, i.e., the group of 2×2 matrices with integer entries and unit determinant. On a complex number, like the complexified zero-temperature dc conductivity

$\sigma = \sigma_{xy} + i\sigma_{xx}$ (measured in units of e^2/h) [11], the modular group takes

$$\sigma \mapsto \frac{p\sigma + q}{r\sigma + s}, \text{ for } \begin{pmatrix} p & q \\ r & s \end{pmatrix} \in PSL(2, \mathbb{Z}). \tag{2.44}$$

Because the modular group is generated by two elements, $\mathcal{T} = \left(\begin{smallmatrix} 1 & 1 \\ 0 & 1 \end{smallmatrix}\right)$ and $\mathcal{S} = \left(\begin{smallmatrix} 0 & 1 \\ -1 & 0 \end{smallmatrix}\right)$, any element of $PSL(2, \mathbb{Z})$ can be decomposed into a product of $\mathcal{T}$ and $\mathcal{S}$ operators.

Ref. [300] showed how the modular group in Eq. (2.44) acts on the Lagrangian of a conformal field theory with $U(1)$ global symmetry. (See [158] for the effects on higher-spin currents.) Denoting the Lagrangian of an arbitrary conformal field theory by $\mathcal{L}(\Phi, A)$, where Φ collectively represents all dynamical fields and A is a background field coupling to the $U(1)$ symmetry, the modular group acts as follows:

$$\begin{aligned} \mathcal{T} &: \mathcal{L}(\Phi, A) \mapsto \mathcal{L}(\Phi, A) + \frac{1}{4\pi} AdA, \\ \mathcal{S} &: \mathcal{L}(\Phi, A) \mapsto \mathcal{L}(\Phi, c) - \frac{1}{2\pi} cdB. \end{aligned} \tag{2.45}$$

Eq. (2.45) induces the action of the modular group on the complexified conductivity of the $U(1)$ symmetry of $\mathcal{L}(\Phi, A)$. $\mathcal{T}$ simply shifts the Hall conductivity by one unit; $\mathcal{S}$ inverts $\sigma \to -1/\sigma$ through its replacement of A with a dynamical $U(1)$ gauge field c and introduction of a new background field B via the coupling $-\frac{1}{2\pi} cdB$.

Reminiscent of the "law of corresponding states" [144] (see Fig. 2.3) we can

---

[11] We define $\sigma = \lim_{\omega \to 0} \lim_{T \to 0} \sigma(\omega, T)$. We only require σ for quantum Hall states described at long distances by Chern-Simons theory, since we only need to know how the Hall conductivity changes across a transition. We caution that the order of limits may not generally commute for either gapped [323] or gapless states [54].

generate using Eq. (2.45) an effective description for a transition between any two quantum Hall states related by a modular transformation to either the insulator ($\sigma = 0$) or integer quantum Hall state ($\sigma = 1$). The pertinent subset of transformations can be decomposed into two operations:

(i) addition of a Landau level = $\mathcal{T}$;

(ii) attachment of m units of flux = $\mathcal{S}^{-1}\mathcal{T}^{-m}\mathcal{S}$.

Any transition from $\sigma = j \to j-1$ between integer quantum Hall states is found by adding $j-1$ Landau levels, i.e., applying $\mathcal{T}^{j-1}$ with $j \in \mathbb{Z}$ to Eq. (2.40). On the other hand, the fractional quantum Hall transition, $1/(m+1) \to 0$, is obtained by applying $\mathcal{S}^{-1}\mathcal{T}^{-m}\mathcal{S}$ to Eq. (2.40). We can combine the operations of adding a Landau level and flux attachment to find a description for the $1/3 \to 2/5$ transition using $\mathcal{S}^{-1}\mathcal{T}^{-2}\mathcal{S}\mathcal{T}$. The $2/3 \to 1$ transition – the lowest Landau level particle-hole conjugate of the $1/3 \to 0$ transition – is obtained by acting on the Lagrangian in Eq. (2.40) with $\mathcal{T}\mathcal{S}^{-1}\mathcal{T}^{2}\mathcal{S}\mathcal{T}^{-1}$. Other transitions can be generated by further iteration of these methods. Hence, modular transformations formalize the "law of corresponding states" [124, 125, 144]. Because we have not included effects of disorder, we are, in a sense, effectively considering the horizontal axis of Fig. 2.3.

In the remainder of the paper, we focus on the $\frac{1}{m+1} \to 0$ transition where the even integer $m \geq 0$; qualitatively similar arguments apply for other transitions. Applying the modular transformation described above to (2.40), we find the Lagrangian,

$$\mathcal{L}_m = \mathcal{L}_{\text{IQHT}}(c) + \mathcal{L}_{\text{mod}}(A), \tag{2.46}$$

where $\mathcal{L}_{\mathrm{IQHT}}(c)$ is given in Eq. (2.40) with the replacement $A \to c$ and

$$\mathcal{L}_{\mathrm{mod}}(A) = -\frac{1}{2\pi} c dg - \frac{m}{4\pi} g dg + \frac{1}{2\pi} g dA, \tag{2.47}$$

with dynamical $U(1)$ gauge fields c and g. Thus, the modular transformation simply introduces additional Chern-Simons gauge fields coupling to the $U(1) \subset U(N)$ gauge field $\mathrm{Tr}[a]$ in $\mathcal{L}_{\mathrm{IQHT}}$. Appendix 2.2.9 lists the corresponding effective Lagrangians, analogous to Eqs. (2.46) and (2.47), for other simple quantum Hall transitions. When $m = 0$, we may integrate out c and g using their equations of motion to recover the Lagrangian in Eq. (2.40); when $m \geq 2$, we can no longer integrate out g to recover an effective Lagrangian whose Chern-Simons terms have integer levels.

It is straightforward to check (see Appendix 2.2.10 for details) using the arguments given below Eq. (2.41) that $\mathcal{L}_m$ in Eq. 2.46 and its generalizations describe a large class of fractional quantum Hall phase transitions, tuned by the fermion mass. We assume these transitions are continuous for any $m \geq 0$.

2.2.4 Superuniversality in the 't Hooft large N limit

Our goal is to determine the correlation length and dynamical critical exponents exhibited by $\mathcal{L}_m$ in Eq. (2.46) for $m \geq 0$. The (inverse) correlation length exponent, $\nu^{-1} = 1 - \gamma_{\bar{\psi}\psi}$, measures the anomalous dimension $\gamma_{\bar{\psi}\psi}$ of the operator $\bar{\psi}\psi(x)$ [12], whose coefficient M_ψ is the tuning parameter for the various fractional quantum Hall transitions we consider. Since our effective theories are Lorentz-invariant, $z = 1$ automatically. Because $\mathcal{L}_m$ depends on the rank N of the $U(N)$

---

[12] The anomalous dimension is determined by the decay of the two-point function $\langle \bar{\psi}\psi(x)\bar{\psi}\psi(0)\rangle \sim |x|^{-2(1+\gamma_{\bar{\psi}\psi})}$

gauge group of a, it is necessary to choose a particular value of N at which to evaluate ν. We choose $N = \infty$ and determine ν in a controlled 't Hooft large N limit. In Sec. 2.2.5, we will argue that the physics of $\mathcal{L}_m$ is independent of N. Consequently, $N = \infty$ represents a reliable value of the parameter N at which to determine the critical exponents of $\mathcal{L}_m$.

In order to determine the correlation length exponent, it is helpful to first simplify the Lagrangian $\mathcal{L}_m$ as follows: we set the background field $A = 0$; next, we integrate out all Abelian gauge fields (i.e., b, c, and g) not minimally coupled to ψ; finally, we decompose $a = a_{SU(N)} + a_{U(1)}\mathbb{I}$, where $a_{SU(N)}$ is a $SU(N) \subset U(N)$ gauge field, $a_{U(1)}$ is an Abelian gauge field, and $\mathbb{I}$ is the $N \times N$ identity matrix. After performing these steps, $\mathcal{L}_m$ becomes

$$\mathcal{L}_{\mathrm{s}} = i\bar{\psi}\, \not{D}_a \psi + \frac{k_{U(1)}}{4\pi} a_{U(1)} d a_{U(1)} + \frac{k_{SU(N)}}{4\pi} \mathrm{Tr}\Big[a_{SU(N)} d a_{SU(N)} - \frac{2}{3} i a_{SU(N)}^3\Big], \quad (2.48)$$

with $k_{U(1)} = \dfrac{N^2 - N - Nm}{2(N+1+m)}$ and $k_{SU(N)} = -\dfrac{1}{2} - N$. We included the one-loop exact correction [301, 42] to the $SU(N) \subset U(N)$ Chern-Simons level $k_{SU(N)}$. Although $\mathcal{L}_{\mathrm{s}}$ obscures the topological structure of our quantum critical state and any gapped phase obtained from it when $M_\psi \neq 0$ [13], the perturbative analysis is unchanged.

To gain some intuition for the possible behavior of $\mathcal{L}_{\mathrm{s}}$ (and, therefore, $\mathcal{L}_m$), suppose the fluctuations of $a_{SU(N)}$ were ignored. Then, $\mathcal{L}_{\mathrm{s}}$ would effectively describe N flavors of fermions interacting with the Abelian Chern-Simons gauge field $a_{U(1)}$. For such theories, it is known that $\gamma_{\bar{\psi}\psi} = 1 + \mathcal{O}(\frac{1}{k_{U(1)}N})$ at large N [41]. Because $k_{U(1)} \propto N$ as $N \to \infty$ for any fixed m, the effects mediated by $a_{U(1)}$ could then be made arbitrarily small as $N \to \infty$. (This is true for the other quan-

---

[13] The allowed Wilson loop observables are not manifest in Chern-Simons Lagrangians with non-quantized levels. If the Chern-Simons theory is to describe a gapped state, additional information is needed to specify the quasiparticle spectrum.

tum Hall transitions considered in Appendix 2.2.9.) Consequently, since m only appears in $k_{U(1)}$, $\gamma_{\bar{\psi}\psi}$ would be independent of m at $N = \infty$, i.e., superuniversal. Our task now is to determine the extent to which this conclusion survives the inclusion of $a_{SU(N)}$ fluctuations.

The 't Hooft large N limit [271] (see [48] for a review) provides an expansion within which to calculate $\gamma_{\bar{\psi}\psi}$. This limit, which is distinct from the limit that obtains within large flavor expansions, is defined by taking the rank of the $U(N)$ gauge group $N \to \infty$ with the ratios $\lambda_{SU(N)} = N/k_{SU(N)}$ and $\lambda_{U(1)} = N/k_{U(1)}$ held fixed. Observables like $\gamma_{\bar{\psi}\psi}$ are then calculated in an expansion in powers of $1/N$; the coefficient of a particular power of $1/N$ is generally a power series in $\lambda_{SU(N)}$ and $\lambda_{U(1)}$. In addition, there could be non-perturbative $\lambda_{SU(N)}$ and $\lambda_{U(1)}$ contributions to $\gamma_{\bar{\psi}\psi}$. Our result in this section ignores any such non-perturbative corrections; our duality argument in the next section indicates such corrections are absent at least when $m = 0$.

As an illustrative example of how large N scaling works, Fig. 2.4(a) decomposes the $a_{SU(N)}$ and $a_{U(1)}$ one-loop contributions to the fermion self-energy. In our conventions, vertices scale as N^0, while gauge field propagators come with factors of $k^{-1}_{SU(N)}$ or $k^{-1}_{U(1)}$ depending upon whether $a_{SU(N)}$ or $a_{U(1)}$ propagates; ψ propagators scale as N^0. At large N, the $a_{SU(N)}$ contribution in Fig. 2.4(a) scales as $\lambda_{SU(N)}$, while the $a_{U(1)}$ correction scales as $\lambda_{U(1)}/N$. (Here, we have assumed the $U(N)$ coupling constant achieves its fixed point value, proportional to N^0.) Thus, the contribution of $a_{U(1)}$ in Fig. 2.4(a) is subdominant to that of $a_{SU(N)}$ as $N \to \infty$ by a factor of $1/N$. This is a general feature: in perturbation theory, the 't Hooft large N limits of $SU(N)$ and $U(N)$ gauge theories give identical results for shared observables [48]. For Chern-Simons gauge theories with $U(N)$ gauge

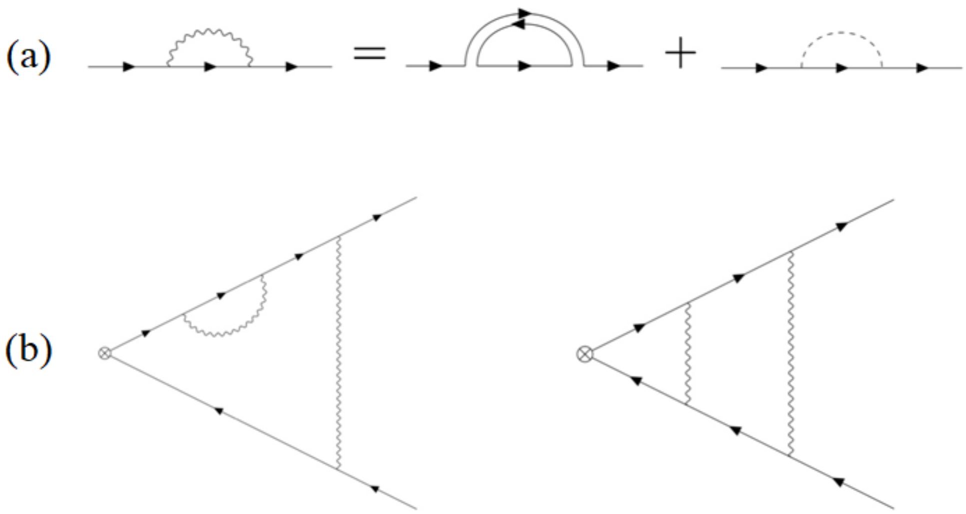

Figure 2.4: (a) One-loop fermion self-energy decomposed into $SU(N) \subset U(N)$ and $U(1) \subset U(N)$ contributions. The closed oriented loop produces the relative factor of N between the second and third diagrams. (b) The leading Feynman diagrams contributing to $\gamma_{\bar{\psi}\psi}$ in the 't Hooft large N limit. Directed lines are fermion propagators; wavy lines are $U(N)$ gauge field propagators; a double line is a $SU(N)$ gauge field propagator; a dashed line denotes a $U(1)$ gauge field propagator; insertion of $\bar{\psi}\psi$ is represented by $\otimes$.

group, this relies on the $1/N$ suppression of diagrams containing closed loops of $a_{U(1)}$ relative to the corresponding planar diagrams that instead contain loops of $a_{SU(N)}$.

So long as $|k_{U(1)}| \propto N$ as $N \to \infty$, the effects of $a_{U(1)}$ are subdominant by a factor of $1/N$ in the 't Hooft large N limit. In particular, only the fluctuations of $a_{SU(N)}$ contribute to $\gamma_{\bar{\psi}\psi}$ at $N = \infty$. The planar contribution to $\gamma_{\bar{\psi}\psi}$ scales with N as N^0 and consists of an infinite expansion in $\lambda_{SU(N)}$; the first sub-planar contribution scales as $1/N$ and consists of an infinite series in $\lambda_{SU(N)}$ and $\lambda_{U(1)}$. Thus, the 't Hooft expansion for $\gamma_{\bar{\psi}\psi}$ has the form:

$$\gamma_{\bar{\psi}\psi} = f_0(\lambda_{SU(N)}) + \frac{1}{N} f_1(\lambda_{SU(N)}, \lambda_{U(1)}) + \dots, \tag{2.49}$$

where the planar term $f_0(\lambda_{SU(N)})$ is a power series in $\lambda_{SU(N)}$, the first sub-planar term $f_1(\lambda_{SU(N)}, \lambda_{U(1)})$ is a power series in $\lambda_{SU(N)}$ and $\lambda_{U(1)}$, and $\ldots$ represent higher powers of $1/N$ which are expected to be subdominant in this expansion. (The assumption that f_0 and f_1 are power series of their arguments is the statement that we are ignoring possible non-perturbative contributions to $\gamma_{\bar{\psi}\psi}$.) Because m only appears in $\lambda_{U(1)}$, through its appearance in the effective Chern-Simons level $k_{U(1)}$ of $a_{U(1)}$ (see Eq. (2.48) and Appendix 2.2.9), ν is insensitive to the particular $1/(m+1) \to 0$ transition at $N = \infty$. This is superuniversality in the 't Hooft large N limit.

The specific value of ν is determined by $f_0(\lambda_{SU(N)})$ at $N = \infty$. An important point is that the 't Hooft large N limits of the theories we consider remain non-trivial even when $N = \infty$. For instance, $|\lambda_{SU(N)}| = 1$ for $N = \infty$, so that an infinite number of terms generally need to be summed to determine $f_0(\lambda_{SU(N)})$. Here, we find $\gamma_{\bar{\psi}\psi}$ in a *controlled* 't Hooft large N limit, where it is necessary to continue $k_{SU(N)}$ away from its physical value (given below Eq. (2.48)) such that $\lambda_{SU(N)} \ll 1$ and $f_0(\lambda_{SU(N)})$ can be reliably approximated by the leading terms in its expansion in $\lambda_{SU(N)}$.

Figure 2.4(b) displays the leading contributions to $\gamma_{\bar{\psi}\psi}$ arising from the fluctuations of $a_{SU(N)}$ [14]. In [85], it was shown that these two contributions cancel, i.e., $\gamma_{\bar{\psi}\psi} = 0$ to two-loop planar order or, equivalently, $f_0(\lambda_{SU(N)}) = 0$ to $\mathcal{O}(\lambda^2_{SU(N)})$. Thus, at the critical point described by $\mathcal{L}_m$ in Eq. (2.46):

$$\nu = 1 + \mathcal{O}\Big(\lambda^3_{SU(N)}\Big), \tag{2.50}$$

for any $m \geq 0$ in the controlled 't Hooft large N limit. In perturbation theory, the dependence on m, i.e., the particular fractional quantum Hall critical point,

---

[14] The one-loop vertex diagram, as well as one-loop and two-loop fermion self-energy diagrams do not contain logarithmic divergences and, consequently, do not contribute to $\gamma_{\bar{\psi}\psi}$ [42, 16, 85].

appears at sub-planar order and is unobservable at $N = \infty$.

2.2.5 N independence and duality

We now explore the degree to which the superuniversality of Eq. (2.50) persists away from this controlled large N limit, i.e., when $k_{SU(N)}$ is continued back to its physical value given below Eq. (2.48). We will use duality to argue that the physics described by $\mathcal{L}_m$ is independent of the particular value of N appearing in the Lagrangian and that one consequence of this N independence is that $\nu = 1$ away from the controlled 't Hooft large N limit.

In Secs. (2.2.2) and (2.2.3), we showed that the effective Lagrangians describing the gapped phases that obtain from $\mathcal{L}_m$ for $M_\psi \neq 0$ do not depend on N. It remains to argue that the physics of the intervening critical point could also be independent of N. For this, we conjecture a duality that equates the long wavelength behavior of the theory in (2.40) to that of a free Dirac fermion for any integer N:

$$i\bar{\Psi}\not{D}_A\Psi + \frac{1}{2}\frac{1}{4\pi}AdA \longleftrightarrow \mathcal{L}_{\mathrm{IQHT}}(A). \tag{2.51}$$

Remarkably, this duality implies that the physics described by $\mathcal{L}_{\mathrm{IQHT}}(A)$ does *not* depend on the particular value of N appearing in its Lagrangian. While a direct proof of Eq. (2.51) is not known, we can show that Eq. (2.51) is a consequence of the web of bosonization dualities in $2+1$ dimensions [137, 243] (see Appendices 2.2.11 and 2.2.13 for details). Furthermore, (2.51) is the statement of fermion particle-vortex duality [257, 285, 193, 137, 243] when $N = 1$. Consequently, the accumulated evidence for the duality web likewise provides support for Eq. (2.51). In the remainder, we study the consequences of Eq. (2.51).

If the duality in Eq. (2.51) holds for *all* integers $N \geq 1$, then ν must be independent of N for the theory in (2.40) and its "modular descendants,", i.e., the theories of fractional quantum Hall transitions given by $\mathcal{L}_m$ in Eq. (2.46). (See Appendix 2.2.11 for the Abelian Chern-Simons dual of $\mathcal{L}_m$.) Furthermore, choosing to determine ν at $N = \infty$, the specific value of ν should be captured at the leading planar order in the 't Hooft large N limit. This is because only planar terms scale as N^0 at large N; sub-planar terms always have an explicit dependence on N through their $1/N$ prefactors (recall that both $k_{SU(N)}$ and $k_{U(1)}$ in Eq. (2.48) scale linearly with N) and so they should not contribute to ν in any planar expansion at $N = \infty$.

Since $\nu = 1$ exactly for the theory of a free Dirac fermion, Eq. (2.51) implies the planar contribution to $\gamma_{\bar{\psi}\psi}$ vanishes for the theory in (2.40). In the absence of non-perturbative corrections to the 't Hooft expansion in Eq. (2.50) when $m \geq 2$, $\nu = 1$ should also hold for transitions involving fractional states, e.g., $\frac{1}{m+1} \to 0$ with $m \geq 2$, because m only enters sub-planar terms in perturbation theory. In other words, duality suggests the critical theories considered in this paper exhibit superuniversality with $\nu = z = 1$.

2.2.6 Conclusion

In this work, we introduced new effective theories with an emergent $U(N)$ gauge symmetry ($N > 1$) for various fractional quantum Hall transitions. We showed that these theories are superuniversal in a controlled 't Hooft large N limit and we argued that this conclusion holds more generality using duality. Our theories function as an example that the effects of electron interactions and disorder can be disentangled from the phenomenon of superuniversality. Furthermore, our theories provide examples of new dualities which are of fundamental interest and may have applications to other instances of quantum criticality.

There are several directions of further study. It is important to better understand nonperturbative corrections to our theories; for instance, additional study of the lattice models in [82, 156] could provide useful insight. The theories in this paper may have direct application to quantum Hall transitions in graphene that can be controlled by varying an external electronic potential ([325] and references therein). Perhaps the most important direction is to incorporate the effects of disorder, which may account for the difference between the measured and theoretically determined correlation length exponent.

Acknowledgements

We thank S. Chakravarty, M. Fisher, E. Fradkin, T. Hartman, S. Kachru, S. Kivelson, O. Motrunich, D. Orgad, S. Raghu, S. Sachdev, E. Shimshoni, S. Sondhi, and S. Trivedi for helpful discussions and comments. A.H. was supported by the National Science Foundation Graduate Research Fellowship under Grant No. DGE-1650441. E.-A.K. was supported by the U.S. Department of Energy, Office of Basic Energy Sciences, Division of Materials Science and Engineering under Award de-sc0010313. M.M. was supported in part by the UCR Academic Senate. M.M. is grateful for the hospitality of the Aspen Center for Physics, which is supported by the National Science Foundation (NSF) grant PHY-1607611. The authors are grateful for the hospitality of the Kavli Institute for Theoretical Physics, under Grant No. NSF PHY-1125915.

2.2.7 Appendix: Chern-Simons conventions

In this appendix, we collect basic facts and definitions for Chern-Simons theories in $2+1$ dimensions. The Chern-Simons term for the $U(N)$ gauge field a is:

$$\mathrm{Tr}\Big[ada - \frac{2}{3}ia^3\Big] = N\epsilon^{\mu\nu\rho}(a^R_\mu \partial_\nu a^R_\rho - \frac{2}{3}if^{RST}a^R_\mu a^S_\nu a^T_\rho), \tag{2.52}$$

where $a = a^R_\mu t^R$ for $U(N)$ (algebra) generators t^R with $R \in \{1,\ldots,N^2\}$. Our normalization convention for these generators is the following: $\mathrm{Tr}[t^R t^S] = N\delta^{RS}$ and $[t^R, t^S] = if^{RST}t^T$ where f^{RST} are the structure constants of $U(N)$. We denote Abelian Chern-Simons terms:

$$AdB = \epsilon^{\mu\nu\rho}A_\mu \partial_\nu B_\rho, \tag{2.53}$$

where $\epsilon^{txy} = 1$.

In the absence of matter fields, only integral linear combinations of the following Chern-Simons terms appearing in Eq. (2.40) make well defined contributions to a $2+1$-dimensional effective action [62, 218]:

$$\begin{aligned}
&\frac{1}{4\pi}\mathrm{Tr}\Big[ada - \frac{2}{3}ia^3\Big],\\
&\frac{1}{4\pi}\mathrm{Tr}[a]d\mathrm{Tr}[a],\\
&\frac{1}{2\pi}\mathrm{Tr}[a]db,\\
&\frac{1}{4\pi}bdb.
\end{aligned} \tag{2.54}$$

Since $\mathrm{Tr}[a]$ extracts the $U(1) \subset U(N)$ component of a, we can think of $\mathrm{Tr}[a]$ as a $U(1)$ gauge field with 2π-quantized flux. The combination of a single Dirac fermion and half-integer Chern-Simons level for a in Eq. (2.40) yields a well defined term in the path integral [207, 228, 9].

We regularize our effective theories with a Yang-Mills term for a and a Maxwell term for the Abelian gauge fields. In a Yang-Mills regularization, the Chern-Simons level $k = -1/2$ for the $SU(N) \subset U(N)$ component of a receives a one-loop exact shift $k \to k + \mathrm{sign}(k)N$ [301, 42]. This correction arises from the interaction between the gauge fields contained in the Yang-Mills term. If regularized by dimensional reduction [42], the Chern-Simons level is not shifted (as the Yang-Mills interaction is no longer present). To describe (2.40) within dimensional reduction, the Chern-Simons level for the $SU(N)$ component $k_{\mathrm{DR}} = k + \mathrm{sign}(k)N$.

2.2.8 Appendix: Integer quantum Hall state and the insulator

In this appendix, we explain how the effective Lagrangian Eq. (2.41) in the main text,

$$\mathcal{L}_{\text{eff}}[A] = \frac{\mathrm{sign}(M_\psi) - 1}{2} \frac{1}{4\pi} \mathrm{Tr}\Big[ada - \frac{2}{3} i a^3\Big] - \frac{1}{2\pi} \mathrm{Tr}[a] db - \frac{N+1}{4\pi} bdb - \frac{1}{2\pi} bdA, \tag{2.55}$$

describes an integer quantum Hall state when the fermion mass $M_\psi < 0$ and a topologically trivial insulator when $M_\psi > 0$. In the effective Lagrangians written above and below, only relevant and marginal terms, in the renormalization group sense, are written; irrelevant operators (like Yang-Mills and Maxwell terms for the gauge fields) are understood to supplement $\mathcal{L}_{\text{eff}}$ with a coefficient that scales inversely with the cutoff of the effective theory.

Our strategy is to identify the integer quantum Hall state and the insulator through their electrical response to the $U(1)$, i.e., electromagnetic, gauge field A. This response is encoded in an effective response Lagrangian, obtained by integrating out all dynamical degrees of freedom (e.g., ψ, a, and b in Eq. (2.40)). Consequently, this effective Lagrangian only contains A. Using the relation $J_\mu = \frac{\delta \mathcal{L}_{\text{eff}}[A]}{\delta A^\mu}$, where J_μ is the electromagnetic current coupling to A, we can read off the electrical response to an applied electromagnetic field A. Focusing on the linear response of the system, we may terminate this effective Lagrangian at quadratic order in A. As a simple example, consider the effective Lagrangian $\mathcal{L}_{CS} = \frac{1}{4\pi} AdA$ describing the integer quantum Hall state. The relation, $J_i = \frac{1}{2\pi}\epsilon_{ij}E_j$, allows us to read off the Hall conductivity, $\sigma_{xy} = 1$, of this state, given in units where $e^2 = \hbar = 1$.

When $M_\psi < 0$, the effective Lagrangian takes the form:

$$\mathcal{L}_{\text{eff}}(M_\psi < 0) = -\frac{1}{4\pi}\text{Tr}\Big[ada - \frac{2}{3}ia^3\Big] - \frac{1}{2\pi}\text{Tr}[a]db - \frac{N+1}{4\pi}bdb - \frac{1}{2\pi}bdA. \quad (2.56)$$

We will show how Eq. (2.56) describes an integer quantum Hall state by applying modular transformations to the rank/level duality $U(N)_1 \leftrightarrow SU(1)_N$ [202, 203, 109]:

$$-\frac{1}{4\pi}\text{Tr}\Big[ada - \frac{2}{3}ia^3\Big] - \frac{1}{2\pi}\text{Tr}[a]dA \leftrightarrow \frac{N}{4\pi}AdA. \quad (2.57)$$

Note that since $SU(1)$ is trivial, there are no dynamical gauge fields on the right-hand side. Eq. (2.57) says that $U(N)$ Chern-Simons theory at level $k = -1$ is equivalent to the theory of N copies of the $\nu = 1$ integer quantum Hall state, i.e., a state with Hall conductivity equal to Ne^2/h. For instance, if the topological field theory on the left-hand side of the duality in (2.57) (or its dual on the right-hand side) is placed on a surface with boundary, there will be N chiral Dirac fermions propagating along the edge. We now sequentially act on both sides of the duality in (2.57) with $\mathcal{S}\mathcal{T}^{-N-1}$, modular transformations defined in Eq. (2.45) in the main text. First acting by $\mathcal{T}^{-N-1}$, we obtain:

$$-\frac{1}{4\pi}\mathrm{Tr}\Big[ada - \frac{2}{3}ia^3\Big] - \frac{1}{2\pi}\mathrm{Tr}[a]dA - \frac{N+1}{4\pi}AdA \leftrightarrow -\frac{1}{4\pi}AdA. \tag{2.58}$$

Then acting by $\mathcal{S}$, we find:

$$-\frac{1}{4\pi}\mathrm{Tr}\Big[ada - \frac{2}{3}ia^3\Big] - \frac{1}{2\pi}\mathrm{Tr}[a]db - \frac{N+1}{4\pi}bdb - \frac{1}{2\pi}bdA \leftrightarrow -\frac{1}{4\pi}cdc - \frac{1}{2\pi}cdA. \tag{2.59}$$

The theory on the left-hand side of the duality in (2.59) is the effective Lagrangian $\mathcal{L}_{\text{eff}}(M_\psi < 0)$ given in Eq. (2.56). The theory on the right-hand side of (2.59) is simply the effective hydrodynamic description of the integer quantum Hall effect [292]. To see this, i.e., to see that the theory exhibits a Hall conductivity equal to one in units of e^2/h, we may integrate out c using its equation of motion to find:

$$-\frac{1}{4\pi}\mathrm{Tr}\Big[ada - \frac{2}{3}ia^3\Big] - \frac{1}{2\pi}\mathrm{Tr}[a]db - \frac{N+1}{4\pi}bdb - \frac{1}{2\pi}bdA \leftrightarrow \frac{1}{4\pi}AdA. \tag{2.60}$$

When $M_\psi > 0$, the effective Lagrangian,

$$\mathcal{L}_{\text{eff}}(M_\psi > 0) = -\frac{1}{2\pi}\mathrm{Tr}[a]db - \frac{N+1}{4\pi}bdb - \frac{1}{2\pi}bdA. \tag{2.61}$$

The $SU(N) \subset U(N)$ component of a is no longer present in the effective Lagrangian. Consequently, at low energies, it decouples from the remaining degrees of freedom: we assume that it confines. The $U(1) \subset U(N)$ component of a, i.e., $\mathrm{Tr}[a]$, and b remain in $\mathcal{L}_{\text{eff}}(M_\psi > 0)$. The equation of motion for $\mathrm{Tr}[a]$ sets $b = 0$, up to gauge transformations. Thus,

$$\mathcal{L}_{\text{eff}}(M_\psi > 0) = 0. \tag{2.62}$$

This Lagrangian describes a topologically trivial insulator as the Maxwell term for A is understood to supplement $\mathcal{L}_{\text{eff}}(M_\psi > 0)$.

A related way to see that $\mathcal{L}_{\text{eff}}(M_\psi > 0)$ describes an insulator is to perform a $PSL(2,\mathbb{Z})$ field redefinition of the dynamical $U(1)$ gauge fields $\text{Tr}[a] \mapsto \tilde{a}$ and $b \mapsto \tilde{b}$ so that $\mathcal{L}_{\text{eff}}(M_\psi > 0) = \frac{1}{4\pi}\tilde{a}d\tilde{a} - \frac{1}{4\pi}\tilde{b}d\tilde{b} - \frac{1}{2\pi}(\tilde{a} - \tilde{b})dA$ for odd N or $\mathcal{L}_{\text{eff}}(M_\psi > 0) = \frac{1}{2\pi}\tilde{a}d\tilde{b} - \frac{1}{2\pi}\tilde{a}dA$ for even N. These effective Lagrangians describe topologically trivial insulators (if no symmetry is preserved) of fermions or bosons. There is no contradiction with the duality in (2.51) (or, alternatively, restriction to odd N), which says that Eq. (2.40) is dual to a free fermion, if we allow ourselves to "stabilize" by a trivial insulator of fermions [29].

2.2.9 Appendix: Effective Lagrangians for fractional quantum Hall transitions

In this appendix, we list the effective Lagrangians of the form given in Eq. (2.46),

$$\mathcal{L}_m = \mathcal{L}_{\text{IQHT}}(c) + \mathcal{L}_{\text{mod}}(A), \tag{2.63}$$

where $\mathcal{L}_{\text{IQHT}}(c)$ is given by Eq. (2.40) with the replacement $A \to c$ and $\mathcal{L}_{\text{mod}}(A)$ is determined by the particular modular transformation for a few other fractional quantum Hall transitions. Because $\mathcal{L}_{\text{IQHT}}(c)$ is the same in each effective Lagrangian, we only specify $\mathcal{L}_{\text{mod}}(A)$. We also determine the effective Chern-Simons level for $a_{U(1)}$ which scales as $|k_{U(1)}| \propto N$ for $N \to \infty$.

$\sigma = 1/3 \to 2/5$ **transition**

The $\sigma = 1/3 \to 2/5$ transition is obtained by acting on Eq. (2.40) by $\mathcal{S}^{-1}\mathcal{T}^{-2}\mathcal{S}\mathcal{T}$. We find:

$$\mathcal{L}_{\text{mod}}(A) = \frac{1}{4\pi}cdc - \frac{1}{2\pi}cdg - \frac{2}{4\pi}gdg + \frac{1}{2\pi}gdA. \tag{2.64}$$

The corresponding effective Chern-Simons level for $a_{U(1)}$ in (2.48) for this transition is $k_{U(1)} = -\frac{N}{2} + \frac{N^2}{N+5/3}$.

$\sigma = m/(m+1) \to 1$ **transition**

The $\sigma = m/(m+1) \to 1$ transition is obtained by acting on Eq. (2.40) by $\mathcal{S}^{-1}\mathcal{T}^{m}\mathcal{S}\mathcal{T}^{-1}$. We find:

$$\mathcal{L}_{\text{mod}}(A) = -\frac{1}{4\pi}cdc - \frac{1}{2\pi}cdg + \frac{m}{4\pi}gdg + \frac{1}{2\pi}gdA + \frac{1}{4\pi}AdA. \tag{2.65}$$

The corresponding effective Chern-Simons level for $a_{U(1)}$ in (2.48) for this transition is $k_{U(1)} = -\frac{N}{2} + \frac{N^2}{N+1/(m+1)}$.

2.2.10 Appendix: Fractional quantum Hall state and the insulator

In this appendix, we show how the effective Lagrangian in Eq. (2.46) in the main text,

$$\mathcal{L}_m = \mathcal{L}_{\text{IQHT}}(c) + \mathcal{L}_{\text{mod}}(A), \tag{2.66}$$

where

$$\mathcal{L}_{\mathrm{IQHT}}(c) = i\bar{\psi}\, \not{D}_a \psi - \frac{1}{2}\frac{1}{4\pi}\mathrm{Tr}\Big[ada - \frac{2}{3}ia^3\Big] - \frac{1}{2\pi}\mathrm{Tr}[a]db - \frac{N+1}{4\pi}bdb - \frac{1}{2\pi}bdc \tag{2.67}$$

and

$$\mathcal{L}_{\mathrm{mod}}(A) = -\frac{1}{2\pi}cdg - \frac{m}{4\pi}gdg + \frac{1}{2\pi}gdA, \tag{2.68}$$

describes a $1/(m+1) \to 0$ transition when $m \geq 0$. Similar to Appendix 2.2.8, when a fermion mass term $M_\psi \bar{\psi}\psi$ is added, we may integrate it out below the scale set by $|M_\psi|$ to find:

$$\begin{aligned}\mathcal{L}_{\mathrm{eff}} =& \frac{\mathrm{sign}(M_\psi) - 1}{2}\frac{1}{4\pi}\mathrm{Tr}\Big[ada - \frac{2}{3}ia^3\Big] - \frac{1}{2\pi}\mathrm{Tr}[a]db - \frac{N+1}{4\pi}bdb \\ & - \frac{1}{2\pi}bdc - \frac{1}{2\pi}cdg - \frac{m}{4\pi}gdg + \frac{1}{2\pi}gdA.\end{aligned} \tag{2.69}$$

We will show that Eq. (2.69) describes a fractional quantum Hall effect with Hall conductivity equal to $1/(m+1)$ (in units of e^2/h) when $M_\psi < 0$ and an insulator when $M_\psi > 0$.

When $M_\psi < 0$,

$$\begin{aligned}\mathcal{L}_{\mathrm{eff}}(M_\psi < 0) =& -\frac{1}{4\pi}\mathrm{Tr}\Big[ada - \frac{2}{3}ia^3\Big] - \frac{1}{2\pi}\mathrm{Tr}[a]db - \frac{N+1}{4\pi}bdb \\ & - \frac{1}{2\pi}bdc - \frac{1}{2\pi}cdg - \frac{m}{4\pi}gdg + \frac{1}{2\pi}gdA.\end{aligned} \tag{2.70}$$

Applying $\mathcal{S}^{-1}\mathcal{T}^{-m}\mathcal{S}^2\mathcal{T}^{-N-1}$ to the rank/level dual pair [202, 203, 109] in (2.57), we find:

$$\begin{gathered}-\frac{1}{4\pi}\mathrm{Tr}\Big[ada - \frac{2}{3}ia^3\Big] - \frac{1}{2\pi}\mathrm{Tr}[a]db - \frac{N+1}{4\pi}bdb - \frac{1}{2\pi}bdc - \frac{1}{2\pi}cdg - \frac{m}{4\pi}gdg + \frac{1}{2\pi}gdA \\ \updownarrow \\ -\frac{1}{4\pi}bdb - \frac{1}{2\pi}bdc - \frac{1}{2\pi}cdg - \frac{m}{4\pi}gdg + \frac{1}{2\pi}gdA.\end{gathered} \tag{2.71}$$

Thus, $\mathcal{L}_\psi(M_\psi < 0)$ (the theory in the top line of (2.71)) is dual to the theory in the bottom line of (2.71). We now sequentially integrate out b and c so that the bottom line of (2.71) simplifies to

$$-\frac{m+1}{4\pi}gdg + \frac{1}{2\pi}gdA. \tag{2.72}$$

This is the hydrodynamic effective Lagrangian for the fractional quantum Hall state with Hall conductivity equal to $1/(m+1)$ [292]. Thus, we find:

$$\begin{gathered}
-\frac{1}{4\pi}\mathrm{Tr}\left[ada - \frac{2}{3}ia^3\right] - \frac{1}{2\pi}\mathrm{Tr}[a]db - \frac{N+1}{4\pi}bdb - \frac{1}{2\pi}bdc - \frac{1}{2\pi}cdg - \frac{m}{4\pi}gdg + \frac{1}{2\pi}gdA \\
\updownarrow \\
-\frac{m+1}{4\pi}gdg + \frac{1}{2\pi}gdA.
\end{gathered} \tag{2.73}$$

When $M_\psi > 0$,

$$\mathcal{L}_{\text{eff}}(M_\psi > 0) = -\frac{1}{2\pi}\mathrm{Tr}[a]db - \frac{N+1}{4\pi}bdb - \frac{1}{2\pi}bdc - \frac{1}{2\pi}cdg - \frac{m}{4\pi}gdg + \frac{1}{2\pi}gdA. \tag{2.74}$$

The $SU(N) \subset U(N)$ component of a again decouples and we assume it confines. The equation of motion for $\mathrm{Tr}[a]$ sets $b = 0$; the equation of motion for c sets $g = 0$ and we are left with the effective Lagrangian for an insulator:

$$\mathcal{L}_{\text{eff}}(M_\psi > 0) = 0. \tag{2.75}$$

2.2.11 Appendix: Duality argument and Abelian Chern-Simons duals

Duality argument

In the first part of this appendix, we argue that Eq. (2.40) is in the same universality class as a free fermion. Our demonstration applies the argument of [137, 243] to the bosonization duality [85, 3, 2, 4, 109],

$$\begin{gathered}
|D_A\phi|^2 - |\phi|^4 + \frac{1}{4\pi}AdA \\
\updownarrow \\
i\bar{\psi}D_a\psi - \frac{1}{8\pi}\mathrm{Tr}[ada - \frac{2}{3}ia^3] - \frac{1}{2\pi}\mathrm{Tr}[a]dA - \frac{N-1}{4\pi}AdA,
\end{gathered} \tag{2.76}$$

that relates the theory of a Wilson-Fisher boson ϕ to the theory of a $U(N)$ Chern-Simons gauge field a coupled to a Dirac fermion ψ. Applying the modular transformation $\mathcal{ST}^{-2}$ to "both sides" of this duality (we introduce c in the Wilson-Fisher theory and b in the gauged Dirac theory in applying the $\mathcal{S}$ transformation), we find the low-energy equivalence:

$$|D_c\phi|^2 - |\phi|^4 - \frac{1}{4\pi}cdc - \frac{1}{2\pi}cdA \leftrightarrow \mathcal{L}_{\mathrm{IQHT}}(A), \tag{2.77}$$

with $\mathcal{L}_{\mathrm{IQHT}}(A)$ given in Eq. (2.40). But the gauged Wilson-Fisher theory on the left-hand side of (2.77) is also dual to the theory of a free Dirac fermion [132, 133, 39, 196]. Thus, we relate the low-energy physics of the theory of a free Dirac fermion to that of our theory in Eq. (2.40),

$$i\bar{\Psi}\not{D}_A\Psi + \frac{1}{2}\frac{1}{4\pi}AdA \leftrightarrow \mathcal{L}_{\mathrm{IQHT}}(A). \tag{2.78}$$

2.2.12 Appendix: Abelian Chern-Simons duals

In the second part of this appendix, we provide the Abelian Chern-Simons duals for the $U(N)$ Chern-Simons theories studied in the main text and listed in Appendix 2.2.9 that are implied by the duality in (2.51) (copied below):

$$i\bar{\Psi}\not{D}_A\Psi + \frac{1}{2}\frac{1}{4\pi}AdA \leftrightarrow \mathcal{L}_{\mathrm{IQHT}}(A). \tag{2.79}$$

The strategy is identical to that of [243]: we perform a modular transformation on each side of the duality (2.79) and then identify the resulting theories. Duality implies that 't Hooft large N limit calculations for the theories with non-Abelian gauge group can be reinterpreted in terms of their Abelian duals.

Dual pair for the $\sigma = 1/(m+1) \to 0$ transition

Acting on (2.79) with $\mathcal{S}^{-1}\mathcal{T}^{-m}\mathcal{S}$, we find the duality:

$$\begin{gathered}
i\bar{\Psi}\not{D}_{\tilde{a}}\Psi + \frac{1}{2}\frac{1}{4\pi}\tilde{a}d\tilde{a} - \frac{1}{2\pi}\tilde{a}d\tilde{b} - \frac{m}{4\pi}\tilde{b}d\tilde{b} + \frac{1}{2\pi}\tilde{b}dA \\
\updownarrow \\
i\bar{\psi}\not{D}_a\psi - \frac{1}{2}\frac{1}{4\pi}\mathrm{Tr}\Big[ada - \frac{2}{3}ia^3\Big] - \frac{1}{2\pi}\mathrm{Tr}[a]db - \frac{N+1}{4\pi}bdb - \frac{1}{2\pi}bdc \\
-\frac{1}{2\pi}cdg - \frac{m}{4\pi}gdg + \frac{1}{2\pi}gdA
\end{gathered} \tag{2.80}$$

where $\tilde{a}$, $\tilde{b}$, b, c, and g are Abelian gauge fields and a is a $U(N)$ gauge field.

Dual pair for the $\sigma = 1/3 \to 2/5$ transition

Acting on (2.79) with $\mathcal{S}^{-1}\mathcal{T}^{-2}\mathcal{S}\mathcal{T}$, we find the duality:

$$\begin{gathered}
i\bar{\Psi}\not{D}_{\tilde{a}}\Psi + \frac{3}{2}\frac{1}{4\pi}\tilde{a}d\tilde{a} - \frac{1}{2\pi}\tilde{a}d\tilde{b} - \frac{2}{4\pi}\tilde{b}d\tilde{b} + \frac{1}{2\pi}\tilde{b}dA \\
\updownarrow \\
i\bar{\psi}\not{D}_a\psi - \frac{1}{2}\frac{1}{4\pi}\mathrm{Tr}\Big[ada - \frac{2}{3}ia^3\Big] - \frac{1}{2\pi}\mathrm{Tr}[a]db - \frac{N+1}{4\pi}bdb - \frac{1}{2\pi}bdc \\
+\frac{1}{4\pi}cdc - \frac{1}{2\pi}cdg - \frac{2}{4\pi}gdg + \frac{1}{2\pi}gdA
\end{gathered} \tag{2.81}$$

where $\tilde{a}$, $\tilde{b}$, b, c, and g are Abelian gauge fields and a is a $U(N)$ gauge field.

Dual pair for the $\sigma = m/(m+1) \to 1$ transition

Acting on (2.79) with $\mathcal{T}\mathcal{S}^{-1}\mathcal{T}^{m}\mathcal{S}\mathcal{T}^{-1}$, we find the duality:

$$\begin{gathered}
i\bar{\Psi}\not{D}_{\tilde{a}}\Psi - \frac{1}{2}\frac{1}{4\pi}\tilde{a}d\tilde{a} - \frac{1}{2\pi}\tilde{a}d\tilde{b} + \frac{m}{4\pi}\tilde{b}d\tilde{b} + \frac{1}{2\pi}\tilde{b}dA + \frac{1}{4\pi}AdA \\
\updownarrow \\
i\bar{\psi}\not{D}_a\psi - \frac{1}{2}\frac{1}{4\pi}\mathrm{Tr}\Big[ada - \frac{2}{3}ia^3\Big] - \frac{1}{2\pi}\mathrm{Tr}[a]db - \frac{N+1}{4\pi}bdb - \frac{1}{2\pi}bdc \\
-\frac{1}{4\pi}cdc - \frac{1}{2\pi}cdg + \frac{m}{4\pi}gdg + \frac{1}{2\pi}gdA + \frac{1}{4\pi}AdA
\end{gathered} \tag{2.82}$$

where $\tilde{a}$, $\tilde{b}$, b, c, and g are Abelian gauge fields and a is a $U(N)$ gauge field.

2.2.13 Appendix: Particle-hole transformation within the lowest Landau level

For the free Dirac theory in the duality in (2.51), the particle-hole transformation with respect to a filled Landau level can be defined as follows. First, the fields are transformed by the anti-unitary ($i \mapsto -i$) transformation that consists of the product of time-reversal and charge-conjugation which takes $t \mapsto -t$,

$$\begin{aligned} \Psi &\mapsto -\gamma^t \Psi^*, \\ (A_t, A_x, A_y) &\mapsto (-A_t, A_x, A_y), \end{aligned} \tag{2.83}$$

and then the Lagrangian is shifted by a filled Landau level using the $\mathcal{T}$ transformation.

The theory of a free Dirac fermion in (2.51) is invariant under a particle-hole transformation with respect to a filled Landau level. Duality implies that the theory in Eq. (2.40) likewise enjoys this symmetry; we believe particle-hole symmetry is realized quantum mechanically and is not visible in the classical Lagrangian of Eq. (2.40) for $N > 1$ (see [5] for a recent discussion of this phenomena in related dualities). It would be interesting to see how this symmetry constrains the conductivity (along with other observables) of different quantum critical states [239, 93].

There is second anti-unitary transformation that we expect to leave physical observables invariant even though it is not a symmetry of Eq. (2.40). It is defined as follows: first, time-reversal acts on the dynamical fields as

$$\begin{aligned} \psi &\mapsto \gamma^y \psi, \\ (a_t, a_x, a_y) &\mapsto (a_t, -a_x, -a_y), \\ (b_t, b_x, b_y) &\mapsto (b_t, -b_x, -b_y); \end{aligned} \tag{2.84}$$

second, the product of time-reversal and charge-conjugation acts on A as

$$(A_t, A_x, A_y) \mapsto (-A_t, A_x, A_y); \tag{2.85}$$

Finally, the Lagrangian in Eq. (2.40) is shifted by a filled Landau level with the $\mathcal{T}$ transformation. This transformation can be employed to generate alternative effective descriptions for the particle-hole conjugate of a given quantum Hall phase transition.

CHAPTER 3

ELECTRON HYDRODYNAMICS

The theory of classical hydrodynamics (e.g. of water) is one of the first historically successful descriptions of a strongly interacting system. Forgoing an exact microscopic description of macroscopic number of degrees of freedom, liquids were instead characterized by a few field quantities subject to conservation laws (e.g. momentum conservation) and constitutive equations (e.g. stress tensor - velocity relation). In condensed matter, the (generalized) hydrodynamic approach is therefore understood to be an effective theory of "conserving approximations," i.e. where conservation laws are at least approximately obeyed. As a non-perturbative technique, hydrodynamics and its applicability in strongly-correlated electronic systems has been of great interest (see [74, 101] for a review).

As our ability to create clean samples improve, experiments are now reporting that hydrodynamic descriptions of electronic fluids may be physically realizable [52, 17, 146, 147, 266, 195, 89, 97, 159, 96]. In particular, the momentum-conserving electron-electron scattering length l_{ee} is thought to be sufficiently short such that momentum is at least approximately conserved. However, a key difficulty in directly observing the hydrodynamic regime is that the electron-electron scattering length l_{ee} is hard to measure. Therefore, to properly identify the hydrodynamic regime, it is important to disentangle contributions of l_{ee} from other length scales in any purportedly hydrodynamic observable (e.g. transport). In what follows, we critically examine these issues and search for sharp signatures of electron hydrodynamics.

3.1 Quantum aspects of hydrodynamic transport from weak electron-impurity scattering

This section is adapted from a PRB paper [116] with Vadim Oganesyan and Eun-Ah Kim.

Recent experimental observations of apparently hydrodynamic electronic transport have generated much excitement. However, the understanding of the observed non-local transport (whirlpool) effects and parabolic (Poiseuille-like) current profiles has largely been motivated by a phenomenological analogy to classical fluids. This is due to difficulty in incorporating strong correlations in quantum mechanical calculation of transport, which has been the primary angle for interpreting the apparently hydrodynamic transport. Here we demonstrate that even free fermion systems, in the presence of (inevitable) disorder, exhibit non-local conductivity effects such as those observed in experiment because of the fermionic system's long-range entangled nature. On the basis of explicit calculations of the conductivity at finite wavevector, $\sigma(\mathbf{q})$, for selected weakly disordered free fermion systems, we propose experimental strategies for demonstrating distinctive quantum effects in non-local transport at odds with the expectations of classical kinetic theory. Our results imply that the observation of whirlpools or other "hydrodynamic" effects does not guarantee the dominance of electron-electron scattering over electron-impurity scattering.

3.1.1 Introduction

Recent experimental reports of peculiar transport phenomena in ultraclean graphene[52, 17, 146, 147, 266] and other materials[195, 89, 97] have generated much excitement regarding the role of hydrodynamic transport in these experiments. In the absence of microscopic understanding of the hydrodynamic transport of electrons, these experiments have been interpreted largely through analogy with classical fluids. Although parabolic velocity profiles[147, 266] and whirlpools[17] are familiar hydrodynamic phenomena in classical fluids, reliance on this analogy deprives us of an angle to learn the role of quantum mechanics in experiment. Most importantly, the question of the role of impurities, always present in materials, remains open although it has been clear that they complicate any analysis[10, 161].

Modern interest in the hydrodynamic theory of electronic transport was motivated by a sore need for a theoretical framework to describe quantum critical transport in a regime dominated by electron-electron scattering.[54, 256, 241] Exotic possibilities have been predicted for graphene near the charge neutrality point,[100, 77, 75, 199, 277, 161] and electron viscosity has been linked to the strange metal normal state of cuprate superconductors[58, 182, 181, 317]. However, a microscopic understanding of such hydrodynamic transport is challenging due to the inherent theoretical difficulty associated with the strongly correlated regime. Pioneering works used kinetic theory to calculate the shear viscosity for graphene[199, 23, 220] and for 2D Fermi liquids[153], yielding non-trivial predictions. However, as the role of (unavoidable) impurity scattering has primarily been treated phenomenologically via relaxation time approximations[49, 277, 161, 180, 266], it has not been examined in microscopic detail.

In this paper, we evaluate the effects of impurity scattering, and identify signatures of the quantum nature of electrons, in the phenomena of whirlpool formation and parabolic current profiles. To do so, we explicitly calculate the non-local conductivity $\sigma(\mathbf{q})$ for free electrons scattering off weak impurities. In contrast to a classical Maxwell-Boltzmann distributed gas, in which the shear viscosity is independent of density[191], our principal result is that viscous effects have a distinctive dependence on carrier concentration. This arises because Fermi statistics introduces a density-dependent velocity scale $v_F \sim \sqrt{n_e}$ (in 2D) and restricts scattering to the vicinity of the Fermi surface, so that scattering is determined by the density of states. We map out experimental strategies to reveal the quantum nature near the bottom of band and in the vicinity of van Hove singularity.

3.1.2 Phenomenology and classical hydrodynamics

The phenomenological description of zero-frequency viscous transport[277, 161] extends Drude theory by including the kinematic shear viscosity (i.e. coefficient of momentum diffusion) as

$$\mathbf{E} = A\left(\gamma - \nu\nabla^2\right)\mathbf{J} \tag{3.1}$$

where A is a dimensionful prefactor ($m/(n_e e^2)$ for Drude theory), γ is the current scattering rate, and ν is the kinematic shear viscosity. This equation has a characteristic length scale $r_d \equiv \sqrt{\nu/\gamma}$, which we dub the viscosity length scale. Note that in the limit of $\gamma \to 0$, Eq. 3.1 becomes a linearized Navier-Stokes equation (assuming $\mathbf{J} \propto \mathbf{p}$), with ν the usual fluid viscosity. [1] Eq. (3.1) amounts to a Taylor expansion in momentum of the usual Drude response (at zero frequency). Hence this equation applies to any system with current; it is agnostic to whether the system is classical or quantum.

The existence of the length scale $r_d \equiv \sqrt{\nu/\gamma}$, associated with the kinematic shear viscosity ν, immediately leads to the familiar hydrodynamic phenomena of parabolic current profiles and whirlpool formation. To see this, one can solve Eq. (3.1) for the local current density $\mathbf{J}(\mathbf{r})$. For no-slip boundary conditions, the longitudinal flow down a rectangular channel of width W is given by the formula[277]

$$\frac{J_x(y)W}{I} = \left(1 - \frac{\cosh \frac{y}{r_d}}{\cosh \frac{W}{2r_d}}\right) \frac{1}{1 - \frac{2r_d}{W} \tanh\left(\frac{W}{2r_d}\right)} \tag{3.2}$$

As shown in Fig. 3.1a, the flow profile is rectangular for $r_d \ll W$ and parabolic for $r_d \gg W$. If one instead injects current laterally across the channel, as shown in Fig. 3.1b, whirlpools of radius $\sim r_d$ will form.[277, 161]

For a 2D classical (Maxwell-Boltzmann) ideal gas of particles scattering off of dilute impurities, the velocity is set by temperature T via the equipartition theorem as $v = \sqrt{2k_BT/m_e}$. Since the mean free path is set by the cross section σ_{imp} and the number density n_{imp} of impurities as $l_{\text{mfp}} \sim 1/(n_{\text{imp}}\sigma_{\text{imp}})$,[2] the scattering rate is $\gamma = v/l_{\text{mfp}}$, independent of gas density. Moreover, it is known[172] that the kinematic shear viscosity for weakly interacting classical gas is given

---

[1] Although the definition of shear viscosity in the absence of momentum conservation is controversial, we take Eq. (3.1) as a phenomenological definition of viscosity following Refs.[277, 161]

[2] This is slightly different from Maxwell's original model [191] of rigid spheres, where $l_{\text{mfp}} \sim 1/(n_{\text{gas}}\sigma_{\text{gas}})$ since the collisions are with other gas particles.

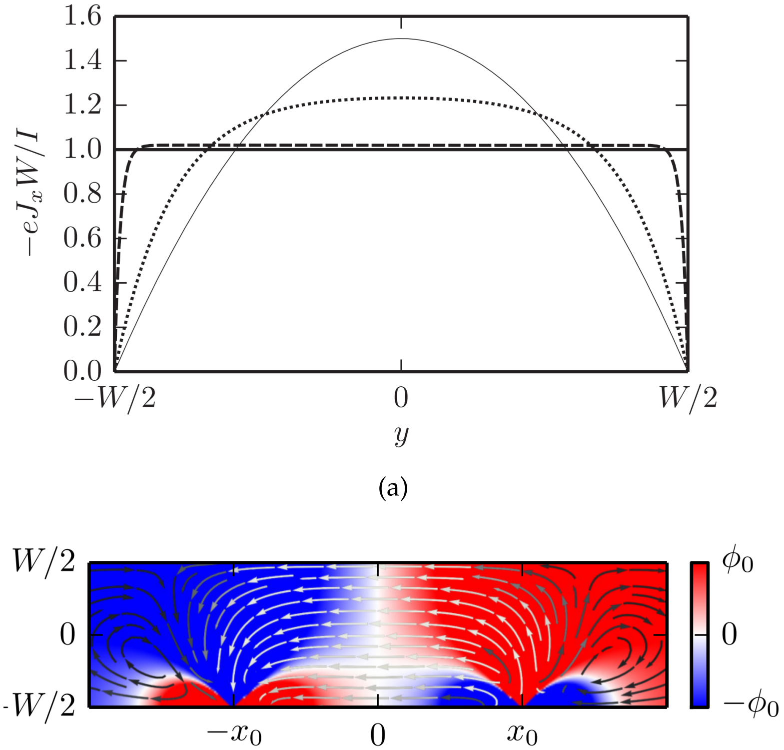

(a)

(b)

Figure 3.1: Results from solving Eq. (3.1) with no-slip boundary conditions, taken from Torre et al.[277] (a) A plot of the flow profile through a rectangular channel given by Eq. (3.2) for various values of r_d/W. For steady flow through a rectangular channel, the normalized current flow is rectangular for $r_d \ll W$ and parabolic for $r_d \gg W$. (b) A heatmap of the potential ϕ and current streamlines for a current source and sink at x_0 and $-x_0$, respectively. White/black streamlines correspond to high/low current density. One finds that vortices form on the scale of r_d.

by

$$\nu \sim v l_{\mathrm{mfp}}. \tag{3.3}$$

Hence in this classical system with impurities, the shear "viscosity" ν (phenomenologically defined in Eq. (3.1)) and the vortex radius $r_d \sim l_{\mathrm{mfp}}$ will be independent of the gas density as sketched in Fig. 3.2a.

Model and Formalism – The finite $\mathbf{q}$ conductivity $\sigma(\mathbf{q})$ is related to the viscosity

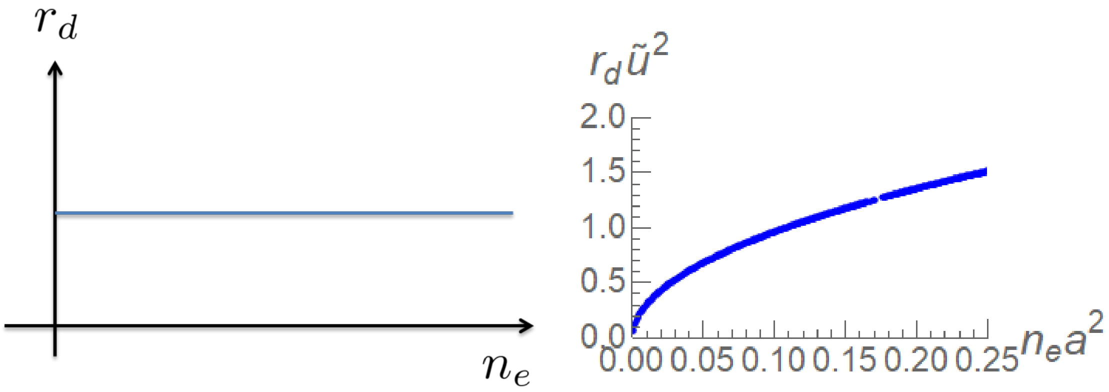

(a) (b)

Figure 3.2: (a) A plot of r_d against (electron) gas density for the classical gas with impurities. The vortex radius is density-independent in this case. (b) The equivalent plot for a degenerate electron gas with a parabolic dispersion, at $u = 0.1\frac{\hbar^2}{ma}$. We measure r_d and n_e in units of the lattice constant a and a^{-2}, respectively, and introduced a dimensionless measure of disorder strength $\tilde{u} = \frac{uma}{\hbar^2}$ so that the quantity $r_d\tilde{u}^2$ is independent of disorder strength.

ν by inverting Eq. (3.1), which in the limit of small momenta gives

$$\mathbf{J} =(\sigma_0 - \sigma_2\nabla^2)\mathbf{E} \tag{3.4}$$

where σ_0 and σ_2 are the $\mathcal{O}(q^0)$ and $\mathcal{O}(q^2)$ pieces of $\sigma(q)$, respectively; the term linear in q vanishes by inversion symmetry. These new parameters are related to the collision rate and viscosity of Eq. (3.1) as $\sigma_0 = 1/(A\gamma)$ and $\sigma_2 = -\nu/(A\gamma^2)$. In terms of σ_0 and σ_2, the viscosity length scale r_d is

$$r_d \sim \sqrt{-\frac{\sigma_2}{\sigma_0}} \tag{3.5}$$

Of course, the conductivity σ^{ij} is in actuality a rank-2 tensor, and hence $(\sigma_2)^{ij}_{\alpha\beta}$ is a rank-4 tensor. We have suppressed the tensor indices because the relevant components are parametrically equivalent,[3] and will be using at $-(\sigma_2)^{xx}_{xx}/\sigma^{xx}_0$ as our estimate for r_d^2. Often, transport calculations are done in the $q \to 0$ limit.

---

[3] There are subtleties regarding the formal equivalence between σ_2 and the shear viscosity ν which we are ignoring[22] in favor of the phenomenological definition of viscosity given by Eq. (3.1). Ultimately, we are interested in the experimental observable r_d, so the subtleties in the definition of viscosity do not pertain to us.

However, obtaining non-local transport phenomena requires calculating at finite $\mathbf{q}$, in particular $\sigma_2 \propto \nu$. The presence of finite $\mathbf{q}$ significantly complicates the calculations,[175] as it breaks spatial symmetries and introduces angular dependencies in the integrand.

For our microscopic fermion model with weak impurity scattering, we consider $H = H_{\text{kin}} + H_{\text{imp}}$ with the kinetic term H_{kin} and the impurity potential H_{imp} given by

$$H_{\text{kin}} =\frac{1}{\beta}\sum_{ik_n} \xi_{\mathbf{k}} c^{\dagger}_{\mathbf{k},ik_n} c_{\mathbf{k},ik_n}, \tag{3.6}$$

$$H_{\text{imp}} =\frac{1}{\beta}\sum_{ik_n} \frac{1}{\beta}\sum_{iq_n} \int \frac{d^2q}{(2\pi)^2} V(\mathbf{k}) c^{\dagger}_{\mathbf{k}^+,ik_n^+} c_{\mathbf{k}^-,ik_n^-}. \tag{3.7}$$

Here $\xi_{\mathbf{k}} = \epsilon_{\mathbf{k}} - \mu$ is the dispersion measured relative to the chemical potential, $(\mathbf{k}^{\pm}, ik_n^{\pm}) = (\mathbf{k} \pm \mathbf{q}/2, ik_n \pm iq_n/2)$ and $V(\mathbf{k})$ is the impurity potential in momentum space. We work in the $T \to 0$ limit. For simplicity, we consider a Gaussian-distributed impurity potential where $\langle V(\mathbf{x})\rangle = 0$ and $\langle V(\mathbf{x})V(\mathbf{y})\rangle = u^2\delta(\mathbf{x}-\mathbf{y})$. Thus, the disorder line transfers all momenta with equal weight u^2 but transfers no frequency. For the most part we will be content with only the perturbative treatment of disorder, which is expected to break down near band edges (dilute electrons or holes) and at the van Hove singularity.

To calculate the conductivity, we use the Kubo formula

$$\sigma^{ij}(\mathbf{q}, \omega + i0^+) = \frac{i}{\omega + i0^+}\left[\Pi^{ij}(\mathbf{q}, \omega + i0^+) + \frac{n_e e^2}{m}\delta^{ij}\right] \tag{3.8}$$

where n_e is the average carrier density and m is the particle mass[4]. This requires us to calculate the current-current correlator Π^{ij}. As we are interested in DC non-local response, we will be working in the limit $\omega \to 0$ and $v_F q \ll \gamma$, where

---

[4] The mass generically has tensor structure which we have suppressed here for ease of presentation, as the diamagnetic piece will not play any significant role throughout this paper

$\gamma = -2\,\mathrm{Im}\,\Sigma(\mathbf{q},\omega)$ is the scattering rate.[5] We can separate contributions to Π^{ij} into self-energy and vertex corrections; vertex corrections are negligible in this limit, as shown in the Appendix. For the self-energy Σ, we will use first Born approximation[6]

$$\Sigma(\mathbf{q}, iq_n) = u^2 \int \frac{d^2k}{(2\pi)^2} G_0(\mathbf{k}, iq_n) \tag{3.9}$$

where $G_0(\mathbf{q}, iq_n) = (iq_n - \xi_{\mathbf{q}})^{-1}$ is the free Green's function. In addition, we will be ignoring the logarithmically UV divergent $\mathrm{Re}\,\Sigma$ by approximating it as a constant, in which case it amounts to a shift of μ. We also ignore the crossing diagrams and self-consistency diagrams of the self-energy.

Since we are only interested in dissipative response, using spectral function techniques we can rewrite the Kubo formula as

$$\begin{aligned} &\mathrm{Re}\sigma^{ij}(\mathbf{q},\omega) \\ &\quad = \int_{-\omega}^{0} \frac{dx}{4\pi} \frac{d^2k}{(2\pi)^2} \frac{A\left(\mathbf{k}^{-}, x\right) A\left(\mathbf{k}^{+}, x+\omega\right)}{-\omega} v^i(\mathbf{k}) v^j(\mathbf{k}) \end{aligned} \tag{3.10}$$

where $A(\mathbf{k},\omega)$ is the spectral function and $v_i(\mathbf{k}) = \frac{\partial \epsilon_{\mathbf{k}}}{\partial k^i}$ is the current vertex factor (or velocity).[7] In 3D the relevant integrals can be evaluated via contour integration,[175] but this approach cannot be extended to 2D. Hence we evaluate Eq. 3.10 numerically. To obtain σ_0 and σ_2 as a function of carrier density n_e, for each fixed density we evaluate σ^{ij} at fixed small ω ($= 10^{-9}\frac{\hbar}{ma^2} \approx 450$ KHz for a lattice constant $a = 5$Å) for a number of momenta $qa \ll u^2m^2a^2/\hbar^2$ and perform a parabolic fit. For additional details, see the Appendix.

---

[5] Although in general this limit requires a self-consistency check, for our disorder configuration Σ is independent of $\mathbf{q}$, the regime always exists for sufficiently small q.

[6] Recall that the $\mathcal{O}(u^1)$ piece amounts to a shift of the chemical potential μ, and thus can be ignored.

[7] We assume that the diamagnetic term and the paramagnetic piece coming from $\mathrm{Im}\,1/(\omega + i\epsilon)\,\mathrm{Re}\langle JJ\rangle$ cancel.

3.1.3 Hydrodynamic transport and quantum effects

To target the manifestation of Fermi statistics through a density-dependent velocity, we consider a system with Fermi energy near the edge of a band. The dispersion is well approximated by the parabolic dispersion $\epsilon_{\mathbf{k}} = k^2/(2m)$. The chemical potential μ is measured relative to the band bottom, i.e. $n_e = m\mu/(2\pi)$. In this case, density of states is constant in 2D and the scattering rate $\gamma = -2\,\mathrm{Im}\,\Sigma(\mathbf{q},\omega) = u^2 m$ is also a constant. We use Eq. (3.10) to evaluate $\mathrm{Re}\,\sigma^{ij}(\mathbf{q},\omega \to 0)$. In our approach, σ_0 reproduces the known DC conductivity result $\sigma_0 = \frac{n_e e^2}{m\gamma}$. Extracting the viscosity length scale r_d according to Eq. (3.5), we obtain the result shown in Fig. 3.2b, where we have plotted $r_d \tilde{u}^2$, where $\tilde{u} = \frac{uma}{\hbar^2}$ is the dimensionless disorder strength for lattice constant a.

The numerical results follow $r_d \sim \sqrt{n_e}$, as expected from the fact that the mean free path l_{mfp} is the only length scale of our model and $l_{\text{mfp}} \sim v_F/\gamma \sim \sqrt{n_e}/(m\gamma)$. Such density dependence of the viscosity length scale is in clear contrast to the density-independent classical result of Fig. 3.2a. For an experimental test of our prediction, the order of magnitude of r_d needs to be experimentally accessible. The scale of r_d will depend on the disorder strength in general, with $r_d \propto 1/u^2$ within the first Born approximation. To obtain $r_d \approx 1\mu$m, assuming m is a free electron mass and $a \approx 5$Å, we need $u \approx .02$ eV Å.

We now turn to the effect of density of states on hydrodynamic transport. To see this effect in 2D, we propose tuning the Fermi level through the van Hove singularity. The recently developed experimental tuning parameters such as twist angle (in Moire systems[312]) and uniaxial strain (in bulk crystals such as Sr_2RuO_4[20]) could enable experimental tests of the proposal below. For our calculation, we work in the limit where the impurity scattering rate is parametrically smaller than the distance $\delta\mu$ to the van Hove point, i.e. $\gamma \ll \delta\mu$, to have asymptotic control. In the vicinity of a van Hove singularity, we consider the model Eq. (3.6-3.7) with the dispersion $\xi_{\mathbf{k}} = (k_x^2 - k_y^2)/(2m) - \delta\mu$, with $\delta\mu$ measuring the distance to the van Hove singularity. This dispersion corresponds to considering only the vicinity of $(\pi, 0)$ in the square lattice tight-binding model. We regulate UV divergences in the continuum dispersion using a square cutoff $|k_x|, |k_y| < \Lambda$. Now the self-energy is given by

$$\operatorname{Im}\Sigma(\mathbf{q}, \omega) = -\frac{mu^2}{2\pi} \operatorname{Re} \coth^{-1}\left(\frac{\Lambda}{\sqrt{-2m|\omega + \delta\mu| + \Lambda^2}}\right) \tag{3.11}$$

The logarithmic IR singularity at $\delta\mu = \omega = 0$ in the self-energy Eq. (3.11) captures the enhancement in impurity scattering due to the logarithmically diverging density of states near the van Hove singularity.

Fig. 3.3 shows the computational results of the viscosity length scale r_d in the vicinity of the van Hove singularity. To convert from $\delta\mu$ to $n_e - n_{\text{vH}}$, one uses the relation $n_e - n_{\text{vH}} = \int_0^{\delta\mu} \rho(x)|x|\, dx$, where $\rho(\mu)$ is the density of states as a function of chemical potential. The singular suppression of r_d reflects a diverging scattering rate as expected on the grounds of dimensional analysis: $r_d \sim v_F/\text{Im}\Sigma$, so that $r_d \to 0$ as $\delta\mu \to 0$. We expect an appropriate resummation of self-consistency diagrams to soften the singularity as impurity scattering blurs out the Fermi surface, and hence the van Hove point. This is expected of any van Hove effect in real systems. Nevertheless, the suppression of the viscosity length scale r_d is expected in the vicinity of the van Hove point. A confirmation of such suppression will be an unmistakable signature of a quantum effect.

Recent experimental observations of the current flow profile in narrow channels [147, 266] and of negative non-local resistance from whirlpools [17] indicate

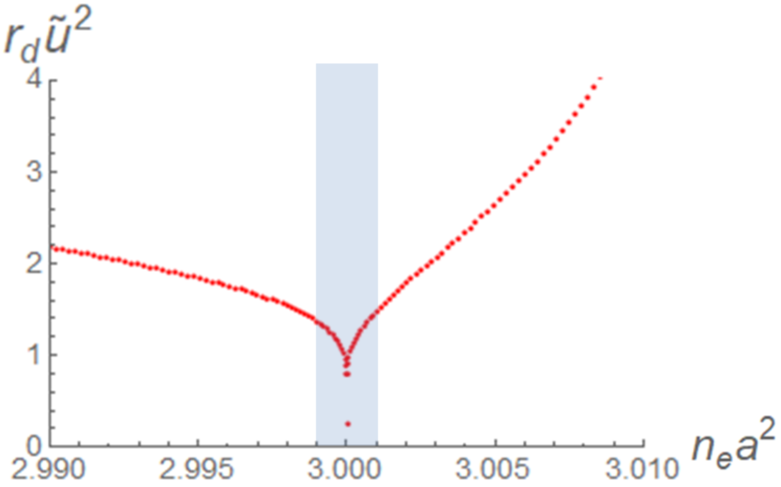

Figure 3.3: A plot of $r_d\tilde{u}^2$ against electron density for $u = 0.5\frac{\hbar^2}{ma}$, where the Van Hove singularity is chosen to sit at $n_e a^2 = 3$. Notice that r_d decreases on approach to the van Hove point due to the scattering enhancement from the logarithmically diverging density of states. The asymmetry about the van Hove point is a reflection of the anisotropy of the dispersion; we are only considering a single van Hove point corresponding to $(\pi, 0)$ in a square lattice tight-binding model. The blue shaded region denotes the regime where $n_e - n_{\text{vH}} \ll \gamma$ and we expect self-consistent resummation of the self-energy to smooth out the singularity.

that the above predictions can be tested. In particular, the ready tunability of Moire systems such as twisted bilayer graphene[162, 312] would allow access to the carrier density dependence of the viscosity length scale $r_d \sim \sqrt{n_e}$ and the suppression of r_d in the vicinity of a van Hove singularity.

Finally, we comment on the finite frequency response, shown in the Appendix. An expansion of the finite frequency conductivity in the low frequency limit yields

$$\left|\frac{\sigma_2(\omega)}{\sigma_0(\omega)}\right| \approx r_d^2(1 + B\omega^2). \tag{3.12}$$

Near the band edge, we find $r_d^2 \sim v_F^2/\gamma^2$ and $B \sim 1/\gamma^2$, so $r_d^2/B \sim v_F^2$ is a disorder-independent quantity. At frequencies $\omega \gtrsim \gamma$, the sign of σ_2 changes, signaling that the current oscillations are out of phase with the drive. For graphene, γ has been estimated to be 650 GHz.[17] In this regime, small finite momentum oscillations enhance rather than suppress the conductivity; we expect the formation of current stripes.

3.1.4 Summary and Discussion

To summarize, we considered hydrodynamic transport in a microscopic model of electrons under weak impurity scattering. The motivation was two-fold: (1) to study the effect of disorder and (2) to reveal quantum aspects. We have shown that apparently hydrodynamic phenomena such as formation of a parabolic current profile and a whirlpool can be caused entirely by weak disorder scattering. For this, we have explicitly calculated the viscosity length scale r_d, which sets the whirlpool size and the curvature of the current flow profile, by calculating the non-local conductivity $\sigma(\mathbf{q})$ and expanding it in powers of q. Furthermore, we proposed experimental strategies to access quantum aspects of such transport phenomena by tracking carrier density dependence of r_d and tuning to the vicinity of a van Hove point. These distinctly quantum signatures arise due to the long-range entangled nature of the free fermion system (i.e. its statistics).

Our results raise the question of how to distinguish impurity scattering effects from electron-electron interaction effects in experiments exhibiting hydrodynamic transport, namely parabolic current profile and whirlpool formation, also raised in Ref. [266]. Indeed, viscosity itself needs to be carefully defined in the presence of impurities as momentum conservation is violated; finite $\mathbf{q}$ conductivity and the stress-strain correlator, both of which give viscosity in the clean limit,[22] are not necessarily linked in a dirty system.[28] The role of impurity scattering in other hydrodynamic transport phenomena such as unusual temperature dependence of charge transport such as the Gurzhi effect [60, 146], thermal transport anomalies [52, 89], and magnetotransport [195] will be topics of future theoretical studies. Here we focused on delta-function correlated disorder; finite-range disorder would introduce a new length scale, and it would be interesting to understand the influence of this length scale on r_d and other transport phenomena. Our results open doors to considering other forms of scattering, including electron-phonon and umklapp scattering in the future. Another interesting future direction is the nature of the boundary, which is known to play an important role in determining viscous transport[143], in the weakly disordered regime. Last but not least, it would be interesting to revisit ultraclean two-dimensional electron gases [60] to test our predictions of density dependence of r_d.

Acknowledgements We thank Philip Kim, Leonid Levitov, Philip Moll, Andy Lucas, Srinivas Raghu, Jeevak Parpia, Subir Sachdev, Joerg Schmalian, Amir Yacoby, and Jan Zaanen for helpful discussions. A.H. was supported by the National Science Foundation Graduate Research Fellowship under Grant No. DGE-1650441 and by the W.M. Keck Foundation. SL was supported by a Bethe/KIC fellowship and by the W.M. Keck Foundation. VO was supported under DMR Grant No. 1508538. E-AK was supported by the W.M. Keck Foundation.

3.1.5 Appendix: Feynman Rules

The Feynman rules for our model are the following:

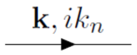

$$G_0(\mathbf{k}, ik_n)$$

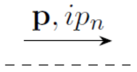

$$u^2\delta(p_n)$$

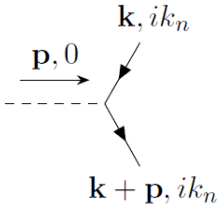

$$1$$

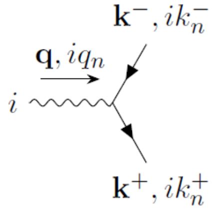

$$v_i(\mathbf{q}, iq_n) = \frac{\partial \epsilon_{\mathbf{q}}}{\partial q^i}$$

where we've defined $(\mathbf{k}^\pm, ik_n^\pm) \equiv (\mathbf{k} \pm \frac{\mathbf{q}}{2}, ik_n \pm \frac{iq_n}{2})$. The solid line corresponds to the free electron propagator $G_0(\mathbf{k}, ik_n) = \frac{1}{ik_n - \xi_{\mathbf{k}}}$. The dashed line corresponds to the impurity interaction, which transfers all momenta but no frequency, and is momentum independent. The impurity scattering vertex is just unit; as noted it transfers momenta but no frequency. The current vertex, with an external photon line with polarization i, has a current vertex factor corresponding to velocity.

3.1.6 Appendix: Kubo Formula: Spectral Function

Calculating the current-current correlator involves evaluating diagrams of the form shown in Fig. 3.4a. In the regime of interest of this paper, namely $\omega \to 0$,

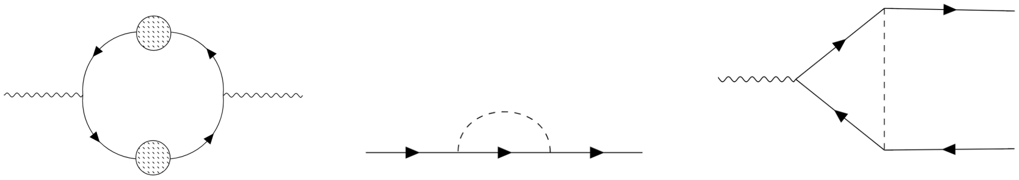

(a) Current-current correlator without vertex corrections

(b) The first Born approximation of the self-energy

(c) Lowest order vertex correction

Figure 3.4: Feynman diagrams

vertex corrections can be neglected at q^2 order in the conductivity σ, as shown in Appendix 3.1.8. Therefore, all that remains are self-energy corrections to the fermion propagator.

When $G(\mathbf{k}, ik_n)$ has self-energy corrections, i.e. $G^{-1}(\mathbf{k}, ik_n) = ik_n - \xi_{\mathbf{k}} - \Sigma(\mathbf{k}, ik_n)$, branch cuts pose complications if one wants to perform Matsubara sums via contour integration. To get around this issue, we use the spectral function approach, which relies on the identity:

$$G(\mathbf{k}, ik_n) = \int \frac{dx}{2\pi} \frac{A(\mathbf{k}, x)}{ik_n - x} \tag{3.13}$$

$$A(\mathbf{k}, \omega) = \frac{-2 \operatorname{Im} \Sigma(\mathbf{k}, \omega)}{\left[\omega - \xi_{\mathbf{k}} - \operatorname{Re} \Sigma(\mathbf{k}, \omega)\right]^2 + \left[\operatorname{Im} \Sigma(\mathbf{k}, \omega)\right]^2} \tag{3.14}$$

where $A(\mathbf{k}, \omega) \equiv -2 \operatorname{Im} G(\mathbf{k}, \omega)$ is called the spectral function. It is a fact that $A(\mathbf{k}, \omega) \geq 0$.[188] This identity allows us to perform the Matsubara sum, moving the difficulties of evaluation to the integration. We define $\mathbf{k}^{\pm} \equiv \mathbf{k} \pm \frac{\mathbf{q}}{2}$ for ease of presentation.

$$\Pi_{\alpha\beta}(\mathbf{q}) =(-1)\int \frac{d^2k}{(2\pi)^2}\frac{dxdy}{(2\pi)^2}A\left(\mathbf{k}^-,x\right)A\left(\mathbf{k}^+,y\right)\frac{n_F(x)-n_F(y)}{iq_n+x-y}v_\alpha(\mathbf{k})v_\beta(\mathbf{k}) \tag{3.15}$$

$$\begin{aligned}\operatorname{Im}\Pi_{\alpha\beta}(\mathbf{q},\omega) =&(-1)\int \frac{d^2k}{(2\pi)^2}\frac{dxdy}{(2\pi)^2}A\left(\mathbf{k}^-,x\right)A\left(\mathbf{k}^+,y\right)\Big[n_F(x)-n_F(y)\Big]\\ &\times(-\pi)\delta(\omega+x-y)v_\alpha(\mathbf{k})v_\beta(\mathbf{k}) \qquad (3.16)\\ =&\int \frac{d^2k}{(2\pi)^2}\frac{dx}{4\pi}A\left(\mathbf{k}^-,x\right)A\left(\mathbf{k}^+,x+\omega\right)\Big[n_F(x)-n_F(x+\omega)\Big]v_\alpha(\mathbf{k})v_\beta(\mathbf{k}) \qquad (3.17)\end{aligned}$$

In these equations, we suppressed $i0^+$ in the frequency, as we don't expect this to play any role due to the presence of an non-zero imaginary self-energy.

To verify this is correct, for the fermion with parabolic dispersion we plotted the zero-momentum conductivity $\sigma_0(\omega)$ and find that it matches precisely with $\sigma_0(\omega) = \frac{k_F^2}{4\pi m}\frac{\gamma}{\omega^2+\gamma^2}$, as shown in Fig. 3.5. This corroborates our Drude theory expectations and that $\sigma_0 = \frac{k_F^2 e^2}{4\pi m\gamma} = \frac{n_e e^2}{m\gamma}$ as stated in the main text.

3.1.7 Appendix: Self-Energy

In the model as stated in the main text, we need to evaluate the integral

$$\Sigma(\mathbf{q},iq_n) = u^2\int \frac{d^2k}{(2\pi)^2}G_0(\mathbf{k},iq_n) \tag{3.18}$$

corresponding to the diagram shown in Fig. 3.4b.

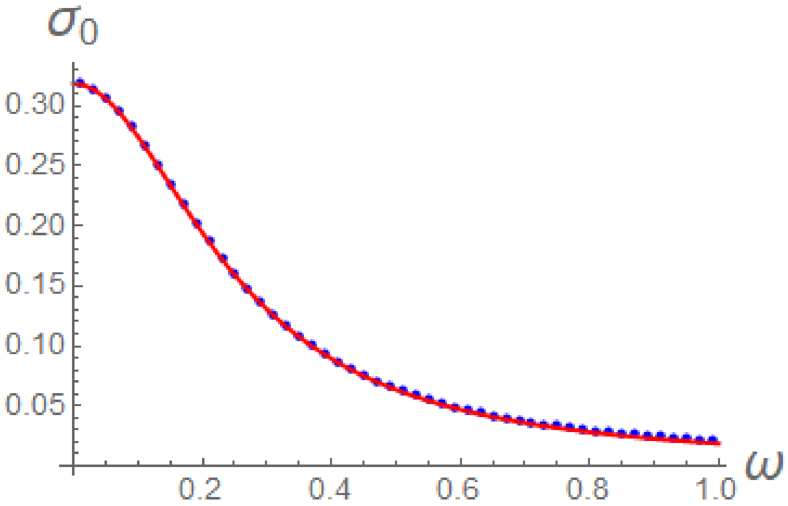

Figure 3.5: A plot of the zero-momentum conductivity $\sigma_0(\omega)$ for the fermion with parabolic dispersion, for $u = .1\frac{\hbar^2}{ma}$. The blue points are numerical data, and the red line is not a fit, but the function $\frac{k_F^2}{4\pi m}\frac{\gamma}{\omega^2+\gamma^2}$.

Parabolic Fermion

The dispersion for the parabolic (spinless) fermion is given by $\xi_{\mathbf{k}} = k^2/(2m) - \mu$. We recall that the 2D density of states for this case is $m/(2\pi)$.

$$\Sigma(\mathbf{q}, iq_n) = u^2 \int \frac{d^2k}{(2\pi)^2} \frac{1}{ik_n - \epsilon_{\mathbf{k}} + \mu} \tag{3.19}$$

$$= u^2 \int d\epsilon_k \frac{m}{2\pi} \frac{1}{ik_n - \epsilon_{\mathbf{k}} + \mu} \tag{3.20}$$

$$\Sigma(\mathbf{q}, \omega + i0^+) = u^2 \frac{m}{2\pi} \int_0^{\Lambda^2/(2m)} d\epsilon_{\mathbf{k}} P \frac{1}{\omega + \mu - \epsilon_{\mathbf{k}}} - i\pi\delta(\omega + \mu - \epsilon_{\mathbf{k}}) \tag{3.21}$$

$$= u^2 \frac{m}{2\pi} \ln\left(\frac{\Lambda^2/(2m)}{\omega + \mu} - 1\right) - iu^2 \frac{m}{2} \tag{3.22}$$

where P denotes the principal value and we take a spherically symmetric cutoff $0 < k < \Lambda$. We find that the real part is logarithmically UV divergent, and the imaginary part is constant.

Van Hove Fermion

The dispersion for van Hove fermion is given by $\xi_{\mathbf{k}} = (k_x^2 - k_y^2)/(2m) - \delta\mu$. We take cutoffs $-\Lambda < k_x, k_y < \Lambda$. As noted in the main text, and similar to the parabolic fermion, we ignore $\operatorname{Re}\Sigma$.

$$\operatorname{Im}\Sigma(\mathbf{q},\omega) = -u^2\pi \int \frac{d^2k}{(2\pi)^2}\delta(\omega + \delta\mu - \epsilon_{\mathbf{k}}) \tag{3.23}$$

$$= -\frac{m}{2\pi}u^2 \operatorname{Re}\coth^{-1}\left(\frac{\Lambda}{\sqrt{-2m|\omega+\delta\mu| + \Lambda^2}}\right) \tag{3.24}$$

3.1.8 Appendix: Vertex Corrections

In this section, we consider the lowest order vertex correction diagram, shown in Fig. 3.4c, and show that the q^2 contribution to the conductivity σ must vanish in the limit of $\omega \to 0$. We show this in two ways.

Vertex corrections vanish as $\omega \to 0$

We define $\mathbf{k}^\pm, ik_n^\pm \equiv \mathbf{k} \pm \frac{\mathbf{q}}{2}, ik_n \pm \frac{q_n}{2}$ and take a dispersion such that $\epsilon_{\mathbf{k}} = \epsilon_{-\mathbf{k}}$. This even-parity condition is satisfied for both the parabolic and van Hove dispersions. Recall that for impurity scattering, the disorder line transfers momenta but no frequency; since the disorder line (and vertex) is momentum-independent, the amputated vertex $\Gamma^i(\mathbf{q}, iq_n; ik_n)$ is independent of the external fermion momentum $\mathbf{k}$.

$$\Gamma^i(\mathbf{q}, iq_n; ik_n) = u^2 \int \frac{d^2k}{(2\pi)^2} G(\mathbf{k}^+, ik_n^+) G(\mathbf{k}^-, ik_n^-) k^i \tag{3.25}$$

$$= u^2 \int \frac{d^2k}{(2\pi)^2} \frac{1}{ik_n^+ - \epsilon_{\mathbf{k}^+} - \Sigma(\mathbf{k}^+, ik_n^+)} \frac{1}{ik_n^- - \epsilon_{\mathbf{k}^-} - \Sigma(\mathbf{k}^-, ik_n^-)} k^i \tag{3.26}$$

$$= u^2 \int \frac{d^2k}{(2\pi)^2} \frac{1}{iq_n - \epsilon_{\mathbf{k}^+} + \epsilon_{\mathbf{k}^-} - \Sigma(\mathbf{k}^+, ik_n^+) + \Sigma(\mathbf{k}^-, ik_n^-)} \times \left[\frac{1}{ik_n^- - \epsilon_{\mathbf{k}^-}} - \frac{1}{ik_n^+ - \epsilon_{\mathbf{k}^+}} \right] k^i \tag{3.27}$$

$$\Gamma^i(\mathbf{q}, \omega + i\epsilon; ik_n) = u^2 \int \frac{d^2k}{(2\pi)^2} \frac{1}{\omega + i\epsilon - \epsilon_{\mathbf{k}^+} + \epsilon_{\mathbf{k}^-} - \Sigma(\mathbf{k}^+, ik_n^+) + \Sigma(\mathbf{k}^-, ik_n^-)} \times \left[\frac{1}{ik_n^- - \epsilon_{\mathbf{k}^-}} - \frac{1}{ik_n^+ - \epsilon_{\mathbf{k}^+}} \right] k^i \tag{3.28}$$

In the second to last line we have decomposed via partial fractions. This is valid as long as the two fractions are never equal to each other (at finite $\mathbf{q}$).

We are interested in the $\omega \to 0$ limit, so we take $iq_n \to \omega + i\epsilon$ and set $\omega = 0$. [8] In this limit, $ik_n^\pm = ik_n \pm i\epsilon$. Because we are considering a momentum-independent disorder strength, the self-energy cannot depend on momentum, i.e. $\Sigma(\mathbf{k}, ik_n) = \Sigma(ik_n)$. We will also take the assumption that $\lim_{\omega \to 0} \Sigma(ik_n^+) = \lim_{\omega \to 0} \Sigma(ik_n^-)$.[9] Moreover, because we are working at finite temperature and $\omega \to 0$, we have $ik_n^\pm - \epsilon_{\mathbf{k}^\pm} = ik_n - \epsilon_{\mathbf{k}^\pm}$, as we take $\epsilon \to 0$ before $T \to 0$. Putting this all together, we have

$$\Gamma^i(\mathbf{q}, \omega + i\epsilon; ik_n) = u^2 \int \frac{d^2k}{(2\pi)^2} \frac{1}{i\epsilon - \epsilon_{\mathbf{k}^+} + \epsilon_{\mathbf{k}^-}} \left[\frac{1}{ik_n - \epsilon_{\mathbf{k}^-}} - \frac{1}{ik_n - \epsilon_{\mathbf{k}^+}} \right] k^i \tag{3.29}$$

$$= u^2 \int \frac{d^2k}{(2\pi)^2} \left(P \frac{1}{-\epsilon_{\mathbf{k}^+} + \epsilon_{\mathbf{k}^-}} - i\pi\delta(-\epsilon_{\mathbf{k}^+} + \epsilon_{\mathbf{k}^-}) \right) \times \left[\frac{1}{ik_n - \epsilon_{\mathbf{k}^-}} - \frac{1}{ik_n - \epsilon_{\mathbf{k}^+}} \right] k^i \tag{3.30}$$

---

[8] Formally $\epsilon \to 0$ first before anything, but we believe this order is fine since it introduces no divergences.

[9] For the free fermion, this is trivially true as $\Sigma = 0$. If one works in the first Born approximation, $\Sigma(ik_n) = i\gamma\,\mathrm{sign}(k_n)$, which also satisfies this condition as $k_n \neq 0$ for any finite T

where P denotes the principal value.

It is immediately clear that the imaginary part vanishes identically due to the delta function. For the real part, consider the momentum inversion $\mathbf{k} \to -\mathbf{k}$ in the integrand. This sends $\epsilon_{\mathbf{k}^\pm} \to \epsilon_{\mathbf{k}^\mp}$ so that the integrand is odd under momentum inversion. Because of this, the real part must also vanish. Hence, Γ^i is identically zero. Assuming that Γ^i is regular in ω, this implies that Γ^i is $\mathcal{O}(\omega)$ so that $\sigma(\mathbf{q},\omega)$ is also $\mathcal{O}(\omega)$.

The q^2 component of σ is purely reactive

Alternatively, we will show that the dissipative q^2 component of σ, i.e. σ_2, is zero. We first Taylor expand in q.

$$\begin{aligned}\Gamma^i(\mathbf{q}, iq_n; ik_n) =& u^2 \int \frac{d^2k}{(2\pi)^2} G(\mathbf{k}, ik_n^+) G(\mathbf{k}, ik_n^-) k^i \\ & + \left[\partial_{k^\alpha} G(\mathbf{k}, ik_n^+) G(\mathbf{k}, ik_n^-) - G(\mathbf{k}, ik_n^+) \partial_{k^\alpha} G(\mathbf{k}, ik_n^-)\right] q^\alpha k^i \end{aligned} \tag{3.31}$$

$$= u^2 \int \frac{d^2k}{(2\pi)^2} \left[\partial_{k^\alpha} G(\mathbf{k}, ik_n^+) G(\mathbf{k}, ik_n^-) - G(\mathbf{k}, ik_n^+) \partial_{k^\alpha} G(\mathbf{k}, ik_n^-)\right] q^\alpha k^i \tag{3.32}$$

Notice that if we Taylor expand in ω, the $\mathcal{O}(\omega^0)$ term vanishes, so that $\Gamma^i \sim \mathcal{O}(\omega)$. This implies that the q^2 component of the current-current correlator is $\mathcal{O}(\omega^2)$. However, we know that dissipative response functions, i.e. the current-current correlator, must be odd in frequency, hence for $\omega \to 0$ the q^2 component is purely reactive. Therefore, we know that σ_2 vanishes in the limit $\omega \to 0$.

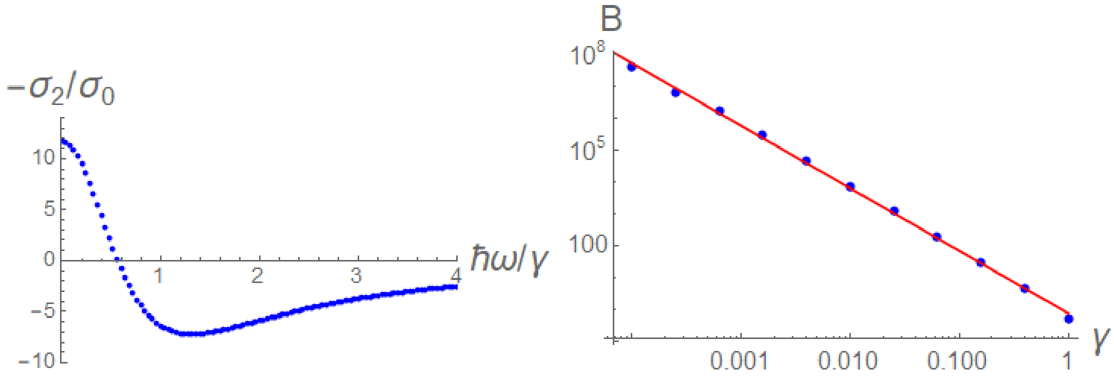

(a) (b)

Figure 3.6: (a) A plot of $-\sigma_2/\sigma_0 \sim r_d^2$ against frequency at $u = .5\frac{\hbar^2}{ma}$, normalized against the scattering rate $\gamma = u^2 m$. Around $\omega \sim \gamma/2$, the sign of $-\sigma_2/\sigma_0$ changes. (b) A log-log plot of the γ dependence of B, where the blue points are numerical data and the red line is a linear fit. We find $B \propto \gamma^{-2}$.

3.1.9 Appendix: Frequency Dependence

We remark on frequency-dependent behavior in the electron with parabolic dispersion. These characteristics also appear in the van Hove fermion as well. In Fig. 3.6a, we see that r_d changes from positive to negative when $\omega \approx \gamma$. As this corresponds to the fact that the current-current correlator changes sign at high frequency, this sign change is a reflection of the fact that the current will go out of phase with the drive. In Fig. 3.6b, we see that for $\frac{\sigma_2(\omega)}{\sigma_0(\omega)} = r_d^2(1+B\omega^2)$, $B \propto \gamma^{-2}$. On dimensional grounds, γ should be the characteristic frequency scale, so this makes intuitive sense.

3.2 Beyond Ohm's law - Bernoulli effect and streaming in electron hydrodynamics

This section is adapted from a PRB paper [119] with Vadim Oganesyan and Eun-Ah Kim.

Recent observations of non-local transport in ultraclean two-dimensional materials raised the tantalizing possibility of accessing hydrodynamic correlated transport of a many-electron state. However, it has been pointed out that non-local transport can also arise from impurity scattering rather than interaction. At the crux of the ambiguity is the focus on linear effects, i.e. Ohm's law, which cannot easily differentiate among different modes of transport. Here we propose experiments that can reveal rich hydrodynamic features in the system by tapping into the non-linearity of the Navier-Stokes equation. Three experiments we propose will each manifest a unique phenomenon that is well known in classical fluids: the Bernoulli effect, Eckart streaming, and Rayleigh streaming. Analysis of known parameters confirms that the proposed experiments are feasible and the hydrodynamic signatures are within reach of graphene-based devices. Experimental realization of any one of the three phenomena will provide a stepping stone to formulating and exploring the notions of nonlinear electron fluid dynamics with an eye to celebrated examples from classical non-laminar flows, e.g. pattern formation and turbulence.

3.3 Introduction

Electron hydrodynamics offers a powerful framework to understand transport in strongly correlated electron systems. [54, 256, 241, 100, 77, 75, 199, 58, 179, 181, 317, 278, 161, 104, 281, 249] The pursuit of electron hydrodynamics gained new impetus with the advent of recent experiments in a number of ultraclean 2D materials[52, 17, 146, 147, 266, 195, 89, 97, 159, 96] making a case for electron hydrodynamics through observations of non-local transport, consistent with viscous flows familiar in classical fluids. Observations such as vortices, Poiseuille-like flow profiles, and unconventional channel width dependencies of resistance are indeed consistent with viscous effects in a linearized Navier-Stokes equation. However, these results are all in the linear-response regime, and they can be ultimately described using a non-local variant of Ohm's law. Indeed, the linearized Navier-Stokes equation can be simply recast using a non-local conductivity $\sigma(q)$.[212, 251, 116] While non-local transport can certainly be couched in the formalism of hydrodynamics, it is also clear that inherently finite length scales of a realistic fermionic system can conspire to produce non-local transport indistinguishable from that implied by the Navier-Stokes equation.[116] Other ways of accessing electron hydrodynamics are of great interest as we seek to understand and isolate competing effects.

The overarching goal of this paper is to highlight the existence of nonlinear electron *phenomena* that may be associated with an effective hydrodynamic description. With that in mind, we adapt the Navier-Stokes (NS) equations of classical fluid dynamics by introducing momentum relaxation and Coulomb effects to make the discussion of the electron phenomenology explicit. We do not tackle the important and difficult question of a proper microscopic derivation

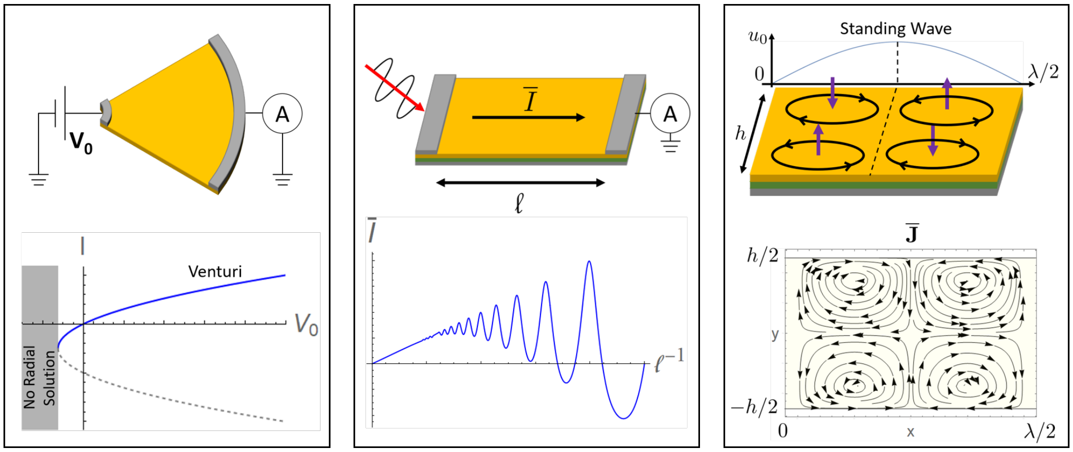

(a) (b) (c)

Figure 3.7: Proposed experimental setups and sketches of their observed effects. (a) The Venturi geometry, comprised of a circular wedge of the hydrodynamic material in yellow. A nonlinear $I - V$ characteristic with $I \sim \sqrt{V_0}$ behavior is expected, marked in blue. The gray dashed line represents an unstable solution branch, while the gray region represents a possible instability towards turbulent and/or intermittent flow. (b) Eckart streaming. A voltage oscillation of zero mean is driven on one side of a back-gated device, leading to a rectified dc current $\bar{I}$. For large l, the dc current scales as l^{-1}. For small l, oscillations due to interference with the reflected wave become visible. (c) Rayleigh streaming. In a similar back-gated geometry of (b), a standing wave of current oscillations of amplitude u_0 and of period λ along x is imposed, leading to an oscillating magnetic field pattern of period $\lambda/2$ along x. These magnetic fields arise due to the formation of vortical current cells of size $\lambda/4$ along x and $h/2$ along y, shown in the lower panel.

of NS – indeed, there is evidence that many available electron devices are not quite in the asymptotic hydrodynamic regime[18, 219]. We do, however, find strong evidence in known material and device parameters to support the feasibility of our proposals. It is worth emphasizing that while the phenomena we focus on in this work are leading deviations from linear response, the NS results we obtain also suggest the presence of instabilities at finite non-linearity. As in traditional classical hydrodynamics, these different regimes are naturally demarcated using dimensionless Reynolds numbers.

In Fig. 3.7, we summarize the three proposals that we discuss in this paper. The rest of the paper is organized as follows. Section 3.4 sets up the notation and formalism of NS, paying particular attention to the spectrum of Reynolds numbers required to quantify nonlinear phenomena. Here, we also collect Reynolds number estimates from known parameters for graphene. Section III focuses on the manifestation of the Bernoulli effect in the nonlinear current-voltage response of an electron funnel. Section IV derives the generation of down-converted dc current from a localized finite-frequency excitation, analogous to Eckart streaming or "quartz wind". Section V describes the generation of static electron vortices (akin to Rayleigh streaming) from an extended ac excitation. Sections II-V are accompanied by Appendixes A-D containing complete details of calculations. Finally, we close with a summary of results and a discussion of open problems, including the role of interactions.

3.4 Formalism and Parameters

3.4.1 Equations of fluid dynamics

The hydrodynamics of an electron fluid, as a long-wavelength effective theory, is described by a set of conservation laws for variables that decay slowly compared to the coarse-graining scale of the system. Although Galilean invariance is not microscopically present in electronic materials (e.g. graphene), the Navier-Stokes equation has been derived from kinetic theory when momentum-relaxing processes are weak.[270, 274, 204] The momentum (Navier-Stokes) and density continuity equations, which will be our primary interest in this paper, are[10]

$$\frac{\partial n}{\partial t} + \nabla\cdot(n\mathbf{v}) = 0 \tag{3.33}$$

$$\begin{aligned}\frac{\partial(\rho\mathbf{v})}{\partial t} =& \mathbf{F}_{\text{conv}} - \nabla p - \rho_e \nabla\phi \\ &+ \left[\frac{4}{D}\nu + \tilde{\zeta}\right]\rho\nabla\nabla\cdot\mathbf{v} - \rho\nu\nabla\times\nabla\times\mathbf{v} - \rho\gamma\mathbf{v}\end{aligned} \tag{3.34}$$

$$\mathbf{F}_{\text{conv}} \equiv - \nabla\cdot(\rho\mathbf{v}\otimes\mathbf{v}) = -\rho\mathbf{v}\cdot\nabla\mathbf{v} - \mathbf{v}\nabla\cdot(\rho\mathbf{v}) \tag{3.35}$$

where $\mathbf{v}$ is the velocity field, n is the number density field with mass m and charge e (ρ and ρ_e are the mass and charge densities, respectively), ν and $\tilde{\zeta}$ are the kinematic shear and bulk viscosities, respectively, and we will be working in dimension $D = 2$.[11] For graphene specifically, we remark that there are quantatitive corrections to Eq. (3.34) (see Ref. [270]). In particular, the hydrodynamic mass m is not the quasiparticle mass in the case of graphene, but is an effective mass related to the local energy density $m \sim \epsilon/v_F^2$ Moreover, there is a multiplicative correction to the convective term. We will approximate m as a constant and ignore this multiplicative correction, which we justify in Sec. 3.4.1. The convective term $\mathbf{F}_{\text{conv}}$ is written to emphasize that it acts as an effective force; this will be the primary source of nonlinear behavior. The remaining terms may also be thought of as (generalized) forces, and we can take their ratios for a particular flow pattern to characterize their relative importance. In addition to the conventional "viscous" Reynolds number Re_ν corresponding to shear dissipation, a momentum-relaxation Reynolds number Re_γ will be of interest. For

---

[10] The curl is interpreted in 3D, so that it sends vectors to vectors.

[11] In our analysis we follow the standard practice in electron hydrodynamics to ignore nonlinear fluctuation effects, such as long-time tails which are known to be non-convergent in low dimensions (including two) at finite temperature. While it is an interesting question to delineate conditions for such nonlinear regimes to be observable in electron fluids, we are not particularly optimistic in the present context, where disorder and low temperatures are of interest.

simple non-singular flow profiles, these may be expressed as

$$\mathrm{Re}_\nu \equiv \frac{\nabla \cdot (\rho \mathbf{v} \otimes \mathbf{v})}{\rho \nu \nabla^2 \mathbf{v}} = \frac{vL}{\nu} = \frac{IL}{\rho_e h \nu} \tag{3.36}$$

$$\mathrm{Re}_\gamma \equiv \frac{\nabla \cdot (\rho \mathbf{v} \otimes \mathbf{v})}{\rho \gamma \mathbf{v}} = \frac{v}{L\gamma} = \frac{I}{\rho_e h L \gamma} \tag{3.37}$$

with help of characteristic velocity v, gradient $1/L$, channel width h and net current $I = \rho_e h v$. In this paper, we primarily focus on the limit of low Reynolds numbers $\mathrm{Re}_\gamma, \mathrm{Re}_\nu \ll 1$, i.e., leading corrections to linear response[12].

Following standard practice, we make a further assumption of local equilibrium to write equations of state for p and ϕ, which closes the set of continuity equations above. We take a back-gated geometry as shown in Fig. 3.7b, where the hydrodynamic metal and the backgate separated by a distance d have a capacitance per unit area $C = \frac{\epsilon\epsilon_0}{d}$. Therefore, we take the following local relationships

$$p = s_{\mathrm{FL}}^2 \rho \tag{3.38}$$

$$\phi = \rho_e / C \tag{3.39}$$

where s_{FL} is a constant corresponding to the speed of sound in an uncharged, undamped fluid (i.e. a Fermi liquid). In Eq. 3.39, also called the "gradual channel approximation," the long-range Coulomb tail is screened by the gate so that the longitudinal dispersion is gapless. This approximation is valid when the distance d between the hydrodynamic metal and the gate is much smaller than the typical wavelength of oscillations.[65, 274, 277] Therefore, both p and ϕ obey the same functional form; if the density $\rho = \rho^{(0)}$ is constant, p can be absorbed into an effective voltage $\phi_{\mathrm{eff}} \equiv \phi + \frac{p}{\rho_e^{(0)}}$ in the momentum equation. In particular,

---

[12] The third dimensionless number which captures the relative strength of pressure (and potential) terms to convection turns out to be related to the Mach number.

as a result of Eq. (3.39) there is also an electronic contribution $s_{\text{cap}}^2 = \frac{n^{(0)}e^2}{Cm}$ to the undamped speed of sound $s_0 \equiv \sqrt{s_{\text{FL}}^2 + s_{\text{cap}}^2}$.

Parameter Estimates

To estimate parameters, as a model system we consider a graphene-hBN stack with gate-channel separation $d = 100$ nm and average carrier density $n^{(0)} \sim 10^{12}$ cm^{-2} tuned away from charge neutrality so that we can consider a single band. In graphene, the relaxation rate $\gamma \sim 650$ GHz and $\nu \sim 0.1$ m^2/s,[17] so that the viscous length scale $r_d = \sqrt{\frac{\nu}{\gamma}} \sim 0.4\mu$m.[116] We also will take $\tilde{\zeta} \sim 0$.[180, 23] The relative dielectric constant of hBN is $\epsilon \sim 3.9$,[151, 277] and we approximate m and e to be the bare electron mass and charge, respectively. Therefore, the electronic contribution to sound is $s_{\text{cap}} \sim 0.9 \times 10^6$ m/s. The speed of sound of Fermi liquids is $s_{\text{FL}} \sim v_F$,[149] and Fermi velocities for metals are generally $v_F \sim 10^6$ m/s.[15] Therefore, we will approximate the undamped speed of sound $s_0 \sim 2 \times 10^6$ m/s. Using the dispersion relation in Eq. 3.53, for $\omega = 1$ THz we have the true speed of sound $s \sim 1.9 \times 10^6$ m/s and attenuation coefficient $\alpha \sim 1/(6\mu\text{m})$. As a rough estimate, for characteristic lengths $h \sim L \sim 5\mu$m the Reynolds numbers are $\text{Re}_\nu \sim I/(160\mu\text{A})$ and $\text{Re}_\gamma \sim I/(26\text{mA})$. The ratio $\text{Re}_\nu \,/\, \text{Re}_\gamma \sim L^2/r_d^2$ is controlled by the viscous length scale $r_d \sim .4\mu$m, so current micrometer-scale experiments will be in a regime where Re_γ tends to dominate the nonlinear behavior. We remark that the apparent paradox that hydrodynamic effects could be dominated by momentum relaxation is due to linear-response considerations; by tuning the sample width h such that $r_d \ll h$, a hydrodynamic description of the material remains valid but becomes indistinguishable from Ohm's law in the absence of convection.

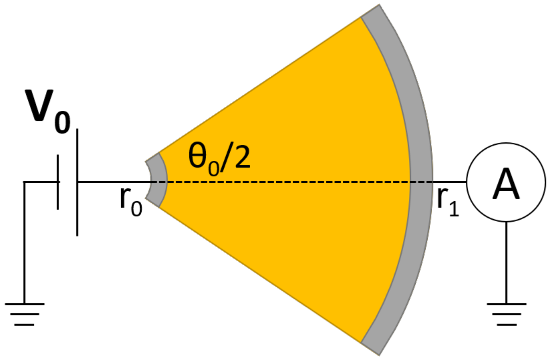

Figure 3.8: A topview of the Venturi geometry, with inner radius r_0 and outer radius r_1 and total wedge angle θ_0.

We now justify our assumptions of m constant and convective correction ξ negligible for the case of graphene. As shown in Ref. [270], the mass fluctuations $\delta m \sim m_0[\mathcal{O}(\delta n/T) + \mathcal{O}(u^2/v_F^2)]$. For our parameters, operating at currents $I \sim 100\mu$A and channel widths $h \sim 5\mu$m at room temperature $T = 300K$, the corrections $\delta m \sim .01m$ and are perturbatively small. Keeping any new nonlinearities introduced by δm up to second-order, we find that it only introduces quantitative $\mathcal{O}(1)$ corrections to the dissipative terms γ, ν, and $\overline{\zeta}$. Therefore, m constant is valid at our level of approximation. For the multiplicative correction to convection, for our parameters where $\mu/T \gtrsim 1$ the multiplicative factor is roughly $1/4$; this is only an $\mathcal{O}(1)$ quantitative correction and it is valid to ignore it at our level of approximation.

3.4.2 Electronic Bernoulli effect

We now apply the hydrodynamic formalism to derive a nonlinear contribution to the I-V characteristic $V \propto I^2$ in what we call the 'Venturi' geometry (see Fig. 3.8), first analytically in the limit $\nu \to 0$. For boundary conditions, we fix the voltage $\phi(r_0) = V_0$ and $\phi(r_1) = 0$ and take no-slip (vanishing velocity) at the side walls $\theta = \pm\theta_0/2$. We find that the stationary, purely radial "plug flow" ansatz $\mathbf{v} = v_r(r)\Theta(\theta_0^2 - 4\theta^2)\hat{\mathbf{r}}$ is a solution (with Θ the Heaviside step-function). The absence of viscosity is crucial as it allows for a zero-thickness boundary layer in this highly symmetric flow.[13] The Navier-Stokes equation (Eq. (3.34)) reduces to a simple ordinary differential equation

$$\frac{\partial}{\partial r}\left[e\phi + \frac{1}{2}mv_r^2\right] + m\gamma v_r = 0 \quad , \tag{3.40}$$

where we have subsumed pressure into ϕ for simplicity.[14] We further take the divergence-free ("incompressible flow") ansatz $v_r = \frac{I}{\rho_e^{(0)}\theta_0}\frac{1}{r}$, where the yet-undetermined constant I is the total current and $\rho_e^{(0)}$ is the average charge density. Substituting this ansatz into Eq. (3.40) and integrating from r_0 to r_1 (see Fig. 3.8), we obtain the nonlinear I-V characteristic

$$V_0 = \frac{1}{\sigma_D}\left[\frac{l\ln(h_1/h_0)}{h_1 - h_0}I - \frac{1}{2}\left(\frac{1}{h_0^2} - \frac{1}{h_1^2}\right)\frac{I^2}{\rho_e\gamma}\right] \tag{3.41}$$

where $\sigma_D = \frac{n^{(0)}e^2}{m\gamma}$ is the Drude conductivity, $l = r_1 - r_0$ is the length, and $h_0 = \theta_0 r_0$ and $h_1 = \theta_0 r_1$ are the widths at the contacts. The first term on the RHS corresponds to the Ohmic contribution, while the second term is the nonlinear I^2 contribution from convection. We emphasize that the nonlinear contribution is strongly geometric, vanishing for typical rectangular geometries[60] where $h_0 = h_1$. To further isolate the nonlinearity, we exploit the parity difference between the two contributions. Because the nonlinearity is of even parity, a non-zero symmetrized current $I_{\text{sym}}(V_0) \equiv \frac{1}{2}[I(V_0) + I(-V_0)]$ provides a direct signature of the nonlinearity. To estimate this effect, in Fig. 3.9 we plot in blue

---

[13] Boundary conditions are effectively inconsequential without viscosity. One could just have well taken no-stress boundary conditions (while including viscosity as the shear viscosity force vanishes[249]). The Corbino geometry is therefore smoothly connected to the $\theta_0 \to 2\pi$ limit, as the Corbino geometry is equivalent to no-stress boundary condition.

[14] When the device is gated, including p is equivalent to renormalizing e/m. In the absence of gating, the long-range Coulomb interaction suppresses density fluctuations, so the pressure contribution is expected to be negligible.

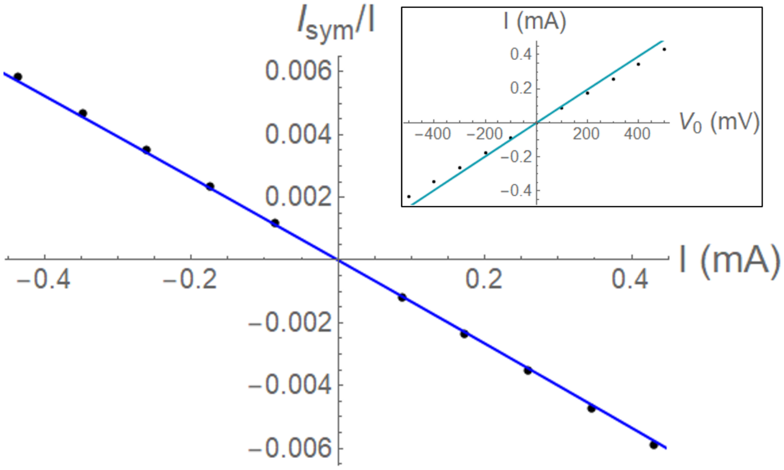

Figure 3.9: Main: A parametric plot of the voltage-symmetrized current $I_{\text{sym}}(V_0) \equiv \frac{1}{2}[I(V_0) + I(-V_0)]$ against total current $I(V_0)$. Inset: The I-V characteristic. The solid lines are obtained analytically from Eq. (3.41) in the $\nu \to 0$ limit, and the points are obtained numerically with finite ν. Fixed-voltage boundary conditions are taken. The inner and outer radius are 5μm and 10μm respectively, with wedge angle $\theta_0 = \pi/2$, with graphene parameters $\nu = .1$ m^2/s and $\gamma = 650$ GHz. Since $r_d \sim .4\mu$m and lengths are $\sim 10\mu$m, viscous corrections to the analytic $\nu \to 0$ solution should be $\sim 5\%$.

the current fraction I_{sym}/I and the I-V characteristic of Eq. (3.41) for wedge angle $\theta_0 = \pi/2$ with $r_0 = 5\mu$m, $r_1 = 10\mu$m, and graphene-hBN parameters as discussed in Sec. 3.4.1. To incorporate a finite shear viscosity, which is difficult to solve analytically (see Appendix 3.4.7), we solve the Navier-Stokes equations numerically and plot the results as points in Fig. 3.7a. The exact ($\nu = 0$) result of Eq. (3.41) matches well with the numerical result, as expected because the viscous length scale $r_d \equiv \sqrt{\frac{\nu}{\gamma}} \ll r_0\theta_0$ is small for experimentally relevant parameters. As demonstrated by Fig. 3.7a, this nonlinear effect ($I_{\text{sym}} \sim 400$ nA for $I \sim 200\mu$A) should be experimentally measurable.

This nonlinear I-V characteristic in electronic hydrodynamics is the analog of the Bernoulli effect in classical hydrodynamics, the prototypical example of convective acceleration, which is traditionally demonstrated using a Venturi tube.

The Bernoulli effect is typically demonstrated in an inviscid fluid of divergence-free (incompressible) flow, analogous to our assumptions. In fact, the classical Bernoulli (energy conservation) equation is analogous to Eq. (3.40); the term in brackets corresponds to the classical Bernoulli contribution (i.e. when $\gamma = 0$), while the γ term accounts for the additional dissipation from a finite conductivity. As a result, the nonlinear term of the I-V characteristic Eq. (3.41) can be calculated exactly by classical Bernoulli considerations.

We turn to the subtle issue of solving for the total current $I(V_0)$ given the input voltage V_0, i.e. verifying that the ansatz satisfies the boundary conditions. Because this requires solving a quadratic equation for I, the solution is generically multivalued and may not even have a solution. In the limit of small V_0, linear response must provide the correct answer on physical grounds; this selects the solution branch continuously connected to the solution $I = 0$ at $V_0 = 0$, where parity was broken by γ. The opposite branch is therefore expected to be unstable to θ-dependent perturbations. The region where the purely radial solution does not exist corresponds to particle flow in the divergent direction; for classical fluids, it is known that divergent flow eventually becomes unstable and develops turbulence.[150, 238] To estimate the scale of nonlinearity at which the radial ansatz fails, one can define a Reynolds number

$$\mathrm{Re}_\gamma \equiv \frac{\int_{r_0}^{r_1} dr F_{\mathrm{conv},r}}{-\int_{r_0}^{r_1} dr \rho\gamma v_r} = \frac{-1}{2lh_0}\frac{I}{\rho_e\gamma}\left[\frac{\frac{h_1}{h_0}-1}{\ln\frac{h_1}{h_0}}\left(1-\frac{h_0^2}{h_1^2}\right)\right] \tag{3.42}$$

which is precisely the ratio of the two terms in Eq. (3.41). The instability point occurs at $\mathrm{Re}_\gamma = -1/2$. We summarize the resolution of these subtleties in Fig. 3.7a.

Finally, we now highlight three aspects of the Bernoulli non-linearity that should help identify it unambiguously in experiments. To start, following Eq.

(3.41) we note that the quadratic term is independent of the momentum relaxation parameter γ, and hence may be identified by comparing I-V traces taken at different temperatures or even from different samples of the same material. Secondly, the simple charge density-dependence may be probed by varying backgate voltage. After factoring out the density-dependent Drude resisitivity $1/\sigma_D$ (cf. Eq. 3.41), the nonlinear term only has an inverse dependence on charge density (and its sign depends on the carrier charge). Lastly, Eq. (3.41) has a distinct geometric dependence interpolating in a somewhat unusual way between conventional and ballistic transport. For a fixed aspect ratios h_1/h_0 and l/h_0, we find that the Ohmic resistance contribution scales with the size of the device as $1/h_0$ while the nonlinear Bernoulli contribution scales as $1/h_0^2$. In addition, the Ohmic resistance contribution has the conventional linear scaling with length l, while the nonlinear Bernoulli contribution has the l-independent hallmark of *ballistic* transport. This effect therefore stands apart from generic nonlinearities, which are expected to be inversion-odd when the crystal structure is inversion-symmetric (e.g in graphene), and from Joule heating effects, which would also provide inversion-odd nonlinearities and would not have the l-independent ballistic scaling.

3.4.3 Eckart Streaming: A "Hydrodynamic Solar Cell"

A dramatic effect of nonlinearity occurs upon applying an oscillatory drive: down-conversion. In a backgated device of length l and width h (see Fig. 3.7b), we consider setting up a traveling longitudinal (sound) wave by application of a voltage oscillation $\phi(x = 0) = V_0 \cos \omega t$ at the left contact with the right contact grounded ($\phi(x = l) = 0$). This will result in a DC current via the downconversion sourced by the convective force (Eq. (3.35)). Such a device can be described as a "hydrodynamic solar cell" providing a DC photocurrent if the (localized) voltage oscillation is driven by EM radiation. For simplicity, we will focus on bulk dissipation (i.e. attenuation due to $\alpha > 0$) contributions to the convective force and neglect those of boundary dissipation, which only results in a quantitative underestimate of the DC current (see Appendix 3.4.8). This is the electronic analog of Eckart streaming in classical hydrodynamics, where the convective force is primarily generated by bulk dissipation.[66, 208, 173, 299] To see this, we need to solve the full Navier-Stokes equation (Eq. (3.34)), whose nonlinearity precludes a single-mode ansatz. To handle this, we will seek a perturbative solution in the input voltage amplitude V_0 (see Appendix 3.4.8 for full mathematical detail).

Perturbative Calculation

We begin by expanding the hydrodynamic variables in a power series expansion of V_0, e.g. $\rho = \rho^{(0)} + \rho^{(1)} + \rho^{(2)} + \ldots$; $\rho^{(0)}$ corresponds to the equilibrium mass density, while $\rho^{(1)}$ and $\rho^{(2)}$ are the first and second order solutions. At leading (linear) order, the single-mode ansatz $\phi^{(1)} \sim V_0 e^{i(\pm k_l x - \omega t)}$ along x with wavenumber $k_l = k + i\alpha$ is appropriate. Imposing the fixed-voltage boundary conditions, the solution of $\phi^{(1)}$ is a traveling wave with a reflected component; the grounded edge acts as a mirror. Because of the backgate providing a capacitance per area C, the voltage oscillation of amplitude V_0 sets up a charge density oscillation $\rho_e^{(1)} = C\phi^{(1)}$ of amplitude CV_0 (see Eq. (3.39)). Via the density continuity equation (Eq. (3.33)), the density oscillations drive a longitudinal velocity oscillation $v_x^{(1)}$, schematically written as

$$v_x^{(1)} \sim u_0 \Re \left[e^{(ik-\alpha)x - i\omega t} + e^{(ik-\alpha)(2l-x)-i\omega t} \right] \tag{3.43}$$

where $\Re$ denotes real part and $u_0 = \frac{CV_0}{\rho_e^{(0)}} \frac{\omega}{|k_l|}$ is the velocity amplitude. We also take a no-slip boundary condition, which is *not* satisfied by $v_x^{(1)}$. However, as previously stated we will neglect the boundary corrections to $v_x^{(1)}$ for simplicity (see Appendix 3.4.8).[15] As a result, the leading order solution $v_x^{(1)}$ results in a DC convective force (see Eq. (3.35))

$$\overline{F_{\text{conv},x}^{(2)}} = \rho^{(0)} u_0^2 \frac{\alpha \sinh[2\alpha(l-x)] - k \sin[2k(l-x)]}{\cosh 2\alpha l - \cos 2kl} \tag{3.44}$$

where the overbar denotes time-average. The first term in the numerator arises from the bulk dissipation α, while the second term arises from interference effects; in the limit $\alpha l \gg 1$, where interference effects are small, the RHS of Eq. (3.44) simplifies to $\alpha e^{-2\alpha x}$. This rectified DC force will result in a DC current.

We now solve for the second-order DC current $\overline{I^{(2)}}$. The DC current density $\overline{\mathbf{J}^{(2)}} \equiv \rho_e^{(0)} \overline{\mathbf{v}^{(2)}} + \overline{\rho_e^{(1)} \mathbf{v}^{(1)}}$ must be divergence-free to satisfy current conservation (i.e. density continuity Eq. (3.33)). With the ansatz $\overline{v_y^{(2)}} = 0$, this implies that the current density $\overline{\mathbf{J}^{(2)}} = \overline{J_x^{(2)}}(y)\hat{\mathbf{x}}$ only varies along y. However, the convective force given by Eq. (3.44) varies along x. This paradox is resolved by static screening, where the x-dependence of convection will be canceled by contributions from the effective voltage $\overline{\phi_{\text{eff}}^{(2)}} \equiv \overline{\phi^{(2)}} + \frac{1}{\rho_e^{(0)}} \overline{p^{(2)}}$. Utilizing separation of variables in the NS equation (Eq. (3.34)), we can solve for $\overline{\phi_{\text{eff}}^{(2)}}$ by applying the voltage-fixed boundary conditions $\overline{\phi^{(2)}}(x=0) = \overline{\phi^{(2)}}(x=l) = 0$. Therefore, the

---

[15] This is effectively equivalent to taking stress-free boundary conditions at leading order; the choice of boundary condition only weakly modifies the final result (see Eq. (3.46) and subsequent footnote on the viscous correction.)

"screened" convective force (which is no longer spatially dependent) becomes

$$\overline{F^{(2)}_{\text{conv},x}} - \rho_e^{(0)}\frac{\partial\overline{\phi^{(2)}_{\text{eff}}}}{\partial x} = \frac{1}{l}\int_0^l dx \overline{F^{(2)}_{\text{conv}}}\,. \tag{3.45}$$

Solving NS for the current density $\overline{J_x^{(2)}}$ and integrating across the channel to get the total current $I^{(2)}$, we get

$$\begin{aligned}\overline{I^{(2)}} =& \frac{I_0^2}{\rho_e^{(0)}h}\frac{1}{2l\gamma}\left[1 - \frac{2-2\cos 2kl}{\cosh 2\alpha l - \cos 2kl}\right] \\ & \times\left(1 - \frac{2r_d}{h}\tanh\frac{h}{2r_d}\right)\end{aligned} \tag{3.46}$$

where $I_0 \equiv \rho_e^{(0)}hu_0$ is the input current amplitude, and we have assumed that convection provides the dominant DC force (see Appendix 3.4.8). The term in parentheses is a viscous correction, reflecting the y-dependence of the current flow due to no-slip.[16] The bracketed terms correspond to dissipation and interference contributions from the convective force (Eq. (3.35)), respectively. The effect of these contributions is demonstrated in Fig. 3.7b, where we have schematically plotted the dependence of DC current on the channel length l. In the limit $\alpha l \ll 1$, the interference term dominates, leading to oscillatory behavior controlled by kl. In the opposite limit $\alpha l \gg 1$, the interference term becomes negligible, and the DC current scales as $\overline{I^{(2)}} \sim l^{-1}$. Other than the device length l, one could also study the frequency dependence of Eq. (3.46) (via $k_l(\omega) = k + i\alpha$), which is plotted in Fig. 3.10 for a fixed I_0.[17] Similarly, interference effects appear at low frequencies and become negligible at high frequencies.

---

[16] This is the only effect of the no-slip BC. For stress-free boundary conditions, this correction will be equal to 1. The DC flow profile will be constant along y, which is equivalent to setting $\nu \to 0$ as there is no shear viscosity force.

[17] Because $I_0 = \rho_e^{(0)}h\frac{CV_0}{\rho_e^{(0)}}\frac{\omega}{|k_l|}$, perturbation theory will break down for sufficiently low ω. This happens when $\omega \ll \gamma$, i.e. when k_l is dominated by γ and tends to a constant.

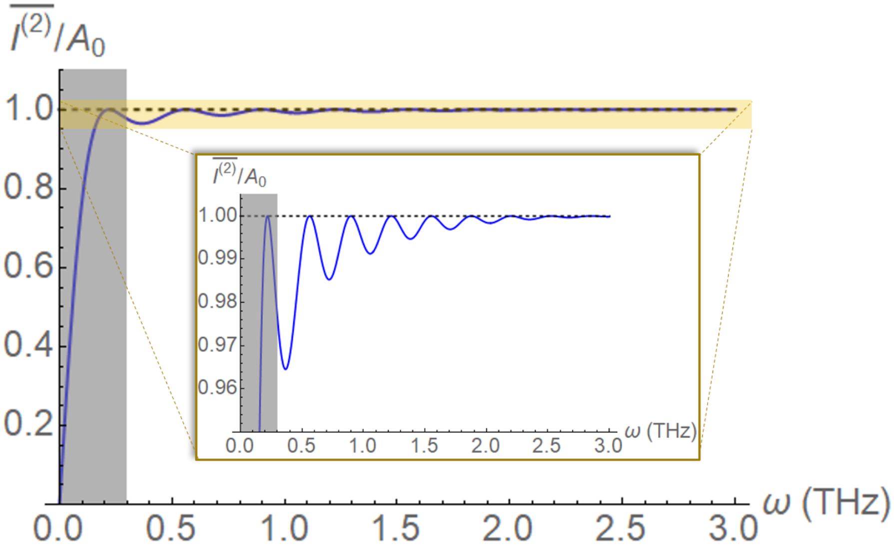

Figure 3.10: Main: A plot of $\overline{I^{(2)}}$ at fixed input current amplitude I_0 for device length $l = 30\mu$m and graphene-hBN parameters stated in Sec. 3.4.1, in units of $A_0 = \frac{I_0^2}{\rho_e^{(0)} h}\frac{1}{2l\gamma}\left(1 - \frac{2r_d}{h}\tanh\frac{h}{2r_d}\right)$. We remark that this is also a scaled plot of the Reynolds number Re_γ. Inset: A blowup of the yellow highlighted portion. At high frequencies, Re_γ saturates to a constant $A_0 = \frac{I_0}{\rho_e^{(0)} h}\frac{1}{2l\gamma}$, while at sufficiently low frequencies the interference oscillations become more visible. The gray box demarcates the low frequency region $\omega \ll \gamma$, where perturbation theory in V_0 breaks down for a fixed I_0.

Discussion and Estimates

An effect similar to Eckart streaming was previously discussed by Dyakonov and Shur[64] and extended in Ref. [277]. They envisaged operating with zero DC current bias $\overline{I} = 0$ instead of zero DC voltage drop, so that one generates a DC voltage instead of a DC current. These theoretical treatments[64, 277] similarly neglected boundary dissipation, which only leads to quantitative corrections to DC voltage. However, for their case, boundary dissipation leads to qualitative flow corrections (see Appendix 3.4.8); further discussion is deferred to Sec. 3.4.4. We point out that, in either case, if the voltage oscillation is driven by an impingent EM wave, the device is a "hydrodynamic solar cell" generating a DC photocurrent (photovoltage). In contrast to typical solar cells (e.g. a p-n junction), the hydrodynamic solar cell does not break parity by construction; parity is intrinsically broken by dissipation, setting the direction of the photocurrent. Therefore, Eckart streaming provides a novel mechanism for photocurrent (photovoltage) generation. Signatures of down-converted DC voltage generation by THz radiation have been measured in ultraclean 2DEGs.[273, 282, 84, 19]

One can define Reynolds numbers to estimate the strength $I^{(2)}/I_0$ of the nonlinearity. The Reynolds number Re_γ for this system can be defined as

$$\mathrm{Re}_\gamma \equiv \frac{\frac{1}{l}\int_0^l \overline{F^{(2)}_{\mathrm{conv},x}}}{\rho_e^{(0)}\gamma u_0} = \frac{I_0}{\rho_e^{(0)} h}\frac{1}{2l\gamma}\left[1 - \frac{2 - 2\cos 2kl}{\cosh 2\alpha l - \cos 2kl}\right] \tag{3.47}$$

which explicitly appears in Eq. (3.46). The viscous Reynolds number can be similarly defined such that $\mathrm{Re}_\nu = \frac{h^2}{r_d^2}\mathrm{Re}_\gamma$, where we approximate the viscous gradients to have length scale $L = h$ (see Eq. (3.36)). The contribution from Re_ν is hidden within r_d; in the limit $r_d \gg h$ where viscous contributions dominate, Re_ν can be made manifest by perturbatively expanding Eq. (3.46) in h/r_d. Since $r_d \gg h$ for the experimental systems of interest, the Reynolds number $\mathrm{Re}_\gamma \sim I^{(2)}/I_0$ corresponds to the scale of DC current (up to a small viscous correction).

We now estimate the size the DC current in experiment (see Appendix 3.4.6 for dispersion relations). We take device size $l = 50\mu\mathrm{m}$ and $h = 5\mu\mathrm{m}$ and operate at $\omega = 1$ THz, with graphene-hBN parameters from Sec. 3.4.1; for these choices, the interference effects are small since $\alpha l \sim 5$. Therefore, we find $\mathrm{Re}_\gamma \sim I_0/(312\mathrm{mA})$ and therefore $\overline{I^{(2)}}/\mathrm{nA} \sim (I_0/24\mu\mathrm{A})^2$. Observing the oscillatory effects is more difficult, requiring smaller l and more measurement precision. Despite this, in an optimistically sized device of length $l = 20\mu\mathrm{m}$, we plot the frequency dependence of Re_γ in Fig. 3.10. The oscillations are suppressed by a factor of 0.01; if one asks for a streaming current $\overline{I^{(2)}} \sim 1$ nA, the oscillations will be of order 10 pA. We therefore conclude that an Eckart streaming current should be visible in current experiments, with interference oscillations being a challenging observable.

3.4.4 Rayleigh Streaming

We now turn to the limit where boundary dissipation dominates, i.e., the bulk dissipation α is negligible. Here, the no-slip condition is critical. In a rectangular backgated device of width h (see Fig. 3.7c), we consider setting up a longitudinal standing wave of wavelength $\lambda \gg \alpha^{-1}$ along x. In this case, the system cannot support a finite DC current due to reflection symmetry in y. Therefore, down-converted DC current flows sourced by the convective force (see Eq. (3.35)) must circulate. The circulating current leads to a measurable orbital magnetization of wavelength $\lambda/2$ along x with reflection-symmetric modulation along y (see Fig. 3.7c). This is the analog of Rayleigh streaming in classical hydrodynamics, where the convective force is primarily generated by boundary dissipation.[173, 208, 234] Remarkably, localized boundary effects lead to nontrivial flows throughout the bulk (see Appendix 3.4.9 for full mathematical detail).

Perturbative Calculation

We begin by working perturbatively in the input current amplitude u_0, where at linear order we take the longitudinal wave ansatz

$$v_{l,x}^{(1)} = u_0 \sin kx \cos \omega t \tag{3.48}$$

This is consistent with a current-fixed boundary condition $J_x(x = 0) = 0$ (i.e. DC current $\overline{I} = 0$). For simplicity, we work in a semi-infinite strip of width h (i.e. $|y| \leq h/2$ and $x \geq 0$) with the above current-fixed boundary condition. To satisfy no-slip, a transverse mode $\mathbf{v}_t^{(1)}$ is necessary to correct the total flow $\mathbf{v}^{(1)} = \mathbf{v}_l^{(1)} + \mathbf{v}_t^{(1)}$. This transverse correction disperses along y with wavenumber $k_t = k_t' + ik_t''$, and hence forms a "boundary layer" of size $1/k_t''$ exponentially localized to the wall. We will work in the thin boundary layer and long wavelength limit $k_t''^{-1} \ll h \ll \lambda$. In this limit, the resulting convective force (see Eq. (3.35)) can be schematically written as

$$\overline{F_{\text{conv},x}^{(2)}} \sim \rho^{(0)} u_0^2 \, k \, e^{-k_t'' y_+} \sin 2kx + (y \leftrightarrow -y) \tag{3.49}$$

where $y_+ = y + \frac{h}{2}$ is the distance from the lower boundary.[18] As a result of the quadratic non-linearity, the wavelength of the convective force is halved to $\lambda/2$. In addition, the convective force is localized to the boundary layer, reflecting the fact that convection is driven by boundary dissipation. It is therefore convenient to divide the flow into bulk and boundary-layer regions, stitched together at the interface. Despite the localized nature of the convective force, its effect will persist into the bulk by providing a slip boundary condition.

Now, we study the second-order DC flow. We first consider the boundary layer region, assuming that the viscous length scale $r_d \equiv \frac{\nu}{\gamma} \ll h$. The convective

---

[18] More precisely, this is schematic form of the "screened" convective force with contributions from the effective voltage $\phi_{\text{eff}}^{(2)} = \phi^{(2)} + \frac{1}{\rho^{(0)}} p^{(2)}$.

force localized to the boundary layer of size $1/k_t''$ leads to a localized flow along x. Because of the shear viscosity ν, the boundary layer momentum propagates into the bulk with the viscous length scale r_d. Therefore, the boundary layer "screens" the no-slip condition, providing instead a slip velocity for the bulk flow. This slip velocity can be written as $v_{\text{slip}}^{(2)} \sin 2kx$, where schematically $v_{\text{slip}}^{(2)} \sim \frac{u_0^2 k}{4\gamma} e^{-1/k_t'' r_d}$. Equipped with the slip boundary, we now solve the NS equation (Eq. (3.34)) for the bulk flow where the convective force vanishes, and we obtain

$$\overline{J_{\text{bulk},x}^{(2)}} = J_{\text{slip}}^{(2)} \sin 2kx \left[\frac{\frac{h}{2r_d} \cosh \frac{y}{r_d} - \sinh \frac{h}{2r_d}}{\frac{h}{2r_d} \cosh \frac{h}{2r_d} - \sinh \frac{h}{2r_d}} \right] \tag{3.50}$$

$$\overline{J_{\text{bulk},y}^{(2)}} = J_{\text{slip}}^{(2)} 2kr_d \cos 2kx \left[\frac{-\frac{h}{2r_d} \sinh \frac{y}{2r_d} + \frac{y}{r_d} \sinh \frac{h}{2r_d}}{\frac{h}{2r_d} \cosh \frac{h}{2r_d} - \sinh \frac{h}{2r_d}} \right] \tag{3.51}$$

The slip current $J_{\text{slip}}^{(2)} \equiv \rho_e^{(0)} v_{\text{slip}}^{(2)}$ results from boundary convection, while the term in brackets is a geometric factor resulting from satisfying the slip velocity boundary condition. The DC current flow is plotted in Fig. 3.7c, where it is clear that the current circulates in cells of length $\lambda/4$ and width $h/2$.

Discussion and Estimates

A previous related proposal by Dyakonov and Shur[64] and its recent extension[277] discussed downconversion effects with a current-fixed boundary $J(x = 0) = 0$, similar to this case. However, they instead took a stress-free boundary condition that has no boundary dissipation. In their case, there is no circulating current; without boundary-layer contributions, the convective force only leads to an excess of DC voltage (see Appendix 3.4.9). Therefore, Rayleigh streaming is qualitatively distinct from previous nonlinear proposals in electron hydrodynamics.

Since the effect of the convective force is to generate a slip velocity $v_{\text{slip}}^{(2)}$, we can estimate the scale $v_{\text{slip}}^{(2)}/u_0$ by an appropriate Reynolds number. The Reynolds number Re_γ is defined in this case to be

$$\text{Re}_\gamma \equiv \frac{\max \overline{F_{\text{conv}}^{(2)}}}{\rho^{(0)}\gamma u_0} = \frac{I_0}{\rho_e^{(0)} h} \frac{k}{4\gamma} f(\omega/\gamma) \tag{3.52}$$

where f is a dimensionless function of ω/γ described in Appendix 3.4.9.[19] We remark that f develops an interesting resonance at $\omega = \frac{\sqrt{5}}{2}\gamma$ where perturbation theory breaks down, but we operate away from this point and will not discuss it further. It turns out $\text{Re}_\gamma \, e^{-1/k_t'' r_d} = v_{\text{slip}}^{(2)}/u_0$, i.e. slip velocity is given by the Reynolds number up to an exponential factor controlled by the viscous length scale r_d. However, the viscous Reynolds number Re_ν does not contribute to the effect; in the limit $\gamma \to 0$, the scale $v_{\text{slip}}^{(2)}/u_0$ is instead set by the Mach number $u_0 k/\omega$. Despite the necessity of a finite shear viscosity ν to generate a convective force, Re_ν does not set the scale $v_{\text{slip}}^{(2)}$ of the result; this curious fact was first remarked by Rayleigh[225] (see Appendix 3.4.9 for additional discussion).

We propose that the circulating flow profile could be detected via magnetometry. To estimate the effect in realistic systems, we set $\omega = 2$ THz and channel width $h = 5\mu$m with graphene-hBN parameters as in Sec.3.4.1 (see Appendix 3.4.6 for dispersion relations). We first verify the assumptions we made: $k_t''^{-1} \ll h \ll \lambda$, $r_d \ll h$, and $\alpha \ll k$. These are $k_t'' h \sim 13$, $h/\lambda \sim 0.80$, $r_d/h \sim .08$ and $\alpha/k \sim 0.2$, so we expect our solution to be roughly correct. For the scale of the DC effect, we find $\text{Re}_\gamma \sim I_0/(23\text{mA})$ and $k_t'' r_d \sim 1.1$, so that $v_{\text{slip}} \sim (I_0/71\text{mA})u_0$. Since Ampere's law implies $-\nabla^2 B_z = \mu_0 \nabla \times \mathbf{J}\delta(z)$, the vorticity $\Omega \equiv \nabla \times \mathbf{J}$ acts as a Coulomb-like point source of magnetic field. The vorticity is plotted for these parameters in Fig. 3.11, where it is concetrated near the edges since the viscous length scale $r_d \ll h$ is small. To make a rough esti-

---

[19] As before, we only consider the "screened" convective force in the above equation, equivalent to including boundary contributions only.

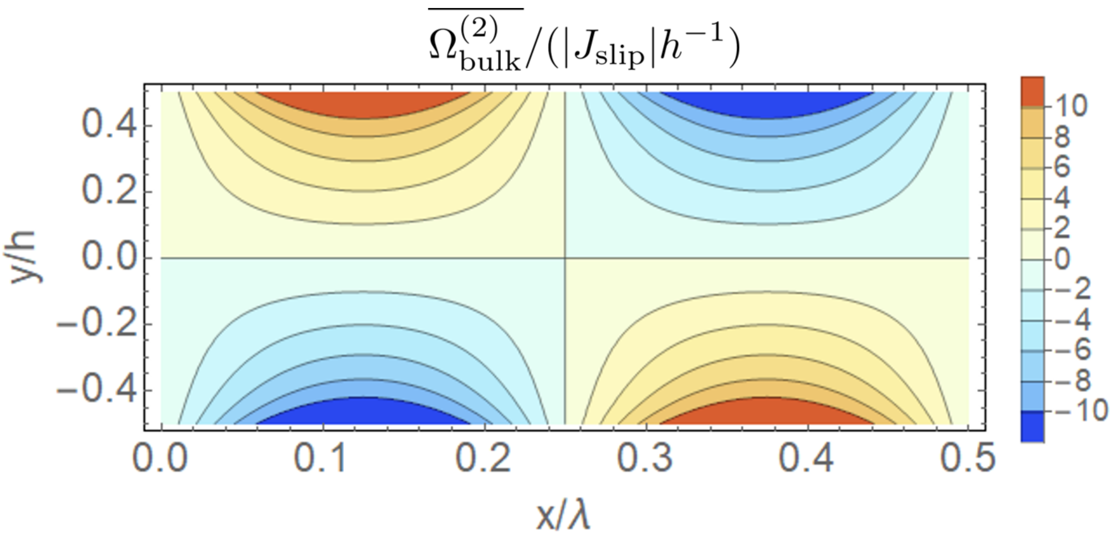

Figure 3.11: A plot of the bulk vorticity distribution $\overline{\Omega^{(2)}_{\text{bulk}}} \equiv \nabla \times \overline{\mathbf{J}^{(2)}_{\text{bulk}}}$ induced by Rayleigh streaming for $h = 5\mu$m and $\omega = 2$ THz with graphene-hBN parameters as in Sec. 3.4.1. The local bulk vorticity corresponds to a Coulomb-like point source of magnetic field due to Ampere's law.

mate of the magnetic field strength, we take $\overline{B_z} \sim \frac{\mu_0}{z} \int_{\text{cell}} \nabla \times \overline{\Omega^{(2)}_{\text{bulk}}}$ at a height z from the sample; we approximate the magnetic field to be sourced by the net circulation in the nearest vortical cell. This gives $B_z \sim \frac{(I_0/9.3\mu\text{A})^2}{z/\mu\text{m}} \times 10^{-10}$T. Therefore, the magnetic fields should be detectable for $I_0 \sim 9.3\mu$A by scanning SQUID magnetometers.

3.4.5 Summary and Outlook

This paper argues for using non-linear DC transport and other manifestations of convective nonlinearity to identify and study electron hydrodynamics. We have laid out three electronic analogs of nonlinear classical phenomena - the Bernoulli effect, Eckart streaming, and Rayleigh streaming - which lead to an experimentally measurable nonlinear I-V characteristic, down-converted DC current, and DC current vortices, respectively (see Fig. 3.7). We have opted to derive and discuss all three effects using the familiar Navier-Stokes formalism, leaving a more complete microscopic treatment for future work. All three effects result from the interplay of the non-dissipative and nonlinear convection force with other dissipative contributions in Navier-Stokes from viscosity and momentum relaxation. As the convection force is a non-dissipative term that couples nearby velocity fields, it seems unlikely that such a term could arise without electron-electron interactions. Therefore, we believe such proposals provide strong evidence for the emergence of a hydrodynamic regime.

It is interesting to note that interactions do not play an explicit role in our results – both convection and momentum relaxation (the dominant form of relaxation) are well understood in the non-interacting limit of the many-electron problem. Instead, strong electron-electron interactions justify the coarse-grained effective description, removing the need to consider the complications of quasi-particle physics. In particular, local equilibration (assumed throughout) is likely to be violated in the limit of weak interactions, requiring a more systematic microscopic treatment. This will be required, for example, before extrapolating our results to low temperatures.

To obtain stronger nonlinear signatures, one would like to make the Reynolds numbers Re_ν and Re_γ as large as possible. Since the viscous length scale $r_d^2 = \nu/\gamma$ is typically smaller than the characteristic lengths in experiment, Re_γ is the limiting factor. In addition to reducing the momentum relaxation rate γ, one could also reduce the density n at fixed current to improve the Reynolds numbers; particles must move more rapidly to maintain the current. Therefore, nonlinear effects should be most prominent in clean, low-density hydrodynamic materials. Our focus has been away from linear response, which is a bedrock foundation of experimental condensed matter physics. Nonlinear phenomena are comparatively more difficult to interpret and tend to be less explored, especially with the purpose of extracting basic information, e.g. where in the phase diagram a given material happens to be. However, since our primary focus has been on *leading* deviations from linear response, we are nonetheless optimistic that identifying electron hydrodynamics from nonlinear behavior is feasible.

In particular, the detection of the AC-generated static current described above would provide strong evidence for the presence of hydrodynamic behavior. Additionally, hydrodynamic nonlinearities should also generate upconverted $2f$ signals, which we leave to future work. This also tantalizingly suggests the possible utility of hydrodynamic materials as a novel platform for creating nonlinear electronic devices.[65, 64] The nonlinear I-V characteristic of the Venturi wedge device clearly displays the onset of instability phenomena far separated from linear response. Such convective instabilities are a known route to classical turbulence[150, 238], i.e. in the absence of momentum relaxation. In the electronic system, where momentum relaxation dominates and viscous length scale r_d is short, we suspect that the behavior may be qualitatively distinct from turbulence. Band-structure modifications to the Navier-Stokes equations, such as a density and flow-dependent hydrodynamic mass[270, 274, 204], and heating effects going beyond our equation-of-state approximations can also give rise to novel nonlinear effects, which we leave to future work. These and other nonlinear phenomena[80, 46, 265] pose a fertile frontier for near-term exploration of electron hydrodynamics.

Acknowledgements We thank Brad Ramshaw, Kin Fai Mak, Jie Shan, Jeevak

Parpia, Peter Armitage, Sriram Ganeshan, Alexander Abanov, Minwoo Jung, and Maytee Chantharayukhonthorn for helpful discussions. A.H. was supported by the National Science Foundation Graduate Research Fellowship under Grant No. DGE-1650441. Both A.H. and E-A.K. are supported by the W.M. Keck Foundation and the U.S. Department of Energy, Office of Basic Energy Sciences, Division of Materials Science and Engineering under Award DE-SC0018946.

3.4.6 Appendix: Oscillatory Hydrodynamic Modes

Here we study the hydrodynamic modes at linear order (without boundary conditions), where the convective term $\mathbf{F}_{\text{conv}}$ is neglected. Because of linearity, the harmonic modes will not mix; the linear-order ansatz $\mathbf{v}^{(1)} \propto e^{i(kx-\omega t)}$ is appropriate. We eliminate the variables p and ϕ in Navier-Stokes (Eq. (3.34)) by using density continuity (Eq. (3.33)) as well as the equations of state (Eq. (3.38) and Eq. (3.39)). The resulting dispersion relation can be separated in longitudinal ($\nabla \times \mathbf{v}^{(1)} = 0$) and transverse ($\nabla \cdot \mathbf{v}^{(1)} = 0$) contributions, which are given by

$$\omega_l^2 = \left(s_0^2 - i\omega_l \left[2\nu + \tilde{\zeta} \right] \right) k_l^2 - i\omega_l \gamma \tag{3.53}$$

$$\omega_t = i\nu k_t^2 - i\gamma \tag{3.54}$$

where $s_0^2 = s_{\text{FL}}^2 + s_{\text{cap}}^2$. The longitudinal dispersion describes a damped sound wave with undamped speed s_0; both pressure and electric forces contribute additively to s_0 as a result of the equations of state. In particular, the electronic contribution relies on backgate screening of the Coulomb interaction to achieve this form. The transverse dispersion describes the propagation of incompressible shear oscillations, whose spatial extent is controlled by the viscous length scale r_d; a finite shear viscosity is necessary for the transfer of momentum into adjacent layers. In contrast to the longitudinal case, the transverse modes do not drive density oscillations and therefore do not generate pressure or electric forces. Therefore, the transverse result is independent of the equations of state, and in particular it does not depend on the presence of a backgate.

We remark that measuring the attenuation of longitudinal and transverse oscillations would provide direct, boundary-independent measures of both shear and bulk viscosity, as opposed to DC flow profiles which require the boundary[195, 266, 147] or inhomogenous current injection profiles[17, 159] to enforce velocity gradients. A careful experimental study of finite-frequency behavior of hydrodynamic materials has yet to be done even at linear order, as far as the authors are aware; in particular, this could provide new cross-checks of previous viscosity measurements. A proposal for for a shear viscometer utilizing oscillatory motion was made in Ref. [275].

3.4.7 Appendix: Electronic Venturi Effect - Treating Viscosity

The full problem, with both finite (kinematic) shear viscosity ν and momentum relaxation γ is challenging. Because viscous effects are controlled by a length-scale $r_d = \sqrt{\frac{\nu}{\gamma}}$, one expects a crossover from viscous-dominated to relaxation-dominated flow as a function of local channel width $h = r\theta_0$. In particular, the resistance of the thin $h \ll r_d$ region should scale as $1/h^2$ (Gurzhi/Poiseuille regime), while the resistance of the $h \gg r_d$ region should scale as $1/h$ (Ohmic regime). Even in the viscous-dominated regime $\gamma \to 0$, a radial flow assumption is inconsistent with the fixed-voltage boundary conditions as described in the main text; angular components of velocity must contribute. Therefore, for finite ν we expect the exact solution of Eq. (3.41) to also break down for strong particle flows in the convergent direction, possibly towards turbulence.

Purely viscous limit - Jeffrey-Hamel flow

In the purely viscous limit $\gamma \to 0$, the leading order flow is a generalization of Poiseuille flow to non-parallel walls. This case also admits an exact solution of the Navier-Stokes equation, known as Jeffrey-Hamel flow.[194, 238, 150] However, as we are only interested in low-velocity flows, a perturbative treatment will suffice. In contrast to fixed-voltage boundary conditions, where one cannot assume purely radial flow and is therefore more difficult to solve, we will assume fixed-current boundary conditions where the θ-dependent radial flow $\mathbf{v} = v_r(\theta)\hat{r}$ is a good ansatz. In addition, we take the divergence-free (incompressible) ansatz $v_r^{(1)} = F(\theta)/r$ for an as yet undetermined function F. Upon substitution and integration of the $\hat{\theta}$ NS equation (Eq. (3.34)), we find that the NS equations give

$$\frac{e}{m}\frac{\partial \phi^{(1)}}{\partial r} = \frac{\nu}{r^3}\frac{d^2 F}{d\theta^2} \tag{3.55}$$

$$\frac{e}{m}\phi^{(1)} = \frac{2\nu}{r^2}F(\theta) + S(r) \tag{3.56}$$

where $S(r)$ is determined from the boundary conditions. Substituting for $\phi^{(1)}$, we find that $S(r) = K\frac{\nu}{2r^2}$ +const for some constant K by separation of variables. The leading order solution is

$$v_r^{(1)} = \frac{I}{ne}\frac{1}{r}\frac{1}{\tan\theta_0 - \theta_0}\left(\frac{\cos 2\theta}{\cos\theta_0} - 1\right) \tag{3.57}$$

$$\frac{e}{m}\phi^{(1)} = \frac{I}{ne}\frac{2\nu}{r^2}\frac{1}{\tan\theta_0 - \theta_0}\frac{\cos 2\theta}{\cos\theta_0} \tag{3.58}$$

Since $v_r^{(2)} = 0$, the pressure gradient must balance the convective force. Therefore, the total potential is given by

$$\frac{e}{m}\phi = \frac{\nu I}{ne}\frac{1}{r^2}\frac{1}{\tan\theta_0 - \theta_0}\left(\frac{\cos 2\theta}{\cos\theta_0} + \frac{I}{2ne\nu}\frac{1}{\tan\theta_0 - \theta_0}\left(\frac{\cos 2\theta}{\cos\theta_0} - 1\right)^2\right) \tag{3.59}$$

We see that $\phi^{(2)}$ is suppressed by a viscous Reynolds number $\mathrm{Re}_\nu \sim \frac{I}{ne\nu}$, as expected. Analogous to the purely Ohmic case discussed in the main text, it is known that divergent Jeffrey-Hamel flow is unstable towards turbulence.[150, 238]

3.4.8 Appendix: Eckart Streaming

In this section, we lay out the mathematical calculation of Sec. 3.4.3 in full detail.

Leading order solution

As mentioned in the main text, we take the ansatz that the leading order solution is described by a longintudinal sound mode with wavevector $k_l = k + i\alpha$ (see Eq. (3.53)). Applying the voltage-fixed boundary conditions and using the density continuity equation (see Eq. (3.33)), we find

$$\phi^{(1)} = V_0 \Re\left[\frac{e^{(ik-\alpha)x} - e^{(ik-\alpha)(2l-x)}}{1 - e^{(ik-\alpha)2l}} e^{-i\omega t}\right] \tag{3.60}$$

$$v_x^{(1)} = u_0 \Re\left[\frac{e^{(ik-\alpha)x} + e^{(ik-\alpha)(2l-x)}}{1 - e^{(ik-\alpha)2l}} e^{-i\,\mathrm{Arg}\,k_l} e^{-i\omega t}\right] \tag{3.61}$$

where $u_0 = \frac{CV_0}{\rho_e^{(0)}}\frac{\omega}{|k_l|}$ and $\Re$ denotes real part. To satisfy the no-slip boundary, we must also include a divergence-free (incompressible) contribution to the flow corresponding to a boundary layer correction, as is done in Sec. 3.4.4. We defer the discussion of this correction to the end of this section, assuming that its contribution is small.

Second-order density continuity equation

We now turn to the time-averaged second-order hydrodynamic equations, where we have assumed $\overline{v_y^{(2)}} = 0$. The density continuity (i.e. current conservation) equation (see Eq. (3.33)) gives

$$\frac{\partial \overline{J_x^{(2)}}}{\partial x} \equiv \frac{\partial}{\partial x}\left[\rho_e^{(0)}\overline{v_x^{(2)}} + \overline{\rho_e^{(1)} v_x^{(1)}}\right] = 0 \tag{3.62}$$

which tells us that $\overline{J_x^{(2)}}(y)$ only depends on y. We remark that it is crucial that $\overline{\mathbf{v}^{(2)}}$ is *not* divergence-free (incompressible); because the "drift" contribution $\overline{\rho_e^{(1)} v_x^{(1)}}$ is non-zero and x-dependent, divergence-ful (compressive) contributions of $v_x^{(2)}$ are necessary to satisfy current conservation.

Second-order Navier-Stokes equation - DC forces and screening

Replacing $\overline{v_x^{(2)}}$ in favor of $\overline{J_x^{(2)}}$ in the Navier-Stokes equation (see Eq. (3.34)), we get

$$\begin{aligned} \frac{m}{e}\left[-\nu\frac{\partial^2}{\partial y^2} + \gamma\right]\overline{J_x^{(2)}} &= \overline{F_{\text{eff}}^{(2)}} && (3.63) \\ -\rho_e^{(0)}\frac{\partial \overline{\phi_{\text{eff}}^{(2)}}}{\partial x} + \overline{F_{\text{conv},x}^{(2)}} + \overline{F_{\text{elec},x}^{(2)}} + \overline{F_{\text{comp},x}^{(2)}} &\equiv \overline{F_{\text{eff}}^{(2)}} && (3.64) \end{aligned}$$

where we used separation of variables with constant $\overline{F_{\text{eff}}}$ to split the momentum equation, and $\rho_e^{(0)}\phi_{\text{eff}}^{(2)} \equiv \rho_e^{(0)}\phi^{(2)} + p^{(2)}$. We remark that Eq. (3.63) is an Ohmic-Poiseuille equation[278] describing steady, divergence-free (incompressible) flow in a rectangular channel, where $\overline{F_{\text{eff}}}$ can be interpreted as the effective force driving the flow. The convective force is defined in Eq. (3.35), while the terms $\overline{F^{(2)}_{\text{elec},x}}$ and $\overline{F^{(2)}_{\text{comp},x}}$ are given by

$$\overline{F^{(2)}_{\text{elec},x}} = \overline{\rho_e^{(1)} \frac{\partial \phi^{(1)}}{\partial x}} \tag{3.65}$$

$$\overline{F^{(2)}_{\text{comp},x}} = (2\nu + \tilde{\zeta}) \left[\overline{\rho^{(1)} \frac{\partial^2 v_x^{(1)}}{\partial x^2}} - \overline{\frac{\partial^2 \left(\rho^{(1)} v_x^{(1)}\right)}{\partial x^2}} \right] \tag{3.66}$$

where in the second line we have used $\frac{\partial}{\partial x}(\overline{\rho^{(0)} v_x^{(2)}}) = -\frac{\partial}{\partial x}(\overline{\rho^{(1)} v_x^{(1)}})$. These provide nonlinear contributions to $\overline{F^{(2)}_{\text{eff}}}$ in addition to the convective force. The first term comes from the backreaction of the electric force; we remark that the presence of this nonlinearity was also noted by Ref. [277]. The second term comes from compressive dissipation. By solving for $\overline{\phi^{(2)}_{\text{eff}}}$ with the zero-voltage boundary conditions, we find the simple result

$$\overline{F_{\text{eff}}} = \frac{1}{l} \int_0^l dx \overline{F^{(2)}_{\text{conv},x}} + \overline{F^{(2)}_{\text{elec},x}} + \overline{F^{(2)}_{\text{comp},x}} \tag{3.67}$$

The action of the effective voltage is to "screen" all the forces via a spatial average, rendering the resulting effective force x-independent. We comment that $\frac{1}{l}\int_0^l dx \overline{F^{(2)}_{\text{elec},x}} = \frac{CV_0^2}{4l}$ has no α or k dependence, and therefore no interference behavior; the value of $\overline{F^{(2)}_{\text{elec},x}}$ is fixed at the ends by the voltage boundary conditions. By dimensional analysis, these contributions are small relative to the convective force when $\frac{s_{\text{cap}}^2 \omega^2}{|k_l|^2} \ll 1$ and $\frac{(2\nu+\tilde{\zeta})|k_l|^2}{\omega} \ll 1$, respectively. For parameters as discussed in the main text, we find that $\frac{s_{\text{cap}}^2 |k_l|^2}{\omega^2} \sim .24$ and $\frac{(2\nu+\tilde{\zeta})|k_l|^2}{\omega} \sim .06$ are small, so that ignoring $\overline{F^{(2)}_{\text{elec},x}}$ and $\overline{F^{(2)}_{\text{comp},x}}$ is valid.

Rectified DC solution

The solution of the Ohmic-Poiseuille equation (Eq. 3.63) is

$$\overline{J_x^{(2)}} = \rho_e^{(0)} u_0 \left[\frac{\overline{F_{\text{eff}}^{(2)}}}{\rho^{(0)} \gamma u_0} \right] \left(1 - \frac{\cosh \frac{y}{r_d}}{\cosh \frac{h}{2r_d}} \right) \tag{3.68}$$

$$\overline{I^{(2)}} = I_0 \left[\frac{\overline{F_{\text{eff}}^{(2)}}}{\rho^{(0)} \gamma u_0} \right] \left(1 - \frac{2r_d}{h} \tanh \frac{h}{2r_d} \right) \tag{3.69}$$

The term in square brackets is suggestively written to resemble momentum-relaxation Reynolds number Re_γ, which is indeed true when the convective force dominates (see Eq. (3.47)). We remark that the convective contribution to $I^{(2)}/I_0$ is largely α-independent (see Eq. (3.46)); in the limit $\alpha l \gg 1$, where the interference term can be neglected, the result is surprisingly α-independent even though α was necessary to generate convective gradients. Instead, the scale of the convective gradient is screened, being controlled by the device length l^{-1}. This α-independence has an analog in Rayleigh streaming, where the shear viscosity ν does not set the scale of the rectified bulk flow even though it was necessary to set up convective forces.

Revisiting Boundary Dissipation (Rayleigh Streaming)

We return to the issue of the no-slip condition and boundary-layer corrections (i.e Rayleigh streaming), which we ignored for the leading order solution. For simplicity, we will neglect contributions from the reflected wave (i.e. $\alpha l \gg 1$). As discussed in Sec. 3.4.4, boundary layer corrections are described by the transverse mode $k_t = k_t' + ik_t''$, decaying exponentially from the wall with length $1/k_t''$. For parameters as discussed in the main text, we find $k_t'' h \sim 8.2 > 1$ so that it is a good assumption that the boundary layer is thin. Therefore, boundary dissipation (i.e. Rayleigh streaming) effects will lead to a non-zero slip velocity for the bulk flow also in the forward x-direction. Upon solving the Ohmic-Poiseuille equation (Eq. (3.63)) with a voltage-fixed boundary condition $\phi(x = l) = 0$ (as in the main text), we get an additional contribution

$$\overline{J^{(2)}_{\text{Rayleigh},x}} = v^{(2)}_{\text{slip}} \frac{\cosh \frac{y}{r_d}}{\cosh \frac{h}{2r_d}} \tag{3.70}$$

$$\overline{I^{(2)}_{\text{Rayleigh}}} = v^{(2)}_{\text{slip}} \tanh \frac{h}{2r_d} \tag{3.71}$$

Therefore, the no-slip boundary (i.e. Rayleigh streaming) only provides a quantitative correction to the DC current. By estimating $v^{(2)}_{\text{slip}} \sim u_0 e^{-1/k_t'' r_d} \frac{I_0 |k_l|}{\rho_e^{(0)} h \gamma}$ from the Rayleigh Reynolds number in Eq. (3.52) with exponential decay arising from the viscous length scale r_d, we find that boundary dissipation contributes additively to the bulk dissipation contribution.

If instead one takes the current-fixed boundary condition $J(x = l) = 0$, a rectified DC voltage will develop as discussed in previous works.[64, 277] However, these previous works did not consider the effect of a no-slip boundary. As a result of no-slip, we expect only a quantitative change to the DC voltage analogous to the previous case. However, a qualitative change occurs in the current flow - a circulating current must develop in the channel as in Sec. 3.4.4. The length and width of the circulation will be set by the device dimensions, as opposed that of Sec. 3.4.4 where the length is set by the wavelength. Surprisingly, the bulk current density flows in an opposite direction to that of the convective force; because convective forces are stronger near the boundary than the bulk, the forward DC flow along x must be near the boundary while the counterflow is in the bulk.[208] This reversed bulk counterflow would be also be interesting evidence for hydrodynamic behavior, though measuring the local current density may prove challenging.

3.4.9 Appendix: Rayleigh Streaming

In this section, we fill out the mathematical details of Sec. 3.4.4.

Leading order solution - Boundary corrections

Recall that we work in the limit $k_t''^{-1} \ll h \ll \lambda$ of a thin boundary layer and long wavelength. In this limit, we can separate the flow into bulk and boundary regions, stitching the flow together at the interface. We first focus on the boundary layer region, concentrating on the lower boundary layer near $y = -h/2$; flow at the upper boundary layer is given by reflection symmetry about $y = 0$. In the lower boundary layer, the leading-order longitudinal (irrotational) and transverse (incompressible) velocity components of $\mathbf{v}^{(1)}_{\text{wall}}$ are

$$v^{(1)}_{\text{wall},l,x} = v^{(1)}_{l,x} = u_0 \sin kx \Re e^{i\omega t} \tag{3.72}$$

$$v^{(1)}_{\text{wall},t,x} = -u_0 \sin kx \Re \left[e^{ik_t y_+} e^{-i\omega t} \right] \tag{3.73}$$

$$v^{(1)}_{\text{wall},t,y} = -u_0 k \cos kx \Re \left[\left(1 - e^{ik_t y_+}\right) \frac{e^{-i\omega t}}{ik_t} \right] \tag{3.74}$$

where $y_+ = y + \frac{h}{2}$ is the distance from the lower wall, we take $k_t'' > 0$, and $\Re$ denotes real part. Although $v^{(1)}_{\text{wall},y}$ is small compared to $v^{(1)}_{\text{wall},x}$, the y-gradients of $v^{(1)}_{\text{wall},y}$ are large and must be included when computing the convective force. The longitudinal contribution $v^{(1)}_{\text{wall},l,x}$ is inherited from the longitudinal ansatz of Eq. (3.48). We remark that we have not assumed that $v^{(1)}_{\text{wall}}$ is divergence-free (incompressible) unlike classic discussions[225, 150, 234]; that the divergence-free (incompressible) ansatz is not correct has been previously pointed out,[296, 208], though it has no consequence in the limit $\gamma \to 0$. In the limit $k_t'' y_+ \gg 1$, we find that $v_{\text{wall},x}$ returns to our longitudinal ansatz $v^{(1)}_{l,x}$ as the boundary-layer corrections exponentially vanish. However, $v^{(1)}_{\text{wall},t,y}$ is non-zero in this limit and requires correction in the bulk. We will not concern ourselves with the bulk corrections to $v_y^{(1)}$, as they are small and do not contribute substantially to the convective force.[208]

Therefore, the convective force in the bulk and boundary layers is

$$\begin{aligned}\overline{F^{(2)}_{\text{conv, bulk},x}} &= \rho^{(0)} u_0^2 k \frac{1}{4} \sin 2kx(-2) && (3.75)\\ \overline{F^{(2)}_{\text{conv, wall},x}} &= \rho^{(0)} u_0^2 k \frac{1}{4} \sin 2kx \left[-2 + (3 + e^{2i\theta_t}) e^{ik_t y_+} - 2e^{-2k_t'' y_+} \cos^2 \theta_t\right] && (3.76)\end{aligned}$$

where $\theta_t \equiv \operatorname{Arg} k_t$.

Second-order Navier-Stokes

We now study the DC second-order flow. We begin by noting that the assumption $k_t''^{-1} \ll h \ll \lambda$ implies that $v_y \ll v_x$, i.e. flow is primarily along x because the channel is thin. By using the NS equations (Eq. (3.34)), this implies that the effective voltage $\phi_{\text{eff}} = \phi + \frac{1}{\rho_e^{(0)}} p$ satisfies $\frac{\partial \phi_{\text{eff}}}{\partial y} \ll \frac{\partial \phi_{\text{eff}}}{\partial x}$, i.e. voltage gradients (and density gradients) are also primarily along x.

Next, we simplify the NS equation (Eq. (3.34)). First, we note that the back-reactive electric force $\mathbf{F}^{(2)}_{\text{elec}} \equiv \overline{\rho_e^{(1)} \nabla \phi^{(1)}} = 0$. We will also assume that compressional dissipation $\mathbf{F}_{\text{comp}} \equiv (2\nu + \tilde{\zeta})\rho \nabla\nabla \cdot \mathbf{v}$ is negligible, which is consistent with our assumption that the longitudinal attenuation α is small. Finally, for simplicity we neglect the additional term $\overline{\nu \rho_e^{(1)} \nabla \times \nabla \times \mathbf{v}^{(1)}}$ as is done in classical treatments of Rayleigh streaming;[225, 150, 208, 296, 234] this term depends on the density dependence of ν, where classical works assumed that the dynamic viscosity $\mu \equiv \rho\nu$ is constant. Therefore, the NS equation becomes

$$\frac{m}{e}\left[-\nu \frac{\partial^2}{\partial y^2} + \gamma\right] \overline{J_x^{(2)}} = \overline{F^{(2)}_{\text{conv},x}} - \rho_e^{(0)} \frac{\partial \overline{\phi^{(2)}_{\text{eff}}}}{\partial x} \tag{3.77}$$

where we have used $k_t''^{-1} \ll h \ll \lambda$ to drop the x-derivatives (cf. Eq. (3.63) and Eq. (3.64)). Note that this form is equivalent to assuming that $\mathbf{v}^{(2)}$ is divergence-free (incompressible).

Since the convective force is only x-dependent in the bulk, we must have

$$\rho_e^{(0)} \frac{\partial \overline{\phi_{\text{eff}}^{(2)}}}{\partial x} = \overline{F_{\text{conv,bulk},x}} \tag{3.78}$$

upon imposing $\overline{I} = 0$ (i.e. $J_x(x = 0) = 0$). More concretely, the boundary conditions for $\overline{v_x^{(2)}}(y = \pm h/2)$ will fix the y-dependent homogeneous solutions of Eq. (3.77), leaving $\overline{\phi_{\text{eff}}^{(2)}}$ to enforce $\overline{I^{(2)}} = 0$. Since $\frac{\partial \overline{\phi_{\text{eff}}^{(2)}}}{\partial y}$ is small, this expression for $\phi_{\text{eff}}^{(2)}$ is also valid in the boundary layer. Therefore, after "screening" from the effective voltage, the resultant force is only non-zero in the boundary layer.

Second-order boundary layer solution

We first solve Eq. (3.77) in the boundary layer, where the "screened" convective force is not negligible. Assuming $r_d \ll h$, the solution for the lower boundary layer is

$$\overline{J^{(2)}_{\text{wall},x}} = \rho_e^{(0)} u_0 \sin 2kx \, \Re\left[\frac{v_{\text{slip}}}{u_0} - \frac{u_0 k}{4\gamma}\left(-\frac{(3 + e^{2i\theta_t})e^{ik_t y_+}}{k_t^2 r_d^2 + 1} - \frac{(2\cos^2\theta_t)e^{-2k_t'' y_+}}{4k_t''^2 r_d^2 - 1}\right)\right] \tag{3.79}$$

$$v_{\text{slip}}^{(2)} = \frac{u_0^2 k}{4\gamma} e^{-\frac{y_+}{r_d}} \Re\left[- \frac{(3 + e^{2i\theta_t})(i\tilde{\omega} + 2)}{4 + \tilde{\omega}^2} - \frac{2\cos^2\theta_t}{-3 + 2\sqrt{1 + \tilde{\omega}^2}}\right] \tag{3.80}$$

where $v_{\text{slip}}^{(2)}$ enforces the no-slip boundary conditions, and we have rewritten $k_t^2 r_d^2$ in terms of $\tilde{\omega} = \omega/\gamma$ using Eq. 3.54. Away from the wall where the convective force vanishes, the velocity $v_{\text{wall},x}^{(2)} \to v_{\text{slip}}^{(2)} \sin 2kx$ achieves a non-zero limiting value if $k_t'' r_d$ is sufficiently large; the boundary layer sets up a slip boundary for the bulk flow. In the main text, we (optimistically) approximate the size of the boundary to be $1/k_t''$ so that we evaluate $v_{\text{slip}}^{(2)}$ at $y_+/r_d = 1/(k_t'' r_d)$. The resulting bulk flow is solved from Eq. (3.77) with a vanishing right-hand side and with the slip boundary generated from the boundary layer; the solution is given in the main text [Eq. (3.50) and (3.51)].

We make three remarks on v_{slip}. First, in the limit $\nu \to 0$, the flow becomes increasingly singular at the walls so the boundary layer will no longer by described by hydrodynamics. Second is the surprising fact that ν is largely ν-independent. In the limit $\gamma \to 0$, we recover the classical result $v_{\text{slip}} = -\frac{3u_0}{8}\frac{u_0 k}{\omega}$ which is ν-independent, despite the necessity of ν to set up convective gradients. Instead of the viscous Reynolds number Re_ν, the slip velocity is controlled by the Mach number $u_0\omega/k$. This was first noted by Rayleigh in the classical situation.[225] Finally, v_{slip} has a resonance at $\omega = \frac{\sqrt{5}}{2}\gamma$ corresponding to $-4k_t''^2 r_d^2 + 1 = 0$. We leave further study of this interesting convective instability to future work; for this paper, we only work in the limit $v_{\text{slip}} \ll u_0$ where perturbation theory is valid.

CHAPTER 4

CHIRAL ANOMALY AND WEYL SEMIMETALS

The recently discovered (3D) Weyl semimetal [310] has been the subject of intense interest as a newly realizable class of gapless topological matter. Though it is a 3D generalization of the 2D Dirac semimetal as found in graphene, the odd space dimensionality gives rise to distinctive phenomena. Here, we briefly review some basic aspects of Weyl semimetals.

The low-energy effective description of a single Weyl point is given by

$$H_\tau = \tau v_F \sigma \cdot \mathbf{k} \tag{4.1}$$

where $\tau = \pm 1$ is the chirality, v_F is the Fermi velocity, and σ are the Pauli matrices. We emphasize that $\mathbf{k} = (k_x, k_y, k_z)$ is in 3D, as opposed to the 2D Dirac semimetal, which gives rise to new topological effects. For instance, local perturbations of H_τ cannot remove the zero-energy Weyl point since the Pauli matrices exhaust the space of 2×2 Hamiltonians (up to chemical potential shifts $\mu\mathbb{I}$). In particular, applying a magnetic field $\mathbf{B} \cdot \sigma$ will not gap the system unlike in a Dirac semimetal. This protection of the gap is actually topological; Weyl points are monopoles of Berry curvature with sign determined by the chirality τ [311] and as a result are required to come in pairs [205].

The topological effect of interest to us is the famous chiral anomaly. With a pair of Weyl points $H_+ + H_-$, one would expect that chiral symmetry is present. However, when one quantizes this theory with an electromagnetic gauge field, it turns out that the quantization necessarily breaks the classically-present chiral symmetry (see [213, 262] for a review). Observing the resulting chiral symmetry breaking has been the subject of intense efforts, but definitively extracting the chiral anomaly contribution has proven difficult. In what follows, we reexamine IR reflectance approaches previously proposed [260, 235, 236] to probe the chiral anomaly. As opposed to previous works, we argue that IR reflectance signatures of the chiral anomaly can be found even in mirror-symmetric Weyl semimetals; this has been recently experimentally confirmed in the mirror-symmetric Weyl semimetal NbAs [316].

4.1 Optical signatures of the chiral anomaly in mirror-symmetric Weyl semimetals

This section is adapted from a PRB Rapid Communications paper [120] with Yi Zhang and Eun-Ah Kim. As opposed to the other works on interacting phases, this is on a non-interacting topological phase.

The chiral anomaly is a characteristic phenomenon of Weyl fermions, which has condensed matter realizations in Weyl semimetals. Efforts to observe smoking gun signatures of the chiral anomaly in Weyl semimetals have mostly focused on a negative longitudinal magnetoresistance in electronic transport. Unfortunately, disentangling the chiral anomaly contribution in transport or optical measurements has proven non-trivial. Recent works have proposed an alternative approach of probing pseudoscalar phonon dynamics for signatures of the chiral anomaly in non-mirror-symmetric crystals. Here, we show that such phonon signatures can be extended to scalar phonon modes and mirror-symmetric crystals, broadening the pool of candidate materials. We show that the presence of the background magnetic field can break mirror symmetry strongly enough to yield observable signatures of the chiral anomaly. Specifically for mirror-symmetric Weyl semimetals such as TaAs and NbAs, including the Zeeman interaction at $|\mathbf{B}| \approx 10$T, we predict that an IR reflectivity peak will develop with an $\mathbf{E}_{\text{IR}} \cdot \mathbf{B}$ dependence.

4.1.1 Introduction

The Weyl semimetal has been generating excitement as a new experimentally realizable class of topological materials in three dimensions.[311, 12] The materials are so named due to the existence of Weyl points in the momentum space, where two non-degenerate bands intersect and disperse linearly. Weyl points are monopoles of Berry curvature and characterized by their chirality, a topological invariant describing the parallel/anti-parallel (right/left-handed) locking between their momentum and spin or pseudo-spin. One of the exciting phenomena predicted in the Weyl semimetal is the condensed matter realization of the chiral anomaly: the chiral charge - the population difference between the left and right-handed Weyl fermions - is not conserved after quantization.

The non-conservation of chiral charge means that, under the application of parallel $\mathbf{E}$ and $\mathbf{B}$ fields, particles will be pumped between left-handed and right-handed Weyl points. Therefore, in the presence of a chiral anomaly, one can think of the $\mathbf{B}$-field as creating a topologically protected channel of charge between left and right-handed Weyl points, whose conductivity and direction are controlled by the magnetic field. The presence of this channel leads to the so-called chiral magnetic effect,[205, 140, 79, 258, 326] where a current will develop along the magnetic field in the presence of a chemical potential difference between Weyl nodes with opposite chirality. In order to balance the charge transfer, scattering between Weyl nodes is required; this scattering process is rare because the Weyl nodes are generically well-separated, so this conduction channel has high conductivity. In the limit of large $\mathbf{B}$, intra-node scattering is suppressed within each chiral Landau level, consisting only of a single linear branch. The inter-node scattering time, which is longer than the $\mathbf{B} = 0$ intra-node scattering time, then controls the conductivity in this limit. Therefore, the chiral anomaly leads to a $\mathbf{B}$-field dependent enhancement in the conductivity.[205] Negative longitudinal magnetoresistance was therefore proposed as a signature of the chiral anomaly in Weyl semimetals.[255, 26, 27]

Indeed, negative magnetoresistance has been observed in a number of Weyl semimetals;[171, 112, 305, 320, 164, 166, 103, 148, 206, 319, 170] however, negative magnetoresistance was not unique to Weyl semimetals and could potentially be caused by other effects.[142, 102, 91, 298, 53, 11] For instance, negative magnetoresistance was also measured in the non-Weyl semimetal materials $PdCoO_2$, $PtCoO_2$, $SrRuO_4$, and Bi_2Se_3.[141, 298] To complicate matters further, the point contacts used for magnetoresistance measurements were susceptible to current jetting, where the current is focused by a magnetic field, artificially enhancing the measured conductivity and potentially overwhelming the chiral anomaly signature.[63, 13] For these reasons, the chiral anomaly interpretation of electronic transport results has been controversial.

In search of sharper signatures of the chiral anomaly and Weyl semimetals, a number of proposals have been put forth.[186, 210, 324, 227, 174, 122, 92, 50, 51, 215, 261, 128, 129] In this paper, we will be particularly interested in phonon-induced optical signatures. Through an axial (chirality-dependent) electron-phonon coupling, a phonon can induce a dynamical chemical potential difference between Weyl points with opposite chirality, which in turn gives rise to a dynamical realization of the chiral anomaly. Recent works have found that this can result in anomalous optical features in IR and Raman spectroscopy.[14, 260, 235, 236] However, based on symmetry considerations, it was argued that a phonon mode in a 1D representation can only have an axial coupling if it is pseudoscalar (changes sign under improper rotations).[260] As the allowed phonon modes are constrained by the crystal symmetry, pseudoscalar phonons only exist in crystals where the mirror symmetries are sufficiently broken.[260] Therefore, previous works ruled out such chiral-anomaly induced optical phenomena in Weyl semimetal candidates with many mirror planes, such as TaAs and NbAs.[260, 235]

We claim, by contrast, that such optical signatures of the chiral anomaly can occur in all mirror-symmetric crystals for both scalar and pseudoscalar phonons, due to the role of a necessary magnetic field. Previous analyses[260, 235] assumed the Weyl points to be locally identical (up to chirality) and the linear dispersion to be isotropic. If one breaks these assumptions and allows the Fermi velocities to differ, a scalar phonon can also develop an effective, nonvanishing axial coupling. Such a difference in Fermi velocities can be induced by the magnetic field necessarily present in the experiments. Because of this, it is important to consider the effect of magnetic field on symmetries neglected in previous analyses.

The magnetic field, a pseudovector, changes sign under improper rotation; under the reflection $x \to -x$, the magnetic field transforms as $(B_x, B_y, B_z) \to (B_x, -B_y, -B_z)$. Therefore, it breaks all mirror symmetries except for the mirror plane normal to it, if such a mirror plane exists. The Zeeman effect and the Landau level quantization are examples of such mirror-symmetry-breaking effects. In the presence of at most one mirror plane, an effective pseudoscalar phonon is allowed to exist, so the axial component of the phonon coupling for this mode is generically non-zero. Since optical signatures of the chiral anomaly require the presence of a static magnetic field, no symmetry restrictions on Weyl semimetals are required to see this signature. In this paper, by considering a suitable microscopic model, we show that the Zeeman effect and the Landau level quantization can result in substantial Fermi velocity asymmetry that can drive detectable optical signatures of chiral anomaly.

The outline of the paper is as follows: In Section II, we introduce a tight-binding model Hamiltonian in the same symmetry class as TaAs and NbAs and analyze the effect of mirror-symmetry-breaking Zeeman effect and Landau level quantization on the fermion dynamics. In Section III, we discuss the electron-phonon coupling and its symmetry constraints for optical signatures. In Section IV, given the magnetic field's mirror-asymmetric effect on the Fermi velocities, we estimate the strength and visibility of the IR reflectivity signal corresponding to the dynamically-driven chiral anomaly. Finally, we conclude our results and discuss their distinction from multiferroic materials in section V.

4.1.2 Tight-binding model of 3D Weyl fermions with magnetic field

To quantitatively analyze the symmetry-breaking effect of the magnetic field, we consider the following 3D electronic tight-binding model with crystal symmetries identical to the Weyl semimetals TaAs and NbAs:[224]

$$H_0 = t \sum_{\langle ij \rangle, s} c_{is}^{\dagger} c_{js} + \sum_{i,s} \Delta_i c_{is}^{\dagger} c_{is} + i\lambda \sum_{\langle\langle ik \rangle\rangle, ss'} c_{is}^{\dagger} c_{ks'} \sum_j \mathbf{d}_{ijk} \cdot \boldsymbol{\sigma}_{ss'} \tag{4.2}$$

where t is the nearest neighbor hopping, $\Delta_i = \pm\Delta$ is a staggered potential whose sign depends on the sublattice being a Ta(Nb) or As site, and λ is the amplitude of the spin-orbit interaction between next-nearest neighbors. $s = \uparrow, \downarrow$ denotes spin, and $\boldsymbol{\sigma}$ are the Pauli matrices. The vector $\mathbf{d}_{ijk} = \mathbf{d}_{ij} \times \mathbf{d}_{jk}$, where j is an intermediate site between i and k, and $\mathbf{d}_{ij}$ is the displacement vector from i to j.

In the absence of the magnetic field, the model is time-reversal invariant and breaks inversion symmetry. Two mirror planes exist in the xz and yz directions. For large values of λ, the model is a 3D topological insulator; for large values of Δ, on the other hand, the model is a normal insulator. In between, a time-reversal-invariant Weyl semimetal exists in a finite phase space, for instance, at $t = 500$meV, $\Delta = 350$meV, $\lambda = 100$meV; we will use these parameters throughout this paper. Comparing this model at $B = 0$T to DFT calculations of the TaAs band structure[112, 311, 187] and the measured Fermi velocities around the Weyl points,[224] we find qualitative agreement. More details on the low-energy electronic properties of the model can be found in the Appendix.

In the presence of a magnetic field, we generally expect the Hamiltonian to change in two ways. One modification is the Zeeman effect, describing the coupling of the electron spin to the magnetic field given by

$$H_z = g\mu_B \sum_{iss'} c_{is}^{\dagger} c_{is'} \mathbf{B} \cdot \boldsymbol{\sigma}_{ss'} \tag{4.3}$$

with g the g-factor, μ_B the Bohr magneton, and $\mathbf{B}$ the magnetic field. We estimate a large g-factor $g \approx 50$ for typical topological Weyl semimetal materials with strong spin-orbit coupling, such as TaAs and NbAs, by analogy to measurements in related materials.[252, 110] The inclusion of the Zeeman effect at finite $\mathbf{B}$ breaks the time-reversal symmetry and all mirror plane symmetries except the mirror plane normal to the magnetic field, if it exists.

The other modification, which we refer to as the Landau level quantization, comes from the minimal coupling of the electromagnetic vector potential to the electron current. To incorporate this effect, we perform the Peierls substitution on the kinetic term and the spin-orbit interaction:

$$\begin{aligned} &c_{is}^{\dagger}c_{js} \rightarrow e^{iA_{ij}}c_{is}^{\dagger}c_{js} \\ &c_{is}^{\dagger}c_{ks'} \rightarrow e^{iA_{ik}}c_{is}^{\dagger}c_{ks'} \end{aligned} \tag{4.4}$$

where A_{ij} and A_{ik} are the electromagnetic vector potentials (integrated) from i to j and from i to k, respectively. We've chosen to set the electron charge $e = 1$ (and $\hbar = 1$, as usual). We also use the lattice constants of TaAs to convert the magnetic flux into the magnetic field in unit of Tesla. As is well known, minimal coupling to a magnetic field leads to a quantization of the electronic dispersion into separate Landau bands. In particular, the dispersion normal to the magnetic field becomes quantized, so the dispersion becomes one-dimensional with bandgap controlled by the magnetic field. Similar to the Zeeman effect, Landau level quantization also breaks time-reversal symmetry and all mirror plane symmetries except the (possibly existent) mirror plane normal to the magnetic field.

Let us focus on the impact of magnetic-field-induced mirror symmetry breaking on the low-energy dispersion of the Weyl nodes near the $k_z \approx 0$ plane in the Brillouin zone. For clarity, we will consider the effects of the Zeeman effect (Eq. 4.2 and 4.3) and the Landau level quantization (Eq. 4.2 and 4.4) sep-

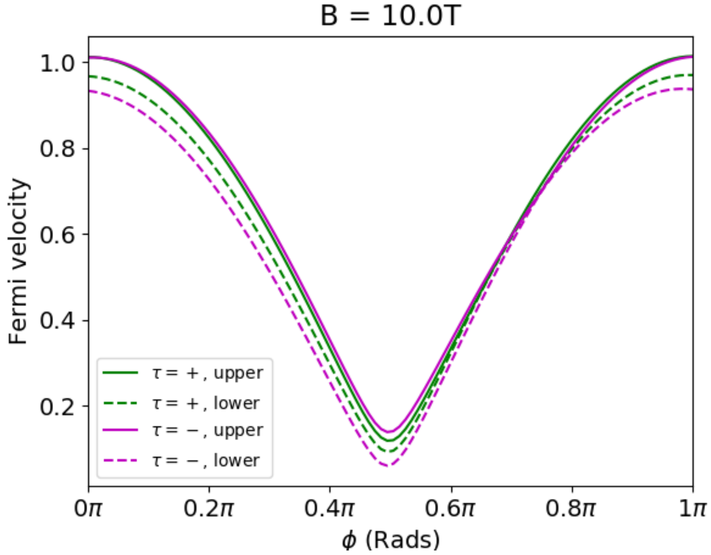

Figure 4.1: The magnitude of the Fermi velocity as a function of the azimuthal angle ϕ in the $k_x - k_y$ plane for a pair of Weyl points, denoted in green and magenta, originally related by the mirror symmetry at $|\mathbf{B}| = 0T$. The solid and dashed lines denote the upper and lower branches of the Weyl dispersion, respectively. For a magnetic field $|\mathbf{B}| \sim 10$T in the $\hat{x}/2 + \sqrt{3}\hat{y}/2$ direction, the differences developed between these curves demonstrate the mirror-symmetry breaking of the Zeeman effect.

arately.

For the Zeeman interaction, we diagonalize the Hamiltonian $H_0 + H_z$ in $\vec{k}$ space as Eq. 4.3 preserves lattice translation symmetries. We find that even with a magnetic field as large as $|\mathbf{B}| = 10T$, the Weyl nodes only displace a scale $\sim 0.1\%$ of the Brillouin zone (see the Appendix). Therefore, the impact of the Zeeman effect due to the k-dependence of the electron-phonon coupling is likely small, and we neglect this contribution. On the other hand, the symmetry breaking from the magnetic field has a more prominent effect on the Fermi velocities, especially in topological semimetal models and materials with strong spin-orbit interactions, so that the Zeeman spin-splitting effect strongly impacts electron velocity. In Fig. 4.1, we see that the Fermi velocities of the Weyl points

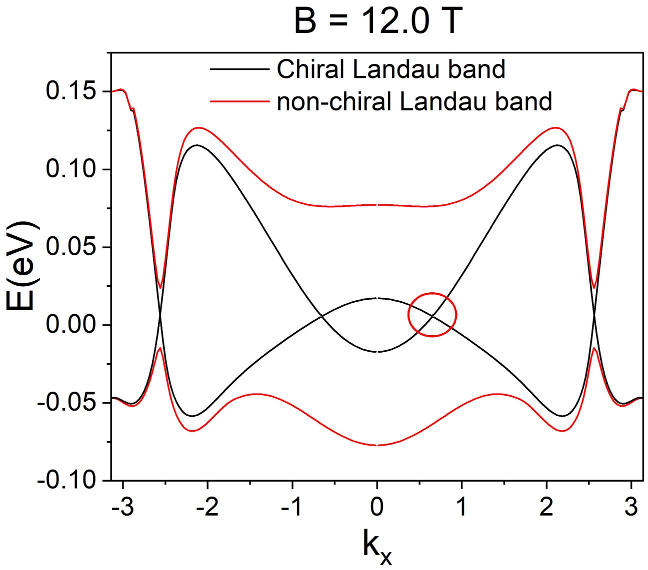

Figure 4.2: The k_x dispersion of the four Landau bands closest to the Weyl node energy in the presence of the Landau level quantization of a magnetic field $|\mathbf{B}| \sim 12$T in the $\hat{x}$ direction. The eight gapless linear branches are the chiral Landau bands descending from the eight Weyl nodes, respectively, and responsible for the electronic properties at low energy. A finite (indirect) gap separates the other Landau bands. As an example, the chiral Landau bands in the red circle as the descendants of a pair of Weyl nodes are illustrated in Fig. 4.3.

connected via mirror symmetries initially identical at zero field clearly become different when a magnetic field is turned on.

For Landau level quantization, we focus our attention on the linear, chiral Landau bands. We specialize to $\mathbf{B} = B\hat{x}$ for simplicity and introduce the electromagnetic vector potential via Eq. (4.4). Consequently, the dispersion along k_y and k_z becomes quenched, and the discrete Landau bands disperse only along k_x, which remains as a good quantum number. Using exact diagonalization for the Hamiltonian within a magnetic unit cell, we obtain the one-dimensional k_x dispersion - see Fig. 4.2 for an example at $|\mathbf{B}| \sim 12$T. It is important to note that the branch of the dispersion that evolves into the chiral Landau band depends on the chirality of each Weyl node,[205] schematically shown in Fig. 4.3. There-

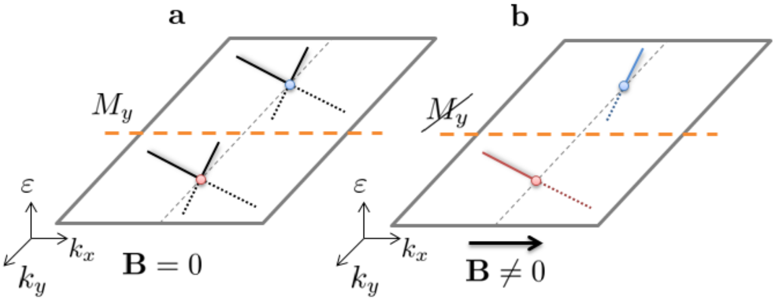

Figure 4.3: (a) A schematic plot of the k_x dispersion of a pair of Weyl nodes of opposite chirality (labeled with blue and red) related by a M_y mirror symmetry at zero field, and (b) the chiral and anti-chiral Landau bands selected out in the presence of a magnetic field along the x-direction. Since the chiral and anti-chiral Landau levels can generically have distinct Fermi velocities, they explicitly break the M_y symmetries and contribute to an effective axial electron-phonon coupling.

fore, despite the identical zero-field dispersion of a pair of mirror-symmetric Weyl nodes, the differing chiralities ensure that the chiral and anti-chiral Landau bands selected out by the magnetic field generally have distinct Fermi velocities. Interestingly, such a difference between the Fermi velocity of the chiral and anti-chiral Landau bands is a form of mirror-symmetry breaking, depending on the anisotropy of the original Weyl fermions instead of the strength of the magnetic field. The remainder of the Landau bands will be gapped by the magnetic field, so that the chiral branches dominate near the Fermi energy, see Fig. 4.2. As a result, chiral anomaly effects may become visible if the cyclotron energy of $\mathbf{B}$ is sufficiently large and the Fermi energy sufficiently close to the Weyl node.

In summary, the mirror symmetry connecting a pair of Weyl nodes is explicitly broken by a magnetic field. The magnetic-field-induced difference between the Weyl nodes' Fermi velocities, induced by the Zeeman effect and the chiral selectivity of Landau level quantization, are physical manifestations of the broken mirror symmetry. We will discuss its phenomenological consequences for the dynamical chiral anomaly in Sec. IV.

4.1.3 Electron-phonon Coupling and Symmetry Constraints

To understand the impact of the Weyl fermion dynamics and its symmetry constraints on the electron-phonon coupling, we consider the interaction between phonons and a pair of Weyl nodes with opposite chirality $\tau = \pm 1$:

$$\mathcal{H}_{\text{ep}} = \sum_{\mathbf{kq}} \sum_{\sigma\sigma'\tau} \left(\sum_{\lambda} u^{\lambda}_{\sigma\sigma',\tau}(\mathbf{q}) v_{\mathbf{q}\lambda} \right) c^{\dagger}_{\mathbf{k}\sigma\tau} c_{\mathbf{k}-\mathbf{q}\sigma'\tau} \tag{4.5}$$

where $v_{\mathbf{q}\lambda}$ is the phonon displacement operator in mode λ at momentum $\mathbf{q}$ and σ, σ' describe the pseudospin of the electrons. We have neglected inter-node electron scattering, since it requires a large momentum transfer q to connect the well-separated Weyl nodes in the momentum space. Decomposing the electron-phonon coupling into its irreducible representations,

$$u^{\lambda}_{\sigma\sigma',\tau} = u^{\lambda}_{00}\delta_{\sigma\sigma'} + \mathbf{u}^{\lambda}_{0} \cdot \boldsymbol{\sigma}_{\sigma\sigma'} + \tau(u^{\lambda}_{0z}\delta_{\sigma\sigma'} + \mathbf{u}^{\lambda}_{z} \cdot \boldsymbol{\sigma}_{\sigma\sigma'}) \tag{4.6}$$

The two latter terms correspond to the (chirality-dependent) axial coupling responsible for the chiral anomaly. We focus on the axial coupling constant u^{λ}_{0z} since the contribution from $\mathbf{u}^{\lambda}_{z}$ is suppressed by a factor of v_{τ}/c, as we will see later.

The symmetries of the system impose constraints on the electron-phonon coupling. In particular, $\mathbf{u}^{\lambda}_{z}$ vanishes in the presence of time-reversal symmetry, while u^{λ}_{0z} vanishes in the presence of two non-coplanar mirror-symmetry planes.[260, 235, 236] Therefore, it seems that the mirror symmetry in the crystal should be sufficiently broken to host a nontrivial phonon signature as a result of the chiral anomaly. We find, on the other hand, that the imposed magnetic field can break the mirror symmetries sufficiently for the signatures to appear in a much broader pool of Weyl semimetal candidates.

For our tight-binding model in Eq. (4.2), we expect the magnetic-field-induced changes to $u^{\lambda}_{\sigma\sigma',\tau}$ due to the small displacements of the Weyl point locations to be sub-dominant; instead, the key ingredient that leads to interesting phonon behavior is the induced change in Fermi velocity, which we discuss next.

4.1.4 Estimating the Effect of Magnetic field on the Fermi Velocity

In this section, we study the chiral anomaly contribution to the phonon dynamics by integrating out the electronic degrees of freedom. The low-energy effective theory of our tight-binding model, described by Eqs. (4.2-4.4), can be captured by the following single-particle Hamiltonian

$$\mathcal{H}_{\tau} = v_{\tau}(\hat{k})\tau\boldsymbol{\sigma}\cdot(-i\boldsymbol{\nabla}+e\mathbf{A}) - eA_0 \tag{4.7}$$

which describes a Weyl point with chirality $\tau = \pm 1$ and anisotropic Fermi velocity $v_{\tau}(\hat{k})$. The terms $A_0, \mathbf{A}$ are the electromagnetic vector potential.[1] Because phonons do not couple electrons between Weyl nodes, the integration over electronic degrees of freedom factorizes between Weyl points (at the leading order); we can restrict our attention to a single pair.

For a pair of Weyl nodes with isotropic and identical Fermi velocity $v_{\tau}(\hat{k}) = v_F$, on integrating out the fermions one finds that the chiral anomaly contributes

---

[1] We assume that the energy separation of the Weyl nodes is zero; the momentum separation is large and presumably irrelevant in the low-energy theory, so it has been dropped.

to a mode-effective phonon charge $\delta\mathbf{Q}$, and hence to a dielectric susceptibility χ:[235]

$$\delta\mathbf{Q}_{-\mathbf{q}\lambda}(-q_0) = i\frac{e^2\mathcal{V}_c\sqrt{N}}{\pi^2\hbar^2}\frac{\mathbf{B}}{q^2}(q_0u^\lambda_{0z} - v_F\mathbf{q}\cdot\mathbf{u}^\lambda_0) \tag{4.8}$$

$$\chi^\lambda_{jj'}(q_0,\mathbf{q}) = \frac{1}{M\mathcal{V}_c}\frac{\delta Q_{\mathbf{q}\lambda j}\delta Q_{\mathbf{q}\lambda j'}}{\omega^2_{\mathbf{q}\lambda} + i\kappa u^\lambda_{00}\mathbf{q}\cdot\delta\mathbf{Q}_{\mathbf{q}\lambda} - q_0^2} \tag{4.9}$$

where $(q_0, \mathbf{q})$ is the frequency-momentum vector of the phonon, $\mathcal{V}_c$ is the unit cell volume, M is the total mass of ions in the unit cell, N is the number of unit cells, and $\mathbf{B}$ is the static background magnetic field. $\kappa = \sqrt{N}/(Me)$, $q^2 = q_0^2 - v_F^2\mathbf{q}^2$, and $\omega_{\mathbf{q}\lambda}$ is the bare phonon dispersion of mode λ. Since $q_0 = c\mathbf{q}$ for light, the $\mathbf{u}^\lambda_0$ term is suppressed by v_F/c. When the IR light is on resonance with the phonon driving the chiral anomaly, the dielectric constant diverges and the reflectivity develops a peak with a form factor $\mathbf{E}_{\text{IR}}\cdot\mathbf{B}$. Also, such chiral anomaly contribution to $\chi^\lambda_{jj'}$ clearly depends on a non-zero axial coupling constant u^λ_{0z}.

In comparison, our generalized model in Eq. (4.7) takes into account the anisotropic Fermi velocity around a Weyl node as well as the different Fermi velocities between the Weyl nodes. We consider a totally-symmetric scalar phonon mode at zero field, where all components of the electron-phonon coupling are 0 except u^λ_{00}. For simplicity, this system can be mapped back to the isotropic case by rescaling the fermions by $v_\tau c^\dagger_\tau c_\tau \to v_F c^\dagger_\tau c_\tau$, which changes the electron-phonon coupling and induces components in the non-identity piece:

$$u^\lambda_{00} \to \frac{v_F}{2}\left(\frac{1}{v_+} + \frac{1}{v_-}\right)u^\lambda_{00} \tag{4.10}$$

$$u^\lambda_{0z} \to \frac{v_F}{2}\left(\frac{1}{v_+} - \frac{1}{v_-}\right)u^\lambda_{00} \tag{4.11}$$

The rescaling of the fermions also changes A_0, but it does not affect the phonon charge and dielectric susceptibility in Eqs. (4.8) and (4.9) so we neglect the change. As is manifest after rescaling, the difference of the Fermi velocity is

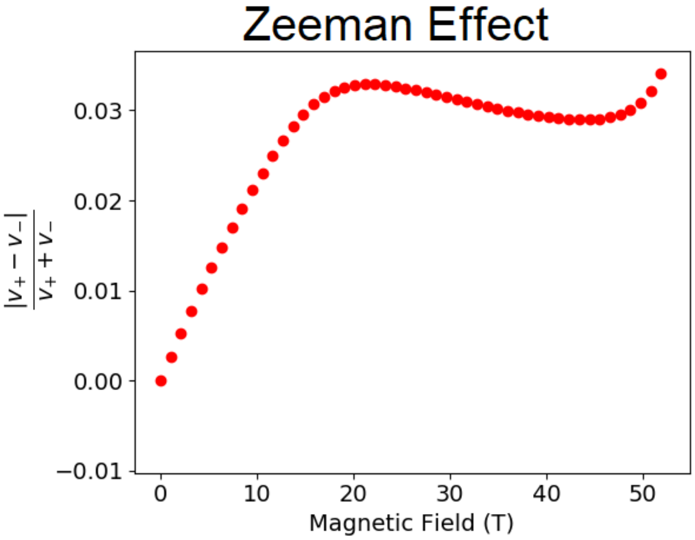

Figure 4.4: The relative difference (induced by the Zeeman effect) between the Fermi velocities of a pair of Weyl nodes as a function of the strength of the magnetic field $\mathbf{B}$ in the $\hat{x}/2 + \sqrt{3}\hat{y}/2$ direction. The ratio is averaged over all directions. Assuming that u^λ_{00} is the only non-zero electron-phonon coupling component at $\mathbf{B} = 0$, this quantity measures the ratio $u^\lambda_{0z}/u^\lambda_{00}$ generated by the inclusion of the magnetic field and the broken symmetry between v_+ and v_- (see Eqs. (4.10) and (4.11)).

equivalent to an axial component u^λ_{0z} in the isotropic setting since $u^\lambda_{0z}/u^\lambda_{00} = |v_+ - v_-|/(v_+ + v_-)$. For the Zeeman effect, a non-zero difference develops between the Fermi velocities of the pair of Weyl nodes related by the original mirror symmetry. The difference is generally greater at larger magnetic field, see Fig. 4.4, and $u^\lambda_{0z} \sim 0.02u^\lambda_{00}$ at $10T$ within our model. For Landau level quantization, on the other hand, the non-zero difference between v_+ and v_- originates from the anisotropy of the dispersion around each Weyl point. Also, the difference is less dependent on $\mathbf{B}$, see Fig. 4.5, as long as $\mathbf{B}$ is large enough to separate the non-chiral Landau bands and suppress their contribution. Landau level quantization gives $u^\lambda_{0z} \sim 0.3u^\lambda_{00}$ within our highly anisotropic model, yet it is also possible that $u^\lambda_{0z} \to 0$ irrespective of $\mathbf{B}$ when the anisotropy vanishes, e.g. for two isotropic Weyl points.

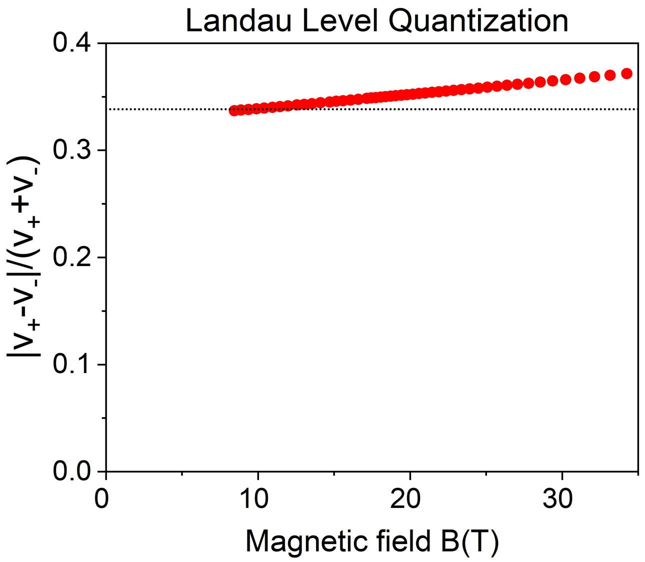

Figure 4.5: The relative difference (induced by the Landau level quantization) between the chiral Landau level Fermi velocities descending from a pair of Weyl nodes as a function of the magnetic field $\mathbf{B}$ along the $\hat{x}$ direction. Similar to Fig. 4.4, the value of $|v_+ - v_-| / (v_+ - v_-)$ measures the ratio $u^\lambda_{0z}/u^\lambda_{00}$ generated by the magnetic field. The black dotted line is the value evaluated with the zero-field dispersion.

Now that we have obtained an estimate for the effective u^λ_{0z}, let's estimate the strength of the corresponding IR signature. For example, we focus on the A_1 phonon mode in TaAs. We take $\omega = 8$ THz to match the experimental observation of an A_1 phonon mode in TaAs[306], $\mathcal{V}_c = 125\text{Å}$, and $M = 10^{-25}$kg. We also take $u^{A_1}_{0z} \sim 0.02 u^{A_1}_{00}$, which is reasonably obtainable given either the Zeeman effect with $g = 50$ at $|\mathbf{B}| = 10$T or Landau level quantization with the anisotropy in the NbAs and TaAs Weyl dispersion, as previously demonstrated. We also estimate $\sqrt{N} u^{\mathrm{A}_1}_{00} \sim 1\mathrm{Ry}/a_B$ on dimensional grounds[235], and neglect the $\mathbf{u}_z$ contribution given $v_F \ll c$. As a result, we obtain $|\delta \mathbf{Q}| \approx .8e$. Next, we calculate the impact of the chiral anomaly on the susceptibility. If we drive the IR frequency at $q_0 = 7.9$ THz, corresponding to a resonance width of 6.7 cm^{-1}, we find that $\chi^{\mathrm{A}_1}_{zz} = 60\epsilon_0$. Comparing to the experimentally measured zero-field

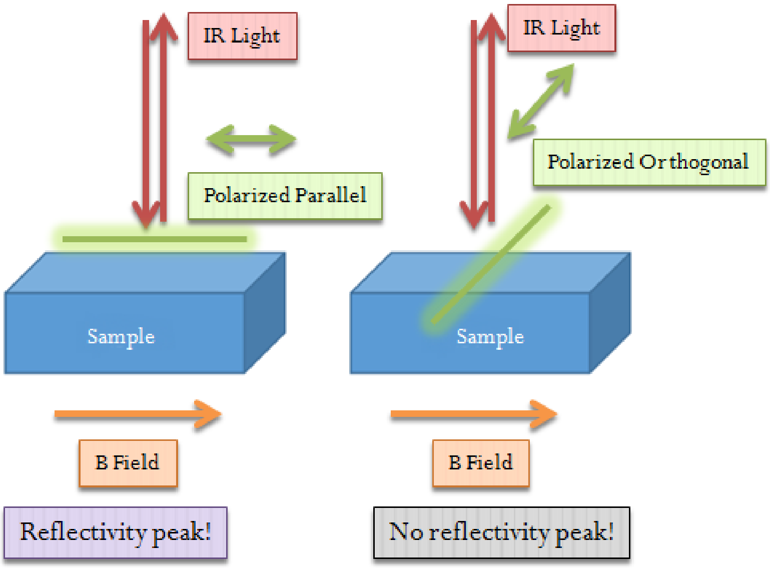

Figure 4.6: Proposed experimental setup to measure the IR signature of the chiral anomaly. In the presence of collinear $\mathbf{E}_{\text{IR}}$ and $\mathbf{B}$ fields, a peak in optical reflectivity is expected for inducing pseudoscalar phonon modes that couple strongly to the Weyl fermion electrons. Such effect also displays a $\mathbf{E}_{\text{IR}} \cdot \mathbf{B}$ dependence as one rotates $\mathbf{E}_{\text{IR}}$ relative to $\mathbf{B}$ in experiments.

reflectivity $R = \frac{|1-\sqrt{\epsilon_r}|^2}{|1+\sqrt{\epsilon_r}|^2}$ on TaAs crystals[306], the chiral anomaly contribution to the reflectivity should be of sufficient weight to be observable over the background of $\chi \approx 400\epsilon_0$. Therefore, we propose an $\mathbf{E}_{\text{IR}} \cdot \mathbf{B}$ dependent peak in the IR reflectivity as a signature of the chiral anomaly following the experimental setup in Fig. 4.6, even for scalar phonon modes and mirror-symmetric Weyl semimetals.[2]

4.1.5 Discussions and Conclusions

In this paper, we have focused on utilizing the mirror-symmetry breaking of the magnetic field to realize dynamical chiral anomaly in mirror-symmetric crystals

---

[2] Note that the proposed signature is a characteristic of the bulk, hence the incident light must penetrate into the bulk for this effect to manifest.

and exhibit optical signatures for scalar phonons in IR spectroscopy. We would like to emphasize that so long as a magnetic field is present, at most one mirror symmetry remains, so that the axial phonon coupling u_{0z}^{λ} is generically *allowed* from symmetry considerations and a chiral-anomaly induced IR response should be present. For the specific case where a single mirror plane remains, a pseudoscalar phonon mode normal to the mirror plane is still allowed[260, 236]. Since both the effective pseudoscalar phonon and the Weyl fermion chirality change sign under mirror symmetry, the axial component of electron-phonon coupling is not restricted to zero, and the corresponding IR signature of the dynamical chiral anomaly survives.[260, 236]

Inducing changes in dielectric susceptibility via a magnetic field is a magnetoelectric effect and not completely new.[235] However, magnetoelectric effects are typically associated with multiferroic materials (e.g., Cr_2O_3) and previous studies have focused on linear magnetoelectric effects (e.g., $\mathbf{P} \propto \mathbf{B}$). For the chiral anomaly, the effect is cubic with a characteristic $\mathbf{E} \cdot \mathbf{B}$ signature (i.e. $\mathbf{P} \propto (\mathbf{E} \cdot \mathbf{B})\,\mathbf{B}$), and known Weyl semimetals are not multiferroic. Therefore, we believe that the chiral-anomaly-activated phonon dynamics and IR signatures should be visible in generic Weyl semimetals.

Acknowledgements We would like to thank C. Fennie, I. Garate, D. Jena, and B. Ramshaw for helpful discussions and comments. A.H. was supported by the National Science Foundation Graduate Research Fellowship under Grant No. DGE-1650441. Y.Z. was supported by the Bethe fellowship at Cornell University and the startup grant at Peking University. E.-A. K. was supported by the National Science Foundation through the Platform for the Accelerated Realization, Analysis, and Discovery of Interface Materials (PARADIM) under Cooperative Agreement No. DMR-1539918.

4.1.6 Appendix: Low-energy Weyl dispersion and Weyl nodes of the tight binding model

The tight-binding model of Eq. (4.2) in the main text has four pairs of Weyl nodes on the $k_z = 0$ plane at $|\mathbf{B}| = 0$T, shown as the red dots in Fig. 4.7 left panel. These Weyl nodes are related to each other by the reflection planes in the xz and yz directions. The low-energy electronic dispersion is approximately linear near each of the Weyl nodes, see Fig. 4.7 right panel.

In the presence of a magnetic field $\mathbf{B}$, these reflection symmetries are generally broken. As a result, the locations of the Weyl nodes are no longer mirror symmetric. However, with the inclusion of the Zeeman effect (Eq. (4.3)), the displacements of the Weyl node locations are relatively small at experimentally relevant parameters, and unlikely to impact the electron-phonon coupling through its k-dependence in a meaningful way.

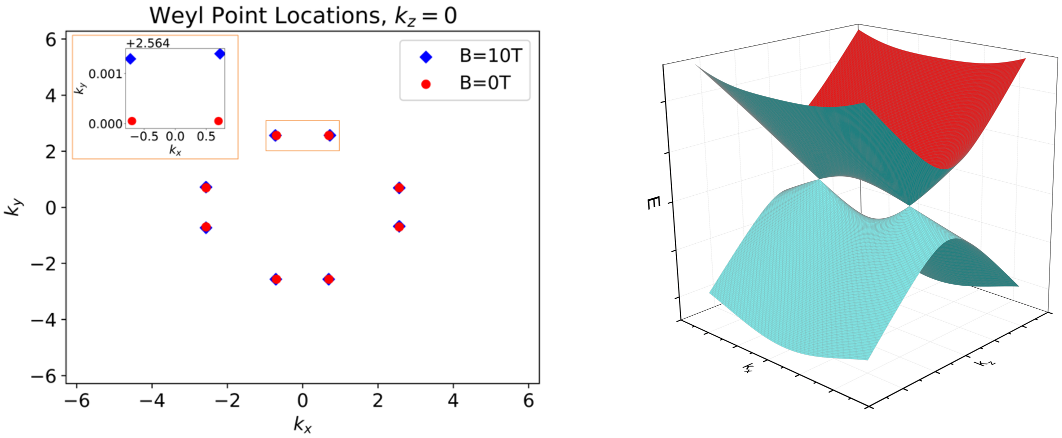

Figure 4.7: Left: the momentum-space locations of the Weyl nodes on the $k_z = 0$ plane show the mirror symmetry is broken in the presence of a magnetic field $|\mathbf{B}| = 10$T along the $\hat{x}/2 + \sqrt{3}\hat{y}/2$ direction. Note that even for a large g-factor $g = 50$ and a large magnetic field of 10T, the Weyl nodes only displaces by a scale $\sim 0.1\%$ of the Brillouin zone. The inset shows a magnified view of the pair of Weyl points in the orange box. Right: The zero-field dispersion in the $k_y - k_z$ plane is approximately linear near the Weyl nodes.

CHAPTER 5

DOMAIN WALL TRANSPORT IN MOIRÉ SYSTEMS

The field of moiré systems has recently become one of the most trendy topics in condensed matter physics. By providing either a twist angle or a lattice mismatch between two layers, a periodic moiré superlattice appears as a result of incommensuration. This moiré period can be much larger than the intrinsic lattice constant of the two layers, leading to a small moiré miniband. In particular, creating moiré patterns provides a straightforward way to change the band structure and enhance the strength of interactions. Beginning with the discovery of unconventional superconductivity in bilayer graphene twisted to a specific magic angle [31], moiré systems have shown to be a burgeoning fountain of strongly correlated phenomena [31, 248, 313, 139, 44, 178, 35, 37, 24, 216, 232, 263, 30, 176, 211, 309, 40, 272, 229, 287, 246, 36, 21]. However, recent experimental works have demonstrated that bilayers with small twist angles or small lattice mismatches can atomically reconstruct away from the moiré pattern to form sharp domain walls [268, 269, 308, 315, 111, 8, 129, 233, 192, 267, 237, 297, 163, 138]. This suggests the novel possibility that transport physics may be dominated by the domain walls, which we explore in what follows.

5.1 Topological moiré domain wall networks - Emergence of orbital antiferromagnetic-ordering

This section is currently being written up for publication in a peer-reviewed journal in collaboration with Eun-Ah Kim.

Moiré structures have recently been shown to host a plethora of correlated behavior, with many works focusing on the effects of the moiré miniband. However, recent experiments suggest that moiré systems can feature sharp domain walls and therefore provide a natural setting to study networks of 1D topological modes. While topological edge physics in moiré systems have been previously studied, many papers worked with non-interacting models. A few interacting network models have found gapped correlated phases by explicitly enforcing a single-particle gap. By contrast, we study a triangular network of valley-helical Luttinger wires where intervalley scattering is suppressed and no single-particle gap can open. We find that transport in this network is inherently non-local unlike the local diffusive behavior of a resistor network. In particular, we predict a novel orbital antiferromagnetic-ordering phase at strong repulsive interactions.

5.1.1 Introduction

Moiré systems have recently been shown to exhibit a plethora of correlated behavior.[31, 32, 248, 313, 139, 44, 178, 35, 37, 24, 216, 232, 263, 30, 176, 211, 309, 40, 272, 229, 287, 246, 36, 21] While most have focused on the physics of the moiré miniband, recent experiments in both homo-bilayer and hetero-bilayer systems suggest that marginal twist angles and/or small lattice mismatches can lead to significant atomic reconstruction and the formation of sharp domain walls.[268, 269, 308, 315, 111, 8, 127, 233, 192, 267, 237, 297, 163, 138] In this regime, a network of topological edge modes can emerge in the presence of an appropriate bulk gap; a prototypical example of such a network is shown in Fig. 5.1a, where domains of staggered Chern number give rise to topolog-

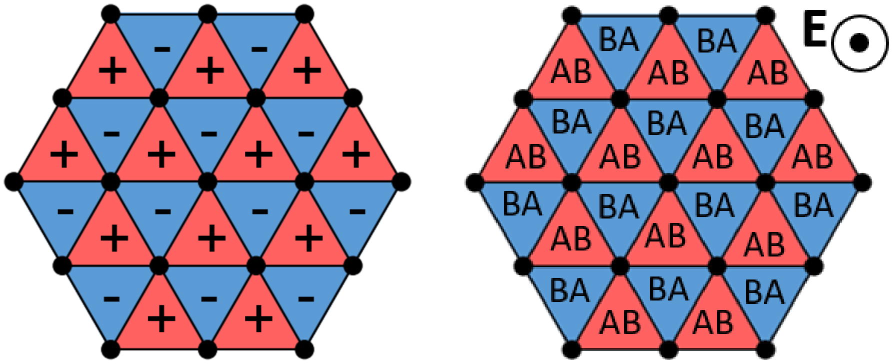

(a) Domains with staggered Chern number

(b) Marginally twisted bilayer graphene realization

Figure 5.1: (a) Domains equipped with a staggered Chern number, giving rise to topological edge physics. (b) A realization of Fig. 5.1a in marginally twisted bilayer graphene, where the AB/BA domains under an out-of-plane electric field develop a valley Chern number $C_v = \pm 1$.

ical edge modes. This network is physically realizable in marginally twisted bilayer graphene as shown in Fig. 5.1b, where the staggered lattice of AB/BA stacking provides a staggered valley Chern number in the presence of an out-of-plane electric field. These domain walls host 1D topological valley-helical edge modes, i.e. confined electronic states whose direction of propagation is opposite in opposite valleys.[190, 280, 321, 165, 314, 130] Control of topological edge modes and their junctions has long been of interest, e.g. for low power technological applications,[222, 221, 209, 264, 165, 231, 61, 38, 230], though engineering substantial networks of 1D topological modes has proven challenging. Moiré systems therefore provide a natural setting to produce and study such networks.

As a natural first step, pioneering works used non-interacting models to study the 1D valley-helical edge modes in marginally twisted bilayer graphene.[67, 283, 59, 279, 107, 108] The valley-helical nature of the wires pro-

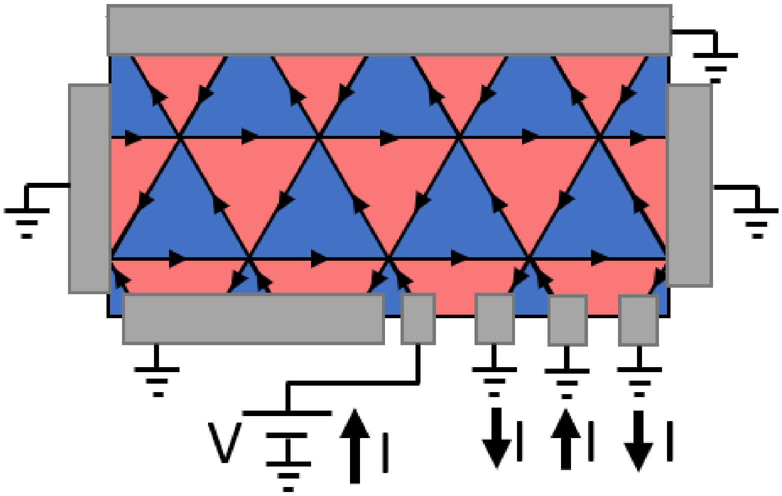

Figure 5.2: A plot of the experimental setup in the orbital AF-ordering phase. All but one of the external wires are grounded, while the remaining wire is held at a raised voltage V. This leads to a charge current pattern as demonstrated by the arrows, where the strength of the charge current is equal on every link. The current injection breaks time-reversal and gives rise to orbital antiferromagnetism.

vides a strong constraint; approximate conservation of valley number provides "topological" protection, and thus led to novel predictions for electronic structure and transport. Interacting network models[45, 304, 34] found gapped correlated phases - e.g. superconductivity and charge density wave (CDW) - reminiscent of the phase diagram near commensurate filllings in magic-angle twisted bilayer graphene. To truly achieve these phases requires generating a single-particle gap, which is generally suppressed by a large momentum transfer away from commensurate fillings. In contrast to these previous works, we treat interactions while enforcing time-reversal symmetry and no intervalley scattering, ensuring that a single-particle gap cannot be opened and valley-helicity is protected.[280]

In this paper, we study the transport features afforded by a triangular network of interacting valley-helical edge modes without intervalley scattering.

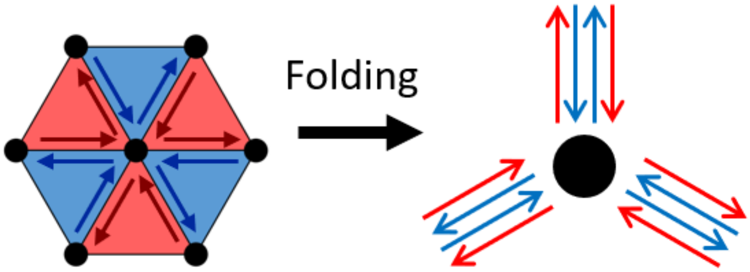

Figure 5.3: Schematic drawing of the single-scattering site Hamiltonian. Six Luttinger wires meet at a central junction, with each wire having an ingoing and outgoing mode. The color of the wire represents the valley (spin) degree of freedom, where the circulation of red arrows is opposite between the red and blue domains (and similarly for blue arrows). One can pair wires of opposite helicity (e.g. adjacent wires) and arrive at the right figure, which is equivalent to junction of three "spinful" Luttinger liquids.

We find that transport in this network is non-local, unlike that of a resistor network, and argue that a orbital antiferromagnetic (AF)-ordering phase will appear for sufficiently repulsive electron-electron interactions (see Fig. 5.2). The rest of the paper is organized as follows. In Sec. II, we provide our model of a single scattering center and outline the phase diagram. In Sec. III, we briefly discuss the ballistic phase. In Sec. IV, we propose a novel orbital AF-ordering phase and argue that this can be observed in the experimental setup of Fig. 5.2. In Sec. V, we summarize our results and make closing remarks.

5.1.2 Mathematical Setup

We begin by modeling a single scattering center as shown in Fig. 5.3. Each half-wire is modeled as a Tomonaga-Luttinger liquid of valley-helicity $\sigma = \pm 1$, with

Hamiltonian

$$H_\sigma = \int_{x>0} dx \Big[-v_F \left(\psi_\sigma^{L\dagger} i\partial_x \psi_\sigma^L - \psi_{-\sigma}^{R\dagger} i\partial_x \psi_{-\sigma}^R \right) + \frac{\lambda_4}{2}(J_{L,\sigma}^2 + J_{R,-\sigma}^2) + \lambda_2 J_{L,\sigma} J_{R,-\sigma} \Big] \tag{5.1}$$

where $\psi_\sigma^{L/R}$ corresponds to an ingoing/outgoing fermion annihilation operator of valley index $\sigma = \pm$ and $J_{L/R,\sigma} = \psi_\sigma^{L/R\dagger}\psi_\sigma^{L/R}$ are the corresponding density operators. Valley-helicity is encoded on each fermion operator by the pinning of L to σ and R to $-\sigma$. In addition to enforcing time-reversal symmetry, we also work away from commensurate fillings and forbid intervalley scattering.[1] We have ignored any "channel" and spin degrees of freedom for simplicity, such as those present in twisted bilayer graphene;[190, 280] in the absence of intervalley scattering, we do not expect these degrees of freedom to gap the wire.[280] Six of these half-wires meet at $x = 0$ to form the junction of interest as shown in Fig. 5.3, with the red and blue arrows denoting the two modes in each half-wire. On this junction, we impose C_3 rotational symmetry and inversion symmetry so that all the half-wires are identical (up to helicity).

It will be convenient to pair the Hamiltonians $H_+ + H_-$ so that the "folded" wire is analogous to a *"spinful"* Luttinger half-wire, as shown in Fig. 5.3 (see also Ref. [106]). Since our wires are related by a C_3 symmetry, this pairing choice enjoys a "folding symmetry". Therefore, our model can be mapped onto a junction of three "spinful" Luttinger liquids. We then bosonize each folded wire in the standard way, arriving at the following Euclidean action:

$$S = \sum_{r=c,v} \sum_{i=1}^{3} \int_{x>0} dx \frac{v_r g_r}{4\pi} \left[\frac{1}{v_r^2} (\partial_\tau \varphi_{i,r})^2 + (\partial_x \varphi_{i,r})^2 \right] \tag{5.2}$$

where v refers to the "valley" mode and i the wire index. In our convention, $g_c > 1$ corresponds to attractive interactions and $g_c < 1$ corresponds to repulsive

---

[1] I.e. particle number in each valley is conserved

Phase	Stabilized Tunnelings	Stable Regime
Orbital AF-ordering	$\psi^{R\dagger}_{j,-\sigma}\psi^{L}_{i,-\sigma}\psi^{R\dagger}_{i,\sigma}\psi^{L}_{j,\sigma}$	$g_c < 2/3$
Ballistic	$\psi^{R\dagger}_{i,\sigma}\psi^{L}_{j,\sigma}$	$1/2 < g_c < 2$
Cooper pair tunneling	$\psi^{R\dagger}_{i,\sigma}\psi^{L\dagger}_{i,-\sigma}\psi^{R}_{j,-\sigma}\psi^{L}_{j,\sigma}$	$g_c > 3/2$

Table 5.1: The three phases in our model and the corresponding stabilized tunneling operators. The tunneling operators are written in the folded-wire basis.

interactions.[2] Under this folding procedure, our model enforces the condition $g_c g_v = 1$ because valley-helicity constrains the form of interactions on the folded half-wire. We refer the reader to the Appendix for our bosonization conventions and additional details.

To complete our model, we specify a boundary condition $\phi^R_i(x = 0, \tau) = \mathcal{R}_{ij}\phi^L_j(x = 0, \tau)$ to relate ingoing (L) and outgoing (R) modes. This boundary condition can be physically understood as relating the currents $J_{R,i} = \mathcal{R}_{ij}J_{L,j}$.[105][3] For simplicity, we only consider boundary conditions which decouple into charge and valley sectors $\mathcal{R}_c, \mathcal{R}_v$. Given a boundary condition $\mathcal{R}_{ij}$, we assess our Hamiltonian's stability under tunneling processes at the boundary; the Hamiltonian is only stable when the boundary operators either have irrelevant scaling dimension or 0 scaling dimension. We will call a boundary operator "stabilized" if it has scaling dimension zero for a particular boundary condition. In this paper, we include all single and two-particle tunneling processes at $x = 0$ that conserve net particle number and net valley number.[4]

The phase diagram of a junction of three spinful Luttinger wires with particle-number and spin-conserving tunneling was studied in Ref. [105], anal-

---

[2] In particular, this is the opposite convention of Ref. [304] and Ref. [34]

[3] This can be shown by taking a time derivative $\partial_\tau \phi^{R/L} = J^{R/L}$.

[4] Higher-order terms are expected to be irrelevant.

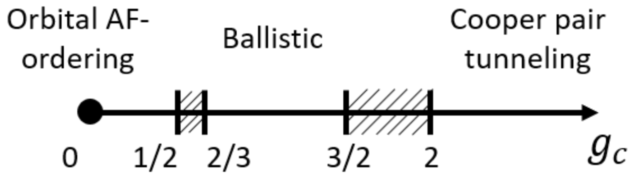

Figure 5.4: The phase diagram of the triangular network of valley-helical wires. The shaded regions denote regimes of overlapping stability.

ogous to our model where spin is replaced with valley. Enforcing our constraint $g_c g_v = 1$ on their results, we find three regimes - cooper pair tunneling, ballistic, and orbital AF-ordering; we list these in Table 5.1. As seen in the phase diagram of Fig. 5.4, there are regions where phases have overlapping stability; determining which fixed point dominates depends on microscopic details and lies outside the scope of this work. As physical electron-electron interactions are expected to be repulsive, we will focus on the regime $g_c < 1$ and defer further discussion of the cooper pair tunneling phase to the Appendix.

5.1.3 Ballistic phase

We begin with a brief discussion of the ballistic phase, stable for interactions of intermediate strength $1/2 < g_c < 2$. This phase is a bit subtle, as there are six co-stable fixed points. One of the fixed points has the boundary condition $\mathcal{R}_{c,ij} = \mathcal{R}_{v,ij} = \delta_{ij}$, corresponding to stabilizing complete backscattering $\psi^{R\dagger}_{i,\sigma}\psi^{L}_{i,\sigma}$ in each folded wire.[5] Unfolding each of the folded wires, we see that this corresponds to forming full valley-helical wires by connecting pairs of half-wires. As this boundary condition is comprised of three decoupled Luttinger wires exhibiting perfect transmission, this motivates the name "ballistic". However, this fixed

---

[5] While Ref. [105] wrote the boundary conditions in a rotated basis, for this paper it is equivalent to our boundary condition in the unrotated basis. See the Appendix for details.

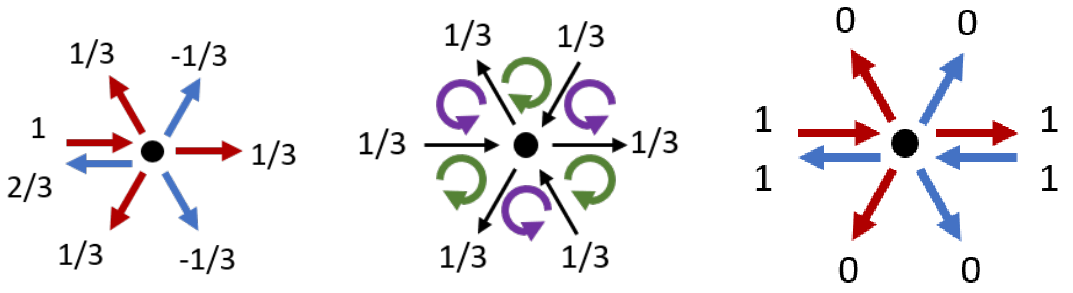

(a) Orbital AF-ordering current profile

(b) Charge current profile

(c) Pair-exchange tunneling

Figure 5.5: (a) The current profile of the orbital AF-ordering phase for ingoing current on one link. Negative numbers signify negative current, or equivalently a positive hole current (b) The corresponding charge current profile (i.e. red minus blue). The current strength on each link is the same, but alternates in sign as one goes around the scattering center. (c) The current profile corresponding to one of the pair-exchange tunneling terms.

point is not symmetric under folding symmetry; as there are six possible choices of folding, giving rise to six co-stable fixed points. In physical systems, the microscopic details will determine which fixed point the system actually adopts, which lies outside the scope of this work. On a network, long ballistic channels will form in this phase. Each channel has the usual Luttinger liquid conductance $G = g_c\frac{e^2}{h}$. This ballistic behavior is consistent with previous works on non-interacting network models of TBG, which predicted transport along ballistic zig-zag modes.[279, 59] For additional discussion of the ballistic phase, see the Appendix.

5.1.4 Orbital AF-ordering phase

We now consider the orbital AF-ordering phase, corresponding to strong repulsive interactions $g_c < 2/3$. The boundary condition of this phase is $\mathcal{R}_{c,ij} = \delta_{ij}$ and $\mathcal{R}_{v,ij} = -\delta_{ij} + 2/3$. As before, we unfold the boundary conditions back to our six-wire basis to manifestly see the current flow profile. Using the relation $\phi_{c(v)} = [(\phi_{L,+} + \phi_{R,+}) \pm (\phi_{L,-} + \phi_{R,-})]/\sqrt{2}$, we find

$$\mathcal{R}^{\mathrm{oAF}}_{ij} = \delta_{ij} - \frac{1}{3}(-1)^{i-j} \tag{5.3}$$

where the basis ordering is chosen such that one goes sequentially around the center. The resulting current profile is shown in Fig. 5.5a for a single wire with ingoing current. Unlike the ballistic case, this fixed point is independent of the choice of folding; the currents are the same on the C_3-related wires excluding the wire with incoming current. In Fig. 5.5b, we see that the resulting net charge current is equal on each wire but alternates in sign as one goes around the scattering center. The currents therefore circulate around each triangular domain in an alternating pattern, reminiscent of orbital antiferromagnetism. By tiling the network with the charge current profile, we find the current pattern shown in Fig. 5.2 with long-range orbital AF order, motivating the name of this phase.

To understand the origin of this peculiar current profile, we rewrite the stabilized (scaling dimension 0) tunneling operators at this fixed point into the 6-wire basis. These are

$$\mathrm{PE}_{i,2n+i+1} = \psi^{R\dagger}_{i,-\sigma}\psi^{L}_{2n+i+1,-\sigma}\psi^{R\dagger}_{2n+i+1,\sigma}\psi^{L}_{i,\sigma} \tag{5.4}$$

for $n \in \mathbb{Z}$, corresponding to pair exchange tunneling from wire i to wire $2n+i+1$ as shown in Fig. 5.5c.[6] These tunnelings were also considered in Refs. [34] and [45], where these promoted a CDW phase. One of these tunnelings provides the current profile shown in Fig. 5.5c, where a pair of ingoing currents of opposite valley number tunnel through the defect. Now we argue in reverse: given that all of the pair exchange tunnelings are stabilized in this phase, we want to

---

[6] The factor $2n + i + 1$ is to ensure that wire $2n + i + 1$ is of opposite valley-helicity to that of wire i, and wire indices are understood modulo 6. We also again remark that σ is a redundant label, fixed by the choice of direction L/R and the helicity of the corresponding wire.

reconstruct the boundary condition in Fig. 5.5a. In particular, this means that we want to reconstruct the two-ingoing-currents picture Fig. 5.5c using the one-ingoing-current picture of Fig. 5.5a. Let us consider one ingoing red ($\sigma = +$) current as shown in Fig. 5.5a. As the set of tunneling operators enjoys the D_3 symmetry $i \leftrightarrow i+2$ on each index, the outgoing red currents must have the same current $1/3$ by current conservation. Similarly, the two outgoing blue ($\sigma = -$) currents have the same current b, while the backscattered current has current $-2b$. Inversion symmetry gives us the corresponding profile with one ingoing blue current coming in from the right. When these two profiles added together, these must recreate Fig. 5.5c. This gives $b = -1/3$, as in Fig. 5.5a Therefore, enforcing that the pair exchange tunnelings are stabilized *requires* the boundary condition $\mathcal{R}^{oAF}$.

We then treat the full triangular network as shown in Fig. 5.2, utilizing our single-site results to compute the current profile and conductance. Rather than solve the large system of equations provided by the boundary condition $\mathcal{R}$ on each scattering site, we use conservation arguments to quickly obtain the result. Here we focus on the experimentally-relevant charge current profile; we discuss the valley current profile in the Appendix. As previously noted, Fig. 5.5b implies that the charge current strength is equal on every link and forms orbital antiferromagnetic domains as shown in Fig. 5.2. It remains to obtain the corresponding current strength on each link and the network conductance. Without loss of generality, we consider exactly one external wire hosting ingoing current. At the input link, the backscattered current fraction b must satisfy $1 - b = I/I_0$, where I_0 is the current of the ingoing portion of the input link. For the external links, excluding the input link, the valley and charge current strength are equal as they only carry outgoing modes. Since the sign of the charge current alternates with valley, by valley current conservation we must also have $1 + b = (N_{\text{ext}} - 1)I/I_0$. Therefore, this gives us $I/I_0 = 2/N_{\text{ext}}$.[7] To obtain the conductance tensor, the Kubo formula gives[105]

$$G_{ij} = g_c \frac{e^2}{h} \left(\delta_{ij} - \mathcal{R}_{ij}^{\text{network}} \right), \tag{5.5}$$

where $\mathcal{R}_{ij}^{\text{network}}$ is the effective boundary condition relating the currents on the external wires. The δ_{ij} corresponds to ingoing current on wire j generated by a voltage V_j, while $\mathcal{R}_{ij}^{\text{network}}$ is the corresponding outgoing current. Therefore, our current pattern solution directly gives

$$G_{ij} = g_c \frac{e^2}{h} \sigma(i)\sigma(j) \frac{2}{N_{\text{ext}}} \tag{5.6}$$

where $\sigma(i)$ is the helicity of the external wire i.[8] Therefore, net current flows when there is a net voltage difference $\sum_i \sigma(i) V_i$, corresponding to a voltage difference between external wires of differing helicity.

To observe this state, we propose an experiment as shown in Fig. 5.2. This is almost a rectangular Hall bar geometry, except that we introduce a "point contact" at the bottom edge to bias the voltage of one particular wire. In a typical Hall bar, where one applies a constant voltage V to the entire bottom edge, we generically expect net insulating $G_{xx} = 0$ behavior; if the bottom edge covers an even number of wires, parity enforces net zero current. By preferentially biasing a point contact, we break the helicity symmetry and generate a net current. In

---

[7] We remark that the result of current cannot be obtained by linking up nodes of Fig. 5.5b and using the single site conductance. Internal links host both modes traveling in both directions, so one must consistently solve for their mode populations. Therefore, one must keep track of the valley information in order to obtain the correct result. At high temperatures, however, excitations on the wire will equilibrate and have a well-defined voltage as in the approach of Ref. [163]. In this regime, the strength of the current will scale as $1/N$ with N the number of scattering centers. Even so, the antiferromagnetic current pattern will remain (up to temperature dependent corrections).

[8] For external wires, a globally-defined helicity is well-defined since ingoing and outgoing directions are well-defined.

the proposed geometry of Fig. 5.2, note that current only flows through contacts covering an odd number of wires. By arranging a series of point contacts, the long-range orbital antiferromagnetic order will give rise to an alternating sequence of ingoing and outgoing currents of equal strength. This is remarkably different from a resistor network which exhibits diffusive behavior in this geometry. Moreover, direct detection of the resultant orbital antiferromagnetism would provide strong evidence of this phase.

5.1.5 Conclusion

In this paper, we have calculated current profiles and conductance of a triangular network of 1D valley-helical edge modes where intervalley scattering is suppressed. At strong repulsive interactions, we find a novel orbital AF-ordering phase (see Fig. 5.2), while at weaker repulsive interactions the system develops 1D ballistic channels. As these phases exhibit a long-range order of currents, they exhibit non-local transport distinct from the local diffusive behavior of typical resistor networks. As these phases may be difficult to observe in typical Hall bar geometries, we propose the geometry of Fig. 5.2 to observe the nontrivial transport behavior.

We made critical use of forbidding intervalley scattering to obtain our conductive phases. Recent experimental measurements of the the AA defect in marginally twisted bilayer graphene estimate its size to be ~ 30Å,[138] which is substantially larger than the graphene lattice constant 2.46Å.[55] Therefore, we expect our assumption of no intervalley scattering at the defect to be good. Moreover, in spin-valley locked systems, intervalley scattering is explicitly prevented by time-reversal symmetry.[303] As a result, moiré domain wall networks involving with strong spin-orbit coupling, such as transition metal dichalcogenide (TMD) bilayers, may also demonstrate these non-local edge transport features if one can induce a topological gap. At finite temperatures and voltages, the single-site conductance, and therefore the network conductance, will acquire power law corrections controlled by the scaling dimension of the leading irrelevant boundary operator Δ_{min} from the Luttinger physics.[135, 106] Observation of this power law behavior would provide preliminary evidence of Luttinger transport and of the applicability of the network model. Detailed analysis of a honeycomb network of spinful Luttinger liquids has already shown non-Fermi liquid temperature dependence of the conductivity[157]. We also remark that, since we have restricted ourselves to boundary conditions which decouple into charge and valley sectors, we have not exhausted the phase diagram (see also the Appendix). However, our phase diagram covers $-\infty < g_c < \infty$, so any additional phase must coexist with one we have already discussed. We leave further exploration of the temperature-dependence and the phase diagram to future work.

Acknowledgements We thank Chao-Ming Jian, Kin Fai Mak, Craig Fennie, and Debdeep Jena for helpful discussions. A.H. was supported by the National Science Foundation Graduate Research Fellowship under Grant No. DGE-1650441. Both A.H. and E.-A.K. were supported by the U.S. Department of Energy, Office of Basic Energy Sciences, Division of Materials Science and Engineering under Award DE-SC0018946.

5.1.6 Appendix: Bosonization and Conventions

In this paper, we follow the bosonization conventions of Ref. [105] and Ref. [106]. The boson φ_r and its dual θ_r satisfy the commutation relation $[\phi(x), \theta(x')] = -i\Theta(x - x')$. We can rewrite these into valley-up and valley-down components via

$$\varphi_\sigma = \frac{\varphi_c + \sigma\varphi_v}{\sqrt{2}}, \qquad \theta_\sigma = \frac{\theta_c + \sigma\theta_v}{\sqrt{2}} \tag{5.7}$$

The left and right mover representations $\phi_{L,\sigma}$ and $\phi_{R,\sigma}$ are given by

$$\phi^L_\sigma = \frac{\varphi_\sigma + \theta_\sigma}{2}, \qquad \phi^R_\sigma = \frac{\varphi_\sigma - \theta_\sigma}{2} \tag{5.8}$$

and the charge and valley components are

$$\phi^a_c = \frac{\phi^a_+ + \phi^a_-}{2}, \qquad \phi^a_v = \frac{\phi^a_+ - \phi^a_-}{\sqrt{2}} \tag{5.9}$$

We identify the fermion annihilation operator as

$$\psi^a_\sigma \propto e^{i\sqrt{2}\phi^a_\sigma} \tag{5.10}$$

where we have suppressed the Klein factors.

To demonstrate $g_c g_v = 1$, we first rewrite the interaction terms in Eq. (5.1) in terms of charge and valley currents, giving

$$\begin{aligned}\mathcal{H}_{\text{int},i} =& v_F \int_{x>0} dx \lambda_2 (J_{L,c}J_{R,c} - J_{L,v}J_{R,v}) \\ &+ \lambda_4 (J^2_{L,c} + J^2_{R,c} + J^2_{L,v} + J^2_{R,v})\end{aligned} \tag{5.11}$$

Then, we use $J_L = \frac{1}{\sqrt{2}}(\partial_x + i\partial_\tau)\theta$ and $J_R = \frac{1}{\sqrt{2}}(\partial_x - i\partial_\tau)\theta$ to bosonize. Therefore, we find $g_{c(v)} = \sqrt{\frac{2\pi v_F + \lambda_4 \mp \lambda_2}{2\pi v_F + \lambda_4 \pm \lambda_2}}$ and obtain the result $g_c g_v = 1$. Additionally, we remark that the expression for g_c explicitly shows that $g_c < 1$ corresponds to repulsive $(\lambda_2, \lambda_4 > 0)$ interactions.

5.1.7 Appendix: Boundary conditions

The boundary conditions in Ref. [105] are written in a rotated basis $\tilde{\phi}$ where $\tilde{\varphi}_r = \sqrt{g_r}\varphi_r$ is rescaled. Therefore, one generically expects the rotated $\tilde{\mathcal{R}}$ to be distinct from $\mathcal{R}$. However, for boundary conditions which are involutions $\mathcal{R}^2 = \mathcal{I}$ (i.e. symmetric orthogonal matrices), we in fact find $\tilde{\mathcal{R}} = \mathcal{R}$. To see this, we first consider the following relations

$$\begin{pmatrix} \tilde{\phi}_c^L \\ \\ \tilde{\phi}_s^L \end{pmatrix} = M_L \begin{pmatrix} \phi_c^L \\ \\ \phi_s^L \end{pmatrix} \tag{5.12}$$

$$\begin{pmatrix} \tilde{\phi}_c^R \\ \\ \tilde{\phi}_s^R \end{pmatrix} = M_R \begin{pmatrix} \phi_c^L \\ \\ \phi_s^L \end{pmatrix} \tag{5.13}$$

$$M_L = \begin{pmatrix} \cosh\alpha_c & 0 \\ \\ 0 & \cosh\alpha_s \end{pmatrix} - \begin{pmatrix} \sinh\alpha_c & 0 \\ \\ 0 & \sinh\alpha_s \end{pmatrix} \mathcal{R} \tag{5.14}$$

$$M_R = \begin{pmatrix} \cosh\alpha_c & 0 \\ \\ 0 & \cosh\alpha_s \end{pmatrix} \mathcal{R} - \begin{pmatrix} \sinh\alpha_c & 0 \\ \\ 0 & \sinh\alpha_s \end{pmatrix} \tag{5.15}$$

where we have used the unrotated boundary condition $\mathcal{R}(\phi_c^L, \phi_v^L)^T = (\phi_c^R, \phi_v^R)^T$. These equations tell us that

$$\tilde{\mathcal{R}} = M_R M_L^{-1} \tag{5.16}$$

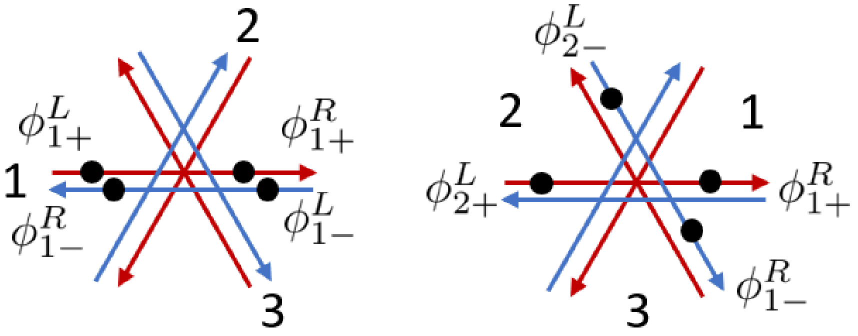

(a) Charge-valley decoupled folding (b) Charge-valley mixed folding

Figure 5.6: Two folding procedures for a ballistic fixed point where the wires are connected across the defect. (a) A folding where opposite wires across the junction are paired. We find $\phi^L_{1,c} = \phi^R_{1,c}$ and $\phi^L_{1,v} = \phi^R_{1,v}$, so the charge and valley boundary conditions are decoupled. (b) A folding where adjacent wires are paired. We find that $\phi^L_{1,c} = \phi^R_{1,+} + \phi^R_{3,-}$. Therefore, this boundary condition mixes charge and valley.

If $\mathcal{R}$ is an involution, then $M_R R = M_L$ and therefore $\tilde{\mathcal{R}} = \mathcal{R}$ as previously claimed. As all the boundary conditions we consider in this paper are involutions, we we freely translate the boundary conditions of Ref. [105] into the unrotated basis.

5.1.8 Appendix: The ballistic phase

For the case $g_c g_s = 1$ in Ref. [105], there are 4 co-stable fixed points when $2/3 < g_c < 3/2$ - namely their NN and three $D^i_A D^i_A$ fixed points. There are also two additional $\chi\chi$ fixed points stable precisely at $g_c = 1$, which we will neglect as they are stable only a single point. By considering all folding procedures, upon unfolding there are a total of 6 fixed points, which fall into the three symmetry classes shown in Fig. 5.7. This shows that the possible fixed points comprise all possible connections of the wires.

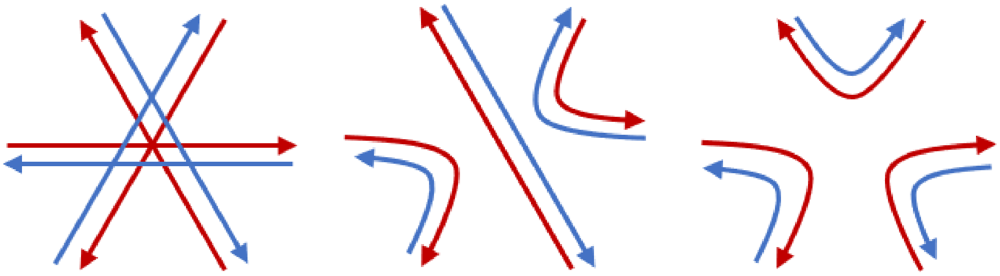

(a) Symmetric (b) C_3-Broken (c) Chiral

Figure 5.7: The three symmetry classes of the fixed point boundary conditions in the ballistic regime. These correspond to all possible permutations of linking together the valley-helical wires.

The discrepancy between the 4 co-stable fixed points found by Ref. [105] and the 6 we find after unfolding is due to their assumption that the boundary condition $\mathcal{R}$ can be decoupled into $\mathcal{R}_c, \mathcal{R}_v$. The remaining two fixed points lie outside this paradigm. To see this, let us consider the fixed point shown in Fig. 5.6 under two separate foldings. We see that under the first folding of Fig. 5.6a, the boundary conditions are $\mathcal{R}_c = \mathcal{R}_v = \mathcal{I}$. However, the second folding of Fig. 5.6b mixes charge and valley. Therefore, to obtain the full phase diagram one must all potential 6×6 boundary conditions instead of those that are simply block-diagonal in charge $\mathcal{R}_c$ and valley $\mathcal{R}_v$.

5.1.9 Appendix: Valley current profile of the orbital AF-ordering phase

In the main text, we only considered the charge current profile of the orbital AF-ordering phase. To complete the solution, we must also solve for the valley current profile. This is subtle since homogeneous solutions are allowed in the network as shown in Fig. 5.8. Arbitrary valley current loops are allowed

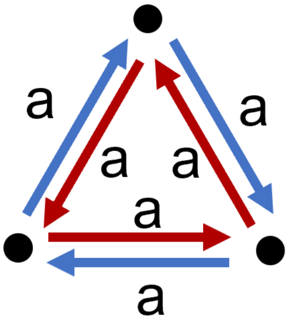

Figure 5.8: A homogeneous solution in the network of orbital AF-ordering phase. An arbitrary valley current is allowed to circulate in triangular loops. However, charge current cannot freely circulate in loops.

to circulate around triangular domains in the bulk, and we expect that its precise value depends on the time-dependent details of instantiating the system. However, the external links do not suffer this issue and therefore have a definite valley current. As argued in the main text, all the grounded external links have the same valley current I_v, and therefore the ingoing link has valley current $(N_{\text{ext}} - 1)I_v$.

5.1.10 Appendix: Cooper pair tunneling phase

For the cooper pair tunneling phase, the boundary conditions are $\mathcal{R}_c = \mathcal{I}$ and $\mathcal{R}_v = -\delta_{ij} + 2/3$. These are precisely the boundary conditions of the orbital AF-ordering phase, but with charge and valley flipped. Therefore, we can read off the solution of the cooper pair tunneling phase from that of the orbital AF-ordering phase by flipping charge and valley. The charge current will allow for arbitrary charge current loops in the bulk, with external conductance $G_{ij} = g_c\frac{e^2}{h}(2\delta_{ij} - 2/N_{\text{ext}})$.

BIBLIOGRAPHY

[1] O. Aharony, S. S. Gubser, J. Maldacena, H. Ooguri, and Y. Oz. Large N field theories, string theory and gravity. *Physics Reports*, 323:183–386, January 2000.

[2] O. Aharony, G. Gur-Ari, and R. Yacoby. Correlation functions of large N Chern-Simons-Matter theories and bosonization in three dimensions. *Journal of High Energy Physics*, 12:28, December 2012.

[3] O. Aharony, G. Gur-Ari, and R. Yacoby. d = 3 bosonic vector models coupled to Chern-Simons gauge theories. *Journal of High Energy Physics*, 3:37, March 2012.

[4] Ofer Aharony. Baryons, monopoles and dualities in Chern-Simons-matter theories. *Journal of High Energy Physics*, 2016(2):93, Feb 2016.

[5] Ofer Aharony, Francesco Benini, Po-Shen Hsin, and Nathan Seiberg. Chern-simons-matter dualities with SO and USp gauge groups. *Journal of High Energy Physics*, 2:72, Feb 2017.

[6] Ofer Aharony, Simone Giombi, Guy Gur-Ari, Juan Maldacena, and Ran Yacoby. The Thermal Free Energy in Large N Chern-Simons-Matter Theories. *Journal of High Energy Physics*, 2013(3):121, Mar 2013.

[7] Ofer Aharony, Guy Gur-Ari, and Ran Yacoby. Correlation Functions of Large N Chern-Simons-Matter Theories and Bosonization in Three Dimensions. *Journal of High Energy Physics*, 2012(12):28, Dec 2012.

[8] Jonathan S. Alden, Adam W. Tsen, Pinshane Y. Huang, Robert Hovden, Lola Brown, Jiwoong Park, David A. Muller, and Paul L. McEuen. Strain solitons and topological defects in bilayer graphene. *Proceedings of the National Academy of Sciences*, 110(28):11256–11260, 2013.

[9] Luis Alvarez-Gaume and Edward Witten. Gravitational Anomalies. *Nucl. Phys. B*, 234:269, 1984.

[10] A. V. Andreev, Steven A. Kivelson, and B. Spivak. Hydrodynamic description of transport in strongly correlated electron systems. *Phys. Rev. Lett.*, 106:256804, Jun 2011.

[11] A. V. Andreev and B. Z. Spivak. Longitudinal negative magnetoresistance and magnetotransport phenomena in conventional and topological conductors. *Phys. Rev. Lett.*, 120:026601, Jan 2018.

[12] N. P. Armitage, E. J. Mele, and Ashvin Vishwanath. Weyl and dirac semimetals in three-dimensional solids. *Rev. Mod. Phys.*, 90:015001, Jan 2018.

[13] Frank Arnold, Chandra Shekhar, Shu-Chun Wu, Yan Sun, Ricardo Donizeth dos Reis, Nitesh Kumar, Marcel Naumann, Mukkattu O. Ajeesh, Marcus Schmidt, Adolfo G. Grushin, Jens H. Bardarson, Michael Baenitz, Dmitry Sokolov, Horst Borrmann, Michael Nicklas, Claudia Felser, Elena Hassinger, and Binghai Yan. Negative magnetoresistance without well-defined chirality in the weyl semimetal tap. *Nature Communications*, 7:11615, May 2016. Article.

[14] Phillip E. C. Ashby and J. P. Carbotte. Chiral anomaly and optical absorption in weyl semimetals. *Phys. Rev. B*, 89:245121, Jun 2014.

[15] N.W. Ashcroft and N.D. Mermin. *Solid State Physics*. HRW international editions. Holt, Rinehart and Winston, 1976.

[16] L. V. Avdeev, D. I. Kazakov, and I. N. Kondrashuk. Renormalizations in supersymmetric and nonsupersymmetric nonAbelian Chern-Simons field theories with matter. *Nucl. Phys.*, B391:333–357, 1993.

[17] D. A. Bandurin, I. Torre, R. Krishna Kumar, M. Ben Shalom, A. Tomadin, A. Principi, G. H. Auton, E. Khestanova, K. S. Novoselov, I. V. Grigorieva, L. A. Ponomarenko, A. K. Geim, and M. Polini. Negative local resistance caused by viscous electron backflow in graphene. *Science*, 351(6277):1055–1058, 2016.

[18] Denis A Bandurin, Andrey V Shytov, Leonid S Levitov, Roshan Krishna Kumar, Alexey I Berdyugin, Moshe Ben Shalom, Irina V Grigorieva, Andre K Geim, and Gregory Falkovich. Fluidity onset in graphene. *Nature communications*, 9(1):1–8, 2018.

[19] Denis A. Bandurin, Dmitry Svintsov, Igor Gayduchenko, Shuigang G. Xu, Alessandro Principi, Maxim Moskotin, Ivan Tretyakov, Denis Yagodkin, Sergey Zhukov, Takashi Taniguchi, Kenji Watanabe, Irina V. Grigorieva, Marco Polini, Gregory N. Goltsman, Andre K. Geim, and Georgy Fedorov. Resonant terahertz detection using graphene plasmons. *Nature Communications*, 9(1):5392, Dec 2018.

[20] M. E. Barber, A. S. Gibbs, Y. Maeno, A. P. Mackenzie, and C. W. Hicks. Resistivity in the vicinity of a van hove singularity: $\mathrm{sr_2ruo_4}$ under uniaxial pressure. *Phys. Rev. Lett.*, 120:076602, Feb 2018.

[21] Rafi Bistritzer and Allan H. MacDonald. Moiré bands in twisted double-layer graphene. *Proceedings of the National Academy of Sciences*, 108(30):12233–12237, 2011.

[22] Barry Bradlyn, Moshe Goldstein, and N. Read. Kubo formulas for viscosity: Hall viscosity, ward identities, and the relation with conductivity. *Phys. Rev. B*, 86:245309, Dec 2012.

[23] U. Briskot, M. Schütt, I. V. Gornyi, M. Titov, B. N. Narozhny, and A. D. Mirlin. Collision-dominated nonlinear hydrodynamics in graphene. *Phys. Rev. B*, 92:115426, Sep 2015.

[24] G. William Burg, Jihang Zhu, Takashi Taniguchi, Kenji Watanabe, Allan H. MacDonald, and Emanuel Tutuc. Correlated insulating states in twisted double bilayer graphene. *Phys. Rev. Lett.*, 123:197702, Nov 2019.

[25] C. P. Burgess and Brian P. Dolan. Particle-vortex duality and the modular group: Applications to the quantum hall effect and other two-dimensional systems. *Phys. Rev. B*, 63:155309, Mar 2001.

[26] A. A. Burkov. Chiral anomaly and diffusive magnetotransport in weyl metals. *Phys. Rev. Lett.*, 113:247203, Dec 2014.

[27] A. A. Burkov. Negative longitudinal magnetoresistance in dirac and weyl metals. *Phys. Rev. B*, 91:245157, Jun 2015.

[28] Igor S. Burmistrov, Moshe Goldstein, Mordecai Kot, Vladislav D. Kurilovich, and Pavel D. Kurilovich. Dissipative and hall viscosity of a disordered 2d electron gas. *Phys. Rev. Lett.*, 123:026804, Jul 2019.

[29] Jennifer Cano, Meng Cheng, Michael Mulligan, Chetan Nayak, Eugeniu Plamadeala, and Jon Yard. Bulk-edge correspondence in (2 + 1)-dimensional abelian topological phases. *Phys. Rev. B*, 89:115116, Mar 2014.

[30] Yuan Cao, Debanjan Chowdhury, Daniel Rodan-Legrain, Oriol Rubies-Bigorda, Kenji Watanabe, Takashi Taniguchi, T. Senthil, and Pablo Jarillo-Herrero. Strange metal in magic-angle graphene with near planckian dissipation. *Phys. Rev. Lett.*, 124:076801, Feb 2020.

[31] Yuan Cao, Valla Fatemi, Ahmet Demir, Shiang Fang, Spencer L. Tomarken, Jason Y. Luo, Javier D. Sanchez-Yamagishi, Kenji Watanabe, Takashi Taniguchi, Efthimios Kaxiras, Ray C. Ashoori, and Pablo Jarillo-Herrero. Correlated insulator behaviour at half-filling in magic-angle graphene superlattices. *Nature*, 556:80–84, 2018.

[32] Yuan Cao, Valla Fatemi, Shiang Fang, Kenji Watanabe, Takashi Taniguchi, Efthimios Kaxiras, and Pablo Jarillo-Herrero. Unconventional superconductivity in magic-angle graphene superlattices. *Nature*, 556:43–50, 2018.

[33] J. T. Chalker and P. D. Coddington. Percolation, quantum tunnelling and the integer hall effect. *J. Phys. C: Solid State Phys.*, 21(14):2665, 1988.

[34] Chuan Chen, A. H. Castro Neto, and Vitor M. Pereira. Correlated states of a triangular net of coupled quantum wires: Implications for the phase diagram of marginally twisted bilayer graphene. *Phys. Rev. B*, 101:165431, Apr 2020.

[35] Guorui Chen, Lili Jiang, Shuang Wu, Bosai Lyu, Hongyuan Li, Bheema Lingam Chittari, Kenji Watanabe, Takashi Taniguchi, Zhiwen Shi, Jeil Jung, Yuanbo Zhang, and Feng Wang. Evidence of a gate-tunable Mott insulator in a trilayer graphene moiré superlattice. *Nat. Phys.*, 15(3):237–241, Mar 2019.

[36] Guorui Chen, Aaron L. Sharpe, Eli J. Fox, Ya-Hui Zhang, Shaoxin Wang, Lili Jiang, Bosai Lyu, Hongyuan Li, Kenji Watanabe, Takashi Taniguchi, Zhiwen Shi, T. Senthil, David Goldhaber-Gordon, Yuanbo Zhang, and Feng Wang. Tunable correlated Chern insulator and ferromagnetism in a moiré superlattice. *Nature*, 579(7797):56–61, Mar 2020.

[37] Guorui Chen, Aaron L. Sharpe, Patrick Gallagher, Ilan T. Rosen, Eli J. Fox, Lili Jiang, Bosai Lyu, Hongyuan Li, Kenji Watanabe, Takashi Taniguchi, Jeil Jung, Zhiwen Shi, David Goldhaber-Gordon, Yuanbo Zhang, and Feng Wang. Signatures of tunable superconductivity in a trilayer graphene moiré superlattice. *Nature*, 572(7768):215–219, Aug 2019.

[38] Hao Chen, Pinjia Zhou, Jiawei Liu, Jiabin Qiao, Barbaros Oezyilmaz, and Jens Martin. Gate controlled valley polarizer in bilayer graphene. *Nat. Commun.*, 11(1202):1–7, Mar 2020.

[39] J.-Y. Chen, J. H. Son, C. Wang, and S. Raghu. Exact Boson-Fermion Duality on a 3D Euclidean Lattice. *Phys. Rev. Lett.*, 120:016602, Jan 2018.

[40] Shaowen Chen, Minhao He, Ya-Hui Zhang, Valerie Hsieh, Zaiyao Fei, K. Watanabe, T. Taniguchi, David H. Cobden, Xiaodong Xu, Cory R. Dean, and Matthew Yankowitz. Electrically tunable correlated and topological states in twisted monolayer–bilayer graphene. *Nat. Phys.*, 17(3):374–380, Mar 2021.

[41] Wei Chen, Matthew P A Fisher, and Yong-Shi Wu. Mott transition in an anyon gas. *Phys. Rev. B.*, 48(18):13749–13761, nov 1993.

[42] Wei Chen, Gordon W Semenoff, and Yong-Shi Wu. Two-loop analysis of non-Abelian Chern-Simons theory. *Physical Review D*, 46(12):5521–5539, dec 1992.

[43] Shai M. Chester and Silviu S. Pufu. Anomalous dimensions of scalar operators in \$QED_3\$. *Journal of High Energy Physics*, 2016(8):69, Aug 2016.

[44] Youngjoon Choi, Jeannette Kemmer, Yang Peng, Alex Thomson, Harpreet Arora, Robert Polski, Yiran Zhang, Hechen Ren, Jason Alicea, Gil Refael, Felix von Oppen, Kenji Watanabe, Takashi Taniguchi, and Stevan Nadj-Perge. Electronic correlations in twisted bilayer graphene near the magic angle. *Nat. Phys.*, 15(11):1174–1180, Nov 2019.

[45] Yang-Zhi Chou, Yu-Ping Lin, Sankar Das Sarma, and Rahul M. Nandkishore. Superconductor versus insulator in twisted bilayer graphene. *Phys. Rev. B*, 100:115128, Sep 2019.

[46] Rodrigo C. V. Coelho, Miller Mendoza, Mauro M. Doria, and Hans J. Herrmann. Kelvin-helmholtz instability of the dirac fluid of charge carriers on graphene. *Phys. Rev. B*, 96:184307, Nov 2017.

[47] Sidney Coleman. Quantum sine-gordon equation as the massive thirring model. *Phys. Rev. D*, 11:2088–2097, Apr 1975.

[48] Sidney Coleman. *Aspects of Symmetry*. Cambridge University Press, Cambridge, 1985.

[49] S. Conti and G. Vignale. Elasticity of an electron liquid. *Phys. Rev. B*, 60:7966–7980, Sep 1999.

[50] Alberto Cortijo, Yago Ferreirós, Karl Landsteiner, and María A. H. Vozmediano. Elastic gauge fields in weyl semimetals. *Phys. Rev. Lett.*, 115:177202, Oct 2015.

[51] Alberto Cortijo, Dmitri Kharzeev, Karl Landsteiner, and Maria A. H. Vozmediano. Strain-induced chiral magnetic effect in weyl semimetals. *Phys. Rev. B*, 94:241405, Dec 2016.

[52] Jesse Crossno, Jing K. Shi, Ke Wang, Xiaomeng Liu, Achim Harzheim, Andrew Lucas, Subir Sachdev, Philip Kim, Takashi Taniguchi, Kenji Watanabe, Thomas A. Ohki, and Kin Chung Fong. Observation of the dirac fluid and the breakdown of the wiedemann-franz law in graphene. *Science*, 351(6277):1058–1061, 2016.

[53] Xin Dai, Z. Z. Du, and Hai-Zhou Lu. Negative magnetoresistance without chiral anomaly in topological insulators. *Phys. Rev. Lett.*, 119:166601, Oct 2017.

[54] Kedar Damle and Subir Sachdev. Nonzero-temperature transport near quantum critical points. *Phys. Rev. B*, 56:8714–8733, Oct 1997.

[55] S. Das Sarma, Shaffique Adam, E. H. Hwang, and Enrico Rossi. Electronic transport in two-dimensional graphene. *Rev. Mod. Phys.*, 83:407–470, May 2011.

[56] C. Dasgupta and B. I. Halperin. Phase Transition in a Lattice Model of Superconductivity. *Phys. Rev. Lett.*, 47(21):1556–1560, nov 1981.

[57] J. L. Davis, P. Kraus, and A. Shah. Gravity dual of a quantum Hall plateau transition. *Journal of High Energy Physics*, 11:020, November 2008.

[58] Richard A. Davison, Koenraad Schalm, and Jan Zaanen. Holographic duality and the resistivity of strange metals. *Phys. Rev. B*, 89:245116, Jun 2014.

[59] C. De Beule, F. Dominguez, and P. Recher. Aharonov-bohm oscillations in minimally twisted bilayer graphene. *Phys. Rev. Lett.*, 125:096402, Aug 2020.

[60] M. J. M. de Jong and L. W. Molenkamp. Hydrodynamic electron flow in high-mobility wires. *Phys. Rev. B*, 51:13389–13402, May 1995.

[61] Folkert K. de Vries, Jihang Zhu, Elías Portolés, Giulia Zheng, Michele Masseroni, Annika Kurzmann, Takashi Taniguchi, Kenji Watanabe, Allan H. MacDonald, Klaus Ensslin, Thomas Ihn, and Peter Rickhaus. Com-

bined minivalley and layer control in twisted double bilayer graphene. *Phys. Rev. Lett.*, 125:176801, Oct 2020.

[62] Stanley Deser, R. Jackiw, and S. Templeton. Topologically Massive Gauge Theories. *Annals Phys.*, 140:372–411, 1982.

[63] R D dos Reis, M O Ajeesh, N Kumar, F Arnold, C Shekhar, M Naumann, M Schmidt, M Nicklas, and E Hassinger. On the search for the chiral anomaly in weyl semimetals: the negative longitudinal magnetoresistance. *New Journal of Physics*, 18(8):085006, 2016.

[64] M. I. Dyakonov and M. S. Shur. Plasma wave electronics: novel terahertz devices using two dimensional electron fluid. *IEEE Transactions on Electron Devices*, 43(10):1640–1645, 1996.

[65] Michael Dyakonov and Michael Shur. Shallow water analogy for a ballistic field effect transistor: New mechanism of plasma wave generation by dc current. *Phys. Rev. Lett.*, 71:2465–2468, Oct 1993.

[66] Carl Eckart. Vortices and streams caused by sound waves. *Phys. Rev.*, 73:68–76, Jan 1948.

[67] Dmitry K. Efimkin and Allan H. MacDonald. Helical network model for twisted bilayer graphene. *Phys. Rev. B*, 98:035404, Jul 2018.

[68] L. Engel, H.P. Wei, D.C. Tsui, and M. Shayegan. Critical exponent in the fractional quantum hall effect. *Surf. Sci.*, 229(1):13 – 15, 1990.

[69] L. W. Engel, D. Shahar, Ç. Kurdak, and D. C. Tsui. Microwave frequency dependence of integer quantum hall effect: Evidence for finite-frequency scaling. *Phys. Rev. Lett.*, 71:2638–2641, Oct 1993.

[70] Richard P. Feynman. The qualitative behavior of yang-mills theory in 2 + 1 dimensions. *Nuclear Physics B*, 188(3):479 – 512, 1981.

[71] Matthew P A Fisher and D. H. Lee. Correspondence between two-dimensional bosons and a bulk superconductor in a magnetic field. *Phys. Rev. B.*, 39(4):2756–2759, feb 1989.

[72] Matthew P. A. Fisher, Peter B Weichman, G. Grinstein, and Daniel S Fisher. Boson localization and the superfluid-insulator transition. *Phys. Rev. B.*, 40(1):546–570, jul 1989.

[73] A. Liam Fitzpatrick, Shamit Kachru, Jared Kaplan, and S. Raghu. Non-Fermi-liquid behavior of large-N_B quantum critical metals. *Phys. Rev. B*, 89:165114, Apr 2014.

[74] D. Forster. *Hydrodynamic Fluctuations, Broken Symmetry, and Correlation Functions*. Frontiers in Physics 47. W.A. Bemjamin, 1975.

[75] Matthew S. Foster and Igor L. Aleiner. Slow imbalance relaxation and thermoelectric transport in graphene. *Phys. Rev. B*, 79:085415, Feb 2009.

[76] Eduardo H. Fradkin and Steven Kivelson. Modular invariance, self-duality and the phase transition between quantum Hall plateaus. *Nucl. Phys.*, B474:543–574, 1996.

[77] Lars Fritz, Jörg Schmalian, Markus Müller, and Subir Sachdev. Quantum critical transport in clean graphene. *Phys. Rev. B*, 78:085416, Aug 2008.

[78] J. Fröhlich and A Zee. Large scale physics of the quantum hall fluid. *Nuclear Physics B*, 364(3):517–540, oct 1991.

[79] Kenji Fukushima, Dmitri E. Kharzeev, and Harmen J. Warringa. Chiral magnetic effect. *Phys. Rev. D*, 78:074033, Oct 2008.

[80] O. Furtmaier, M. Mendoza, I. Karlin, S. Succi, and H. J. Herrmann. Rayleigh-bénard instability in graphene. *Phys. Rev. B*, 91:085401, Feb 2015.

[81] M. Geracie, M. Goykhman, and D. T. Son. Dense Chern-Simons matter with fermions at large N. *Journal of High Energy Physics*, 4:103, April 2016.

[82] S. D. Geraedts and O. I. Motrunich. Monte Carlo study of a $U(1) \times U(1)$ loop model with modular invariance. *Phys. Rev. B.*, 86:245121, December 2012.

[83] S. D. Geraedts, M. P. Zaletel, R. S. K. Mong, M. A. Metlitski, A. Vishwanath, and O. I. Motrunich. The half-filled Landau level: The case for Dirac composite fermions. *Science*, 352:197, 2016.

[84] Valeria Giliberti, Alessandra Di Gaspare, Ennio Giovine, Michele Ortolani, Lucia Sorba, Giorgio Biasiol, Vyacheslav V. Popov, Denis V. Fateev, and Florestano Evangelisti. Downconversion of terahertz radiation due to intrinsic hydrodynamic nonlinearity of a two-dimensional electron plasma. *Phys. Rev. B*, 91:165313, Apr 2015.

[85] S. Giombi, V. Gurucharan, V. Kirilin, S. Prakash, and E. Skvortsov. On the Higher-Spin Spectrum in Large N Chern-Simons Vector Models. *Journal of High Energy Physics*, 2017(1):58, Jan 2017.

[86] Simone Giombi, Shiraz Minwalla, Shiroman Prakash, Sandip P. Trivedi, Spenta R. Wadia, and Xi Yin. Chern-Simons Theory with Vector Fermion Matter. *The European Physical Journal C*, 72(8):2112, Aug 2012.

[87] S. M. Girvin and A. H. MacDonald. Off-diagonal long-range order, oblique confinement, and the fractional quantum Hall effect. *Phys. Rev. Lett.*, 58:1252–1255, Mar 1987.

[88] Hart Goldman and Eduardo Fradkin. Loop models, modular invariance, and three-dimensional bosonization. *Phys. Rev. B*, 97:195112, May 2018.

[89] J. Gooth, F. Menges, N. Kumar, V. Süb, C. Shekhar, Y. Sun, U. Drechsler, R. Zierold, C. Felser, and B. Gotsmann. Thermal and electrical signatures of a hydrodynamic electron fluid in tungsten diphosphide. *Nature Communications*, 9(1):4093, 2018.

[90] P. Goswami and S. Chakravarty. Superuniversality of topological quantum phase transition and global phase diagram of dirty topological systems in three dimensions. *Phys. Rev. B*, 95:075131, February 2017.

[91] Pallab Goswami, J. H. Pixley, and S. Das Sarma. Axial anomaly and longitudinal magnetoresistance of a generic three-dimensional metal. *Phys. Rev. B*, 92:075205, Aug 2015.

[92] Adolfo G. Grushin, Jörn W. F. Venderbos, Ashvin Vishwanath, and Roni Ilan. Inhomogeneous weyl and dirac semimetals: Transport in axial magnetic fields and fermi arc surface states from pseudo-landau levels. *Phys. Rev. X*, 6:041046, Dec 2016.

[93] G. Gur-Ari, S. Hartnoll, and R. Mahajan. Transport in Chern-Simons-matter theories. *Journal of High Energy Physics*, 7:90, July 2016.

[94] G. Gur-Ari and R. Yacoby. Three dimensional bosonization from supersymmetry. *Journal of High Energy Physics*, 11:13, November 2015.

[95] V. Gurucharan and Shiroman Prakash. Anomalous Dimensions in Non-Supersymmetric Bifundamental Chern-Simons Theories. *Journal of High Energy Physics*, 2014(9):9, Sep 2014.

[96] G. M. Gusev, A. S. Jaroshevich, A. D. Levin, Z. D. Kvon, and A. K. Bakarov. Stokes flow around an obstacle in viscous two-dimensional electron liquid. *Scientific Reports*, 10(1):7860, May 2020.

[97] G. M. Gusev, A. D. Levin, E. V. Levinson, and A. K. Bakarov. Viscous electron flow in mesoscopic two-dimensional electron gas. *AIP Advances*, 8(2):025318, 2018.

[98] F. D. M. Haldane. Model for a Quantum Hall Effect without Landau Levels: Condensed-Matter Realization of the "Parity Anomaly". *Phys. Rev. Lett.*, 61:2015–2018, Oct 1988.

[99] B. I. Halperin, Patrick A. Lee, and Nicholas Read. Theory of the half-filled landau level. *Phys. Rev. B*, 47:7312–7343, Mar 1993.

[100] Sean A. Hartnoll, Pavel K. Kovtun, Markus Müller, and Subir Sachdev. Theory of the nernst effect near quantum phase transitions in condensed matter and in dyonic black holes. *Phys. Rev. B*, 76:144502, Oct 2007.

[101] Sean A. Hartnoll, Andrew Lucas, and Subir Sachdev. Holographic quantum matter. *arXiv*, Dec 2016.

[102] H. T. He, H. C. Liu, B. K. Li, X. Guo, Z. J. Xu, M. H. Xie, and J. N. Wang. Disorder-induced linear magnetoresistance in (221) topological insulator bi2se3 films. *Applied Physics Letters*, 103(3):031606, 2013.

[103] Max Hirschberger, Satya Kushwaha, Zhijun Wang, Quinn Gibson, Sihang Liang, Carina A. Belvin, B. A. Bernevig, R. J. Cava, and N. P. Ong. The chiral anomaly and thermopower of Weyl fermions in the half-Heusler GdPtBi. *Nat. Mater.*, 15(11):1161–1165, Nov 2016.

[104] Tobias Holder, Raquel Queiroz, Thomas Scaffidi, Navot Silberstein, Asaf Rozen, Joseph A. Sulpizio, Lior Ella, Shahal Ilani, and Ady Stern. Ballistic and hydrodynamic magnetotransport in narrow channels. *Phys. Rev. B*, 100:245305, Dec 2019.

[105] Chang-Yu Hou and Claudio Chamon. Junctions of three quantum wires for spin-$\frac{1}{2}$ electrons. *Phys. Rev. B*, 77:155422, Apr 2008.

[106] Chang-Yu Hou, Eun-Ah Kim, and Claudio Chamon. Corner junction as a probe of helical edge states. *Phys. Rev. Lett.*, 102:076602, Feb 2009.

[107] Tao Hou, Yafei Ren, Yujie Quan, Jeil Jung, Wei Ren, and Zhenhua Qiao. Metallic network of topological domain walls. *Phys. Rev. B*, 101:201403, May 2020.

[108] Tao Hou, Yafei Ren, Yujie Quan, Jeil Jung, Wei Ren, and Zhenhua Qiao. Valley current splitter in minimally twisted bilayer graphene. *Phys. Rev. B*, 102:085433, Aug 2020.

[109] Po-Shen Hsin and Nathan Seiberg. Level/rank Duality and Chern-Simons-Matter Theories. *JHEP*, 09:095, 2016.

[110] J. Hu, J. Y. Liu, D. Graf, S. M. A. Radmanesh, D. J. Adams, A. Chuang, Y. Wang, I. Chiorescu, J. Wei, L. Spinu, and Z. Q. Mao. p berry phase and zeeman splitting of weyl semimetal tap. *Scientific Reports*, 6:18674, Jan 2016.

[111] Shengqiang Huang, Kyounghwan Kim, Dmitry K. Efimkin, Timothy Lovorn, Takashi Taniguchi, Kenji Watanabe, Allan H. MacDonald, Emanuel Tutuc, and Brian J. LeRoy. Topologically protected helical states in minimally twisted bilayer graphene. *Phys. Rev. Lett.*, 121:037702, Jul 2018.

[112] Xiaochun Huang, Lingxiao Zhao, Yujia Long, Peipei Wang, Dong Chen, Zhanhai Yang, Hui Liang, Mianqi Xue, Hongming Weng, Zhong Fang, Xi Dai, and Genfu Chen. Observation of the chiral-anomaly-induced negative magnetoresistance in 3d weyl semimetal taas. *Phys. Rev. X*, 5:031023, Aug 2015.

[113] Bodo Huckestein. Scaling theory of the integer quantum Hall effect. *Rev. Mod. Phys.*, 67:357–396, Apr 1995.

[114] A. Hui, E.-A. Kim, and M. Mulligan. Superuniversality and non-abelian bosonization in $2 + 1$ dimensions. *ArXiv e-prints*, December 2017.

[115] Aaron Hui, Eun-Ah Kim, and Michael Mulligan. Non-abelian bosonization and modular transformation approach to superuniversality. *Phys. Rev. B*, 99:125135, Mar 2019.

[116] Aaron Hui, Samuel Lederer, Vadim Oganesyan, and Eun-Ah Kim. Quantum aspects of hydrodynamic transport from weak electron-impurity scattering. *Phys. Rev. B*, 101:121107, Mar 2020.

[117] Aaron Hui, Michael Mulligan, and Eun-Ah Kim. Non-abelian fermionization and fractional quantum hall transitions. *Phys. Rev. B*, 97:085112, Feb 2018.

[118] Aaron Hui, Michael Mulligan, and Eun-Ah Kim. Non-abelian fermionization and fractional quantum hall transitions. *Phys. Rev. B*, 97:085112, Feb 2018.

[119] Aaron Hui, Vadim Oganesyan, and Eun-Ah Kim. Beyond ohm's law: Bernoulli effect and streaming in electron hydrodynamics. *Phys. Rev. B*, 103:235152, Jun 2021.

[120] Aaron Hui, Yi Zhang, and Eun-Ah Kim. Optical signatures of the chiral anomaly in mirror-symmetric weyl semimetals. *Phys. Rev. B*, 100:085144, Aug 2019.

[121] Y. Huo, R. E. Hetzel, and R. N. Bhatt. Universal conductance in the lowest Landau level. *Phys. Rev. Lett.*, 70:481–484, Jan 1993.

[122] Jimmy A. Hutasoit, Jiadong Zang, Radu Roiban, and Chao-Xing Liu. Weyl fermions induced magnon electrodynamics in a weyl semimetal. *Phys. Rev. B*, 90:134409, Oct 2014.

[123] K. Intriligator and N. Seiberg. Lectures on supersymmetric gauge theories and electric-magnetic duality. *Nuclear Physics B Proceedings Supplements*, 45:1–28, February 1996.

[124] J. K. Jain. Composite-fermion approach for the fractional quantum Hall effect. *Phys. Rev. Lett.*, 63(2):199–202, jul 1989.

[125] J. K. Jain, S. A. Kivelson, and Nandini Trivedi. Scaling theory of the fractional quantum hall effect. *Phys. Rev. Lett.*, 64:1297–1300, Mar 1990.

[126] S. Jain, S. Minwalla, and S. Yokoyama. Chern Simons duality with a fundamental boson and fermion. *Journal of High Energy Physics*, 11:37, November 2013.

[127] Lili Jiang, Zhiwen Shi, Bo Zeng, Sheng Wang, Ji-Hun Kang, Trinity Joshi, Chenhao Jin, Long Ju, Jonghwan Kim, Tairu Lyu, Yuen-Ron Shen, Michael Crommie, Hong-Jun Gao, and Feng Wang. Soliton-dependent plasmon reflection at bilayer graphene domain walls. *Nature Materials*, 15(8):840–844, Aug 2016.

[128] Qing-Dong Jiang, Hua Jiang, Haiwen Liu, Qing-Feng Sun, and X. C. Xie. Topological imbert-fedorov shift in weyl semimetals. *Phys. Rev. Lett.*, 115:156602, Oct 2015.

[129] Qing-Dong Jiang, Hua Jiang, Haiwen Liu, Qing-Feng Sun, and X. C. Xie. Chiral wave-packet scattering in weyl semimetals. *Phys. Rev. B*, 93:195165, May 2016.

[130] Long Ju, Zhiwen Shi, Nityan Nair, Yinchuan Lv, Chenhao Jin, Jairo Velasco, Claudia Ojeda-Aristizabal, Hans A. Bechtel, Michael C. Martin, Alex Zettl, James Analytis, and Feng Wang. Topological valley transport at bilayer graphene domain walls. *Nature*, 520(7549):650–655, Apr 2015.

[131] Shamit Kachru, Michael Mulligan, Gonzalo Torroba, and Huajia Wang. Mirror symmetry and the half-filled landau level. *Phys. Rev. B*, 92:235105, Dec 2015.

[132] Shamit Kachru, Michael Mulligan, Gonzalo Torroba, and Huajia Wang. Bosonization and mirror symmetry. *Phys. Rev. D*, 94:085009, Oct 2016.

[133] Shamit Kachru, Michael Mulligan, Gonzalo Torroba, and Huajia Wang. Nonsupersymmetric dualities from mirror symmetry. *Phys. Rev. Lett.*, 118:011602, Jan 2017.

[134] Vadim Kalmeyer and Shou-Cheng Zhang. Metallic phase of the quantum Hall system at even-denominator filling fractions. *Phys. Rev. B*, 46:9889, 1992.

[135] C. L. Kane and Matthew P. A. Fisher. Transmission through barriers and resonant tunneling in an interacting one-dimensional electron gas. *Phys. Rev. B*, 46:15233–15262, Dec 1992.

[136] Andreas Karch, Brandon Robinson, and David Tong. More abelian dualities in 2 + 1 dimensions. *Journal of High Energy Physics*, 2017(1):17, Jan 2017.

[137] Andreas Karch and David Tong. Particle-vortex duality from 3d bosonization. *Phys. Rev. X*, 6:031043, Sep 2016.

[138] Nathanael P. Kazmierczak, Madeline Van Winkle, Colin Ophus, Karen C. Bustillo, Stephen Carr, Hamish G. Brown, Jim Ciston, Takashi Taniguchi,

Kenji Watanabe, and D. Kwabena Bediako. Strain fields in twisted bilayer graphene. *Nat. Mater.*, pages 1–8, Apr 2021.

[139] Alexander Kerelsky, Leo J. McGilly, Dante M. Kennes, Lede Xian, Matthew Yankowitz, Shaowen Chen, K. Watanabe, T. Taniguchi, James Hone, Cory Dean, Angel Rubio, and Abhay N. Pasupathy. Maximized electron interactions at the magic angle in twisted bilayer graphene. *Nature*, 572(7767):95–100, Aug 2019.

[140] Dmitri E. Kharzeev, Larry D. McLerran, and Harmen J. Warringa. The effects of topological charge change in heavy ion collisions: "event by event p and cp violation". *Nuclear Physics A*, 803(3):227 – 253, 2008.

[141] N. Kikugawa, P. Goswami, A. Kiswandhi, E. S. Choi, D. Graf, R. E. Baumbach, J. S. Brooks, K. Sugii, Y. Iida, M. Nishio, S. Uji, T. Terashima, P. M. C. Rourke, N. E. Hussey, H. Takatsu, S. Yonezawa, Y. Maeno, and L. Balicas. Interplanar coupling-dependent magnetoresistivity in high-purity layered metals. *Nature Communications*, 7:10903, Mar 2016. Article.

[142] Heon-Jung Kim, Ki-Seok Kim, J.-F. Wang, M. Sasaki, N. Satoh, A. Ohnishi, M. Kitaura, M. Yang, and L. Li. Dirac versus weyl fermions in topological insulators: Adler-bell-jackiw anomaly in transport phenomena. *Phys. Rev. Lett.*, 111:246603, Dec 2013.

[143] Egor I. Kiselev and Jörg Schmalian. Boundary conditions of viscous electron flow. *Phys. Rev. B*, 99:035430, Jan 2019.

[144] Steven Kivelson, Dung-Hai Lee, and Shou-Cheng Zhang. Global phase diagram in the quantum Hall effect. *Phys. Rev. B.*, 46(4):2223–2238, jul 1992.

[145] S. Koch, R. J. Haug, K. v. Klitzing, and K. Ploog. Size-dependent analysis of the metal-insulator transition in the integral quantum hall effect. *Phys. Rev. Lett.*, 67:883–886, Aug 1991.

[146] R. Krishna Kumar, D. A. Bandurin, F. M. D. Pellegrino, Y. Cao, A. Principi, H. Guo, G. H. Auton, M. Ben Shalom, L. A. Ponomarenko, G. Falkovich, K. Watanabe, T. Taniguchi, I. V. Grigorieva, L. S. Levitov, M. Polini, and A. K. Geim. Superballistic flow of viscous electron fluid through graphene constrictions. *Nat. Phys.*, 13(12):1182–1185, Dec 2017.

[147] Mark J. H. Ku, Tony X. Zhou, Qing Li, Young J. Shin, Jing K. Shi, Claire Burch, Laurel E. Anderson, Andrew T. Pierce, Yonglong Xie, Assaf Hamo,

Uri Vool, Huiliang Zhang, Francesco Casola, Takashi Taniguchi, Kenji Watanabe, Michael M. Fogler, Philip Kim, Amir Yacoby, and Ronald L. Walsworth. Imaging viscous flow of the dirac fluid in graphene. *Nature*, 583(7817):537–541, Jul 2020.

[148] K. Kuroda, T. Tomita, M.-T. Suzuki, C. Bareille, A. A. Nugroho, P. Goswami, M. Ochi, M. Ikhlas, M. Nakayama, S. Akebi, R. Noguchi, R. Ishii, N. Inami, K. Ono, H. Kumigashira, A. Varykhalov, T. Muro, T. Koretsune, R. Arita, S. Shin, Takeshi Kondo, and S. Nakatsuji. Evidence for magnetic weyl fermions in a correlated metal. *Nature Materials*, 16:1090, Sep 2017.

[149] LD Landau. Soviet phys. jetp 3, 920 (1957). *Soviet Phys. JETP*, 5:101, 1957.

[150] L.D. Landau and E.M. Lifshitz. *Fluid Mechanics: Volume 6*. Number v. 6. Elsevier Science, 2013.

[151] Akash Laturia, Maarten L. Van de Put, and William G. Vandenberghe. Dielectric properties of hexagonal boron nitride and transition metal dichalcogenides: from monolayer to bulk. *npj 2D Materials and Applications*, 2(1):6, Mar 2018.

[152] R. B. Laughlin, Marvin L. Cohen, J. M. Kosterlitz, Herbert Levine, Stephen B. Libby, and Adrianus M. M. Pruisken. Scaling of conductivities in the fractional quantum hall effect. *Phys. Rev. B*, 32:1311–1314, Jul 1985.

[153] Patrick Ledwith, Haoyu Guo, Andrey Shytov, and Leonid Levitov. Tomographic dynamics and scale-dependent viscosity in 2d electron systems. *Phys. Rev. Lett.*, 123:116601, Sep 2019.

[154] Dung-Hai Lee. Anyon Superconductivity and the Fractional Quantum-Hall Effect. *International Journal of Modern Physics B*, 05(10):1695–1713, jun 1991.

[155] Dung-Hai Lee, Ziqiang Wang, and Steven Kivelson. Quantum percolation and plateau transitions in the quantum hall effect. *Phys. Rev. Lett.*, 70:4130–4133, Jun 1993.

[156] J. Y. Lee, S. Geraedts, and O. I. Motrunich. Monte Carlo study of phase transitions out of symmetry-enriched topological phases of bosons in two dimensions. *Phys. Rev. B*, 93:035103, January 2016.

[157] Jongjun M. Lee, Masaki Oshikawa, and Gil Young Cho. Non-fermi liquids in conducting two-dimensional networks. *Phys. Rev. Lett.*, 126:186601, May 2021.

[158] Robert G. Leigh and Anastasios C. Petkou. SL(2,Z) action on three-dimensional CFTs and holography. *JHEP*, 12:020, 2003.

[159] A. D. Levin, G. M. Gusev, E. V. Levinson, Z. D. Kvon, and A. K. Bakarov. Vorticity-induced negative nonlocal resistance in a viscous two-dimensional electron system. *Phys. Rev. B*, 97:245308, Jun 2018.

[160] Herbert Levine, Stephen B. Libby, and Adrianus M. M. Pruisken. Theory of the Quantized Hall Effect. 1. *Nucl. Phys.*, B240:30–48, 1984.

[161] Leonid Levitov and Gregory Falkovich. Electron viscosity, current vortices and negative nonlocal resistance in graphene. *Nature Physics*, 12:672, Feb 2016.

[162] Guohong Li, A. Luican, J. M. B. Lopes dos Santos, A. H. Castro Neto, A. Reina, J. Kong, and E. Y. Andrei. Observation of van hove singularities in twisted graphene layers. *Nature Physics*, 6(2):109–113, 2010.

[163] Hongyuan Li, Shaowei Li, Mit H. Naik, Jingxu Xie, Xinyu Li, Jiayin Wang, Emma Regan, Danqing Wang, Wenyu Zhao, Sihan Zhao, Salman Kahn, Kentaro Yumigeta, Mark Blei, Takashi Taniguchi, Kenji Watanabe, Sefaattin Tongay, Alex Zettl, Steven G. Louie, Feng Wang, and Michael F. Crommie. Imaging moiré flat bands in three-dimensional reconstructed WSe2/WS2 superlattices. *Nat. Mater.*, pages 1–6, Feb 2021.

[164] Hui Li, Hongtao He, Hai-Zhou Lu, Huachen Zhang, Hongchao Liu, Rong Ma, Zhiyong Fan, Shun-Qing Shen, and Jiannong Wang. Negative magnetoresistance in dirac semimetal cd3as2. *Nature Communications*, 7:10301, Jan 2016. Article.

[165] Jing Li, Ke Wang, Kenton J. McFaul, Zachary Zern, Yafei Ren, Kenji Watanabe, Takashi Taniguchi, Zhenhua Qiao, and Jun Zhu. Gate-controlled topological conducting channels in bilayer graphene. *Nat. Nanotechnol.*, 11(12):1060–1065, Dec 2016.

[166] Qiang Li, Dmitri E. Kharzeev, Cheng Zhang, Yuan Huang, I. Pletikosic, A. ?. V. Fedorov, R. ?. D. Zhong, J. ?. A. Schneeloch, G. ?. D. Gu, and T. Valla. Chiral magnetic effect in zrte5. *Nature Physics*, 12:550, Feb 2016.

[167] Wanli Li, G. A. Csáthy, D. C. Tsui, L. N. Pfeiffer, and K. W. West. Scaling and universality of integer quantum hall plateau-to-plateau transitions. *Phys. Rev. Lett.*, 94:206807, May 2005.

[168] Wanli Li, C. L. Vicente, J. S. Xia, W. Pan, D. C. Tsui, L. N. Pfeiffer, and K. W. West. Scaling in plateau-to-plateau transition: A direct connection of quantum hall systems with the anderson localization model. *Phys. Rev. Lett.*, 102:216801, May 2009.

[169] Wanli Li, J. S. Xia, C. Vicente, N. S. Sullivan, W. Pan, D. C. Tsui, L. N. Pfeiffer, and K. W. West. Crossover from the nonuniversal scaling regime to the universal scaling regime in quantum hall plateau transitions. *Phys. Rev. B*, 81:033305, Jan 2010.

[170] Sihang Liang, Jingjing Lin, Satya Kushwaha, Jie Xing, Ni Ni, R. J. Cava, and N. P. Ong. Experimental tests of the chiral anomaly magnetoresistance in the dirac-weyl semimetals $\mathrm{na}_3\mathrm{Bi}$ and gdptbi. *Phys. Rev. X*, 8:031002, Jul 2018.

[171] Tian Liang, Quinn Gibson, Mazhar N. Ali, Minhao Liu, R. J. Cava, and N. P. Ong. Ultrahigh mobility and giant magnetoresistance in the dirac semimetal?cd3as2. *Nature Materials*, 14:280, Nov 2014.

[172] E.M. Lifshitz and L.P. Pitaevskii. *Physical Kinetics*. Number v. 10. Elsevier Science, 2012.

[173] Sir James Lighthill. Acoustic streaming. *Journal of Sound and Vibration*, 61(3):391 – 418, 1978.

[174] Chao-Xing Liu, Peng Ye, and Xiao-Liang Qi. Chiral gauge field and axial anomaly in a weyl semimetal. *Phys. Rev. B*, 87:235306, Jun 2013.

[175] S.H. Liu. Nonlocal conductivities and dielectric functions of free electron gas with impurity scattering. *Annals of Physics*, 59(1):165 – 200, 1970.

[176] Xiaomeng Liu, Zeyu Hao, Eslam Khalaf, Jong Yeon Lee, Yuval Ronen, Hyobin Yoo, Danial Haei Najafabadi, Kenji Watanabe, Takashi Taniguchi, Ashvin Vishwanath, and Philip Kim. Tunable spin-polarized correlated states in twisted double bilayer graphene. *Nature*, 583(7815):221–225, Jul 2020.

[177] Ana Lopez and Eduardo Fradkin. Fractional quantum Hall effect and Chern-Simons gauge theories. *Phys. Rev. B.*, 44(10):5246–5262, sep 1991.

[178] Xiaobo Lu, Petr Stepanov, Wei Yang, Ming Xie, Mohammed Ali Aamir, Ipsita Das, Carles Urgell, Kenji Watanabe, Takashi Taniguchi, Guangyu Zhang, Adrian Bachtold, Allan H. MacDonald, and Dmitri K. Efetov. Superconductors, orbital magnets and correlated states in magic-angle bilayer graphene. *Nature*, 574(7780):653–657, Oct 2019.

[179] Andrew Lucas. Hydrodynamic transport in strongly coupled disordered quantum field theories. *New Journal of Physics*, 17(11):113007, oct 2015.

[180] Andrew Lucas and Kin Chung Fong. Hydrodynamics of electrons in graphene. *Journal of Physics: Condensed Matter*, 30(5):053001, jan 2018.

[181] Andrew Lucas and Sean A. Hartnoll. Resistivity bound for hydrodynamic bad metals. *Proceedings of the National Academy of Sciences*, 114(43):11344–11349, 2017.

[182] Andrew Lucas and Subir Sachdev. Memory matrix theory of magnetotransport in strange metals. *Phys. Rev. B*, 91:195122, May 2015.

[183] Andreas W. W. Ludwig, Matthew P. A. Fisher, R. Shankar, and G. Grinstein. Integer quantum Hall transition: An alternative approach and exact results. *Phys. Rev. B*, 50:7526–7552, Sep 1994.

[184] A. Luther and I. Peschel. Single-particle states, kohn anomaly, and pairing fluctuations in one dimension. *Phys. Rev. B*, 9:2911–2919, Apr 1974.

[185] C. A. Lutken and Graham G. Ross. Duality in the quantum Hall system. *Phys. Rev. B*, 45(20):11837, 1992.

[186] Min Lv and Shou-Cheng Zhang. Dielectric function, friedel oscillation and plasmons in weyl semimetals. *International Journal of Modern Physics B*, 27(25):1350177, 2013.

[187] Qiong Ma, Su-Yang Xu, Ching-Kit Chan, Cheng-Long Zhang, Guoqing Chang, Yuxuan Lin, Weiwei Xie, Tomás Palacios, Hsin Lin, Shuang Jia, Patrick A. Lee, Pablo Jarillo-Herrero, and Nuh Gedik. Direct optical detection of weyl fermion chirality in a topological semimetal. *Nature Physics*, 13:842 EP –, May 2017.

[188] G.D. Mahan. *Many-Particle Physics*. Physics of Solids and Liquids. Springer US, 2000.

[189] S. Mandelstam. Soliton operators for the quantized sine-gordon equation. *Phys. Rev. D*, 11:3026–3030, May 1975.

[190] Ivar Martin, Ya. M. Blanter, and A. F. Morpurgo. Topological confinement in bilayer graphene. *Phys. Rev. Lett.*, 100:036804, Jan 2008.

[191] James Clerk Maxwell. V. illustrations of the dynamical theory of gases.—part i. on the motions and collisions of perfectly elastic spheres. *The London, Edinburgh, and Dublin Philosophical Magazine and Journal of Science*, 19(124):19–32, 1860.

[192] Leo J. McGilly, Alexander Kerelsky, Nathan R. Finney, Konstantin Shapovalov, En-Min Shih, Augusto Ghiotto, Yihang Zeng, Samuel L. Moore, Wenjing Wu, Yusong Bai, Kenji Watanabe, Takashi Taniguchi, Massimiliano Stengel, Lin Zhou, James Hone, Xiaoyang Zhu, Dmitri N. Basov, Cory Dean, Cyrus E. Dreyer, and Abhay N. Pasupathy. Visualization of moiré superlattices. *Nature Nanotechnology*, 15:580–584, 2020.

[193] Max A. Metlitski and Ashvin Vishwanath. Particle-vortex duality of two-dimensional Dirac fermion from electric-magnetic duality of three-dimensional topological insulators. *Phys. Rev. B.*, 93(24):245151, jun 2016.

[194] KNOX MILLSAPS and KARL POHLHAUSEN. Thermal distributions in jeffery-hamel flows between nonparallel plane walls. *Journal of the Aeronautical Sciences*, 20(3):187–196, 1953.

[195] Philip J. W. Moll, Pallavi Kushwaha, Nabhanila Nandi, Burkhard Schmidt, and Andrew P. Mackenzie. Evidence for hydrodynamic electron flow in pdcoo2. *Science*, 351(6277):1061–1064, 2016.

[196] D. F. Mross, J. Alicea, and O. I. Motrunich. Symmetry and duality in bosonization of two-dimensional Dirac fermions. *Phys. Rev. X*, 7:041016, Oct 2017.

[197] David F. Mross, Jason Alicea, and Olexei I. Motrunich. Bosonic Analogue of Dirac Composite Fermi Liquid. *Phys. Rev. Lett.*, 117:136802, Sep 2016.

[198] David F. Mross, Jason Alicea, and Olexei I. Motrunich. Explicit Derivation

of Duality between a Free Dirac Cone and Quantum Electrodynamics in $(2+1)$ Dimensions. *Phys. Rev. Lett.*, 117:016802, Jun 2016.

[199] Markus Müller, Jörg Schmalian, and Lars Fritz. Graphene: A nearly perfect fluid. *Phys. Rev. Lett.*, 103:025301, Jul 2009.

[200] Michael Mulligan, S. Raghu, and Matthew P. A. Fisher. Emergent particle-hole symmetry in the half-filled landau level. *Phys. Rev. B*, 94:075101, Aug 2016.

[201] J. Murugan and H. Nastase. Particle-vortex duality in topological insulators and superconductors. *Journal of High Energy Physics*, 5:159, May 2017.

[202] Stephen G. Naculich and Howard J. Schnitzer. Duality between $SU(N)_k$ and $SU(k)_N$ WZW models. *Nucl. Phys. B*, 347:687 – 742, 1990.

[203] Tomoki Nakanishi and Akihiro Tsuchiya. Level-rank duality of wzw models in conformal field theory. *Communications in Mathematical Physics*, 144(2):351–372, Feb 1992.

[204] B. N. Narozhny and M. Schütt. Magnetohydrodynamics in graphene: Shear and hall viscosities. *Phys. Rev. B*, 100:035125, Jul 2019.

[205] H.B. Nielsen and Masao Ninomiya. The adler-bell-jackiw anomaly and weyl fermions in a crystal. *Physics Letters B*, 130(6):389 – 396, 1983.

[206] Anna Corinna Niemann, Johannes Gooth, Shu-Chun Wu, Svenja Bäßler, Philip Sergelius, Ruben Hühne, Bernd Rellinghaus, Chandra Shekhar, Vicky Süß, Marcus Schmidt, Claudia Felser, Binghai Yan, and Kornelius Nielsch. Chiral magnetoresistance in the weyl semimetal nbp. *Scientific Reports*, 7:43394, Mar 2017. Article.

[207] A.J. Niemi and G.W. Semenoff. Axial Anomaly Induced Fermion Fractionization and Effective Gauge Theory Actions in Odd Dimensional Space-Times. *Phys. Rev. Lett.*, 51:2077, 1983.

[208] WESLEY LE MARS NYBORG. 11 - acoustic streaming. In WARREN P. MASON, editor, *Properties of Polymers and Nonlinear Acoustics*, volume 2 of *Physical Acoustics*, pages 265 – 331. Academic Press, 1965.

[209] Hui Pan, Xin Li, Fan Zhang, and Shengyuan A. Yang. Perfect valley filter in a topological domain wall. *Phys. Rev. B*, 92:041404, Jul 2015.

[210] I. Panfilov, A. A. Burkov, and D. A. Pesin. Density response in weyl metals. *Phys. Rev. B*, 89:245103, Jun 2014.

[211] Jeong Min Park, Yuan Cao, Kenji Watanabe, Takashi Taniguchi, and Pablo Jarillo-Herrero. Tunable strongly coupled superconductivity in magic-angle twisted trilayer graphene. *Nature*, 590:249–255, 2021.

[212] Francesco M. D. Pellegrino, Iacopo Torre, Andre K. Geim, and Marco Polini. Electron hydrodynamics dilemma: Whirlpools or no whirlpools. *Phys. Rev. B*, 94:155414, Oct 2016.

[213] M.E. Peskin. *An Introduction To Quantum Field Theory*. CRC Press, 2018.

[214] Michael E Peskin. Mandelstam-'t Hooft duality in abelian lattice models. *Annals of Physics*, 113(1):122–152, jul 1978.

[215] D. I. Pikulin, Anffany Chen, and M. Franz. Chiral anomaly from strain-induced gauge fields in dirac and weyl semimetals. *Phys. Rev. X*, 6:041021, Oct 2016.

[216] H. Polshyn, J. Zhu, M. A. Kumar, Y. Zhang, F. Yang, C. L. Tschirhart, M. Serlin, K. Watanabe, T. Taniguchi, A. H. MacDonald, and A. F. Young. Electrical switching of magnetic order in an orbital Chern insulator. *Nature*, 588(7836):66–70, Dec 2020.

[217] D. G. Polyakov and B. I. Shklovskii. Variable range hopping as the mechanism of the conductivity peak broadening in the quantum hall regime. *Phys. Rev. Lett.*, 70:3796–3799, Jun 1993.

[218] Alexios P. Polychronakos. Topological mass quantiztion and parity violation in (2+1)-dimensional QED. *Nucl. Phys. B*, 281:241, 1987.

[219] Alessandro Principi, Denis Bandurin, Habib Rostami, and Marco Polini. Pseudo-euler equations from nonlinear optics: Plasmon-assisted photodetection beyond hydrodynamics. *Phys. Rev. B*, 99:075410, Feb 2019.

[220] Alessandro Principi, Giovanni Vignale, Matteo Carrega, and Marco Polini. Bulk and shear viscosities of the two-dimensional electron liquid in a doped graphene sheet. *Phys. Rev. B*, 93:125410, Mar 2016.

[221] Zhenhua Qiao, Jeil Jung, Chungwei Lin, Yafei Ren, Allan H. MacDonald,

and Qian Niu. Current partition at topological channel intersections. *Phys. Rev. Lett.*, 112:206601, May 2014.

[222] Zhenhua Qiao, Jeil Jung, Qian Niu, and Allan H. MacDonald. Electronic highways in bilayer graphene. *Nano Letters*, 11(8):3453–3459, 2011. PMID: 21766817.

[223] S. Raghu, Gonzalo Torroba, and Huajia Wang. Metallic quantum critical points with finite BCS couplings. *Phys. Rev. B*, 92:205104, Nov 2015.

[224] B. J. Ramshaw, K. A. Modic, Arkady Shekhter, Yi Zhang, Eun-Ah Kim, Philip J. W. Moll, Maja D. Bachmann, M. K. Chan, J. B. Betts, F. Balakirev, A. Migliori, N. J. Ghimire, E. D. Bauer, F. Ronning, and R. D. McDonald. Quantum limit transport and destruction of the weyl nodes in taas. *Nature Communications*, 9(1):2217, 2018.

[225] Lord Rayleigh. On the circulation of air observed in kundt's tubes, and on some allied acoustical problems. *Philosophical Transactions of the Royal Society of London*, 175:1–21, 2020/08/24/ 1883. Full publication date: 1884.

[226] N. Read. Order Parameter and Ginzburg-Landau Theory for the Fractional Quantum Hall Effect. *Phys. Rev. Lett.*, 62:86, 1989.

[227] Matthew D. Redell, Shantanu Mukherjee, and Wei-Cheng Lee. Resonant plasmon-axion excitations induced by charge density wave order in a weyl semimetal. *Phys. Rev. B*, 93:241201, Jun 2016.

[228] A.N. Redlich. Parity Violation and Gauge Noninvariance of the Effective Gauge Field Action in Three-Dimensions. *Phys. Rev. D*, 29:2366–2374, May 1984.

[229] Emma C. Regan, Danqing Wang, Chenhao Jin, M. Iqbal Bakti Utama, Beini Gao, Xin Wei, Sihan Zhao, Wenyu Zhao, Zuocheng Zhang, Kentaro Yumigeta, Mark Blei, Johan D. Carlström, Kenji Watanabe, Takashi Taniguchi, Sefaattin Tongay, Michael Crommie, Alex Zettl, and Feng Wang. Mott and generalized Wigner crystal states in WSe2/WS2 moiré superlattices. *Nature*, 579(7799):359–363, Mar 2020.

[230] Yafei Ren, Zhenhua Qiao, and Qian Niu. Topological phases in two-dimensional materials: a review. *Reports on Progress in Physics*, 79(6):066501, may 2016.

[231] Yafei Ren, Junjie Zeng, Ke Wang, Fuming Xu, and Zhenhua Qiao. Tunable current partition at zero-line intersection of quantum anomalous hall topologies. *Phys. Rev. B*, 96:155445, Oct 2017.

[232] Peter Rickhaus, Folkert de Vries, Jihang Zhu, Elías Portolés, Giulia Zheng, Michele Masseroni, Annika Kurzmann, Takashi Taniguchi, Kenji Wantanabe, Allan H. MacDonald, Thomas Ihn, and Klaus Ensslin. Density-wave states in twisted double-bilayer graphene, 2020.

[233] Peter Rickhaus, John Wallbank, Sergey Slizovskiy, Riccardo Pisoni, Hiske Overweg, Yongjin Lee, Marius Eich, Ming-Hao Liu, Kenji Watanabe, Takashi Taniguchi, Thomas Ihn, and Klaus Ensslin. Transport through a network of topological channels in twisted bilayer graphene. *Nano Letters*, 18(11):6725–6730, Nov 2018.

[234] N Riley. Steady streaming. *Annual Review of Fluid Mechanics*, 33(1):43–65, 2001.

[235] P. Rinkel, P. L. S. Lopes, and Ion Garate. Signatures of the chiral anomaly in phonon dynamics. *Phys. Rev. Lett.*, 119:107401, Sep 2017.

[236] P. Rinkel, P. L. S. Lopes, and Ion Garate. Influence of landau levels on the phonon dispersion of weyl semimetals. *Phys. Rev. B*, 99:144301, Apr 2019.

[237] Matthew R. Rosenberger, Hsun-Jen Chuang, Madeleine Phillips, Vladimir P. Oleshko, Kathleen M. McCreary, Saujan V. Sivaram, C. Stephen Hellberg, and Berend T. Jonker. Twist Angle-Dependent Atomic Reconstruction and Moiré Patterns in Transition Metal Dichalcogenide Heterostructures. *ACS Nano*, 14(4):4550–4558, Apr 2020.

[238] L. Rosenhead. *Laminar Boundary Layers: An Account of the Development, Structure, and Stability of Laminar Boundary Layers in Incompressible Fluids, Together with a Description of the Associated Experimental Techniques*. Dover books on engineering and engineering physics. Dover Publications, 1988.

[239] Subir Sachdev. Nonzero-temperature transport near fractional quantum hall critical points. *Phys. Rev. B*, 57:7157–7173, Mar 1998.

[240] Subir Sachdev. *Quantum Phase Transitions*. Cambridge University Press, 2011.

[241] Subir Sachdev and Markus Müller. Quantum criticality and black holes. *Journal of Physics: Condensed Matter*, 21(16):164216, mar 2009.

[242] Robert Savit. Duality in field theory and statistical systems. *Rev. Mod. Phys.*, 52:453–487, Apr 1980.

[243] N. Seiberg, T. Senthil, C. Wang, and E. Witten. A duality web in 2 + 1 dimensions and condensed matter physics. *Annals of Physics*, 374:395–433, November 2016.

[244] N. Seiberg and E. Witten. Monopoles, duality and chiral symmetry breaking in N = 2 supersymmetric QCD. *Nuclear Physics B*, 431:484–550, December 1994.

[245] Nathan Seiberg, T. Senthil, Chong Wang, and Edward Witten. A Duality Web in 2+1 Dimensions and Condensed Matter Physics. *Annals of Physics*, 374(Supplement C):395 – 433, 2016.

[246] M. Serlin, C. L. Tschirhart, H. Polshyn, Y. Zhang, J. Zhu, K. Watanabe, T. Taniguchi, L. Balents, and A. F. Young. Intrinsic quantized anomalous hall effect in a moiré heterostructure. *Science*, 367(6480):900–903, 2020.

[247] D. Shahar, D. C. Tsui, M. Shayegan, R. N. Bhatt, and J. E. Cunningham. Universal conductivity at the quantum hall liquid to insulator transition. *Phys. Rev. Lett.*, 74:4511–4514, May 1995.

[248] Aaron L. Sharpe, Eli J. Fox, Arthur W. Barnard, Joe Finney, Kenji Watanabe, Takashi Taniguchi, M. A. Kastner, and David Goldhaber-Gordon. Emergent ferromagnetism near three-quarters filling in twisted bilayer graphene. *Science*, 365(6453):605–608, 2019.

[249] Michal Shavit, Andrey Shytov, and Gregory Falkovich. Freely flowing currents and electric field expulsion in viscous electronics. *Phys. Rev. Lett.*, 123:026801, Jul 2019.

[250] E. Shimshoni, S. L. Sondhi, and D. Shahar. Duality near quantum hall transitions. *Phys. Rev. B*, 55:13730–13738, May 1997.

[251] Andrey Shytov, Jian Feng Kong, Gregory Falkovich, and Leonid Levitov. Particle collisions and negative nonlocal response of ballistic electrons. *Phys. Rev. Lett.*, 121:176805, Oct 2018.

[252] M Singh, P R Wallace, and S Askenazy. Effect of 'free-electron' terms on the g-factor of some semiconductors and semimetals. *Journal of Physics C: Solid State Physics*, 15(33):6731, 1982.

[253] Keith Slevin and Tomi Ohtsuki. Critical exponent for the quantum hall transition. *Phys. Rev. B*, 80:041304, Jul 2009.

[254] Inti Sodemann, Itamar Kimchi, Chong Wang, and T. Senthil. Composite fermion duality for half-filled multicomponent landau levels. *Phys. Rev. B*, 95:085135, Feb 2017.

[255] D. T. Son and B. Z. Spivak. Chiral anomaly and classical negative magnetoresistance of weyl metals. *Phys. Rev. B*, 88:104412, Sep 2013.

[256] Dam T. Son and Andrei O. Starinets. Viscosity, black holes, and quantum field theory. *Annual Review of Nuclear and Particle Science*, 57(1):95–118, 2007.

[257] Dam Thanh Son. Is the Composite Fermion a Dirac Particle? *Physical Review X*, 5(3):1–13, feb 2015.

[258] Dam Thanh Son and Naoki Yamamoto. Berry curvature, triangle anomalies, and the chiral magnetic effect in fermi liquids. *Phys. Rev. Lett.*, 109:181602, Nov 2012.

[259] S L Sondhi, S M Girvin, J P Carini, and D Shahar. Continuous quantum phase transitions. *Rev. Mod. Phys.*, 69(1):315–333, jan 1997.

[260] Zhida Song, Jimin Zhao, Zhong Fang, and Xi Dai. Detecting the chiral magnetic effect by lattice dynamics in weyl semimetals. *Phys. Rev. B*, 94:214306, Dec 2016.

[261] B. Z. Spivak and A. V. Andreev. Magnetotransport phenomena related to the chiral anomaly in weyl semimetals. *Phys. Rev. B*, 93:085107, Feb 2016.

[262] M. Srednicki. *Quantum Field Theory*. Cambridge University Press, 2007.

[263] Petr Stepanov, Ipsita Das, Xiaobo Lu, Ali Fahimniya, Kenji Watanabe, Takashi Taniguchi, Frank H. L. Koppens, Johannes Lischner, Leonid Levitov, and Dmitri K. Efetov. Untying the insulating and superconducting orders in magic-angle graphene. *Nature*, 583:375–378, 2020.

[264] Mengqiao Sui, Guorui Chen, Liguo Ma, Wen-Yu Shan, Dai Tian, Kenji Watanabe, Takashi Taniguchi, Xiaofeng Jin, Wang Yao, Di Xiao, and Yuanbo Zhang. Gate-tunable topological valley transport in bilayer graphene. *Nat. Phys.*, 11(12):1027–1031, Dec 2015.

[265] P. O. Sukhachov, E. V. Gorbar, and I. A. Shovkovy. Hydrodynamics in dirac semimetals: Convection impossible, 2021.

[266] Joseph A. Sulpizio, Lior Ella, Asaf Rozen, John Birkbeck, David J. Perello, Debarghya Dutta, Moshe Ben-Shalom, Takashi Taniguchi, Kenji Watanabe, Tobias Holder, Raquel Queiroz, Alessandro Principi, Ady Stern, Thomas Scaffidi, Andre K. Geim, and Shahal Ilani. Visualizing poiseuille flow of hydrodynamic electrons. *Nature*, 576(7785):75–79, 2019.

[267] S. S. Sunku, D. Halbertal, T. Stauber, S. Chen, A. S. McLeod, A. Rikhter, M. E. Berkowitz, C. F. B. Lo, D. E. Gonzalez-Acevedo, J. C. Hone, C. R. Dean, M. M. Fogler, and D. N. Basov. Hyperbolic enhancement of photocurrent patterns in minimally twisted bilayer graphene. *Nat. Commun.*, 12(1641):1–7, Mar 2021.

[268] S. S. Sunku, G. X. Ni, B. Y. Jiang, H. Yoo, A. Sternbach, A. S. McLeod, T. Stauber, L. Xiong, T. Taniguchi, K. Watanabe, P. Kim, M. M. Fogler, and D. N. Basov. Photonic crystals for nano-light in moiré graphene superlattices. *Science*, 362(6419):1153–1156, 2018.

[269] Sai S. Sunku, Alexander S. McLeod, Tobias Stauber, Hyobin Yoo, Dorri Halbertal, Guangxin Ni, Aaron Sternbach, Bor-Yuan Jiang, Takashi Taniguchi, Kenji Watanabe, Philip Kim, Michael M. Fogler, and D. N. Basov. Nano-photocurrent mapping of local electronic structure in twisted bilayer graphene. *Nano Letters*, 20(5):2958–2964, May 2020.

[270] D. Svintsov, V. Vyurkov, V. Ryzhii, and T. Otsuji. Hydrodynamic electron transport and nonlinear waves in graphene. *Phys. Rev. B*, 88:245444, Dec 2013.

[271] Gerard 't Hooft. A Planar Diagram Theory for Strong Interactions. *Nucl. Phys.*, B72:461, 1974.

[272] Yanhao Tang, Lizhong Li, Tingxin Li, Yang Xu, Song Liu, Katayun Barmak, Kenji Watanabe, Takashi Taniguchi, Allan H. MacDonald, Jie Shan, and Kin Fai Mak. Simulation of Hubbard model physics in WSe2/WS2 moiré superlattices. *Nature*, 579(7799):353–358, Mar 2020.

[273] R. Tauk, F. Teppe, S. Boubanga, D. Coquillat, W. Knap, Y. M. Meziani, C. Gallon, F. Boeuf, T. Skotnicki, C. Fenouillet-Beranger, D. K. Maude, S. Rumyantsev, and M. S. Shur. Plasma wave detection of terahertz radiation by silicon field effects transistors: Responsivity and noise equivalent power. *Applied Physics Letters*, 89(25):253511, 2006.

[274] Andrea Tomadin and Marco Polini. Theory of the plasma-wave photoresponse of a gated graphene sheet. *Phys. Rev. B*, 88:205426, Nov 2013.

[275] Andrea Tomadin, Giovanni Vignale, and Marco Polini. Corbino disk viscometer for 2d quantum electron liquids. *Phys. Rev. Lett.*, 113:235901, Dec 2014.

[276] David Tong. Lectures on the Quantum Hall Effect, jun 2016.

[277] Iacopo Torre, Andrea Tomadin, Andre K. Geim, and Marco Polini. Nonlocal transport and the hydrodynamic shear viscosity in graphene. *Phys. Rev. B*, 92:165433, Oct 2015.

[278] Iacopo Torre, Andrea Tomadin, Roman Krahne, Vittorio Pellegrini, and Marco Polini. Electrical plasmon detection in graphene waveguides. *Phys. Rev. B*, 91:081402, Feb 2015.

[279] Bonnie Tsim, Nguyen N. T. Nam, and Mikito Koshino. Perfect one-dimensional chiral states in biased twisted bilayer graphene. *Phys. Rev. B*, 101:125409, Mar 2020.

[280] Abolhassan Vaezi, Yufeng Liang, Darryl H. Ngai, Li Yang, and Eun-Ah Kim. Topological edge states at a tilt boundary in gated multilayer graphene. *Phys. Rev. X*, 3:021018, Jun 2013.

[281] Georgios Varnavides, Adam S. Jermyn, Polina Anikeeva, Claudia Felser, and Prineha Narang. Electron hydrodynamics in anisotropic materials. *Nature Communications*, 11(1):4710, Sep 2020.

[282] L. Vicarelli, M. S. Vitiello, D. Coquillat, A. Lombardo, A. C. Ferrari, W. Knap, M. Polini, V. Pellegrini, and A. Tredicucci. Graphene field-effect transistors as room-temperature terahertz detectors. *Nature Materials*, 11(10):865–871, Oct 2012.

[283] Niels R Walet and Francisco Guinea. The emergence of one-dimensional

channels in marginal-angle twisted bilayer graphene. *2D Materials*, 7(1):015023, dec 2019.

[284] C. Wang, A. Nahum, M. A. Metlitski, C. Xu, and T. Senthil. Deconfined Quantum Critical Points: Symmetries and Dualities. *Phys. Rev. X*, 7:031051, July 2017.

[285] Chong Wang and T. Senthil. Dual dirac liquid on the surface of the electron topological insulator. *Phys. Rev. X*, 5:041031, Nov 2015.

[286] Chong Wang and T. Senthil. Half-filled landau level, topological insulator surfaces, and three-dimensional quantum spin liquids. *Phys. Rev. B*, 93:085110, Feb 2016.

[287] Lei Wang, En-Min Shih, Augusto Ghiotto, Lede Xian, Daniel A. Rhodes, Cheng Tan, Martin Claassen, Dante M. Kennes, Yusong Bai, Bumho Kim, Kenji Watanabe, Takashi Taniguchi, Xiaoyang Zhu, James Hone, Angel Rubio, Abhay N. Pasupathy, and Cory R. Dean. Correlated electronic phases in twisted bilayer transition metal dichalcogenides. *Nat. Mater.*, 19(8):861–866, Aug 2020.

[288] Yuxuan Wang, Artem Abanov, Boris L. Altshuler, Emil A. Yuzbashyan, and Andrey V. Chubukov. Superconductivity near a quantum-critical point: The special role of the first matsubara frequency. *Phys. Rev. Lett.*, 117:157001, Oct 2016.

[289] Ziqiang Wang, Bo židar Jovanović, and Dung-Hai Lee. Critical conductance and its fluctuations at integer hall plateau transitions. *Phys. Rev. Lett.*, 77:4426–4429, Nov 1996.

[290] H. P. Wei, L. W. Engel, and D. C. Tsui. Current scaling in the integer quantum hall effect. *Phys. Rev. B*, 50:14609–14612, Nov 1994.

[291] H. P. Wei, D. C. Tsui, M. A. Paalanen, and A. M. M. Pruisken. Experiments on delocalization and university in the integral quantum hall effect. *Phys. Rev. Lett.*, 61:1294–1296, Sep 1988.

[292] Xiao-Gang Wen. Topological orders and Edge excitations in FQH states. *Advances in Physics*, 44(5):405–473, jun 1995.

[293] Xiao-Gang Wen and Yong-Shi Wu. Transitions between the quantum

Hall states and insulators induced by periodic potentials. *Phys. Rev. Lett.*, 70(10):1501–1504, mar 1993.

[294] Xiao-Gang Wen and Yong-Shi Wu. Transitions between the quantum hall states and insulators induced by periodic potentials. *Phys. Rev. Lett.*, 70:1501–1504, Mar 1993.

[295] Y. Werman, S. A. Kivelson, and E. Berg. Non-quasiparticle transport and resistivity saturation: A view from the large-N limit. *npj Quantum Materials*, 2(1):7, July 2017.

[296] Peter J. Westervelt. The theory of steady rotational flow generated by a sound field. *The Journal of the Acoustical Society of America*, 25(1):60–67, 1953.

[297] Astrid Weston, Yichao Zou, Vladimir Enaldiev, Alex Summerfield, Nicholas Clark, Viktor Zólyomi, Abigail Graham, Celal Yelgel, Samuel Magorrian, Mingwei Zhou, Johanna Zultak, David Hopkinson, Alexei Barinov, Thomas H. Bointon, Andrey Kretinin, Neil R. Wilson, Peter H. Beton, Vladimir I. Fal'ko, Sarah J. Haigh, and Roman Gorbachev. Atomic reconstruction in twisted bilayers of transition metal dichalcogenides. *Nat. Nanotechnol.*, 15(7):592–597, Jul 2020.

[298] S. Wiedmann, A. Jost, B. Fauqué, J. van Dijk, M. J. Meijer, T. Khouri, S. Pezzini, S. Grauer, S. Schreyeck, C. Brüne, H. Buhmann, L. W. Molenkamp, and N. E. Hussey. Anisotropic and strong negative magnetoresistance in the three-dimensional topological insulator $\mathrm{bi}_2\mathrm{se}_3$. *Phys. Rev. B*, 94:081302, Aug 2016.

[299] Martin Wiklund, Roy Green, and Mathias Ohlin. Acoustofluidics 14: Applications of acoustic streaming in microfluidic devices. *Lab Chip*, 12:2438–2451, 2012.

[300] E. Witten. SL(2,Z) Action On Three-Dimensional Conformal Field Theories With Abelian Symmetry. *ArXiv High Energy Physics - Theory e-prints*, July 2003.

[301] Edward Witten. Quantum field theory and the jones polynomial. *Comm. Math. Phys.*, 121(3):351–399, 1989.

[302] L. W. Wong, H. W. Jiang, N. Trivedi, and E. Palm. Disorder-tuned transition between a quantum hall liquid and hall insulator. *Phys. Rev. B*, 51:18033–18036, Jun 1995.

[303] Congjun Wu, B. Andrei Bernevig, and Shou-Cheng Zhang. Helical liquid and the edge of quantum spin hall systems. *Phys. Rev. Lett.*, 96:106401, Mar 2006.

[304] Xiao-Chuan Wu, Chao-Ming Jian, and Cenke Xu. Coupled-wire description of the correlated physics in twisted bilayer graphene. *Phys. Rev. B*, 99:161405, Apr 2019.

[305] Jun Xiong, Satya K. Kushwaha, Tian Liang, Jason W. Krizan, Max Hirschberger, Wudi Wang, R. J. Cava, and N. P. Ong. Evidence for the chiral anomaly in the dirac semimetal na3bi. *Science*, 350(6259):413–416, 2015.

[306] B. Xu, Y. M. Dai, L. X. Zhao, K. Wang, R. Yang, W. Zhang, J. Y. Liu, H. Xiao, G. F. Chen, S. A. Trugman, J.-X. Zhu, A. J. Taylor, D. A. Yarotski, R. P. Prasankumar, and X. G. Qiu. Temperature-tunable fano resonance induced by strong coupling between weyl fermions and phonons in taas. *Nature Communications*, 8:14933, Mar 2017.

[307] Cenke Xu and Yi-Zhuang You. Self-dual quantum electrodynamics as boundary state of the three-dimensional bosonic topological insulator. *Phys. Rev. B*, 92:220416, Dec 2015.

[308] S. G. Xu, A. I. Berdyugin, P. Kumaravadivel, F. Guinea, R. Krishna Kumar, D. A. Bandurin, S. V. Morozov, W. Kuang, B. Tsim, S. Liu, J. H. Edgar, I. V. Grigorieva, V. I. Fal'ko, M. Kim, and A. K. Geim. Giant oscillations in a triangular network of one-dimensional states in marginally twisted graphene. *Nature Communications*, 10(1):4008, Sep 2019.

[309] Shuigang Xu, Mohammed M. Al Ezzi, Nilanthy Balakrishnan, Aitor Garcia-Ruiz, Bonnie Tsim, Ciaran Mullan, Julien Barrier, Na Xin, Benjamin A. Piot, Takashi Taniguchi, Kenji Watanabe, Alexandra Carvalho, Artem Mishchenko, A. K. Geim, Vladimir I. Fal'ko, Shaffique Adam, Antonio Helio Castro Neto, Kostya S. Novoselov, and Yanmeng Shi. Tunable van Hove singularities and correlated states in twisted monolayer–bilayer graphene. *Nat. Phys.*, pages 1–8, Feb 2021.

[310] Su-Yang Xu, Ilya Belopolski, Nasser Alidoust, Madhab Neupane, Guang Bian, Chenglong Zhang, Raman Sankar, Guoqing Chang, Zhujun Yuan, Chi-Cheng Lee, Shin-Ming Huang, Hao Zheng, Jie Ma, Daniel S. Sanchez, BaoKai Wang, Arun Bansil, Fangcheng Chou, Pavel P. Shibayev, Hsin Lin, Shuang Jia, and M. Zahid Hasan. Discovery of a Weyl fermion semimetal and topological Fermi arcs. *Science*, 349(6248):613–617, Aug 2015.

[311] Binghai Yan and Claudia Felser. Topological materials: Weyl semimetals. *Annual Review of Condensed Matter Physics*, 8(1):337–354, 2017.

[312] Wei Yan, Mengxi Liu, Rui-Fen Dou, Lan Meng, Lei Feng, Zhao-Dong Chu, Yanfeng Zhang, Zhongfan Liu, Jia-Cai Nie, and Lin He. Angle-dependent van hove singularities in a slightly twisted graphene bilayer. *Phys. Rev. Lett.*, 109:126801, Sep 2012.

[313] Matthew Yankowitz, Shaowen Chen, Hryhoriy Polshyn, Yuxuan Zhang, K. Watanabe, T. Taniguchi, David Graf, Andrea F. Young, and Cory R. Dean. Tuning superconductivity in twisted bilayer graphene. *Science*, 363(6431):1059–1064, 2019.

[314] Long-Jing Yin, Hua Jiang, Jia-Bin Qiao, and Lin He. Direct imaging of topological edge states at a bilayer graphene domain wall. *Nat. Commun.*, 7(11760):1–6, Jun 2016.

[315] Hyobin Yoo, Rebecca Engelke, Stephen Carr, Shiang Fang, Kuan Zhang, Paul Cazeaux, Suk Hyun Sung, Robert Hovden, Adam W. Tsen, Takashi Taniguchi, Kenji Watanabe, Gyu-Chul Yi, Miyoung Kim, Mitchell Luskin, Ellad B. Tadmor, Efthimios Kaxiras, and Philip Kim. Atomic and electronic reconstruction at the van der waals interface in twisted bilayer graphene. *Nature Materials*, 18(5):448–453, May 2019.

[316] Xiang Yuan, Cheng Zhang, Yi Zhang, Zhongbo Yan, Tairu Lyu, Mengyao Zhang, Zhilin Li, Chaoyu Song, Minhao Zhao, Pengliang Leng, Mykhaylo Ozerov, Xiaolong Chen, Nanlin Wang, Yi Shi, Hugen Yan, and Faxian Xiu. The discovery of dynamic chiral anomaly in a Weyl semimetal NbAs. *Nat. Commun.*, 11(1259):1–7, Mar 2020.

[317] Jan Zaanen. Planckian dissipation, minimal viscosity and the transport in cuprate strange metals. *SciPost Phys.*, 6:61, 2019.

[318] Anthony Zee. Quantum Hall Fluids. *Field Theory, Topology and Condensed Matter Physics*, (1):82, 1995.

[319] Cheng Zhang, Enze Zhang, Weiyi Wang, Yanwen Liu, Zhi-Gang Chen, Shiheng Lu, Sihang Liang, Junzhi Cao, Xiang Yuan, Lei Tang, Qian Li, Chao Zhou, Teng Gu, Yizheng Wu, Jin Zou, and Faxian Xiu. Room-temperature chiral charge pumping in dirac semimetals. *Nature Communications*, 8:13741, Jan 2017. Article.

[320] Cheng-Long Zhang, Su-Yang Xu, Ilya Belopolski, Zhujun Yuan, Ziquan Lin, Bingbing Tong, Guang Bian, Nasser Alidoust, Chi-Cheng Lee, Shin-Ming Huang, Tay-Rong Chang, Guoqing Chang, Chuang-Han Hsu, Horng-Tay Jeng, Madhab Neupane, Daniel S. Sanchez, Hao Zheng, Junfeng Wang, Hsin Lin, Chi Zhang, Hai-Zhou Lu, Shun-Qing Shen, Titus Neupert, M. Zahid Hasan, and Shuang Jia. Signatures of the adler-bell-jackiw chiral anomaly in a weyl fermion semimetal. *Nature Communications*, 7:10735, Feb 2016. Article.

[321] Fan Zhang, Allan H. MacDonald, and Eugene J. Mele. Valley chern numbers and boundary modes in gapped bilayer graphene. *Proceedings of the National Academy of Sciences*, 110(26):10546–10551, 2013.

[322] S. C. Zhang, T. H. Hansson, and S Kivelson. Effective-Field-Theory Model for the Fractional Quantum Hall Effect. *Phys. Rev. Lett.*, 62(8):980–980, feb 1989.

[323] Shou Cheng Zhang. THE CHERN-SIMONS-LANDAU-GINZBURG THEORY OF THE FRACTIONAL QUANTUM HALL EFFECT. *International Journal of Modern Physics B*, 06(05n06):803–804, mar 1992.

[324] Jianhui Zhou, Hao-Ran Chang, and Di Xiao. Plasmon mode as a detection of the chiral anomaly in weyl semimetals. *Phys. Rev. B*, 91:035114, Jan 2015.

[325] A. A. Zibrov, C. Kometter, H. Zhou, E. M. Spanton, T. Taniguchi, K. Watanabe, M. P. Zaletel, and A. F. Young. Tunable interacting composite fermion phases in a half-filled bilayer-graphene landau level. *Nature*, 549:360, Sep 2017.

[326] A. A. Zyuzin and A. A. Burkov. Topological response in weyl semimetals and the chiral anomaly. *Phys. Rev. B*, 86:115133, Sep 2012.